Universität Rostock Traditio et Innovatio

Methods for the Design and Analysis of Higher-Order Mode Couplers applied to Superconducting Accelerating Structures

Dissertation
submitted to the
Faculty of Computer Science and Electrical Engineering
of the University of Rostock, Germany
for the degree of
Doctor of Engineering (Dr.-Ing.)

Rostock, June 24, 2020

put forward by
Kai Papke, born on February 13, 1986 in Grevesmühlen, Germany

https://doi.org/10.18453/rosdok_id00002899

Date of submission: 24.06.2020
Date of oral examination: 26.11.2020

Referees:

Dr. Frank Gerigk, European Organization for Nuclear Research (CERN)
Prof. Dr. Ursula van Rienen, University of Rostock
Prof. Dr. Thomas Eibert, Technical University of Munich

Abstract

Higher-order modes (HOMs) may affect beam stability and refrigeration requirements of superconducting proton linacs such as the SPL which is being studied at CERN as a driver for future neutrino programs. One option being considered to limit these effects is the use of coaxial HOM couplers mounted on the cutoff tubes of the five-cell cavities.

In this work, potentially dangerous modes are analyzed and corresponding damping requirements defined, primarily on the basis of longitudinal beam dynamics and eigenmode simulations. A novel approach is worked out to characterize entire HOM spectra based on truncated wake potentials and an extended formulation of vector fitting.

The design process of coaxial HOM couplers is examined under new aspects. The first contribution to systematically design coaxial microwave filters on the basis of filter functions is elaborated. Prior to this are empirical studies of certain microwave structures that have not yet been well understood. Furthermore, the problem of transmission zeros inherent to cutoff tubes is formulated.

Finally, coaxial HOM couplers are discussed in a more general context. Besides the characteristic frequency response, the designs of several HOM couplers applied to SPL cavities are investigated and compared in terms of mode damping, mechanical tolerances, thermal loads, structural deformations, and multipacting. Some of the computational analyses are validated by prototype measurements.

Zusammenfassung

Moden höherer Ordnung (HOMs) können einen beträchtlichen Einfluss auf die Strahldynamik und Kühlanforderungen supraleitender Linearbeschleuniger ausüben, wie dem SPL, der im Rahmen einer Studie für zukünftige Neutrino-Experimente am CERN untersucht wurde. Um Auswirkungen entsprechender Moden zu begrenzen, sind koaxiale HOM Koppler an den Grenzhohlleitern der Beschleunigerresonatoren vorgesehen.

Im Rahmen dieser Arbeit wurden potentiell gefährliche Moden analysiert und entsprechende Dämpfungsanforderungen definiert basierend auf Simulationen der Strahldynamik und Eigenmoden. Die Ausarbeitung einer neuen Methode ermöglicht zudem die Charakterisierung ganzer Modenspektren ausgehend von begrenzten Wakepotentialen und einer erweiterten Formulierung des sogenannten Vektor-Fittings.

Der Entwurf koaxialer HOM-Koppler wurde unter neuen Gesichtspunkten aufgegriffen. Ein erster Beitrag zur Synthese von Filterfunktionen anhand koaxialer Hochfrequenzstrukturen wird vorgestellt. Diesem gehen empirische Untersuchungen bestimmter Strukturen voraus, deren Streueigenschaften noch nicht vollständig verstanden sind. Weiterhin wurde das Problem von Transmissionsnullstellen bedingt durch Grenzhohlleiter behandelt.

Verschiedene für SPL vorgesehene HOM-Koppler wurden außerdem untersucht und verglichen. Neben dem charakteristischen Frequenzverhalten werden die Modendämpfung, mechanische Toleranzen, das thermische Verhalten, strukturmechanische Verformungen sowie Multipacting berücksichtigt. Letzteres steht im Zusammenhang mit Entladungseffekten die in Hochfrequenzstrukturen auftreten können bedingt durch Sekundäremission und die damit verbundene lawinenartige Zunahme von Elektronen. Die betrachteten numerischen Simulationen sind in Teilen durch entsprechende Messungen an Prototypen validiert.

To My Parents

To Masi

Acknowledgments

I would like to thank my supervisors Ursula van Rienen and Frank Gerigk for giving me the opportunity to carry out this thesis, for their patience, vision, and encouragement over the years. Their guidance and invaluable experience allowed me to develop my career in the field of accelerator physics. I am indebted to Thomas Eibert for his agreement to be referee and for his interest in the subject. The thesis was carried out in part in the framework of the Gentner Program provided the German Federal Ministry of Education and Research (BMBF), and excellently managed by Michael Hauschild.

A special gratitude appertains to Rama Calaga, Alexej Grudiev, and Graeme Burt, who certainly take credit for a good portion of this thesis. In countless discussions, they pointed me to interesting problems and avenues, and yet triggered new ideas.

During the exceptional time being part of the RF - Radio Frequency Group at CERN, I appreciated the full support of both the Linacs RF Section and Superconducting RF Cavity Technology Section. In particular, I would like to thank Sarah Aull, Jean-Michel Giguet, Szabina Horvath-Mikulas, Tobias Junginger, Alick Macpherson, and Sotirios Papadopoulos for their help to accommodate my requests. Without the support of Jørgen Apeland, Ofelia Capatina, Luca Dassa, Julien Pascal Dequaire, Thomas Sahner, Nuria Valverde Alonso, and many others of the mechanical engineering and workshop crews, most if not even all of the experimental tests would have simply been thoughts. François Pillon needs a special mention here; I cannot thank him enough for the time and effort he has spent despite a lot of other work.

My gratitude goes to former and present colleagues of the accelerator and bioelectromagnetics teams at the Chair of Electromagnetic Field Theory at University of Rostock. In particular, Thomas Flisgen, Hermann Pommerenke, and Shahnam Gorgi Zadeh have helped me through numerous illuminating discussions and careful reviews.

Sincere apologies go to all those whom I have not been able to name personally here. I would like to assure that your contribution to this dissertation will not be forgotten. Many people accompanied my journey over the past years, some of whom became closest friends. This thesis would have remained a faraway dream without their selfless support and confidence in my capabilities. Most of all thanks must go to my family, my parents, and to Masi, my better half.

Contents

1 Introduction

Particle accelerators have come to play a key role not only in fundamental research but also in industry and medicine. They are used, for example, as a driver for synchrotron radiation, very short coherent laser pulses, or neutron sources with numerous applications involving photon and materials science. Huge particle colliders became an essential means for particle physicists to study elementary particles, as well as the interactions and forces among them. A significant percentage of particle accelerators is being operated for medical purposes, mostly related to diagnostics and treatments with X-rays or electrons. Various therapies have been developed since the 1930s to cure diseases such as cancer without using surgical tools. Among these are the widely applied radiation and hadron therapies. The concept of an energy amplifier that is a sub-critical reactor driven by an energetic particle beam calls for accelerators with unprecedented reliability, and is still the subject of frequent studies. Safe accelerator-driven reactors may produce less long-lived radioactive waste compared to the conventional nuclear power plants. In addition, they may consume very-long-lived elements such as plutonium. This list of applications for particle accelerators is by no means comprehensive but covers some of the main fields.

The longitudinal and transverse emittance growth, distortions of the beam distribution, and beam collective instabilities observed in particle accelerators can be the causes of beam induced electromagnetic fields. These *wake fields* may ultimately limit the beam current, which is usually manifested through various collective effects when ramping up the beam intensity, in particular, for large scale projects. Among these are the Spallation Neutron Source (SNS) [1] at Oak Ridge National Laboratory (ORNL), USA, the European X-ray Free Electron Laser (XFEL) [2] in Germany, or the Large Hadron Collider (LHC) [3] at the European Organization for Nuclear Research (CERN), Switzerland, which all make use of superconducting radio frequency (rf) cavities.[1] It is worthwhile to note that there is a natural phenomenon present in accelerators, called *Landau damping* [4, 5] which causes the damping of coherent instabilities by nonlinear spreads in betatron or synchrotron oscillations. Dedicated devices, for instance, octupole magnets [6], wide-band transverse feedback kickers [7], or the recently investigated radio frequency quadrupole resonator as studied for the Future Circular Collider (FCC) [8, 9] exploit this mechanism in order to enhance the stability range of the particular machine.

[1] The notations radio frequency, high frequency, and microwave frequency are used as synonyms and refer to a range from few tens of megahertz to $\sim$10 GHz for the considered applications.

Naturally, the accelerating rf cavities are strongly interacting with the beam. They are designed for a desired momentum transfer from the fundamental mode to the beam while limiting surface peak fields and losses. However, a bunch of charged particles propagating through a cavity will not only absorb energy from the rf field in order to be accelerated, but it also excites other resonant modes to some extent, which are usually of higher order with respect to the fundamental mode. Depending on the beam spectrum, cavity shape, repetition rate, and bunch pattern, beam induced fields may resonantly accumulate and potentially influence the performance of the cavity or eventually cause the loss of some fraction of the beam current. In order to limit these effects and to avoid beam instabilities, the accelerating cavities are often equipped with *Higher-Order Mode (HOM) couplers* intended to extract a fraction of power associated with corresponding parasitic fields. The most common implementations are waveguides with appropriate cutoff frequencies, coaxial couplers including microwave filters, and the beam pipe. The latter may enclose absorbers to damp potentially dangerous *Higher-Order Modes (HOMs)*. This treatise is focused on the second category of implementations.

1.1 Applications of Coaxial HOM Couplers

Coaxial HOM couplers have been developed for accelerating cavities operating at tens of megahertz up to few gigahertz while the extracted power may reach the level of 1 kW in particular cases. Examples are the 56 MHz cavities of the Relativistic Heavy Ion Collider (RHIC) at Brookhaven National Laboratory in Upton, New York, USA [10], the 400 MHz LHC cavities [11], or the TESLA cavities of the free-electron Laser facility in Hamburg, Germany, operating at 1.3 GHz [12]. Besides accelerating cavities, coaxial HOM couplers are further employed for deflecting type cavities such as the different crab cavities being developed and tested in the frame of the high-luminosity upgrade for LHC [13–16].

These couplers, which are either attached directly to the cavity or to the beam pipe next to the cavity, can have fairly versatile designs, all of which share the challenge of maximizing the coupling to fields over the broad frequency band of concerned HOMs while ensuring certain rejection of the fundamental mode for the particular case. The notation ‘coaxial’ coupler [17, pp. 361] is somewhat confusing since these couplers generally do not provide any concentric geometry. However, they show similarities to coaxial guides, in that they have an inner and outer conductor. To introduce the particular filter characteristic, the microwave structures are comprised of multiple discontinuities along the wave propagation.

A study about a superconducting proton linac (SPL) being operated at CERN will now be introduced. The conceptional design of this particle accelerator constitutes the reference framework of most of the activities in the present treatise.

1.2 SPL Study

The proposal of the Superconducting Proton Linac (SPL) at CERN became very attractive as a potential driver for a neutrino facility after P. Zucchelli published his concept based on beta-decaying radioactive ions [18]. Correspondingly, the first conceptional design report of the SPL in 2000 was mainly influenced by the high beam power needs of a CERN based neutrino factory but also by the idea of reusing existing rf equipment from the decommissioned Large Electron Positron (LEP) collider, for instance, klystrons and waveguides. It is important to note that most resources were oriented towards the LHC for economical reasons. As the possible LHC luminosity upgrades became clearer, the design of the SPL was revised in 2006, also taking into account the needs of other potential users, such as the Isotope-Separation-On-Line Device (ISOLDE) and Radioactive Ion Beam (RIB) facility [19]. An international collaboration was launched by CERN in 2008 to share the work between different accelerator laboratories and institutes [20]. The collaboration meetings with focus on the SPL were the precursor of the Open Collaboration Meeting on Superconducting Linacs for High Power Proton beams (SLHiPP) starting in 2011. Besides the SPL, various other projects were involved such as the European Spallation Source (ESS) in Lund, Sweden, the Multi-Purpose Irradiation Facility (MYRRHA) at Mol, Belgium, the Proton Improvement Plan-II (PIP-II) at Fermilab in Batavia, United States, or the Chinese Accelerator Driven Sub-Critical System (C-ADS) at the Institute of Modern Physics in Lanzhou, China.

In recent years, the SPL, in particular, its low-energy part (LP-SPL), has been investigated as a component of a new LHC injector complex which is shown in Fig. 1.1. The proposal foresees increasing the injection energy of the Super Proton Synchrotron (SPS) from 26 GeV to 50 GeV by replacing the Linac2, PS Booster and PS with, respectively, the Linac4, LP-SPL, and a high-energy PS (PS2). The new injector complex is designed to create bunches of 3.4×10^{11} protons within 3.75 mm mrad in the LHC and, thus, to increase its luminosity by a factor of more

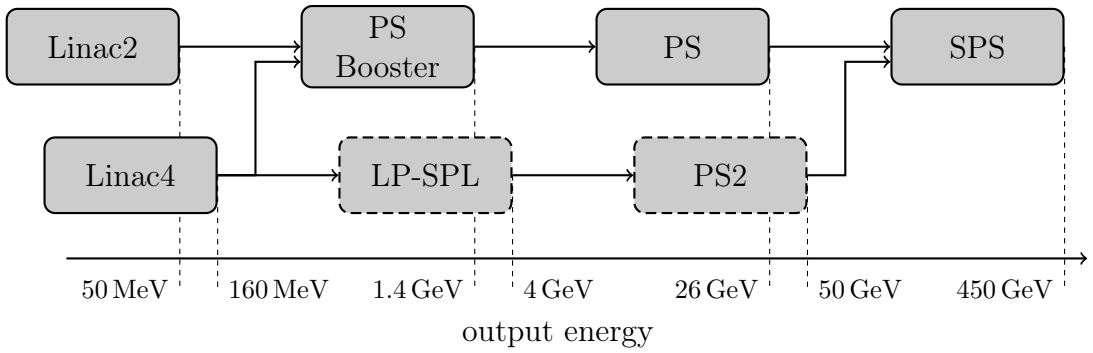

Fig. 1.1. The injector complex of the LHC with alternative concept. In solid, the present accelerators. In dashed, the proposed future accelerators including the low-energy part of the SPL [19].

than two. The normal conducting front-end of the SPL, Linac4 became an integral part of the LHC Injector Upgrade (LIU) Project [21] and will replace the Linac2 after the long shutdown 2 (LS2) between 2019 and 2021. Linac4 will operate as injector for the PS Booster with a maximum average xbeam current of 17.8 µA and a maximum repetition rate of 1.1 Hz. The proton beam is seeded by an H^- ion source and initially accelerated by a radio frequency quadrupole from 45 keV to 3 MeV. Before further acceleration by a Drift Tube Linac (DTL), cell-coupled DTLs, and PI Mode Structures (PIMS), the beam passes a so-called chopper line, also known as the medium energy beam transport section of the Linac4, which forms a specific bunch pattern. The HOM damping requirements for the SPL are significantly influenced by the demand of various chopping patterns requested by the different clients such as LHC, ISOLDE, RIB, and PS2. A superconducting cavity design without the option of installing dedicated HOM damping facilities was, therefore, excluded from the very beginning.

A schematic layout of the SPL according to the latest conceptional design [19] is shown in Fig. 1.2 using the Linac4 as a normal conducting front-end. Energy, pulse length, repetition rate, and beam power of the SPL can be adapted to the needs of many high-power proton beam applications. The high-power version of the SPL (HP-SPL), foreseen as a driver for neutrino facilities, is anticipated to provide a proton beam of 5 GeV energy. For the previously mentioned low-power version as PS2 injector, a proton beam of 4 GeV energy meets the requirements. The current layout further conceives beam ejections at two intermediate stages to drive radioactive ion beam facilities with a proton beam of 1.5 GeV and 2.6 GeV, respectively. In addition, a low-current and high-current version is proposed for the HP-SPL which essentially differs from the LP-SPL with respect to the amount of power delivered to each cavity in order to compensate beam loading. The main parameters of all mentioned SPL versions are summarized in Table 1.1.

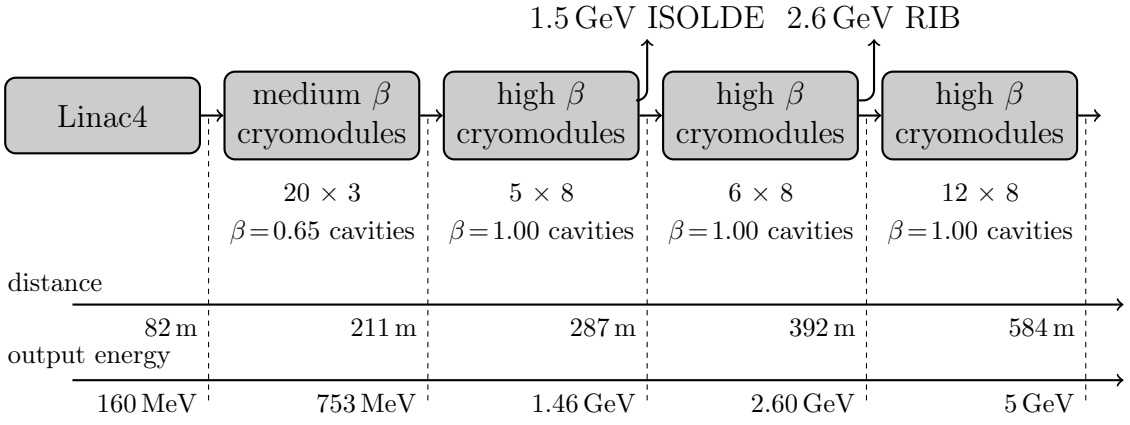

Fig. 1.2. Schematic view of the SPL with the Linac4 as normal conducting front-end. Each cryomodule contains four medium or high-β SPL cavities.

Table 1.1. Nominal beam parameters for the SPL versions†.

Parameter	Units	HP-SPL		LP-SPL
		low-current	high-current	
energy	[GeV]	5	5	4
beam power	[MW]	4	4	0.144
repetition rate	[Hz]	50	50	2
average pulse current	[mA]	20	40	20
peak pulse current	[mA]	32	64	32
source current	[mA]	40	80	40
chopping ratio	[%]	62	62	62
beam pulse length	[ms]	0.8	0.4	0.9
protons per pulse	[10^{14}]	1.0	1.0	1.13

† low-power (LP) and high-power (HP) version.

The superconducting part of the SPL is composed of two types of cavities, both operating at 704.4 MHz in pulsed mode. They are denoted as medium-β and high-β SPL cavities according to their geometric β's of 0.65 and 1, respectively.[2] The superconducting rf cavities, designed by CEA Saclay and IPN Orsay, France, are aimed at accelerating gradients of 19 MV/m and 25 MV/m for the medium-β and high-β type, respectively [23]. Figure 1.3 shows the entire accelerating profile along the SPL. The

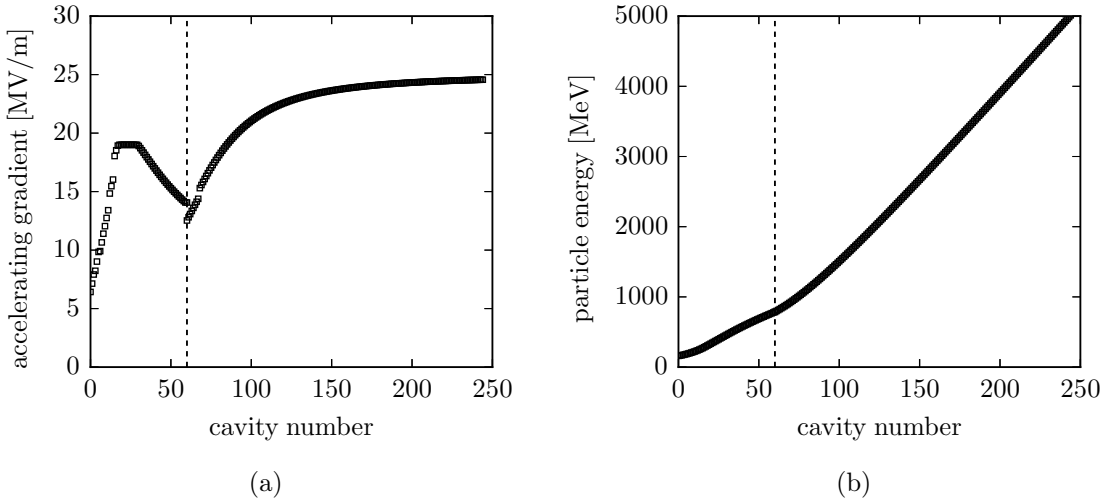

Fig. 1.3. Accelerating profile of the SPL. (a) Accelerating gradient in each cavity and (b) the particle energy evolving along the linac structure. The dashed lines mark the transition between the medium-β and high-β cavity sections.

[2]Here, β is the ratio of the particle velocity and the speed of light. The cavities are designed for specific (geometric) β values but, in operation, they cover a range of particle velocities [22].

challenging gradients are achieved by elliptical multi-cell cavities immersed in liquid helium to operate at a cryogenic temperature of 2 K. The first prototypes have been fabricated by RI Research Instruments GmbH in Bergisch Gladbach, Germany. For the present thesis, several rf measurements of the high-β SPL cavities were carried out and are discussed in Chapter 3. Numerous other institutes and companies were involved in the progress towards a fully dressed SPL cavity. Their contribution is beyond the scope of this thesis and the reader is referred to [19] for further details. The bare cryomodule and a schematic view of the dressed high-β SPL cavity are shown in Fig. 1.4.

In the meantime the option of a LP-SPL as a replacement of the PS-Booster has been superseded by an upgrade of the Booster within the LIU Project. The HP-SPL is no longer actively pursued but remains an option for future physics programs at CERN.

1.3 Objectives and Structure of the Thesis

In particle accelerators, the design of coaxial HOM couplers is often linked to an intuitively chosen topology for the microwave structure being adapted to individual HOM damping needs [24]. Besides the elaboration of corresponding requirements for SPL as well as the design and analysis of appropriate coaxial HOM couplers, the objective of this work is the development of a systematic design procedure for coaxial microwave filters on the basis of filter or transfer functions detached from any predefined topology.

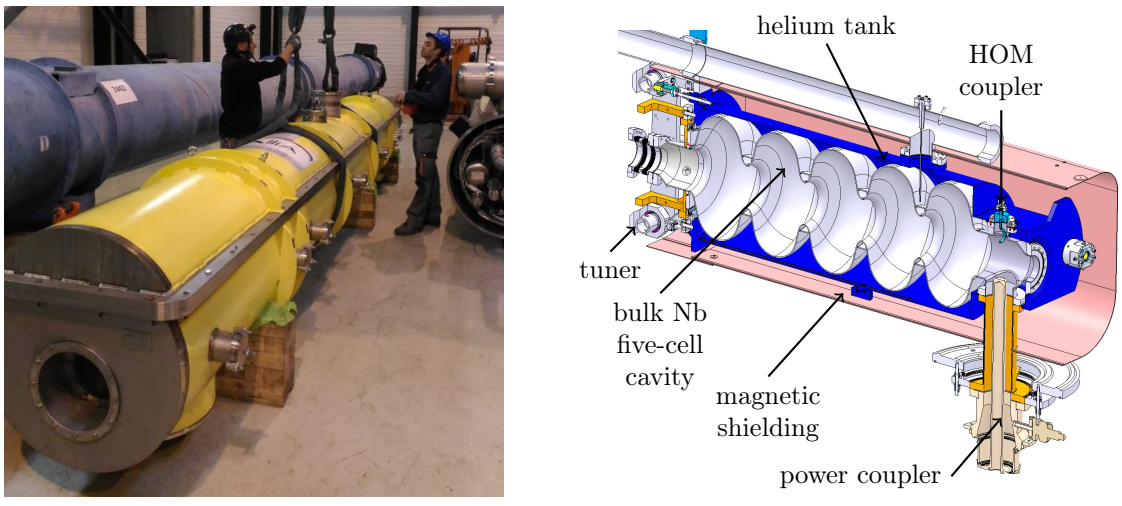

(a) (b)

Fig. 1.4. (a) Cryomodule to house four high-β SPL cavities. (b) Schematic view of the dressed cavity, with one HOM coupler being located on each cutoff tube [19].

For the convenience of the reader, Chapter 2 collects in a more orderly presentation some of the more useful material related to network theory and accelerator physics. Basic ideas of the widely used finite element method are outlined and the different physics problems are discussed to provide the reader with certain background knowledge for the applied numerical simulations. Furthermore, the theory of vector fitting is introduced, a procedure which is frequently used to evaluate simulated or measured scattering functions of resonant microwave structures.

Chapter 3 addresses the various demands made on HOM couplers by means of the SPL. Frequency spectra of both cavity types are analyzed to identify potentially dangerous HOMs. Besides the common approach of using eigenmode simulations, the particular modes are also characterized on the basis of wake field simulations, with the corresponding beam coupling impedances being processed by an extended formulation of vector fitting. The impact of selected modes on the emittance growth along the linac is studied taking into account certain HOM frequency spreads, the beam input jitter, different bunch patterns, as well as amplitude and phase errors of the rf source. In the view of these statistical analyzes and feasibility, fundamental damping and power limits are introduced. Apart from these simulation studies, the results of various low power rf measurements are presented, carried out on high-β SPL cavity prototypes.

Chapter 4 redefines the design process of coaxial HOM couplers in several aspects regarding the rf properties. It may be considered as a general tutorial not being restricted only to the SPL. The scattering properties of certain discontinuities in coaxial guides are investigated, some of which reveal unexpected behavior that is not found in standard textbooks. Furthermore, certain aspects of the antenna penetrating into a waveguide, cutoff tube, or cavity are discussed in the context of mode coupling, in particular, the topic of transmission zeros inherent to cutoff tubes. On the basis of previous results, the synthesis of filter functions by means of coaxial microwave structures is developed. The method is compared to the classical approach using reactance coupled $\lambda/2$ resonators in combination with band-stop filters. A detailed discussion on the topology of appropriate coaxial microwave structures is provided. The novel design procedure is drawn for two examples.

Finally, in Chapter 5, the design of HOM couplers is considered in a more general context. Several designs adapted to the needs of high-β SPL cavities are introduced while pointing out topological peculiarities and their impact on rf properties, in particular, the damping of concerned HOMs. The various coupler designs are further discussed in terms of mechanical tolerances and robustness. Certain heat loads are analyzed to eventually define appropriate mechanisms for the thermalization. Likewise, the multipacting behavior of selected designs is studied. The computational analyses are, in part, accompanied and validated by prototype measurements.

2 Fundamentals

This chapter presents some of the elementary results of network theory and particle accelerator physics that are useful for the study of various problems in the present treatise. Apart from that, details on the applied numerical simulations are provided as well as the theory of a particular data fitting procedure is outlined.

2.1 Elements of Network Theory

A network or circuit is the assembly of elements whose terminals are connected at nodes. It is defined as the collection $\mathcal{N}$ of terminal voltages $v_k(t)$ and currents $i_k(t)$ obeying *Kirchhoff's voltage* and *current law* in each loop or node, respectively. With regard to microwave structures, it is convenient to introduce complex voltages and currents using the Laplace transform according to

$$V_k(s) = \int_{-\infty}^{\infty} v_k(t) e^{-st} dt, \tag{2.1}$$

with the complex frequency s defined as

$$s = \sigma + j\omega. \tag{2.2}$$

It is assumed that $V_k(s)$ and $I_k(s)$ belong to $L^2(j\mathbb{R})$ where $\mathbb{R}$ is the real axis. Consequently, they are quadratically integrable functions, i. e. for the complex voltage

$$V_k : j\mathbb{R} \mapsto \mathbb{C} \text{ square integrable} \iff \int_{-\infty}^{\infty} |V_k(j\omega)|^2 d\omega < \infty. \tag{2.3}$$

Using this notation, the network as a collection $\mathcal{N}$ of complex terminal voltages and currents $V_k(s)$, $I_k(s)$, may be formulated as [25, p. 3]

$$\mathcal{N} \subseteq L^2(j\mathbb{R}, \mathbb{C}^N) \times L^2(j\mathbb{R}, \mathbb{C}^N), \tag{2.4}$$

where N is the number of elements whose terminals are connected at nodes. The considerations are further confined to linear subspaces $\mathcal{N}$, where the set of voltages and currents satisfy homogeneity and additivity properties. Implied by the definition, such linear circuits underlie the *superposition theorem* which can be expressed as follows [26, p. 14]. Let $E_k(s)$ be a voltage excitation inserted at some point in the

network $\mathcal{N}$ and $V_k(s)$ be the corresponding voltage response measured across some element. Furthermore, let $V_l(s)$ be the voltage measured across the same element as before but for a different excitation source $E_l(s)$ inserted at another point of the network. The superposition theorem states that $V_k(s)+V_l(s)$ is the voltage response measured when simultaneously applying the excitations $E_k(s)$ and $E_l(s)$. The same concept can be extended to the current.

Linear circuits not containing any sources, thus denoted as passive networks, are further characterized by the *reciprocity theorem* [27, p. 90]. Let the terminal voltage $V_{kl}(s)$ as measured from the node k to some reference node, be the response to the current excitation at the node l. Then, the reciprocity theorem states that

$$V_{kl}(s) = V_{lk}(s). \tag{2.5}$$

Likewise, the concept can be applied for a voltage source and current measurement.

In the context of equivalent circuits, *Tévenin's theorem* is another important finding of the network theory [27, pp. 90]. Across a pair of terminals, a source whose internal composition is not necessarily known may equivalently be described by a single voltage or current excitation, respectively, in series or shunt with an impedance. This theorem is essential for the various equivalent circuits used to describe the rf behavior of HOM couplers in Chapter 4.

2.1.1 Impedance Function

The ratio of the voltage across an element and corresponding terminal current is defined as the impedance $Z(s)$ of an element, in general, being a function of the complex frequency. Its real and imaginary part are, respectively, denoted as resistance and reactance according to

$$Z(s) = R(s) + jX(s). \tag{2.6}$$

Consequently, a network $\mathcal{N}$ as a collection of terminal voltages and currents may be written as [25, p. 4]

$$\mathcal{N} = \left\{ \begin{pmatrix} \mathbf{Z}(s)\mathbf{I}(s) \\ \mathbf{I}(s) \end{pmatrix} : \mathbf{I}(s) \in L^2(j\mathbb{R}, \mathbb{C}^N) \right\}, \tag{2.7}$$

where $\mathbf{I}(s)$ is the vector of terminal currents and $\mathbf{Z}(s)$ is a matrix of impedance functions associating the voltages and currents for all N elements of the network. In mathematical terms, $\mathcal{N}$ is the graph of the impedance matrix. Similarly, the admittance $Y(s)$ of an element, defined as the ratio of the terminal current to voltage across the element, is characterized by a real conductance and imaginary susceptance according to

$$Y(s) = G(s) + jB(s), \tag{2.8}$$

and yields an alternative formalism to (2.7). Using the vector $\mathbf{V}(s)$ which contains the voltages across all N elements and the corresponding admittance matrix $\mathbf{Y}(s)$ to associate voltages and terminal currents, the network may be written as

$$\mathcal{N} = \left\{ \begin{pmatrix} \mathbf{Y}(s)\mathbf{V}(s) \\ \mathbf{V}(s) \end{pmatrix} : \mathbf{V}(s) \in L^2(j\mathbb{R}, \mathbb{C}^N) \right\}. \tag{2.9}$$

As a consequence of the reciprocity theorem, linear passive networks admit impedance and admittance matrices which are symmetric, hence $\mathbf{Z} = \mathbf{Z}^\mathsf{T}$ and $\mathbf{Y} = \mathbf{Y}^\mathsf{T}$. A particular case is lossless networks containing exclusively reactive elements, i. e. the real parts in (2.6) and (2.8) vanish for all N elements.

The classical *lumped elements*, that are the resistance R, capacitance C and inductance L, constitute the fundamental voltage-current relations of linear passive networks, and are given in the frequency domain by

$$V(s) = RI(s), \qquad I(s) = sCV(s), \qquad V(s) = sLI(s). \tag{2.10}$$

It is worth noting that in spite of the very idealized models, the impedance behavior of discontinuities in microwave structures often allows an equivalent description by lumped circuit elements. Section 4.1 provides detailed studies on this topic with the focus on coaxial microwave structures.

The concept of impedance and admittance is further generalized towards terminal pairs across multiple elements in the network $\mathcal{N}$. By energy conservation, it can be shown that any impedance or admittance functions, given a passive network consisting of lumped elements, is *positive real* [28, pp. 127]. In terms of the impedance function, this means that

$$Z : \mathbb{C} \mapsto \mathbb{C} \text{ positive real} \iff \begin{array}{l} \Re\{Z(s)\} \geq 0 \; \forall \; \sigma \geq 0, \\ \Im\{Z(s)\} = 0 \text{ if } \omega = 0. \end{array} \tag{2.11}$$

Positive realness is both necessary and sufficient for realizability, in the sense that the impedance function can be constructed from a finite number of lumped elements [26, pp. 89]. It is the essential ingredient for the synthesis of filters and frequency selective networks. Some important properties of positive real functions are: (i) The sum of two positive real functions is positive real. (ii) Let $F(s)$ be a positive real function, then $F^{-1}(s)$ and $F(s^{-1})$ are positive real. (iii) Positive real functions cannot have any poles or zeros in the right half plane. They may have simple poles on the imaginary axis with strictly positive residues. (iv) Let $F(s)$ be a positive real rational function. It follows that the degrees of numerator and denominator polynomial differ by at most one.

With the focusing on lossless passive network whose elements are exclusively inductances and capacitances, the immittance $F(s)$, that is either treated as imped-

ance or admittance function, admits the form

$$F(s) = \frac{r_0}{s} + s\sum_{k=1}^{n}\frac{r_k}{s^2+\omega_k^2} + r_\infty s, \tag{2.12}$$

where r_0 and r_∞ are the residues at $s=0$ or $s=\infty$, respectively, while r_k is the residue associated with the conjugated complex pole pair $s = \pm j\omega_k$, if any. Functions of the form (2.12) are characterized by alternating poles and zeros, all being on the imaginary axis. This is a consequence of *Foster's reactance theorem* stating that the reactance X and susceptance B defined on linear, passive, and lossless networks are strictly monotonically increasing functions [29, pp. 230]. Figure 2.1 shows two realizations of an immittance function $F(s)$ whose element values are readily obtained from the residues and poles of a partial fraction decomposition according to (2.12). Another set of realizations known as *Cauer realizations*, is based on continued fraction expansion of $F(s)$ [28, pp. 199]. Using the notation of Pringsheim [30],

$$\beta_0 + \frac{\alpha_1|}{|\beta_1} + \frac{\alpha_2|}{|\beta_2} + \ldots \;\coloneqq\; \beta_0 + \cfrac{\alpha_1}{\beta_1 + \cfrac{\alpha_2}{\beta_2 + \ldots}}, \tag{2.13}$$

a positive real rational function $F(s)$ of degree n, having a pole at $s=0$, may be expanded into a finite continued fraction according to

$$F(s) = e_1 s^{-1} + \frac{1\;|}{|e_2 s^{-1}} + \frac{1\;|}{|e_3 s^{-1}} + \cdots + \frac{1\;|}{|e_n s^{-1}}, \tag{2.14}$$

with positive real coefficients e_k. The single terms alternately correspond to the reactance or susceptance of branches in a ladder circuit as shown in Fig. 2.2(a). The formulation (2.14) is achieved by successively removing a single pole at $s = 0$ and succeeding with the reciprocal of the resultant remainder until the latter vanishes. Note, positive realness implies the continued fraction of a rational function to be

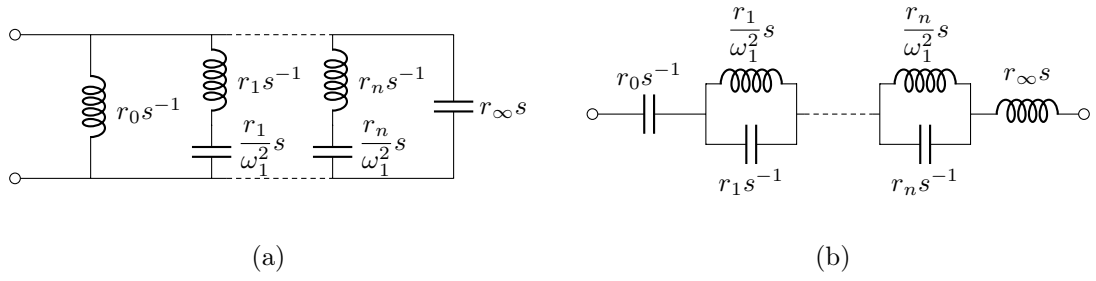

(a) (b)

Fig. 2.1. *Foster realizations* based on partial fraction decomposition according to the expression (2.12), with the immittance function $F(s)$ considered as (a) admittance and (b) impedance.

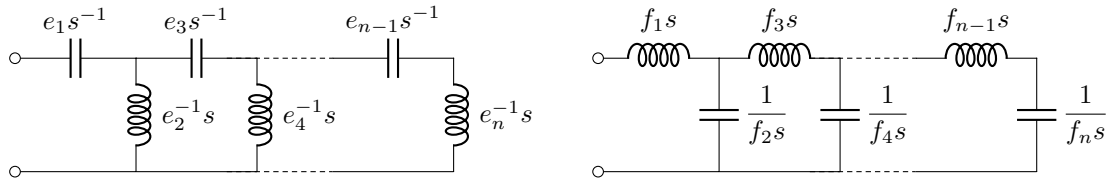

(a) (b)

Fig. 2.2. Equivalent realizations of an impedance function $Z(s)$ providing a pole (a) at $s=0$ and (b) at $s=\infty$. The reactances correspond to the single terms of continued fraction expansions (2.14) and (2.15) based on consecutive pole removal at $s=0$ or $s=\infty$, respectively.

finite. Another continued fraction may be derived by consecutively removing a pole at $s=\infty$, which leads to

$$F(s) = \; f_1 s \; + \frac{1 \;\;|}{|\; f_2 s} + \frac{1 \;\;|}{|\; f_3 s} + \cdots + \frac{1 \;\;|}{|\; f_n s}, \tag{2.15}$$

with positive real coefficients with f_k. The corresponding realization is shown in Fig. 2.2(b) assuming $F(s)$ is an impedance function. The synthesis of impedance and admittance functions is a versatile problem, with the resulting networks being equivalent. Particularly interesting are those solutions which provide the minimum number of elements given by the degree n of the rational function, and are denoted as *canonical networks*. The general strategy is to remove some part from the given realizable function $F(s)$ as partial impedance or admittance associated with a known element or assembly of elements. The process is continued for the leaving remainder until it vanishes as for the continued fraction expansions (2.14) and (2.15). The following properties of positive real functions are relevant for the synthesis and adopted from [26, p. 96].

Property 2.1.1. *Let $F(s)$ be a positive real rational function of degree $n > 1$ with a pole at $s = \infty$. Let the corresponding residue be r_∞. Then*

$$F'(s) = F(s) - r_\infty s \tag{2.16}$$

is a positive real rational function of degree $n - 1$ with no pole at $s = \infty$.

Property 2.1.2. *Let $F(s)$ be a positive real rational function of degree $n > 1$ with a pole at $s = 0$. Let the corresponding residue be r_0. Then*

$$F'(s) = F(s) - \frac{r_0}{s} \tag{2.17}$$

is a positive real rational function of degree $n - 1$ with no pole at $s = 0$.

Property 2.1.3. *Let $F(s)$ be a positive real rational function of degree $n > 2$ with a conjugated complex pole pair at $s = \pm j\omega_k$. Let the corresponding residue be r_k. Then*

$$F'(s) = F(s) - \frac{r_k s}{s^2 + \omega_k^2} \tag{2.18}$$

is a positive real rational function of degree $n - 2$ with no poles at $s = \pm j\omega_k$.

Property 2.1.4. *Let $F(s)$ be a positive real rational function of degree $n \geq 2$ with no zeros at $s = \pm j\omega_k$. If the numerator degree is larger than the denominator degree, then there is a strictly positive residue r_k such that*

$$F'(s) = F(s) - r_k s \tag{2.19}$$

is a positive real rational function of degree n providing zeros at $s = \pm j\omega_k$.

Residues are associated with capacitance and inductances as shown in Fig. 2.1. Property 2.1.4 refers to *zero shifting* which does not remove any pole from the reactance function $F(s)$. It is a preparation step to invoke a conjugated complex pole pair at a desired frequency for the subsequent removal based on Property 2.1.3. A detailed survey about removal of reactance poles is given in [31].

Rational impedance functions as discussed above are a particular case in microwave engineering, for example, to describe waveguide junctions. However, waveguides and micro-strips do not provide impedances which are concentrated in a single location, thus not being lumped. As a consequence, impedance functions are, in general, irrational in the complex frequency variable s, yielding the so-called *distributed elements*. Before continuing with the latter one in Sec. 2.1.5, some basic properties of passive two terminal-pair networks are summarized in the following.

2.1.2 Two-Port

A network whose voltage-current relations are solely known at N distinct terminal-pairs may be described, if any, by a reduced set of impedance or admittance functions similar to (2.7) or (2.9), respectively. However, the network is not completely defined due to missing topology information, which raises the idea of equivalent circuits providing the same voltage-current relations at the given terminal planes. A two terminal-pair structure also denoted as *two-port* is defined as the collection $\mathcal{N}^2$ of complex voltages $V_k(s)$ and currents $I_k(s)$ with $k = 1, 2$ that can appear on its ports,

$$\mathcal{N}^2 \subseteq L^2(j\mathbb{R}, \mathbb{C}^2) \times L^2(j\mathbb{R}, \mathbb{C}^2). \tag{2.20}$$

Given a linear two-port with the notation shown in Fig. 2.3, the relationship between voltages and currents may be described in various ways, each on the basis of the superposition theorem. Let the terminal currents be considered as independent vari-

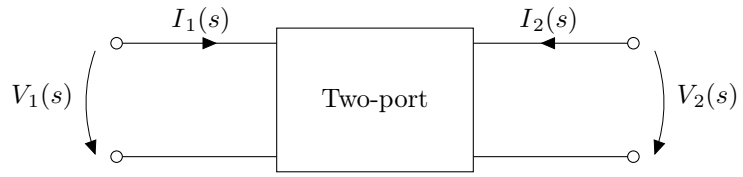

Fig. 2.3. Two-port formalism. Voltages and currents are functions of the complex frequency s.

ables, the corresponding voltages result from an impedance formulation according to

$$\begin{pmatrix} V_1(s) \\ V_2(s) \end{pmatrix} = \begin{pmatrix} z_{11}(s) & z_{12}(s) \\ z_{21}(s) & z_{22}(s) \end{pmatrix} \begin{pmatrix} I_1(s) \\ I_2(s) \end{pmatrix}. \tag{2.21}$$

The matrix is called open-circuit impedance matrix $\mathbf{Z}(s)$ in association with the definition of its elements,

$$\begin{aligned} z_{11}(s) &= \left.\frac{V_1(s)}{I_1(s)}\right|_{I_2=0}, & z_{12}(s) &= \left.\frac{V_1(s)}{I_2(s)}\right|_{I_1=0}, \\ z_{21}(s) &= \left.\frac{V_2(s)}{I_1(s)}\right|_{I_2=0}, & z_{22}(s) &= \left.\frac{V_2(s)}{I_2(s)}\right|_{I_1=0}. \end{aligned} \tag{2.22}$$

The impedance functions z_{11}, z_{22} are called *driving point impedances* while z_{12}, z_{21} are the *transfer impedances*. By focusing on passive two terminal-pair structures, the reciprocity theorem requires $z_{12} = z_{21}$. Assuming the two-port can be realized by a lumped lossless network, each impedance function must admit the form (2.12), with simple poles on the imaginary axis. By energy conservation, it is required that the driving point impedances z_{11} and z_{22} are positive real, thus yielding strictly positive residues $r_{11}^{(k)}$ or $r_{22}^{(k)}$, respectively, where the index k refers to the k^{th} common pole. The residues $r_{12}^{(k)}$ of the transfer impedance function z_{12} where $z_{12} = z_{21}$, is not required to be positive but real. It is subjected to the *residue condition* [32, p. 218]

$$r_{11}^{(k)} r_{22}^{(k)} - {r_{12}^{(k)}}^2 \geq 0. \tag{2.23}$$

In addition to the common set of poles, driving point impedances may provide private poles [26, p. 155]. Similar results are obtained for the admittance formulation, with the port voltages being independent variables while the terminal currents are given by

$$\begin{pmatrix} I_1(s) \\ I_2(s) \end{pmatrix} = \begin{pmatrix} y_{11}(s) & y_{12}(s) \\ y_{21}(s) & y_{22}(s) \end{pmatrix} \begin{pmatrix} V_1(s) \\ V_2(s) \end{pmatrix}. \tag{2.24}$$

The matrix is called short-circuit admittance matrix $\mathbf{Y}(s)$ following the definition of its elements in the analogue way to (2.22). Figure 2.4 shows equivalent two terminal-pair networks based on the impedance and admittance formulation. Except for some simple cases, they are abstract realizations whose elements correspond to networks

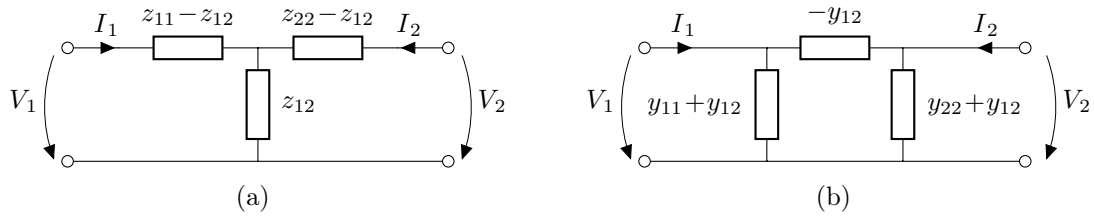

Fig. 2.4. Equivalent circuits for a reciprocal two-port network. (a) T equivalent with open-circuit impedance parameters. (b) Π equivalent with short-circuit admittance parameters.

of lumped elements including coupled inductances [32, p. 224]. The relationship between open-circuit impedance and short-circuit admittance matrix of the same two-port is given by

$$\mathbf{Y}(s) = \mathbf{Z}^{-1}(s). \tag{2.25}$$

It is important to note that the impedance and admittance formalism fail to exist for many two-ports, for instance, the single series impedance Z_s or shunt admittance Y_p as depicted in Figs. 2.5(a) and (b), respectively. While the first admits an admittance matrix as

$$\mathbf{Y}_s(s) = \frac{1}{Z_s(s)} \begin{pmatrix} 1 & -1 \\ -1 & 1 \end{pmatrix}, \tag{2.26}$$

but no appropriate impedance matrix, the two-port constructed from a shunt-admittance function admits an impedance matrix according to

$$\mathbf{Z}_p(s) = \frac{1}{Y_p(s)} \begin{pmatrix} 1 & 1 \\ 1 & 1 \end{pmatrix}, \tag{2.27}$$

but no appropriate admittance matrix. Another formalism, particularly suitable for the concatenation of linear two-ports, relates the voltage V_1 and current I_1 of the first terminal-pair to the voltage V_2 and current I_2 of the second terminal-pair as

$$\begin{pmatrix} V_1(s) \\ I_1(s) \end{pmatrix} = \begin{pmatrix} A(s) & B(s) \\ C(s) & D(s) \end{pmatrix} \begin{pmatrix} V_2(s) \\ -I_2(s) \end{pmatrix}. \tag{2.28}$$

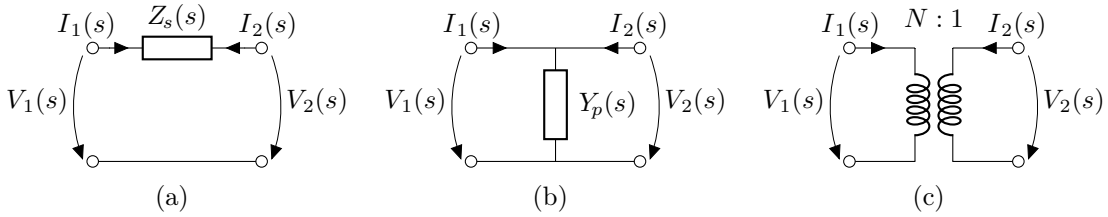

Fig. 2.5. (a) Series impedance two-port. (b) Shunt admittance two-port. (c) Ideal transformer with a turns ratio of N.

The elements of the so-called transmission matrix which is sometimes denoted as $ABCD$ matrix, are defined as [32, pp. 186]

$$A(s) = \left.\frac{V_1(s)}{V_2(s)}\right|_{I_2=0} = \frac{z_{11}(s)}{z_{21}(s)} = -\frac{y_{22}(s)}{y_{21}(s)}, \tag{2.29}$$

$$B(s) = -\left.\frac{V_1(s)}{I_2(s)}\right|_{V_2=0} = -\frac{1}{y_{21}(s)} = \frac{\det \mathbf{Z}(s)}{z_{21}(s)}, \tag{2.30}$$

$$C(s) = \left.\frac{I_1(s)}{V_2(s)}\right|_{I_2=0} = \frac{1}{z_{21}(s)} = -\frac{\det \mathbf{Y}(s)}{y_{21}(s)}, \tag{2.31}$$

$$D(s) = -\left.\frac{I_1(s)}{I_2(s)}\right|_{V_2=0} = -\frac{y_{11}(s)}{y_{21}(s)} = \frac{z_{22}(s)}{z_{21}(s)}. \tag{2.32}$$

A concatenation of two-ports in a chain corresponds to matrix multiplications of their transmission matrices. Reciprocity of passive linear networks is reflected by the condition

$$AD - BC = 1. \tag{2.33}$$

The two-port shown in Fig. 2.5(a) consisting of a series impedance function admits a transmission matrix according to

$$\mathbf{T}_s(s) = \begin{pmatrix} 1 & Z_s(s) \\ 0 & 1 \end{pmatrix}, \tag{2.34}$$

whereas the two-port shown in Fig. 2.5(b) consisting of a shunt admittance function admits a transmission matrix according to

$$\mathbf{T}_p(s) = \begin{pmatrix} 1 & 0 \\ Y_p(s) & 1 \end{pmatrix}. \tag{2.35}$$

The ideal transformer shown in Fig 2.5(c) with a turns ratio N does not permit a formulation by the impedance or admittance matrix according to (2.21) or (2.24), respectively. However, it is well represented by the chain formalism as its transmission matrix takes the form

$$\mathbf{T}_{\text{trafo}} = \begin{pmatrix} N^{-1} & 0 \\ 0 & N \end{pmatrix}. \tag{2.36}$$

The chain formalism is frequently used when dealing with ladder networks as they are essentially a composition of the three two-ports summarized in Fig. 2.5.

2.1.3 Scattering Matrix Formalism

The scattering matrix widely used in microwave engineering [29, pp. 248], provides another formalism to describe two-terminal structures or generally N-ports similar to the impedance, admittance or transmission formalisms. The particular difference

to the previously introduced formalisms is that a scattering matrix always exists for a linear, causal, passive, and time-invariant N-port [33, p. 63].

Instead of considering the voltage $V_k(s)$ and current $I_k(s)$ at the terminal pair k, the incident and reflected waves $a_k(s)$, $b_k(s)$ are introduced according to [25, p. 8]

$$a_k(s) = \frac{1}{2\sqrt{R_k}} \left[V_k(s) + R_k I_k(s) \right] \tag{2.37}$$

$$b_k(s) = \frac{1}{2\sqrt{R_k}} \left[V_k(s) - R_k I_k(s) \right] \tag{2.38}$$

They are measures of the incident and reflected power, which is a more natural choice of physical quantities in the view of microwave structures since voltages and currents are typically not measurable at frequencies where the propagation of electromagnetic waves becomes evident. In the context of power flow, it is appropriate to use the notation terminal planes or ports instead of terminal pairs. It should be noted here that microwave devices such as waveguides do not need to have two conductors in order to transmit or reflect power. According to the definitions (2.37)–(2.38), the incident and reflected power at the terminal plane k are given by $|a_k(s)|^2/2$ and $|b_k(s)|^2/2$, respectively.[1] The resistance R_k is a reference resistance typically associated with a source or load attached to the considered terminal plane.

With the focus on two-ports as depicted in Fig. 2.6, let the incident waves $a_1(s)$, $a_2(s)$ be independent. Then, the scattering matrix $\mathbf{S}$ is defined as

$$\begin{pmatrix} b_1(s) \\ b_2(s) \end{pmatrix} = \begin{pmatrix} s_{11}(s) & s_{12}(s) \\ s_{21}(s) & s_{22}(s) \end{pmatrix} \begin{pmatrix} a_1(s) \\ a_2(s) \end{pmatrix}. \tag{2.39}$$

The matrix elements s_{11}, s_{22} are called reflection coefficients with respect to the particular port while s_{21} and s_{12} are referred to as the transmission coefficients from port 1 to port 2 or vice versa, respectively.

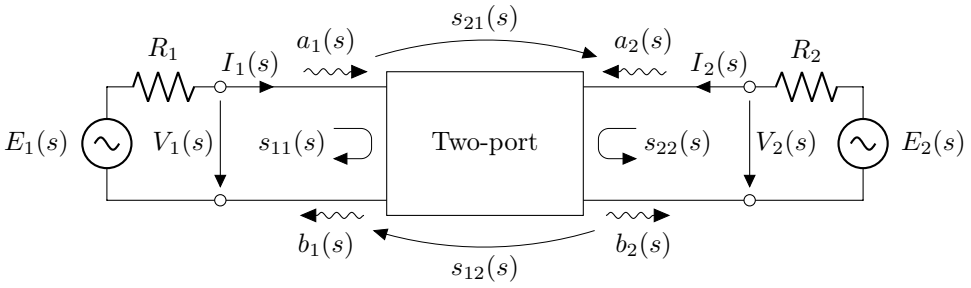

Fig. 2.6. Scattering matrix formalism for a two-port with resistive terminations.

[1] The definitions of incident and reflected waves defer in literature by the normalization which needs to be accounted in the power definition. For instance, Baher [33, pp. 63] omits the factor $1/2$ in (2.37)–(2.38) while Wing [26, pp. 132] adds a factor of $1/\sqrt{2}$.

Under reciprocity, the scattering matrix $\mathbf{S}$ is symmetric, thus $s_{12} = s_{21}$. Based on the definitions (2.37) and (2.38), reflection and transmission coefficients, generally functions of the complex frequency s, are computed under the assumption that the ports are terminated by their particular reference resistance, according to

$$s_{11}(s) = \left.\frac{b_1(s)}{a_1(s)}\right|_{a_2=0} = \left.\frac{b_1(s)}{a_1(s)}\right|_{V_2=-R_2 I_2} = \frac{Z_{\text{in},1} - R_1}{Z_{\text{in},1} + R_1}, \tag{2.40}$$

$$s_{12}(s) = \left.\frac{b_1(s)}{a_2(s)}\right|_{a_1=0} = \left.\frac{b_1(s)}{a_1(s)}\right|_{V_1=-R_1 I_1} = -2\sqrt{R_1 R_2}\left.\frac{I_1(s)}{E_2(s)}\right|_{E_1=0}, \tag{2.41}$$

$$s_{21}(s) = \left.\frac{b_2(s)}{a_1(s)}\right|_{a_2=0} = \left.\frac{b_2(s)}{a_1(s)}\right|_{V_2=-R_2 I_2} = -2\sqrt{R_1 R_2}\left.\frac{I_2(s)}{E_1(s)}\right|_{E_2=0}, \tag{2.42}$$

$$s_{22}(s) = \left.\frac{b_2(s)}{a_2(s)}\right|_{a_1=0} = \left.\frac{b_2(s)}{a_2(s)}\right|_{V_1=-R_1 I_1} = \frac{Z_{\text{in},2} - R_2}{Z_{\text{in},2} + R_2}. \tag{2.43}$$

Here, $Z_{\text{in},k} = V_k / I_k$ is the input impedance seen at the terminal plane k, which must fulfill the requirements of a positive real function (2.11), if the two-port is realizable as equivalently behaving passive networks.

Referring to Fig. 2.6, the term $|s_{21}|^2$ corresponds to the ratio of power delivered to the load R_2 and maximum available power provided by the voltage source $E_1(s)$ taking into account a source resistance R_1. Given the symmetry of a reciprocal behavior, it is denoted as the transmission power gain of the two-port with respect to the resistances R_1 and R_2. Closely related to the transmission coefficient $s_{21}(s)$ of a two-port is the transfer function which is defined as

$$H(s) = \left.\frac{V_2(s)}{E_1(s)}\right|_{E_2=0} = \frac{1}{2}\sqrt{\frac{R_2}{R_1}}\, s_{21}(s). \tag{2.44}$$

The transfer function is typically considered in the design of filters as it permits a convenient way to formulate conditions on the frequency response of desired two-ports without specifying the internal topology. The frequency response is typically described by a filter function $D(j\omega)$ defined on the imaginary axis of the complex s-plane, and is closely related to the magnitude of the transfer function according to [34, pp. 32]

$$|H(j\omega)|^2 = \frac{c_0}{1 + |D(j\omega)|^2}. \tag{2.45}$$

The real scalar c_0 is used for normalization. Consequently, the zeros or poles of the filter function correspond to the frequencies of maximum or vanishing power transfer, respectively. The latter are also referred to as *transmission zeros* [32, pp. 231].

Based on *Tellegen's theorem* [26, pp. 20], the average power delivered to an N-port equals the sum of average power available at all terminal planes, and may be

written as

$$\frac{1}{2}\sum_{k=1}^{N}\Re\{V_k(s)I_k^*(s)\} = \frac{1}{2}(\mathbf{a}^{\mathsf{H}}\mathbf{a} - \mathbf{b}^{\mathsf{H}}\mathbf{b}) = \frac{1}{2}\mathbf{a}^{\mathsf{H}}(\mathbf{I} - \mathbf{S}^{\mathsf{H}}\mathbf{S})\mathbf{a}. \tag{2.46}$$

The vectors $\mathbf{a}$ and $\mathbf{b}$ contain the incident and reflected waves for each terminal plane and $\mathbf{I}$ is the identity matrix. The notation $(.)^{\mathsf{H}}$ refers to the conjugate transpose of a vector or matrix. It follows that the scattering matrix of a loss-less N-port is unitary, that is

$$\mathbf{S}^{\mathsf{H}}(j\omega)\mathbf{S}(j\omega) = \mathbf{I}\ \forall\ \omega \in \mathbb{R}. \tag{2.47}$$

Scattering functions arising from physical networks have similar properties as the impedance and admittance functions discussed in Sec. 2.1.1. Scattering functions are real for real arguments and analytic in the right half plane. Moreover, they are bounded to the closed unit disk for real arguments, hence [26, p. 135]

$$|s_{kl}(s)| \leq 1 \text{ if } \Re\{s\} \geq 0, \tag{2.48}$$

assuming the N-port is passive. This property follows from the positive semi-definite character of the matrix $(\mathbf{I}-\mathbf{S}^{\mathsf{H}}\mathbf{S})$ in (2.46). Any N-port defined on a lossless lumped network admits a real, rational scattering matrix. Conversely, any real, rational scattering matrix can be realized by a network composed of a finite number of lumped elements [35, pp. 90].

Finally, the impedance and admittance matrices can be expressed by *Cayley transforms* of the scattering matrix according to [33, pp. 68]

$$\mathbf{Z} = \mathbf{P}^{\frac{1}{2}}(\mathbf{I}+\mathbf{S})(\mathbf{I}-\mathbf{S})^{-1}\mathbf{P}^{\frac{1}{2}}, \tag{2.49}$$

$$\mathbf{Y} = \mathbf{P}^{-\frac{1}{2}}(\mathbf{I}-\mathbf{S})(\mathbf{I}+\mathbf{S})^{-1}\mathbf{P}^{-\frac{1}{2}}, \tag{2.50}$$

where $\mathbf{P} = \mathrm{diag}\{R_1, R_2, \ldots, R_N\}$ accounts for the reference resistances at each terminal plane. Note, the scattering matrix formalism introduced in this section is referred to N-ports and particularly two-ports with resistive terminations. A generalization towards impedance terminations is given in [26, pp. 139].

2.1.4 Synthesis of Rational Transfer Functions

By referring to Fig. 2.6, synthesis is meant as a systematic procedure to find a realization for the two-port such that a prescribed transmission behavior is achieved, provided the resistive terminations R_1 and R_2. The starting point is the squared magnitude of a rational transfer function according to

$$|H(j\omega)|^2 = \left|\frac{V_2(j\omega)}{E_1(j\omega)}\right|^2_{E_2=0} = \frac{\alpha_0 + \alpha_1\omega^2 + \alpha_2\omega^4 + \ldots + \alpha_m\omega^{2m}}{\beta_0 + \beta_1\omega^2 + \beta_2\omega^4 + \ldots + \beta_n\omega^{2n}}, \tag{2.51}$$

with real coefficients α_i, β_j. It may be derived from an approximation of the desired frequency response. The two-port is considered to be passive, thus reciprocal. From (2.44) and (2.48), it is required that

$$0 \leq |H(j\omega)|^2 \leq \frac{R_2}{4R_1} \; \forall \; \omega \in \mathbb{R}. \tag{2.52}$$

Such transfer functions can be realized by lumped lossless networks as shown by Darlington [36], Cauer [28, pp. 395], and Belevitch [37] among others. Of the various procedures well known in literature, the following synthesis is based on bilateral ladder development of the driving point impedances z_{11}, z_{22}, taking into account the zeros of the transfer impedance z_{21}, associated with transmission zeros [32, pp. 231]. The impedance functions are derived from a specific representation of the scattering matrix introduced by Belevitch [37].

Following (2.44) and the fact that the magnitude of the transfer function is given for purely imaginary arguments s, the transmission power gain may be written as [35, pp. 60]

$$|s_{21}(j\omega)|^2 = 4\frac{R_1}{R_2}|H(j\omega)|^2 = \frac{f(s)f(-s)}{g(s)g(-s)}, \tag{2.53}$$

where $f(s)$ and $g(s)$ are polynomials with real coefficients. More specifically, $g(s)$ is a Hurwitz polynomial, so it does not provide any zeros in the closed right half plane. Under these conditions the transmission coefficient can be defined as $s_{21}(s) = f(s)/g(s)$ keeping in mind that scattering functions of passive networks are bounded to the closed unit disk and analytic in the closed right half plane (Sec. 2.1.3). Assuming a lossless two-port, the reflected power gain is obtained from the unitary condition of the scattering matrix according to (2.47), and may be written as

$$|s_{11}(j\omega)|^2 = 1 - |s_{21}(j\omega)|^2 = \frac{h(s)h(-s)}{g(s)g(-s)}, \tag{2.54}$$

where $h(s)$ is likewise a polynomial of real coefficients. Let the corresponding reflection coefficient be defined as $s_{11}(s) = h(s)/g(s)$. It is important to note that the choice of the polynomials $f(s)$ and $h(s)$ is not unique due to the missing phase information of the transfer function. Available zeros may be freely chosen from the left and right half plane, provided the resultant polynomials are real. Let $f(s)$ be necessarily either an even or odd polynomial ensuring that $h(s)$ and $g(s)$ are relatively prime [38]. Consequently, the relationship between all three polynomials is given by

$$h(s)h(-s) \pm f^2(s) = g(s)g(-s), \tag{2.55}$$

where the upper sign applies when $f(s)$ is an even polynomial while the lower sign corresponds to an odd polynomial $f(s)$. This notation is continued in the following. With these requirements, the lumped lossless two-port admits a scattering matrix

according to [37]

$$\mathbf{S}(s) = \frac{1}{g(s)} \begin{pmatrix} h(s) & f(s) \\ f(s) & \mp h(-s) \end{pmatrix}. \tag{2.56}$$

The open-circuit impedance matrix normalized to the reference resistances R_1 and R_2 is deduced from (2.49). With the argument s being omitted, it becomes

$$\mathbf{P}^{-\frac{1}{2}}\mathbf{Z}\mathbf{P}^{-\frac{1}{2}} = \frac{1}{g-h\mp(g_*-h_*)} \begin{pmatrix} g+h\pm(g_*+h_*) & 2f \\ 2f & g-h\pm(g_*-h_*) \end{pmatrix}, \tag{2.57}$$

where the diagonal matrix $\mathbf{P} = \mathrm{diag}\{R_1, R_2\}$ accounts for the normalization. The subscript asterisk denotes a negative variable as argument, for instance, $g = g(s)$ while $g_* = g(-s)$. A more elegant expression of the impedance matrix is achieved by using one of the input impedances $Z_{\mathrm{in},1}$ or $Z_{\mathrm{in},2}$. From (2.40), the input impedance at port 1 normalized to the reference resistance R_1 may be written as

$$\frac{Z_{\mathrm{in},1}(s)}{R_1} = \frac{1 + s_{11}(s)}{1 - s_{11}(s)} = \frac{g(s) + h(s)}{g(s) - h(s)}. \tag{2.58}$$

Note, the numerator and denominator polynomials appear directly in the impedance formulation (2.57). Splitting them into their even and odd parts according to

$$\frac{g(s) + h(s)}{g(s) - h(s)} = \frac{m_1(s) + n_1(s)}{m_2(s) + n_2(s)}, \tag{2.59}$$

where $m_1(s)$, $m_2(s)$ refer to even polynomials while $n_1(s)$, $n_2(s)$ are odd polynomials, the impedance matrix calculates as either

$$\mathbf{Z} = \frac{1}{n_2(s)} \begin{pmatrix} R_1 m_1(s) & \sqrt{R_1 R_2 e(s^2)} \\ \sqrt{R_1 R_2 e(s^2)} & R_2 m_2(s) \end{pmatrix}, \qquad \text{if } f(s) \text{ even}, \tag{2.60}$$

or

$$\mathbf{Z} = \frac{1}{m_2(s)} \begin{pmatrix} R_1 n_1(s) & \sqrt{-R_1 R_2 e(s^2)} \\ \sqrt{-R_1 R_2 e(s^2)} & R_2 n_2(s) \end{pmatrix}, \quad \text{if } f(s) \text{ odd}. \tag{2.61}$$

The polynomial $e(s^2)$ is denoted as *ensignant* of the rational function (2.59), and is given by [26, pp. 94]

$$e(s^2) = m_1(s)m_2(s) - n_1(s)n_2(s). \tag{2.62}$$

Once the reactance functions z_{11}, z_{22}, and z_{21} are available, both driving point impedances are realized by continued fraction expansions in order to derive a ladder network. The latter becomes, in general, a concatenation of the basic elements shown in Fig. 2.7. The procedure is based on Properties 2.1.1–2.1.4 of positive real functions and the alteration between impedance and admittance function as discussed in Sec. 2.1.1. Note, the ladder development from both ports allows the procedure to account for possible private poles of z_{11} and z_{22}. Furthermore, it in-

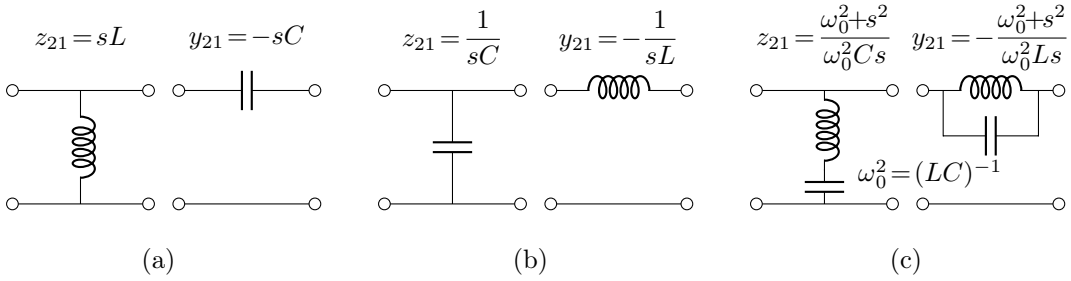

Fig. 2.7. Fundamental lumped two-port networks to construct general ladder network without coupled inductances. Transmission zeros occur (a) at zero frequency (b) at infinity, and (c) at finite, nonzero frequency, taking into consideration that z_{21} or y_{21} must vanish.

creases the accuracy of resultant lumped element values. Transmission zeros at finite, nonvanishing frequency, which correspond to roots of the transfer impedance z_{21}, are respected during the continued fraction expansion by introducing either shunt admittance or series impedance functions according to Fig. 2.7(c), providing pairs of conjugated complex poles at the desired frequencies. Prior to each pole removal at finite, nonzero frequency is a zero shifting step according to Property 2.1.4, such that the reciprocal of the remainder indeed provides the desired conjugated complex pole pair. In the presence of m finite transmission zeros, the order in which they need to be invoked during the realization process is found by [39]

$$\arg\min\left\{\frac{F(j\omega_1)}{j\omega_1},\frac{F(j\omega_2)}{j\omega_2},\ldots,\frac{F(j\omega_m)}{j\omega_m},\lim_{s\to\infty}\frac{F(s)}{s}\right\}, \tag{2.63}$$

This expression is recursively evaluated for the remaining impedance or admittance function, involving only the transmission zeros left over. Various examples are discussed in textbooks, such as Wing [26, pp. 171], Guillemin [32, pp. 237], and Baher [33, pp. 118].

2.1.5 Uniform Transmission Lines

Passive microwave networks describing the behavior of rf devices, such as waveguide filters, antennas, or impedance matching components, generally consist of lumped and distributed elements. The first may be applied to model energy dissipation by resistances or the excitation of evanescent modes at waveguide discontinuities using capacitances or inductances. In contrast, distributed elements are required to model, for instance, the electromagnetic wave propagation in materials. Figure 2.8 sketches a one-dimensional distributed element between two terminal-pairs. The voltage and current are functions of the complex frequency s and longitudinal position z along the element which may be, for example, a coaxial line or waveguide. Other than lumped networks which are describable by rational functions and matrices of one

complex variable, distributed networks yield, in general, functions and matrices of several complex variables. As a consequence of *Maxwell equations*, the equivalent voltage $V(z,s)$ and current $I(z,s)$ obey partial differential equations of the form [40, pp. 7]

$$\frac{\partial V(z,s)}{\partial z} = -jk_z(z,s)Z_c(z,s)I(z,s), \tag{2.64}$$

$$\frac{\partial I(z,s)}{\partial z} = -jk_z(z,s)Y_c(z,s)V(z,s), \tag{2.65}$$

with the characteristic impedance $Z_c(z,s) = V(z,s)/I(z,s)$ and corresponding admittance $Y_c(z,s) = {Z_c}^{-1}(z,s)$ of the transmission line. Eliminating either V or I in (2.64)–(2.65) leads to one-dimensional wave equations where $jk_z(z,s)$ is identified as the complex propagation constant sometimes denoted as γ. Note, the voltage and current are equivalents to electric and magnetic field components of a single propagating mode, that is either transverse electric (TE), transverse magnetic (TM) or transverse electromagnetic (TEM) [35, pp. 125]. In the particular case of uniform lossless transmission lines, with the lines being of equal length, thus being commensurate to the same length l, the characteristic impedance and propagation constant become independent of the longitudinal position z. In literature, such a two-port is called a *unit element*.

The propagation of a transverse electromagnetic wave through a lossless coaxial line of uniform cross-section and filled with homogeneously distributed, isotropic material, is described by a purely imaginary propagation constant according to [41, p. 56]

$$k_z(z,s) = \beta(\omega) = \frac{\omega}{v_{ph}} = \omega\sqrt{\varepsilon\mu}, \tag{2.66}$$

with the permittivity ε and permeability μ given by the material properties and the phase velocity v_{ph} which becomes the speed of light in vacuum. Furthermore, the characteristic impedance is given by

$$Z_c(z,s) = Z_c = \frac{1}{2\pi}\sqrt{\frac{\mu}{\varepsilon}}\ln\frac{r_o}{r_i}, \tag{2.67}$$

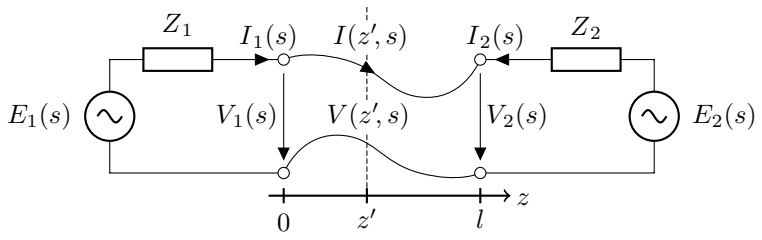

Fig. 2.8. Distributed network between two sources providing internal impedances. Voltage and current are functions of the complex frequency s and longitudinal coordinate z, where $0 \leq z \leq l$.

where r_o and r_i are the outer and inner radii of the coaxial line. The corresponding two-port admits a transmission matrix of the form [33, pp. 134]

$$\mathbf{T}_{\text{UE}}(s) = \begin{pmatrix} \cosh \tau s & Z_c \sinh \tau s \\ Y_c \sinh \tau s & \cosh \tau s \end{pmatrix}. \tag{2.68}$$

Here, the propagation constant is accounted for by the complex frequency s and commensurate one-way delay $\tau = l/v_{ph}$ which is determined by the phase velocity v_{ph} and length of the transmission line, l, as sketched in Fig. 2.8. Two equivalent circuits in T and Π configuration are shown in Fig. 2.9 in correspondence to the abstract realizations depicted in Fig. 2.4 using open-circuit impedance or short-circuit admittance parameters. Note, the transmission matrix of the unit element depends only on one variable. However, its elements are irrational functions of this complex frequency variable s. Using the Richards variable defined as

$$p = \Sigma + j\Omega = \tanh \tau s, \tag{2.69}$$

a frequency mapping as illustrated in Fig. 2.10 is introduced. It allows the representation of the two-port by a rational transmission matrix apart from a factor $\sqrt{(1-p^2)}$, and may be written as

$$\mathbf{T}_{\text{UE}}(p) = \frac{1}{\sqrt{(1-p^2)}} \begin{pmatrix} 1 & Z_c\, p \\ Y_c\, p & 1 \end{pmatrix}. \tag{2.70}$$

It is important to note that the positive real character of driving point impedance and admittance functions is preserved under the frequency transformation (2.69). The right half p-plane maps onto the right half s-plane. Likewise, the real and imaginary axes of the p-plane map onto the corresponding axes in the s-plane. In principle, the same procedure as described in Sec. 2.1.4 may be applied to realize a transfer function, provided that the two-port network consists exclusively of unit elements of the same one-way delay τ. Various examples are provided, among others,

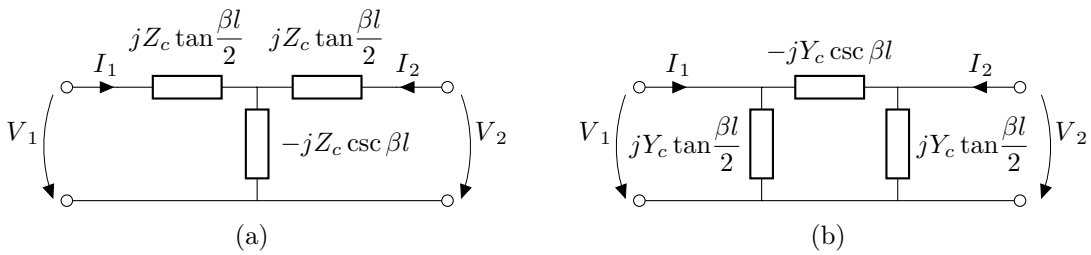

Fig. 2.9. Equivalent circuits for a lossless transmission line describing the propagation of a transverse electromagnetic mode through a uniform coaxial line of length l and characteristic impedance Z_c given by (2.67). (a) T equivalent using impedance functions and (b) Π equivalent using admittance functions [40, p. 12].

by Baher [33, pp. 235]. Referring to Fig. 2.10(b), the frequency response of a commensurate distributed network reveals an inherent periodic behavior with respect to the angular frequency ω. For instance, a low-pass filter will also provide band-pass characteristic in the vicinity of $\omega = k\pi/\tau$ with $k = 1, 2, \ldots$.

The impedance transformation of a unit element is directly deduced from (2.68). Assuming an impedance Z_2 at the output of the two-port, represented by the corresponding voltage-current ratio $Z_2(s) = V_2(s)/I_2(s)$, the impedance seen from the input port calculates as

$$Z_{in,1}(s) = \frac{V_1(s)}{I_1(s)} = Z_c \frac{Z_2 + Z_c \tanh \tau s}{Z_c + Z_2 \tanh \tau s}. \tag{2.71}$$

In case of vanishing real part $\sigma \to 0$, the frequency variable becomes purely imaginary and the input impedance of the unit element can be written as

$$Z_{in,1}(j\omega) = Z_c \frac{Z_2 + jZ_c \tan \beta l}{Z_c + jZ_2 \tan \beta l}. \tag{2.72}$$

The scattering matrix of the unit element, provided the reference resistances at both terminal planes equal the characteristic impedance Z_c of the uniform transmission line, is given by [33, p. 135]

$$\mathbf{S}_{\text{UE}}(s) = \begin{pmatrix} 0 & e^{-\tau s} \\ e^{-\tau s} & 0 \end{pmatrix}. \tag{2.73}$$

Consequently, a unit element yields a phase shift by $\tau\omega = \beta l$ [29, p. 250].

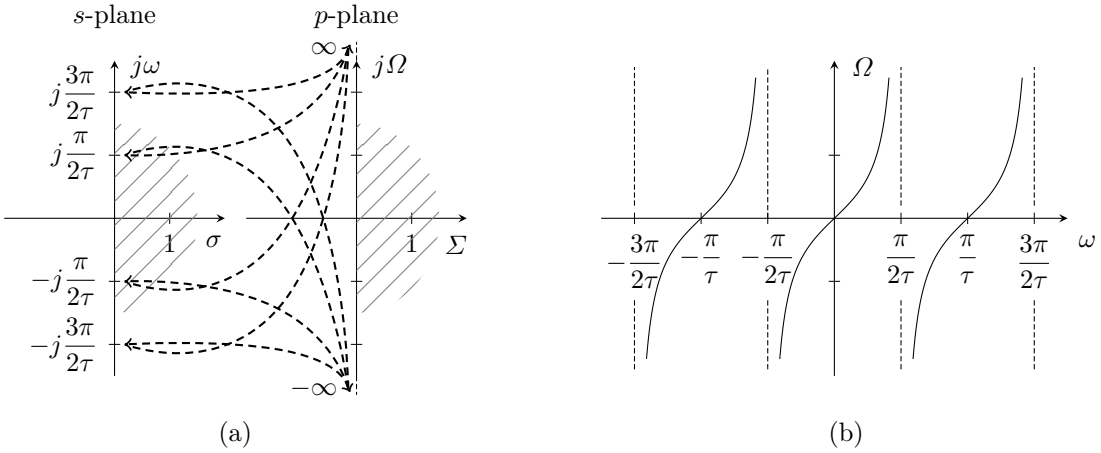

Fig. 2.10. (a) Mapping between the s- and p-plane. The left and right half p-plane, respectively, map onto the left and right half s-plane. The real and imaginary axes of the p-plane map onto the corresponding ones in the s-plane. (b) Mapping between the imaginary axes of both planes.

2.2 Elements of Particle Accelerator Physics

In the following, some fundamental properties of the electromagnetic field in rf cavities are discussed. Important parameters are introduced to describe the coupling between the field and particle bunch. These parameters are typically involved not only in the frame of cavity design but also in the analysis of beam dynamics to derive HOM damping requirements for a stable operation.

2.2.1 Problem Formulation

Let the bunch be characterized by the charge distribution ρ and the electric current density by $\mathbf{j} = \beta c_0 \rho \mathbf{e}_z$ where β is the ratio of the particle velocity to the speed of light c_0 and $\mathbf{e}_z$, the unit vector in z-direction. Here, the z-axis coincides with the longitudinal center axis of the rf cavity as in the example shown in Fig. 2.11. Consequently, let the influence of the wake field on the bunch motion be neglected. The electric and magnetic field intensities $\mathbf{e}$, $\mathbf{h}$, in the cavity which is represented by the domain $\mathbf{\Omega}$, are linked to each other via *Maxwell's equations* according to

$$\begin{aligned} \nabla \times \mathbf{e}(\mathbf{r},t) &= -\frac{\partial}{\partial t}\mathbf{b}(\mathbf{r},t), \quad \nabla \times \mathbf{h}(\mathbf{r},t) = \frac{\partial}{\partial t}\mathbf{d}(\mathbf{r},t) + \mathbf{j}(\mathbf{r},t), \\ \nabla \cdot \mathbf{d}(\mathbf{r},t) &= \rho(\mathbf{r},t), \qquad \nabla \cdot \mathbf{b}(\mathbf{r},t) = 0, \\ \mathbf{b}(\mathbf{r},t) &= \mu \mathbf{h}(\mathbf{r},t), \qquad \mathbf{d}(\mathbf{r},t) = \varepsilon \mathbf{e}(\mathbf{r},t), \qquad \mathbf{r} \in \mathbf{\Omega} \cup \partial\mathbf{\Omega}, \end{aligned} \tag{2.74}$$

with the magnetic flux density $\mathbf{b}$ and the electric displacement $\mathbf{d}$. The permittivity and permeability ε, μ, are equal to the permittivity constant ε_0 and permeability constant μ_0, respectively, since the particle propagation is considered through vacuum. The boundary conditions that specify the solution of the Maxwell equations

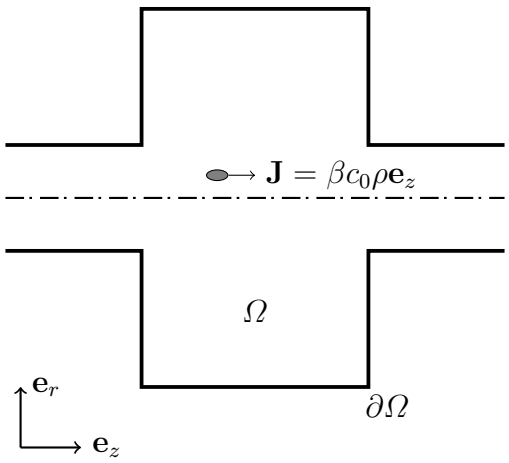

Fig. 2.11. Particle bunch traversing a circular cylindrical cavity with the velocity βc_0 and the charge distribution $\rho(\mathbf{r},t)$.

can be well approximated by

$$\mathbf{n} \times \mathbf{e}(\mathbf{r}, t) = 0, \qquad \mathbf{r} \in \partial\mathbf{\Omega}, \tag{2.75}$$

assuming perfectly conducting walls. The unit vector $\mathbf{n}$ is normal to the surface $\partial\mathbf{\Omega}$. For understanding the behavior of a time-harmonic electromagnetic field in resonant structures it is useful to consider the Fourier transform of (2.74) and (2.75), which leads to the Maxwell equations in phasor notation [42]

$$\begin{aligned} \nabla \times \mathbf{E}(\mathbf{r}) &= -j\omega\mathbf{B}(\mathbf{r}), & \nabla \times \mathbf{H}(\mathbf{r}) &= j\omega\mathbf{D}(\mathbf{r}) + \mathbf{J}(\mathbf{r}), \\ \nabla \cdot \mathbf{D}(\mathbf{r}) &= \mathrm{P}(\mathbf{r}), & \nabla \cdot \mathbf{B}(\mathbf{r}) &= 0, \\ \mathbf{B}(\mathbf{r}) &= \mu\mathbf{H}(\mathbf{r}), & \mathbf{D}(\mathbf{r}) &= \varepsilon\mathbf{E}(\mathbf{r}), & \mathbf{r} &\in \mathbf{\Omega} \cup \partial\mathbf{\Omega}, \end{aligned} \tag{2.76}$$

and

$$\mathbf{n} \times \mathbf{E}(\mathbf{r}) = 0, \qquad \mathbf{r} \in \partial\mathbf{\Omega}, \tag{2.77}$$

with the equivalent phasors of the field quantities in (2.74) assuming sinusoidal time dependence, the angular frequency ω, and the imaginary unit $j = \sqrt{-1}$. The consideration in frequency domain facilitates the description of material properties which are often assumed to be homogeneous and time-invariant but frequency dependent such as the surface impedance of the cavity wall Z_s.[2] The following boundary condition extends (2.75) towards finite electric conductivity in the frequency domain [43]

$$\mathbf{n} \times \mathbf{E}(\mathbf{r}) = Z_s(j\omega)\, \mathbf{n} \times \mathbf{H}(\mathbf{r}) \qquad \mathbf{r} \in \partial\mathbf{\Omega}. \tag{2.78}$$

Furthermore, for rf cavities with a rotational symmetry, it is appropriate to consider the problem in cylindrical coordinates (r, φ, z). In the azimuthal direction φ, the field inside the cavity must be periodic with 2π. Correspondingly, the electromagnetic field in rotational symmetric structures can be decomposed into multipolar components proportional to $\exp(jm\varphi)$ where $m = 0, 1, 2, \ldots$.[3] Depending on the azimuthal periodicity, the field solution is associated with a monopole component ($m = 0$), dipole component ($m = 1$), quadrupole component ($m = 2$), et cetera. Following this approach, the electric field can be expanded by a double Fourier series

$$\mathbf{e}(\mathbf{r}, t) = \frac{1}{4\pi^2} \sum_{m=-\infty}^{\infty} e^{-jm\varphi} \int_{-\infty}^{\infty} \tilde{\mathbf{E}}^{(m)}(r, z, j\omega)\, e^{-j\omega t} d\omega, \tag{2.79}$$

[2] Normal conducting metals such as Cu provide a surface resistance proportional to $\omega^{0.5}$ according to the Skin effect, while Nb in the superconducting state provides a surface resistance proportional to $\omega^{1.3\ldots2}$ depending on the technique used. The electromagnetic properties of superconducting thin-films can be quite different from those of bulk superconductors.

[3] This method is often applied to analyze the field quality in realistic magnets [44, pp. 26-32] and rf cavities [8, 45].

with the Fourier coefficients

$$\tilde{\mathbf{E}}^{(m)}(r,z,j\omega) = \int_0^{2\pi}\int_{-\infty}^{\infty} \mathbf{e}(\mathbf{r},t)e^{j\omega t}e^{jm\varphi}dtd\varphi. \tag{2.80}$$

Similar relations hold for the other field and source quantities. The problem (2.74) and (2.75) is thus simplified to a two dimensional problem in (r,z). Generally, the solution of realistic structures, even if rotational symmetric, requires numerical simulations to be found. It is worthwhile at this point to consider the problem first without sources in order to derive fundamental properties of the electromagnetic field inside rotationally symmetric cavities.

2.2.2 Eigenmodes of a Cavity

Let the cavity be described by a closed metallic structure with vacuum inside. The permittivity and permeability are thus equal to the permittivity and permeability constants ε_0, μ_0, respectively. Furthermore, no sources are considered, hence, $\mathbf{J} = \mathbf{0}, \mathrm{P} = 0$. The problem given in (2.76) and (2.78) can be simplified according to

$$\begin{aligned} -\nabla\times\nabla\times\mathbf{E}(\mathbf{r}) + k^2\mathbf{E}(\mathbf{r}) &= 0, & & \\ \Delta\mathbf{E}(\mathbf{r}) + k^2\mathbf{E}(\mathbf{r}) &= 0, & \mathbf{r}&\in\boldsymbol{\Omega}\cup\partial\boldsymbol{\Omega}, \\ \mathbf{n}\times\mathbf{E}(\mathbf{r}) &= Z_s(j\omega)\,\mathbf{n}\times\mathbf{H}(\mathbf{r}), & \mathbf{r}&\in\partial\boldsymbol{\Omega}. \end{aligned} \tag{2.81}$$

The values $k^2 = \omega^2\varepsilon\mu$ for which the system (2.81) admits nontrivial solutions are called eigenvalues. Correspondingly, the solutions for $\mathbf{E}$ and $\mathbf{H}$ are denoted as electric and magnetic eigenfields, so-called *eigenmodes* or simply modes. A general solution of the interior problem is given, for example, in [46, pp. 297–302] by an expansion of the fields in terms of electric and magnetic eigenvectors. Generally, numerical methods are required to evaluate the eigenmodes in realistic cavities even if rotational symmetric. Qualitative properties of eigenmodes in rotational symmetric structures can be derived in analogy to the problem of the closed circular-cylindrical cavity [47]. This simplest rotational symmetric structure is commonly called a *pill-box* cavity and allows for analytical solutions.

For a pillbox cavity with perfect conducting walls described by (2.77), the solution, either a transverse electric (TE) or transverse magnetic (TM) field, is characterized by discrete propagation constants in the radial and longitudinal directions, k_r, k_z. The azimuthal periodicity leads to the multipolar decomposition as discussed before. The electric and magnetic field components of the TM modes can be expressed as

follows [48, pp. 352–406]

$$E_r^{(m,n,p)} = -E_0 \frac{k_z}{k_r} J'_m(k_r r)\cos(m\varphi)\sin(k_z z), \tag{2.82}$$

$$E_\varphi^{(m,n,p)} = E_0 \frac{m k_z}{{k_r}^2 r} J_m(k_r r)\sin(m\varphi)\sin(k_z z), \tag{2.83}$$

$$E_z^{(m,n,p)} = E_0 J_m(k_r r)\cos(m\varphi)\cos(k_z z), \tag{2.84}$$

$$H_r^{(m,n,p)} = jH_0 \frac{m\omega}{c_0 {k_r}^2 r} J_m(k_r r)\sin(m\varphi)\cos(k_z z), \tag{2.85}$$

$$H_\varphi^{(m,n,p)} = jH_0 \frac{\omega}{c_0 k_r} J'_m(k_r r)\cos(m\varphi)\cos(k_z z), \tag{2.86}$$

where J_m and J'_m are the Bessel function of first kind and m^{th} order and its derivative, respectively, and $E_0 = Z_0 H_0$ with $Z_0 = \sqrt{\mu_0/\varepsilon_0}$, the impedance of free space. To satisfy the boundary condition (2.77), the propagation constants must be chosen such that the tangential electric field at the surface vanishes (2.75). This means for a TM mode in a pillbox cavity of radius R and length L

$$k_r = \frac{j_{mn}}{R},\ n = 1, 2, \ldots, \tag{2.87}$$

$$k_z = \frac{p\pi}{L},\ p = 0, 2, \ldots. \tag{2.88}$$

Here, j_{mn} corresponds to the n^{th} root of the Bessel function of first order and m^{th} mode. The frequency is related to the propagation constants via the dispersion equation according to

$$\omega = c_0 k = c_0 \sqrt{{k_r}^2 + {k_z}^2}, \tag{2.89}$$

with c_0 as the speed of light. Similar results can be obtained for the TE modes.

A resonant mode with specific indices m, n, and p is commonly written as either TE_{mnp} or TM_{mnp}. It is important to note that this classification is only approximately applicable to modes in realistic cavities since finite wall conductivity, smooth transitions between cavity and beam pipe, and inter-mode coupling lead to hybridization between TE and TM modes. A Resonant mode in rf cavities is further classified as either Lower-Order Mode (LOM), Same-Order Mode (SOM), or Higher-Order Mode (HOM). This notation is meant relative to the fundamental mode used for operation, with the mode order being defined via the parameters m, n and p in azimuthal, radial and longitudinal direction, respectively. Note, the fundamental mode is generally not the mode with the lowest frequency or lowest order. Accelerating type rf cavities typically operate in the TM_{010} monopole mode whose frequency can be above the one of the TE_{111} dipole mode. Additionally, there are deflecting type cavities operating in a dipole or quadrupole mode [8, 49]. In multi-cell cavities, the modes are further distinguished by the particular phase advance per cell. The weak coupling between the cells breaks the degeneracy of modes

and causes the formation of passbands, hence modes of the same order (SOM) but with different phase advance per cell. Figure 2.12 shows an equivalent circuit model to describe the coupling between modes within one passband. For a structure with periodic boundary conditions, the following dispersion relation can be derived [50, pp. 75–85]

$$\omega_n = \frac{\omega_{\text{cell}}}{\sqrt{1 + \kappa \cos(\phi_n)}}, \tag{2.90}$$

with the angular resonant frequency of the single cell, ω_{cell}, the cell-to-cell coupling κ, and the phase advance per cell ϕ_n of the mode n in the considered passband. Note, the index n should not be confused with the previous definition introduced in (2.87) as a result of the boundary condition. Equation (2.90) describes the dispersion behavior in multi-cell cavities as long as only adjacent cells couple to each other and the coupling between modes of different bands is negligible. It is worthwhile mentioning that the latter requirement does generally not apply to dipole bands in realistic structures due to the hybridization between TE and TM modes [51].

In realistic structures, the eigenmodes further exhibit certain loss mechanisms which are described by the quality factor or simply Q factor according to

$$Q = \omega \frac{\mathcal{U}}{P_{\text{loss}}}. \tag{2.91}$$

The quality factor is defined as the ratio of the time-averaged energy of the considered mode stored in the cavity, $\mathcal{U}$, and the corresponding energy loss per rf cycle (P_{loss}/ω). The power dissipated into the cavity walls as a result of finite conductivity is associated with the intrinsic quality factor Q_0 while external coupling mechanisms are quantified by the particular external quality factors Q_{ext}. The latter one is related, for instance, to the coupling through the beam pipe, to the fundamental mode coupler, and to HOM couplers. The total quality factor of the considered mode, denoted as the loaded quality factor Q_L, is calculated according to

$$\frac{1}{Q_L} = \frac{1}{Q_0} + \frac{1}{Q_{\text{ext}}}. \tag{2.92}$$

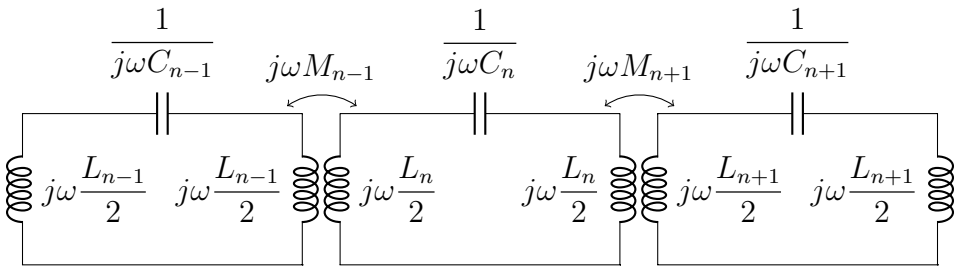

Fig. 2.12. Equivalent circuit of a multi-cell cavity to describe the inter-mode coupling within one passband.

The ratio of the power lost by external coupling mechanisms and the power dissipated within the cavity due to its intrinsic properties is denoted as coupling coefficient κ, and is given by [52]

$$\kappa = \frac{Q_0}{Q_{\text{ext}}}, \tag{2.93}$$

If the cavity is described as a one-port so that power dissipates through only a single terminal plane, the coupling coefficient may be written as [17, p. 154]

$$\kappa = \frac{1 \pm |s_{11}|}{1 \mp |s_{11}|} = \text{SWR}^{\pm 1}, \tag{2.94}$$

with SWR as the voltage standing wave ratio [41, p. 58]. The upper sign applies in case of overcritical coupling which means that more power is lost through the terminal plane than within the cavity. The lower sign applies for undercritical coupling, that is if more power dissipates in the cavity walls than through the port.

It is important to note that the cavity shape shown in Fig. 2.11 can be well represented by a pillbox cavity as long as the considered resonant mode is only weakly damped by fields radiating into waveguide modes of the beam pipe. This again is determined by the (lowest) cutoff frequency of the coupled waveguide modes. Above this threshold the spectrum of the cavity becomes continuous and significantly diverges from the analytic solutions (2.82)–(2.86).

2.2.3 Low Field Surface Impedance of Superconductors

The surface impedance of superconductors exposed to an rf field may qualitatively be understood by the *two-fluid model* [53]. Given a time-varying magnetic field exponentially decaying with the penetration into the superconductor as predicted by the *London equations* [54], the surface impedance of a superconductor can be derived as [55]

$$Z_s = R_s + jX = \frac{1}{2}\omega^2 \mu_0^2 \, \sigma' \lambda_L^3 + j\omega\mu_0\lambda_L, \tag{2.95}$$

where λ_L is the London penetration depth and σ' refers to the electric conductivity in the normal conducting state at the transition temperature. The latter one is related to the purity of the material represented by the residual resistance ratio RRR, and the electric conductivity σ at room temperature, i. e. 293 K, according to

$$\sigma' = \text{RRR}\,\sigma. \tag{2.96}$$

The temperature dependence of the surface resistance R_s may be deduced from the temperature dependence of the penetration depth described by [53, 56]

$$\frac{1}{\lambda_L^2(T)} \propto 1 - \frac{T^4}{{T_c}^4}, \tag{2.97}$$

which applies well near the critical temperature T_c, below which the resistance drops abruptly to zero in the presence of static electric currents. The critical temperature for niobium is about $T_c = 9.2\,\mathrm{K}$. In addition, the proportionality to σ for the real part in (2.95) yields an exponential correlation with the temperature valid for $T < 0.5T_c$, that is

$$R_s \propto \omega^2 \lambda_L^3 \xi \exp\left(-\frac{\Delta}{k_B T}\right) \tag{2.98}$$

Here, Δ refers to the superconducting energy gap, and k_B is the Boltzmann constant. Furthermore, the mean free path of a single electron, ξ, accounts for the material purity according to (2.96). Given the exponential decrease of the surface resistance with the temperature, in order to minimize rf losses in a superconducting cavity, it is preferable to operate them at a low temperature, such as 2 K for SPL cavities.

An implicit formulation for the surface resistance has been worked out by Mattis and Bardeen [57] based on the BCS theory, and allows for quantitative predictions apart from a residual resistance R_{res} typically being in the order of few nanoohms for niobium [58]. Consequently, the surface resistance may be written as

$$R_s = R_{\mathrm{BCS}} + R_{\mathrm{res}}. \tag{2.99}$$

It is important to note that the first term on the right-hand side associated with the BCS theory applies for low fields, that is below 20 mT with respect to niobium [59].

2.2.4 Wake Potentials and Beam Coupling Impedances

The electromagnetic field in a cavity induced by a traversing particle bunch may be expressed as superposition of infinitely many eigenmodes [60]. The mode excitation is essentially determined by the charge and spectrum of the particle bunch. Rather than the wake fields itself, it is more comparative to analyze the force acting back on trailing particles due to the presence of wake fields.[4] This leads to the concept of *wake potentials*.

Let a driving charge q be considered with vanishing transverse dimensions but distributed in the longitudinal direction in which it propagates at the speed of light c_0. Furthermore, let this beam be generally off-centered. Using cylindrical coordinates, the sources in Maxwell's equations (2.74) can be formulated as

$$\rho(r_0, \varphi_0, r, \varphi, \zeta) = \frac{q}{r}\delta(r - r_0)\delta(\varphi - \varphi_0)\lambda(\zeta), \tag{2.100}$$

$$\mathbf{j}(r_0, \varphi_0, r, \varphi, \zeta) = \mathbf{e}_z c_0 \rho(r, \varphi, r_0, \varphi_0, \zeta). \tag{2.101}$$

where r_0 and φ_0 are defined as the radial and azimuthal displacement of the driving beam, $-\zeta = z - c_0 t$ with $\zeta \leq 0$ is the relative longitudinal coordinate to the bunch

[4] In the non-ultra-relativistic case ($\beta < 1$) additional static fields are present which impact not only trailing particles [5, 50, 61].

center (assuming $z = 0$ at the time $t = 0$), and $\lambda(\zeta)$ is the normalized distribution function describing the longitudinal particle bunch profile.

The longitudinal force f_z acting on a trailing point charge q' at $(r,\, \varphi,\, \zeta)$ is represented by the longitudinal wake potential defined as [61, p. 46],

$$w_z(r_0, \varphi_0, r, \varphi, \zeta) = \frac{1}{qq'} \int_{-\infty}^{\infty} f_z(r_0, \varphi_0, r, \varphi, z, c_0 t = z - \zeta)\, dz, \tag{2.102}$$

where f_z is the longitudinal component of the Lorentz force resulting from the solution of the Maxwell (2.74) for the given boundary problem and sources (2.100)–(2.101). The transverse wake potential results in analogue way from the transverse Lorentz force acting on a trailing point charge q' at $(r,\, \varphi,\, \zeta)$. Its components in cylindrical coordinates are defined as,

$$w_{r,\varphi}(r_0, \varphi_0, r, \varphi, \zeta) = \frac{1}{qq'} \int_{-\infty}^{\infty} f_{r,\varphi}(r_0, \varphi_0, r, \varphi, z, c_0 t = z - \zeta)\, dz, \tag{2.103}$$

Note, the transverse wake potential has two orthogonal components which can be chosen as horizontal and vertical, or as radial and azimuthal. For comparative analyses, it is often more suitable to choose the directions such that the transverse components maximize. The relationship between the transverse and longitudinal wake potentials can be expressed as [44, p. 497]

$$\partial_s w_{r,\varphi}(r_0, \varphi_0, r, \varphi, \zeta) = \partial_{r,\varphi} w_z(r_0, \varphi_0, r, \varphi, \zeta), \tag{2.104}$$

with $\partial_u = \partial/\partial u$. Equation (2.104) is often referred to as *Panofsky-Wenzel theorem* [62]. Similar as described in Sec. 2.2.1, the components of the wake potential can be decomposed into multipolar components according to [5, p. 58]

$$w_z(r_0, \varphi_0, r, \varphi, \zeta) = \sum_{m=0}^{\infty} r_0^m r^m w_z^{(m)}(\zeta) \cos(m(\varphi - \varphi_0)), \tag{2.105}$$

$$w_r(r_0, \varphi_0, r, \varphi, \zeta) = \sum_{m=1}^{\infty} m r_0^m r^{m-1} w_r^{(m)}(\zeta) \cos(m(\varphi - \varphi_0)), \tag{2.106}$$

$$w_\varphi(r_0, \varphi_0, r, \varphi, \zeta) = -\sum_{m=1}^{\infty} m r_0^m r^{m-1} w_\varphi^{(m)}(\zeta) \sin(m(\varphi - \varphi_0)). \tag{2.107}$$

In most cases, the longitudinal wake potential is dominated by monopole modes ($m = 0$) while the transverse wake potential is dominated by dipole modes ($m = 1$). Higher-order field components are usually quite weak due to their radial dependency according to $\propto r^m$ or $\propto r^{m-1}$ for the longitudinal or transverse components, respectively [44, 48, 61]. Recalling the pillbox problem, these radial dependencies are reflected in the Bessel functions of the analytic solutions (2.82)–(2.86). Due to

the dominance of monopole and dipole modes, it is appropriate to introduce simplified representations of the longitudinal and transverse wake potentials, respectively, according to

$$w_{\parallel}(\zeta) = w_z^{(m)}(\zeta)|_{m=0}, \tag{2.108}$$

$$w_{\perp}(\zeta) = w_{r,\varphi}^{(m)}(\zeta)|_{m=1}, \tag{2.109}$$

where the latter one, generally, consists of two orthogonal components as mentioned before. If the structure is rotational symmetric, both transverse components are identical. Though the definitions (2.108) and (2.109) only account for bunch induced monopole and dipole modes, they are commonly considered for comparative analyses of general structures. Note, if the transverse beam size is comparable to the size of the beam pipe, quadrupole modes may also drive transverse instabilities so they need to be carefully considered in the cavity design [5].

The longitudinal beam coupling impedance is defined as the Fourier transform of the corresponding wake potential normalized by the current spectrum according to

$$Z_{\parallel}(j\omega) = -\frac{1}{I(j\omega)} \; q \int_{-\infty}^{\infty} w_{\parallel}(t) e^{-j\omega t} dt, \tag{2.110}$$

with the current spectrum

$$I(j\omega) = q \int_{-\infty}^{\infty} \lambda(t) e^{-j\omega t} dt. \tag{2.111}$$

The impedance is thus the Fourier transform of the wake potential which corresponds to a particle bunch of vanishing size, the so-called *wake function*. Equation (2.110) is equivalent to Ohm's law. The minus sign results from the definition of the wake potential, that is the energy gain of a point charge as it passes through the structure. The transverse beam coupling impedance is defined as [61, p. 77]

$$Z_{\perp}(j\omega) = \frac{j}{I(j\omega)} \; q \int_{-\infty}^{\infty} w_{\perp}(t) e^{-j\omega t} dt, \tag{2.112}$$

where the phase shift introduced by the imaginary unit accounts for the fact that a localized transverse force does not change the transverse position of the particle but rather the slope of its trajectory. The relationship between transverse and longitudinal impedances can be derived from (2.104)–(2.112), and is given by

$$Z_{\perp}{}^{(m)}(j\omega) = \frac{c_0}{\omega} Z_{\parallel}{}^{(m)}(j\omega). \tag{2.113}$$

Figs. 2.13 and 2.14 show the longitudinal and transverse impedances of a circular-cylindrical cavity with left-opened beam pipe ports as sketched in Fig. 2.11. Gen-

erally, the impedance spectra of rf cavities are characterized by resonances which become rapidly denser with increasing frequency, while their quality factors tend to decrease and eventually overlap at high frequencies. In particular, this occurs above the lowest cutoff frequency of waveguide modes in the beam pipe. Note, the two structures analyzed in Figs. 2.13 and 2.14 differ only in the radius of the beam pipe, which is for the latter twice as large as for the first one. The impedance drop around 10 GHz in Fig 2.14(b) is related to fields radiating into the beam pipe. It applies likewise to the longitudinal impedance shown in 2.14(a), though the corresponding drop appears smooth rather than abrupt. The pillbox with smaller beam pipe aperture reveals similar beam coupling impedances depicted in Fig. 2.13, however, with the particular impedance drop being at much higher frequency

2.2.5 Resonator Impedance and Shunt Resistance

Narrow band resonances in a cavity can be well approximated by a parallel *RLC* resonator circuit as shown in Fig. 2.15(a). This applies, in particular, to all trapped modes, i.e., modes below the lowest cutoff frequency of waveguide modes in the beam pipe. The equivalence of the narrow band resonances between a cavity and the parallel *RLC* circuit has been derived, for example, in [44, p. 504] and applies to the longitudinal impedance. Accordingly, the contribution of the n-th monopole

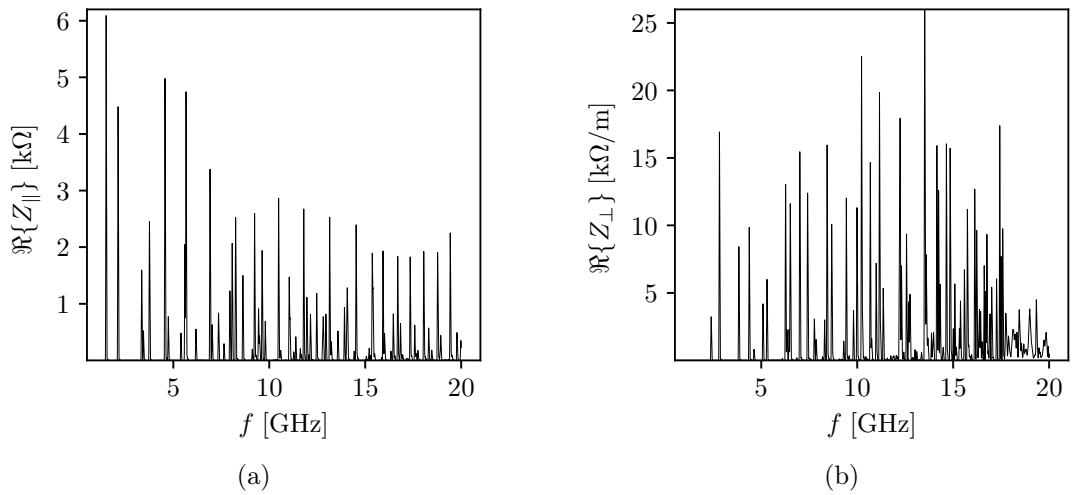

Fig. 2.13. (a) Longitudinal and (b) transverse beam coupling impedances of a circular-cylindrical cavity with left-opened beam pipe ports (cavity diameter = 153 mm, cavity length = 100 mm, beam pipe diameter = 10 mm). The impedances are derived from truncated wake potentials of 100 m length simulated in ABCI [63] with a Gaussian bunch of $\sigma_z = 5$ mm RMS length.

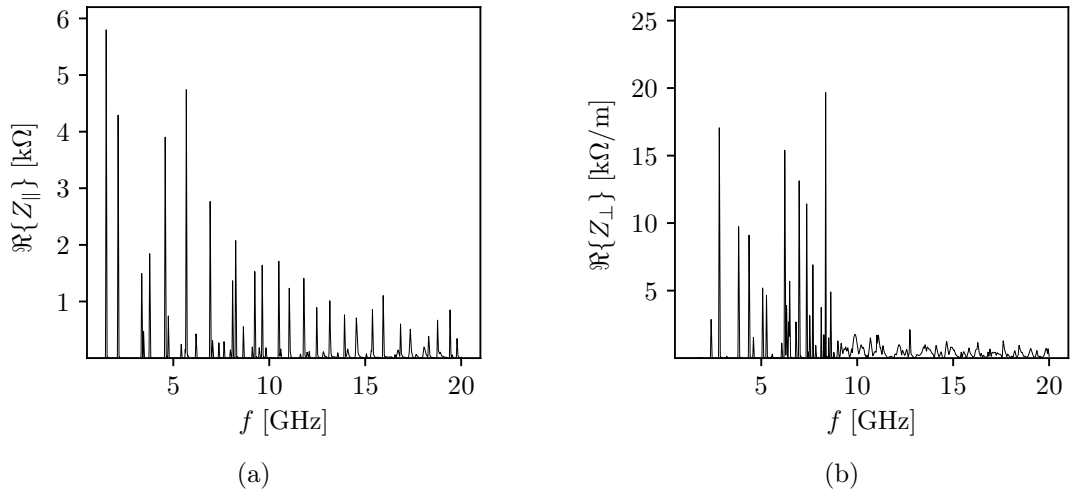

Fig. 2.14. (a) Longitudinal and (b) transverse beam coupling impedances of a circular-cylindrical cavity with left-opened beam pipe ports (cavity diameter = 153 mm, cavity length = 100 mm, beam pipe diameter = 20 mm). The impedances are derived from truncated wake potentials of 100 m length simulated in ABCI [63] with a Gaussian bunch of $\sigma_z = 5$ mm RMS length.

mode to the longitudinal impedance, can be expressed as

$$Z_\parallel = \frac{1}{1/R_n + j\omega C_n - j/(\omega L_n)} = \frac{R_n}{1 + jQ_n\,(\omega/\omega_n - \omega_n/\omega)}, \tag{2.114}$$

with the shunt resistance R_n, the angular resonant frequency $\omega_n = 1/\sqrt{L_n C_n}$, and the quality factor $Q_n = R_n\sqrt{C_n/L_n}$. The transverse impedance follows from (2.113), with the shunt resistance, resonant frequency, and quality factor of a monopole mode being replaced by the corresponding quantities of a dipole mode. It is important to note that the shunt resistance is not a physical resistance as it connects voltage and current of two different phenomena. The voltage $V^{(n)}$ can be correlated to a

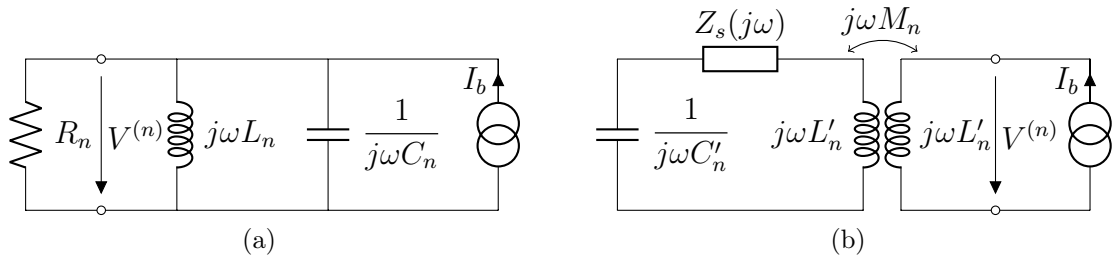

Fig. 2.15. Equivalent circuits to model the narrow-band impedance of a rf cavity for a specific mode. The current source represents the beam. (a) Parallel RLC circuit. The shunt resistance R_n characterizes the interaction between beam and cavity mode. (b) Refined model using a transformer to describe the field coupling. The surface impedance $Z_s(j\omega)$ accounts for wall losses.

mode specific wake potential, that is the voltage induced in the eigenmode n by the particle traversing the cavity. The longitudinal and transverse voltages are defined in analogy to (2.102) and (2.103)

$$V_{\parallel}^{(n)}(r,\varphi) = \frac{1}{q'}\int_{-\infty}^{\infty} F_z^{(n)}(r,\varphi,z)\exp\left(j\frac{\omega_n}{c_0}z\right)dz, \tag{2.115}$$

$$V_{\perp}^{(n)}(r,\varphi) = \frac{1}{q'}\int_{-\infty}^{\infty} F_{r,\varphi}^{(n)}(r,\varphi,z)\exp\left(j\frac{\omega_n}{c_0}z\right)dz, \tag{2.116}$$

where $F_z^{(n)}$ is the longitudinal and $F_r^{(n)}$, $F_\varphi^{(n)}$ are the transverse components of the Lorentz force phasor resulting from the n-th eigenmode and a test particle of charge q' propagating through the structure at the speed of light c_0 and at constant transverse offset. The current flowing through the shunt resistance accounts for any loss mechanism present in the cavity, for instance, the surface currents in the cavity walls induced by the magnetic field or external coupling mechanisms. Hence, for a specific eigenmode n, the shunt resistance associates the power loss of the mode and the longitudinal or transverse voltage experienced by a particle traversing the cavity according to

$$|V^{(n)}|^2 = R_n P_{\text{loss}}^{(n)}. \tag{2.117}$$

Note, (2.117) corresponds to the *linac definition* while the *circuit definition* provides an additional factor of two on the right hand side. Both mechanisms, the energy gain of the particle and the power loss are instantaneously coupled via the wake field, in particular, the magnetic field that induces the surface current in the cavity walls. Figure 2.15(b) shows an equivalent circuit model according to [61, p. 316] using a transformer with a mutual inductance M_n to respect the magnetic field coupling. However, it does not involve loss mechanisms other than the dissipated power into the cavity walls.

To separate the two mechanisms present in the shunt resistance, another quantity, called *geometric shunt resistance*, is typically used in accelerator physics, which describes the beam-mode coupling independent off the losses

$$(R/Q)_n = \frac{R_n}{Q_n} = \frac{|V^{(n)}|^2}{\omega_n \mathcal{U}^{(n)}}, \tag{2.118}$$

where $\mathcal{U}^{(n)}$ is the energy contribution of the mode n stored in the cavity. Note, the linac definition is considered according to (2.117). As the beam coupling impedances, the shunt resistance and geometric shunt resistance are defined for a bunch with vanishing size (point charge) and are related to either the longitudinal or transverse impedance corresponding to (2.115) and (2.116), respectively. Furthermore it is common to express the geometric shunt resistance as a function of the relativistic β, hence the ratio of the particle velocity to the speed of light. In this case, the particle velocity in definitions (2.115)–(2.116) needs to be adapted. Often, the following

alternative definitions are used for the longitudinal and transverse geometric shunt resistances [64]

$$(R/Q)_{\parallel,n}(\varphi,\beta) = \frac{1}{r^{2m}} \frac{|V_{\parallel}^{(n)}(r,\varphi,\beta)|^2}{\omega_n \mathcal{U}^{(n)}}, \tag{2.119}$$

$$(R/Q)_{\perp,n}(\varphi,\beta) = \frac{1}{r^{2m-1}} \frac{|V_{\perp}^{(n)}(r,\varphi,\beta)|^2}{\omega_n \mathcal{U}^{(n)}}. \tag{2.120}$$

The longitudinal and transverse voltage are divided by r^{2m} or r^{2m-1}, respectively, in order to compensate the radial dependency. Consequently, definitions (2.119) and (2.120) only depend on the azimuthal angle and particle velocity. Note, they are mentioned for completeness but not applied in the present treatise. For comparative cavity analyses, it is appropriate to consider the azimuthal angle of maximum geometric shunt resistance independent of the definition used. It is worthwhile to note that the transverse beam displacement, described by the radial displacement r, needs to be taken into account for transverse beam dynamic studies in order to determine the effective impedance of the cavity.

Finally, a few properties of the geometric shunt resistance with respect to monopole and multipole modes are summarized. Taking into account that the longitudinal field components of eigenmodes in rotational symmetric structures are approximately proportional to r^m while the transverse field components are approximately proportional to r^{m-1}, monopole modes ($m = 0$) do not provide any transverse momenta on the beam axis. Consequently, $(R/Q)_{\perp}$ vanishes on the beam axis. Moreover $(R/Q)_{\parallel}$ only marginally varies even for relatively large transverse beam displacements in the order of the beam pipe aperture. Multipolar modes with $m > 0$ do not provide any longitudinal field components on the beam axis, hence, $(R/Q)_{\parallel} = 0$. The transverse geometric shunt resistance of a dipole mode ($m = 1$) is independent of the transverse beam displacement r. It is worth noting that the transverse and longitudinal voltages are directly related to each other via the Panofsy-Wenzel theorem [65]

$$V_{\perp}^{(n)} = j\beta c_0/\omega_n \, \partial_{\rho,\varphi} V_{\parallel}^{(n)}, \tag{2.121}$$

Equation (2.121) is often used in numerical simulations to calculate $(R/Q)_{\perp}$ from the longitudinal field components.

2.2.6 Mode Excitation and Loss Factor

The excitation of eigenmodes in a cavity due to a traversing particle bunch substantially depends on the bunch shape, in particular, on its RMS length since a long bunch does not contain the high frequency components excited by a shorter bunch. Consequently, the parasitic effects of HOMs become more pronounced, the shorter the bunch is. The fraction of energy that a single bunch of charge q loses while

passing the structure is given by [17, p. 333]

$$\Delta\mathcal{E} = -k_{\parallel} q^2, \tag{2.122}$$

where the total *loss factor* $k_{\parallel}$ is the integral of the longitudinal wake potential weighted by the normalized distribution function of the longitudinal bunch profile [61, p. 99]

$$k_{\parallel}(\sigma_t) = \int_{-\infty}^{\infty} w_{\parallel}(\zeta)\lambda(\zeta, \sigma_t)\, d\zeta. \tag{2.123}$$

Note, due to its dependency on the bunch shape, the RMS bunch length σ_t (in time) is typically written as an argument of the loss factor. The meaning of the loss factor becomes more obvious by substituting the longitudinal wake potential in (2.123) by the corresponding impedance using (2.110) and (2.111), which result in

$$k_{\parallel}(\sigma_t) = \frac{1}{2\pi} \int_{-\infty}^{\infty} Z_{\parallel}(j\omega)|\Lambda(j\omega, \sigma_t)|^2 d\omega. \tag{2.124}$$

In other words, the loss factor is the integral of the longitudinal impedance weighted by the normalized power density spectrum of the bunch, $|\Lambda|^2$. The power density spectrum of a Gaussian bunch profile with the RMS length σ_t is proportional to $\exp(\omega^2\sigma_t^2)$. In literature, it is, therefore, often stated that an effective excitation of the monopole n is only possible if the condition $\omega_n \lesssim 1/\sigma_t$ is satisfied [17, 66]. However, this necessary condition should be seen as a rough estimate only. The beam coupling impedances may provide much lower frequency limits than expected from the bunch profile due to external coupling mechanisms as it is the case for the circular symmetric structure studied in Fig. 2.14. In a resonator, the total loss factor can be further expanded into a series of modal loss factors, each of them corresponding to a distinct monopole mode. The relationship between the modal loss factor and the geometric shunt resistance of the mode n is given by [67]

$$k_{\parallel,n} = \frac{\omega_n}{4}(R/Q)_n. \tag{2.125}$$

Note, the linac definition is used according to (2.117).

The *kick factor* $k_{\perp}$ is defined in analogy to (2.123) and (2.124) using the transverse wake potential and impedance, respectively. It describes the transverse momentum change that the bunch experiences while passing through the structure.

2.2.7 Longitudinal Beam Dynamics

The length of a particle bunch is in the order of millimetres whereas the wave lengths are hundreds of times larger, so this allows the greatly simplified description as a point-like charge also known as macro particle. Note, this assumption is valid, in particular, for high-energy proton linacs such as the SPL. Let the longitudinal

voltage be defined according to (2.115). From (2.122) and (2.125) it follows that a point charge q traversing the cavity excites a longitudinal voltage in each TM monopole mode n according to

$$\Delta V_{q,n}(\beta) = -q\,\frac{\omega_n}{4}(R/Q)_n(\beta). \tag{2.126}$$

To ensure energy conservation, the bunch must lose the equivalent amount of energy given by the *fundamental theorem of beam loading* [65]. With the particular mode already present in the cavity, the parasitic energy change of a bunch during the transit and with respect to the mode n can be written as

$$\Delta\mathcal{E}_n(t,\beta) = -q\,\frac{1}{2}\Delta V_{q,n}(\beta) + q\,\Re\{V_n(t,\beta)\}. \tag{2.127}$$

The second term in (2.127), which corresponds to the field already present in the cavity, is object to different damping mechanisms expressed by the loaded quality factor $Q_{L,n}$ of the particular mode according to

$$V_n(t,\beta) = \sum_{k=1}^{N} \Delta V_{q,n}(\beta)\exp\left(-\frac{t-t_k}{\tau_{d,n}}\right)\exp[j\omega_n(t-t_k)]\,\theta(t-t_k), \tag{2.128}$$

with the decay constant $\tau_{d,n} = 2Q_{L,n}/\omega_n$. The sum is taken over all N previous bunches which passed the mid-plain of the cavity at the instances t_k. The function θ represents the Heaviside step function using the maximum convention, $\theta(0) = 1$.

Furthermore, fluctuations in amplitude and phase of the accelerating voltage lead to additional errors in the energy gain per cavity. Note, these rf errors are always present to a certain amount despite the low-level rf system to stabilize the accelerating voltage and lock the phase [19]. The error of the energy gain per cavity due to the fundamental mode can be written as

$$\Delta\mathcal{E}_0(t,\beta) = q\,[V_0(\beta) + \Delta V_0(t)]\cos(\omega_0 t + [\phi_s + \Delta\phi_s(t)]) - q\,V_0(\beta)\cos(\phi_s), \tag{2.129}$$

where V_0 is the nominal accelerating voltage at synchronous phase ϕ_s, ΔV_0 and $\Delta\phi_s$ are the time-dependent fluctuations of the accelerating voltage and synchronous phase, respectively, and $\omega_0 t$ is the arrival phase error of the particle bunch. The fluctuations $\Delta\phi_s$ are also denoted as the jitter provided by the rf source.

The total energy error of a bunch in the m-th cavity is given by [50, p. 166]

$$\Delta\mathcal{E}^{(m+1)}(t,\beta) = \Delta\mathcal{E}^{(m)}(t,\beta) + \Delta\mathcal{E}_0^{(m)}(t,\beta) + \sum_{n=1}^{\infty}\Delta\mathcal{E}_n{}^{(m)}(t,\beta), \tag{2.130}$$

where the sum is typically limited to few modes being particularly close to a harmonic of the bunch or chopping frequency due to the resonance condition of subse-

quent bunches in (2.128). The energy error $\Delta\mathcal{E}^{(m)}$ which is present in front of the cavity m translates into an arrival time error when passing through the drift space towards the next cavity $m+1$. Since the particle velocity is below the speed of light, the energy error is tightly connected to the time of arrival error at each cavity according to

$$\Delta t^{(m+1)} = \Delta t^{(m)} + \left(\frac{dt}{d\mathcal{E}}\right)_{\beta} \Delta\mathcal{E}^{(m)}(t,\beta), \tag{2.131}$$

where the gradient is determined by the drift length between the considered cavities, L, the resting mass of the particle m_0 and its velocity according to

$$\left(\frac{dt}{d\mathcal{E}}\right) = -\frac{L^{(m)}}{m_0 c_0 (\gamma^2-1)^{3/2}}. \tag{2.132}$$

Here, γ is the relativistic factor.

2.3 Numerical Analyses, Techniques, and Algorithms

Apart from the measurements, most analyses across the subsequent chapters are based on computational methods. This section provides a survey of partial differential equations and boundary conditions describing the various problems being assessed by numerical approaches, such as the finite difference and finite element methods, or the finite integration technique [68–70]. Basic ideas of the widely used finite element method are outlined along with an example to provide the reader with certain background knowledge for the applied numerical simulations. Moreover, a particular data fitting procedure is described that is frequently employed to analyze simulated or measured scattering functions of resonant rf structures.

2.3.1 Finite Element Method

The finite element method allows solving partial differential equations computationally, with the solution of the particular problem being approximated by polynomials defined on typically unstructured meshes. Depending on the spatial dimension, the latter are usually composed of line elements, triangles, quadrilaterals, or tetrahedrons [68, pp. 87]. This procedure is appropriate for a wide variety of problems, such as the mode propagation through a waveguide, heat transfer at the surface of an HOM coupler, or the structural deformation of components as a result of thermal contraction. The finite element method is the basis for most of the numerical simulations presented in this treatise.

To illustrate the principles of finite element methods, let the solution $u(x,t)$ be considered, which satisfies the one-dimensional problem

$$\frac{\partial u}{\partial t} + a\frac{\partial u}{\partial x} = 0, \quad a \in \mathbb{R}, \quad x \in \Omega. \tag{2.133}$$

Note, a more detailed discussion of a similar problem provides [71, pp. 1]. The solution $u(x,t)$ as a function of space and time depends on boundary conditions and the initial value $u(x,0)$. To begin with, let the calculation domain Ω_h be discretized into K subdomains or elements according to

$$\Omega \simeq \Omega_h = \bigcup_{k=1}^{K} D^k. \tag{2.134}$$

For each element D^k, the solution is approximated by an ansatz of the form

$$u_h^k(x,t) = \sum_{i=1}^{N_p} u_i^k(t)\ell_i^k(x), \tag{2.135}$$

where the unknown time-dependent coefficients u_i^k define the degrees of freedom while $\ell_i^k(x)$ are chosen as orthogonal nodal basis functions represented by *Lagrange polynomials*. Thus, u_i^k approximates the exact solution $u(x,t)$ at the i-th node x_i of the k-th element D^k as sketched in Fig. 2.16(a). Suitable choices for the basis functions and their representations are discussed in [69, 72]. Furthermore, a residual $R_h^k(x,t)$ is introduced to account for the approximation error in (2.133) according to

$$R_h^k(x,t) = \frac{\partial u_h^k}{\partial t} + a\frac{\partial u_h^k}{\partial x}, \qquad x \in D^k. \tag{2.136}$$

The coefficients u_i^k are determined in a way that the error becomes small. Following *Galerkin*'s approach, this may be achieved by the method of mean weighted residuals, that is

$$\int_{D^k} R_h^k(x,t) \cdot \upsilon_j^k(x)dx = 0, \tag{2.137}$$

with the test functions $\upsilon_j^k(x)$ being from the same set as the basis functions $\ell_i^k(x)$. Equation (2.137) may be written as

$$\int_{D^k} \frac{\partial u_h^k}{\partial t}\ell_j^k + a\frac{\partial u_h^k}{\partial x}\ell_j^k dx = 0, \tag{2.138}$$

which corresponds to a system of first order ordinary differential equations. It is evaluated for each element taking into account a certain coupling between local solutions in order to approximate the exact solution $u(x,t)$ globally. The coupling may be introduced by forcing the numerical solution $u_h(x,t)$ to be continuous across adjacent elements as illustrated in Fig. 2.16(b).

In contrast, the discontinuous Galerkin finite element method uses a numerical flux to imply coupling between neighboring elements. This may be illustrated as follows. By applying *Gauss's theorem* on the second term in (2.138), so that it

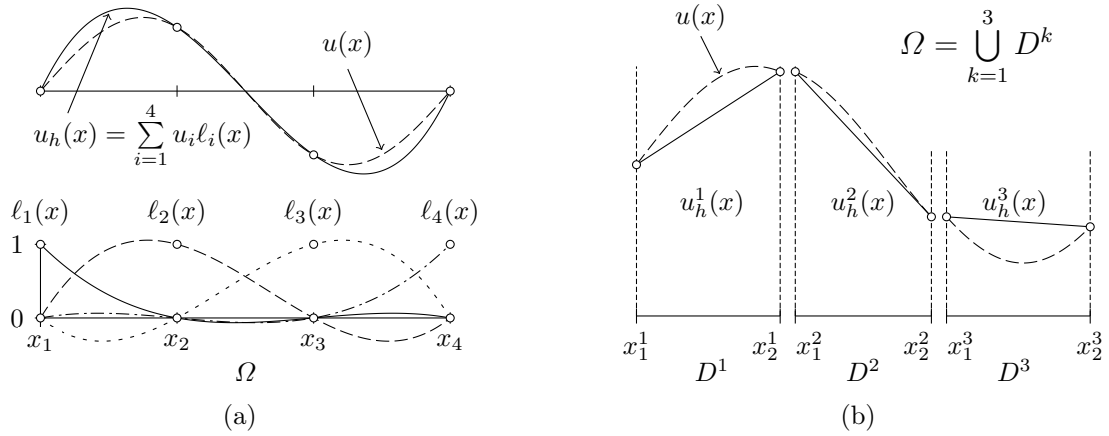

Fig. 2.16. (a) Approximation of the exact solution $u(x) = \sin(x)$ satisfying (2.133) in the computational domain Ω while the time dependence is disregarded. The solution is approximated using Lagrange polynomials $\ell_i(x)$ defined on the set of nodes x_i. (b) Partitioning of the computational domain Ω into three elements D^k, each characterized by two nodes. Note, the elements are only separated for visual reasons. As the basis functions are linear the numerical approximation of the exact solution $u(x)$ becomes piece-wise linear. In this particular example, the approximation $u_h(x)$ is continuous across the elements.

becomes

$$\int_{D^k} \frac{\partial u_h^k}{\partial t} \ell_j^k - a u_h^k \frac{d\ell_j^k}{dx} dx = - \left[a u_h^k \ell_j^k \right]_{x^k}^{x^{k+1}} . \tag{2.139}$$

Though, the present form only considers boundary values of the local element, the resulting right-hand side may be interpreted as information flow across the element surface. By introducing a numerical flux $(a u_h^k)^*$ according to

$$\int_{D^k} \frac{\partial u_h^k}{\partial t} \ell_j^k - a u_h^k \frac{d\ell_j^k}{dx} dx = - \int_{\partial D^k} \mathbf{n} (a u_h^k)^* \ell_j^k dx, \tag{2.140}$$

with $\mathbf{n}$ being the surface normal vector, the coupling between adjacent elements can be achieved. The flux must be defined in a way that it involves the local solutions of both considered elements. Figure 2.17 depicts numerical solutions for the problem (2.133) using different flux definitions which are further discussed in [71, p. 25]. It is seen that the approximate solution is, in general, discontinuous across element interfaces. Applying Gauss's theorem on (2.140) yields

$$\int_{D^k} \frac{\partial u_h^k}{\partial t} \ell_j^k + a \frac{\partial u_h^k}{\partial x} \ell_j^k dx = \int_{\partial D^k} \boldsymbol{n} \left(a u_h^k - (a u_h^k)^* \right) \ell_j^k dx, \tag{2.141}$$

which is known as the strong form of the discontinuous Galerkin finite element scheme [71, p. 8] applied to the problem (2.133).

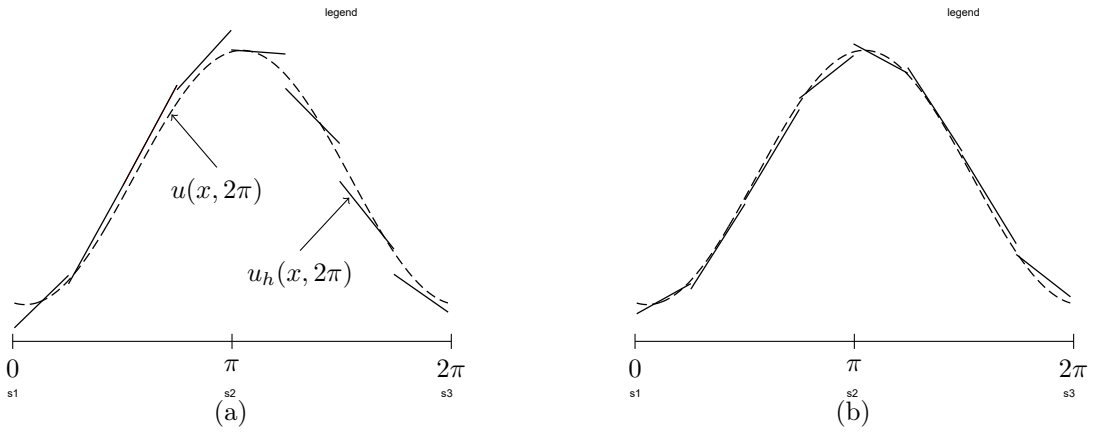

Fig. 2.17. Approximation of the exact solution $u(x,t)$ for the problem (2.133) with $a = 2\pi$ and $u(x,0) = \sin(x)$. The computation domain is split into eight elements of equal length. Using the discontinuous Galerkin finite element method with linear basis functions, two choices for the numerical flux are compared with each other. (a) The *central flux* and (b) *upwind flux* [71, pp. 25].

Equation (2.141) for the element D^k may be written in matrix form as

$$\mathbf{M}^k \frac{d\boldsymbol{u}_{\boldsymbol{h}}^{\boldsymbol{k}}}{dt} + \mathbf{S}^k \boldsymbol{u}_{\boldsymbol{h}}^{\boldsymbol{k}} = \left[\left(a u_h^k - (a u_h^k)^* \right) \boldsymbol{\ell}^{\boldsymbol{k}} \right]_{x^k}^{x^{k+1}} \tag{2.142}$$

where $\boldsymbol{u}_{\boldsymbol{h}}^{\boldsymbol{k}} = [u_1^k, u_2^k, \ldots, u_{Np}^k]^\mathsf{T}$ contains all unknowns at the instant of time while $\boldsymbol{\ell}^{\boldsymbol{k}} = [\ell_1^k, \ell_2^k, \ldots, \ell_{Np}^k]^\mathsf{T}$ is the vector of orthogonal nodal basis functions. Furthermore,

$$\mathbf{M}_{ij}^k = \int_{D^k} \ell_i^k(x) \ell_j^k(x) dx, \quad \mathbf{S}_{ij}^k = \int_{D^k} \frac{d\ell_i^k(x)}{dx} \ell_j^k(x) dx$$

refer to the mass and stiffness matrices, respectively. Similar expressions are found for the continuous Galerkin finite element method, though their detailed implementations notably differ. It is worthwhile to note that nodal basis functions are suitable for scalar problems. In contrast, to solve vector field problems such as the wave propagation in the three-dimensional space, a particular basis which forms the so-called *Nédélec finite element* is usually employed [72, pp. 28].

The discretization of time succeeds via implicit or explicit integration schemes applied to (2.142), for instance, Runge-Kutta, Adams-Bashforth, or the expansion in a Taylor series using higher-order spatial differential operators [73–75].

2.3.2 Electromagnetic Waves and Scattering Functions

Section 2.2 has already dealt with wake fields and eigenmodes of accelerating cavities. Another important analysis comprises the scattering properties and frequency response of rf structures. For this purpose, the Helmholtz equation is solved for a set of discrete frequency points in the range of interest. Using the electric field

intensity, the interior scattering problem is described by

$$\nabla \times \nabla \times \mathbf{E} - k^2 \mathbf{E} = 0, \qquad \mathbf{r} \in \mathbf{\Omega}_{\mathrm{vac}}. \tag{2.143}$$

where the source-free domain $\mathbf{\Omega}_{\mathrm{vac}}$ refers to the inner volume of the considered structure, such as, a cavity or rf filter. For the sake of simplicity, it is assumed to be filled with vacuum. Accordingly, the scattering problem is characterized by the wave number $k = k_0 = \omega/c_0$ where $\omega = 2\pi f$ is the angular frequency.

To account for inward and outward propagating waves across predefined terminal planes, mode specific boundary conditions are applied, which behave approximately like infinitely long waveguides [76]. They are typically restricted to a certain number of propagating modes satisfying two-dimensional Helmholtz equations. For instance, a transverse electric waveguide mode must fulfill the following eigenvalue problem on the particular port boundary $\partial\mathbf{\Omega}_{\mathrm{p}}$,

$$\nabla \times \nabla \times H_\nu \mathbf{n} + (\beta^2 - k_0^2) H_\nu \mathbf{n} = 0, \qquad \mathbf{r} \in \partial\mathbf{\Omega}_{\mathrm{p}}, \tag{2.144}$$

with H_ν being the component of the magnetic field intensity perpendicular to the boundary and in parallel to the normal unit vector $\mathbf{n}$. The generalized index ν specifies the periodicity of the solution in both transverse directions spanning the port boundary.

As for the eigenvalue problem considered in Sec. 2.2.2, energy dissipation implied by surface currents on the interior structure walls is represented by an impedance boundary condition according to

$$\mathbf{n} \times \mathbf{E}(\mathbf{r}) = Z_{\mathrm{s}}\, \mathbf{n} \times \mathbf{H}(\mathbf{r}) \qquad \mathbf{r} \in \partial\mathbf{\Omega}_{\mathrm{solid}} \cap \partial\mathbf{\Omega}_{\mathrm{vac}}. \tag{2.145}$$

It applies to the common boundary between the vacuum filled domain $\mathbf{\Omega}_{\mathrm{vac}}$ and surrounding structure $\partial\mathbf{\Omega}_{\mathrm{solid}}$. The surface impedance of materials such as niobium in the superconducting state has been already outlined in Sec. 2.2.3. For the sake of completion, the surface impedance of normal conductors calculates as [42, p. 429]

$$Z_{\mathrm{s}} = (1 + j)\sqrt{\frac{\mu_0 \omega}{2\sigma}} = \frac{1 + j}{\sigma\delta}, \tag{2.146}$$

with the permittivity constant μ_0, angular frequency ω, electric conductivity σ given by the material, and penetration depth δ.

Furthermore, the SPL cavities including the fundamental mode coupler provide one symmetry plane which allows the application of eigenmode and scattering analyses on half the model. Depending on the excited resonant mode, the tangential components of either the magnetic or electric field may vanish at this symmetry

plane $\partial\mathbf{\Omega}_{\mathrm{sym}}$, that is

$$\mathbf{H}(\mathbf{r}) \times \mathbf{n} = 0, \qquad \mathbf{r} \in \partial\mathbf{\Omega}_{\mathrm{sym}}, \text{ if TE}, \tag{2.147}$$

$$\mathbf{E}(\mathbf{r}) \times \mathbf{n} = 0, \qquad \mathbf{r} \in \partial\mathbf{\Omega}_{\mathrm{sym}}, \text{ if TM}, \tag{2.148}$$

where the unit vector $\mathbf{n}$ is normal to the particular plane. Note, in the presence of HOM couplers, the symmetry conditions do not apply anymore, and the entire model must be considered such as in Sec. 5.2.3.

Finally, given a structure with two terminal planes denoted as port 1 and port 2, the corresponding reflected and transmitted scattering functions, respectively, calculate as

$$s_{11} = \frac{\iint_{\mathrm{p}_1} (\mathbf{E} - \mathbf{E}_{\mathrm{p}_1}) \cdot \mathbf{E}^*_{\mathrm{p}_1} dA}{\iint_{\mathrm{p}_1} \mathbf{E}_{\mathrm{p}_1} \cdot \mathbf{E}^*_{\mathrm{p}_1} dA,} \tag{2.149}$$

$$s_{21} = \frac{\iint_{\mathrm{p}_2} \mathbf{E} \cdot \mathbf{E}^*_{\mathrm{p}_2} dA}{\iint_{\mathrm{p}_2} \mathbf{E}_{\mathrm{p}_2} \cdot \mathbf{E}^*_{\mathrm{p}_2} dA} \tag{2.150}$$

Here, $\mathbf{E}$ is the interior electric field which solves (2.143) and $\mathbf{E}_{p_i}$ refers to the specific waveguide mode satisfying the two-dimensional Helmholtz equation (2.144) at the port boundary $\partial\mathbf{\Omega}_{p_i}$.

2.3.3 Vector Fitting

In this section, the classical and modified formulations of vector fitting by Gustavsen [77, 78] are introduced. Vector fitting is a general and very robust methodology to approximate a measured or calculated frequency response $\{\omega_k, H_k\}_{k=1}^{N_k}$ with a rational function $H(s)$. The original formulation by Gustavsen [77, 79] considers an ansatz of a rational function which is given by a state space representation of a linear system according to

$$s\mathbf{x} = \mathbf{A}\mathbf{x} + \mathbf{b}u(s), \tag{2.151}$$

$$y(s) = \mathbf{c}^{\mathsf{T}}\mathbf{x} + du(s) + sh, \tag{2.152}$$

where u and y are the input or, respectively, output signal given as functions of the complex frequency according to (2.1)–(2.3). Both are linked via the vector of state variables $\mathbf{x}$. The system poles $\{a_n\}_{n=1}^{N}$ in the diagonal matrix $\mathbf{A}$ and the residues $\{c_n\}_{n=1}^{N}$ in the vector $\mathbf{c}$ are either real quantities or come in complex conjugated pairs, while d and h are real quantities. The vector $\mathbf{b}$ contains ones. With these definitions the transfer function as the ratio of the output to the input signal in

frequency domain can be written as

$$H(s) = \mathbf{c}^{\mathsf{T}}(s\mathbf{I} - \mathbf{A})^{-1}\mathbf{b} + d + sh, \tag{2.153}$$

$$= \sum_{n=1}^{N} \frac{c_n}{s - a_n} + d + sh. \tag{2.154}$$

The matrix $\mathbf{I}$ is the identity matrix. It is worth noting that the vectors $\mathbf{b}$ and $\mathbf{c}$ can be chosen differently to obtain (2.154) since the absolute values of the state variables are not important to describe the frequency response. The approximation problem in the least square sense, corresponding to

$$\min_{\{a_n, c_n\}_{n=1}^{N}, d, h} \sum_{k=1}^{N_k} \left| H(s_k) - H_k \right|^2, \tag{2.155}$$

is non-linear due to the unknown poles $\{a_n\}_{n=1}^{N}$ in the ansatz (2.154). Vector fitting solves (2.155) sequentially using a helper function $\sigma(s)$ with a set of known poles $\{\bar{a}_n\}_{n=1}^{N}$ but unknown residues $\{\tilde{c}_n\}_{n=1}^{N}$, such that the augmented least square problem, given by

$$\min_{\{\tilde{c}_n, c_n\}_{n=1}^{N}, d, h} \sum_{k=1}^{N_k} \left| \sigma(s_k) H(s_k) - \sigma(s_k) H_k \right|^2, \tag{2.156}$$

becomes linear in each iteration. This requires that the zeros of $\sigma(s)$ and poles of $H(s)$ exactly cancel out in each iteration. Consequently, the first term in (2.156) can be written as

$$\sigma(s)H(s) = \sum_{n=1}^{N} \frac{c_n}{s - \bar{a}_n} + d + sh. \tag{2.157}$$

The residues of this expression are chosen as identical to the residues of the transfer function $H(s)$ merely for the sake of simplicity. The same applies to the parameters d and h. Once, the augmented problem (2.156) is solved, the zeros of $\sigma(s)$ provide a set of corrected poles used for the subsequent iteration. The helper function is intended to approach one in the considered frequency interval while iterating. Hence, its poles and zeros are anticipated to become approximately identical. The convergence and robustness of the scheme depends very much on the choice of the helper function. The classical vector fitting considers an ansatz according to [77]

$$\sigma(s) = \sum_{n=1}^{N} \frac{\tilde{c}_n}{s - \bar{a}_n} + 1. \tag{2.158}$$

Note, by forcing the helper function to approach unity at very high frequencies, the solution of $\sigma(s)$ in the augmented problem (2.156) becomes unique in each iteration. The modified vector fitting published by Gustavsen [78] greatly improves the convergence and robustness of the scheme by replacing the high-frequency asymptotic requirement in (2.158) with a more relaxed condition using an additional free parameter $\tilde{d}$ in the ansatz of the helper function:

$$\sigma(s) = \sum_{n=1}^{N} \frac{\tilde{c}_n}{s - \bar{a}_n} + \tilde{d}. \tag{2.159}$$

To avoid the trivial null solution of $\tilde{d}$, the augmented least square problem is extended by the equation

$$\Re \left\{ \sum_{k=1}^{N_k} \sigma(s_k) \right\} = N_k, \tag{2.160}$$

which should be weighted in relation to the size of $\{H_k\}_{k=1}^{N_k}$ as described in [78].

The zeros of $\sigma(s)$ and, thus the corrected poles of $H(s)$ can be calculated by solving an eigenvalue problem based on a minimal state space representation [79]. By comparing (2.154) with (2.151)–(2.152), the minimal state space representation of the somewhat more general ansatz of the helper function (2.159) is given by

$$s\mathbf{x} = \bar{\mathbf{A}}\mathbf{x} + \mathbf{b}u(s), \tag{2.161}$$

$$y(s) = \tilde{\mathbf{c}}^{\mathsf{T}}\mathbf{x} + \tilde{d}u(s), \tag{2.162}$$

where the augmented poles and residues $\{\bar{a}_n, \tilde{c}_n\}_{n=1}^{N}$ are contained in the diagonal system matrix $\bar{\mathbf{A}}$ and vector $\tilde{\mathbf{c}}$, respectively. The elements of the vector $\mathbf{b}$ are again arbitrarily chosen to unity in conjunction to the residue vector $\tilde{\mathbf{c}}$. It is a fundamental property of linear systems that the poles of the transfer function are equivalent to the eigenvalues of the corresponding system matrices independent of the particular state space representation. Consequently, the zeros of the helper function $\sigma(s)$ are associated with the eigenvalues of the system matrix which corresponds to a state space representation of $1/\sigma(s)$. This is equivalent to interchanging the input and output signals in (2.161)–(2.162), and leads to

$$s\mathbf{x} = (\bar{\mathbf{A}} - \mathbf{b}\tilde{d}^{-1}\tilde{\mathbf{c}}^{\mathsf{T}})\mathbf{x} + \mathbf{b}\tilde{d}^{-1}y(s), \tag{2.163}$$

$$u(s) = -\tilde{d}^{-1}\tilde{\mathbf{c}}^{\mathsf{T}}\mathbf{x} + \tilde{d}^{-1}y(s). \tag{2.164}$$

Thus, the corrected set of poles is calculated as

$$\mathrm{eig}(\bar{\mathbf{A}} - \mathbf{b}\tilde{d}^{-1}\tilde{\mathbf{c}}^{\mathsf{T}}). \tag{2.165}$$

It is important to note that the particular requirement of vector fitting, that is the poles and residues $\{\bar{a}_n, \tilde{c}_n\}_{n=1}^{N}$ being either real quantities or part of complex conjugated pairs, allows (2.165) to be represented as an eigenvalue problem of a real matrix. This has several numerical advantages concerning the convergence and consistency of corresponding algorithms, and further ensures that the resulting eigenvalues are again either real quantities or come in perfect complex conjugated pairs.

2.3.4 Heat Transfer and Structural Deformation

The temperature distribution inside solid structures, such as the cavity wall or the inner and outer conductor of coaxial HOM couplers, is governed by the *energy conservation law* according to

$$\nabla \cdot (k \nabla T) = \varrho c_p \frac{\partial T}{\partial t}, \qquad \mathbf{r} \in \mathbf{\Omega}_{\text{solid}}, \tag{2.166}$$

where ϱ, c_p and k are the material specific density, heat capacity at constant pressure, and thermal conductivity, respectively. The analyses carried out in Sec. 5.3.3 throughout refer to the stationary case where the right-hand side in (2.166) vanishes. Moreover, the thermal conductivity k generally varies with the temperature and purity of the material. The latter dependence is described by the residual resistance ratio as introduced in Sec. 2.2.3.

Exterior surfaces which are in contact with the helium bath at 2 K, for instance, the cavity wall, are well described by a Dirichlet boundary condition forcing the predefined temperature. More general, the heat transfer to the exterior is determined by the particular convection heat transfer coefficient h_{amb} according to

$$\mathbf{n} \cdot (k \nabla T) = h_{\text{amb}}(T - T_{\text{amb}}), \qquad \mathbf{r} \in \partial\mathbf{\Omega}_{\text{solid}} \setminus \partial\mathbf{\Omega}_{\text{vac}}, \tag{2.167}$$

where T_{amb} is the corresponding ambient temperature. In accordance to the previously introduced notation in Sec. 2.3.2, $\mathbf{\Omega}_{\text{vac}}$ refers to the vacuum filled domain inside the structure so that $\partial\mathbf{\Omega}_{\text{vac}}$ corresponds to the interior surface including eventual terminal planes. In contrast, $\partial\mathbf{\Omega}_{\text{solid}}$ represents the entire structure boundary involving interior and exterior surfaces. For the transition from niobium to liquid or superfluid helium, h_{amb} is basically the Kapitza conductance, measured and published by Saclay in [80].

Interior surfaces exposed to electromagnetic fields receive a net heat flux which is well described by

$$\mathbf{n} \cdot (k \nabla T) = \frac{1}{2} \Re\{Z_{\text{s}}\} |\mathbf{H}|^2, \qquad \mathbf{r} \in \partial\mathbf{\Omega}_{\text{solid}} \cap \partial\mathbf{\Omega}_{\text{vac}}, \tag{2.168}$$

with the frequency dependent surface impedance Z_{s}.

In addition, the right-hand side of (2.167) may be extended by heat radiation. The corresponding heat flux contribution $\mathbf{q}_{\mathrm{rad}}$ satisfies [81, pp. 27]

$$\mathbf{n} \cdot \mathbf{q}_{\mathrm{rad}} = \varepsilon\sigma(T^4 - T_{\mathrm{amb}}^4), \qquad \mathbf{r} \in \partial\mathbf{\Omega}_{\mathrm{solid}} \setminus \partial\mathbf{\Omega}_{\mathrm{vac}}, \tag{2.169}$$

with the material specific emissivity factor ε and σ is the Stefan-Boltzmann constant [82, pp. 724]. It is worth noting that the impact of heat radiation is marginal for all considered problems in Sec. 5.3.

The deformation of an isotropic linear elastic solid with the material specific Youngs modulus E, Poisson ratio ν, and density ϱ is described by *Navier's equations* according to [83]

$$\frac{E}{2(1+\nu)}\left(\frac{1}{1-2\nu}\nabla(\nabla\cdot\mathbf{u}) + \nabla^2\mathbf{u}\right) + \mathbf{f} = \varrho\frac{\partial^2\mathbf{u}}{\partial t^2} \qquad \mathbf{r} \in \mathbf{\Omega}_{\mathrm{solid}}, \tag{2.170}$$

where $\mathbf{u}$ corresponds to the unknown displacement vector field. The force per unit volume due to thermal expansion is given by [84]

$$\mathbf{f} = -\frac{E}{3(1-2\nu)}\alpha_T\nabla T, \tag{2.171}$$

with α_T as the temperature dependent coefficient of linear thermal expansion. In the stationary case, the right-hand side of (2.170) becomes zero. Furthermore, a boundary condition must be added in order to allow for a unique solution. For instance, the structure may be anchored at three points or across symmetry planes.

In order to study the impact of thermal expansion on scattering properties or resonant modes provided by the particular rf structure, it is necessary to transfer the structural displacements onto the interior vacuum filled domain $\mathbf{\Omega}_{\mathrm{vac}}$. Note, the latter constitutes the calculation domain of the electromagnetic field problem, and is naturally not involved in structural simulations. There are various approaches available for this purpose either based on geometry modifications, mesh displacements, or the use of perturbation theory. The latter approach is usually restricted to small deformations, however explicit changes of the geometry or mesh are generally applicable. A detailed study on this subject provides [85]. In the frame of thermal contraction analyses presented in Sec. 5.3.3, the evaluated structural deformations are directly transferred onto the mesh associated with $\mathbf{\Omega}_{\mathrm{vac}}$. The displacement field at the interior surface is used as a boundary condition for moving nodes of the enclosed mesh. A particular difficulty is the treatment of terminal planes as they are not bounded by the solid part. Consequently, there is no solution for the displacement vector field $\mathbf{u}$ available that could serve as a boundary condition for eventual mesh deformations. However, keeping the ports at their original position may yield artificial rf reflections due to mesh distortions. To move such open boundaries consistently with the surrounding structure, the displacement vector field $\mathbf{u}$ within the

particular port surface $\partial\mathbf{\Omega}_\mathrm{p}$ may be obtained by solving the problem

$$\nabla(\nabla\cdot\mathbf{u}) = 0, \qquad \mathbf{r}\in\partial\mathbf{\Omega}_\mathrm{p}, \tag{2.172}$$

$$\mathbf{u} = \mathbf{u}_0, \qquad \mathbf{r}\in\partial\mathbf{\Omega}_\mathrm{p}\cap\partial\mathbf{\Omega}_\mathrm{solid}. \tag{2.173}$$

Here, $\mathbf{u}_0$ refers to the solution of problem (2.170) within the solid part, and is used as Dirichlet boundary condition at the port edges in (2.173). Note, the same approach may be applied on symmetry planes if available. The set of partial differential equations is solved for each terminal or symmetry plane individually. The mesh displacement within the vacuum filled domain may be obtained in analogy to (2.172)–(2.173), given the constraints placed on the boundary $\partial\mathbf{\Omega}_\mathrm{vac}$. This method is also known as *Laplacian smoothing* [86].

3 Specifications and Requirements

This chapter focuses on HOMs of the superconducting rf cavities of the SPL as depicted in Fig. 3.1, and their influence on the longitudinal beam dynamics. Similar studies have been carried out in [87, 88] but are more focused on the cavities or the SPL itself. The purpose of this chapter is to provide a detailed and conclusive view on the transmissive needs of the HOM couplers foreseen on each cutoff tube of the rf cavities. Monopole modes with largest geometric shunt resistance or a frequency closest to harmonics of the bunch frequency are given particular attention. It has been shown in [50, 87] that transverse effects caused by dipolar HOMs are negligible in high-energy proton linacs such as the SPL. With regards to energy recovering linacs as an alternative application for the SPL cavities, the situation becomes much different. For completeness, the subsequent eigenmode analyses cover both monopole and dipole modes.

The investigations are based on eigenmode and wake field simulations of the single cavities as well as beam dynamic simulations of the SPL linac configuration. Potentially harmful HOMs are identified and the maximum rf power dissipated in those HOMs is estimated at various operating scenarios. With a view to feasibility, fundamental power limits need to be introduced to prevent excessive power dissipation on the HOM couplers or cavity surface. These limits are of great importance

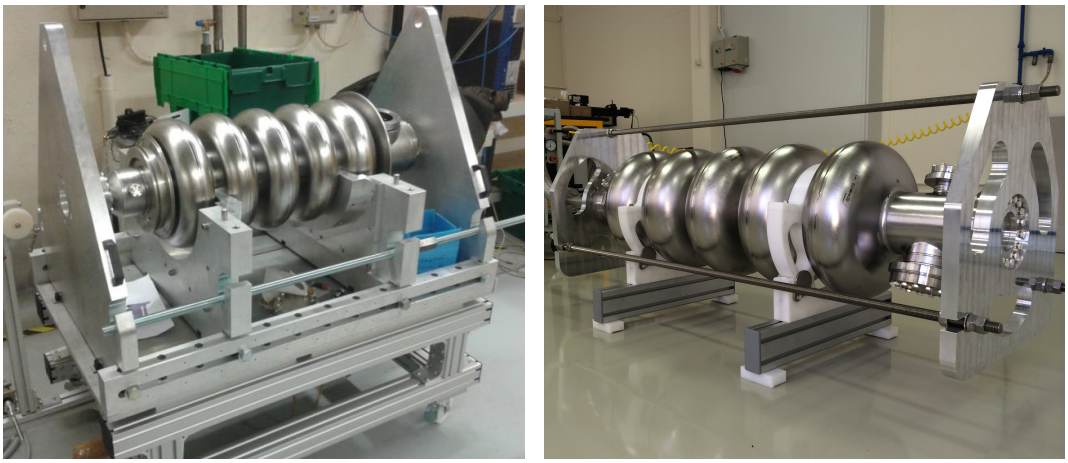

(a) (b)

Fig. 3.1. Bulk Nb prototypes of (a) the medium-β SPL cavity [23] and (b) the high-β SPL cavity.

for the cavity control and tuning. Finally in this chapter, various low power rf measurements are presented. The author took primary responsibility for most of the HOM measurements on the high-β SPL cavity prototypes between 2014 and 2015. Novel work undertaken by the author includes an improved method for eigenmode classification following up the work of [47], the vector fitting algorithm [77] applied on longitudinal and transverse beam coupling impedances, as well as extensions and significant performance improvements of the beam dynamics code SMD [87]. It is important to note that the present results are not all consistent with preceding studies due to their use of simplified and/or preliminary cavity designs as well as a linac configuration different from the latest specification. These differences are stated in the corresponding passages in the text.

3.1 Design Parameters of the SPL Cavities

The superconducting section of the SPL linac provides two families of elliptical cavities covering a velocity range of the protons between 160 MeV and 5 GeV [22]. Table 3.1 lists the main rf parameters of both cavity types. The operating fre-

Table 3.1. Parameters of the medium-β and high-β SPL cavities [19, 23].

property	unit	medium-β	high-β
fundamental mode frequency	[MHz]	704.4	704.4
number of gaps (cells)	–	5	5
geometric β value	–	0.65	1.00
particle velocity range (β)	–	0.52 to 0.84	0.84 to 0.99
active length	[mm]	692	1065
iris diameter (inner cells)	[mm]	96	129.2
cell-to-cell coupling	[%]	1.45	1.92
geometry factor G	[Ω]	197	270
geometric shunt impedance (R/Q)	[Ω]	275	566
nominal accelerating gradient E_{acc}	[MV/m]	19.3	25
quality factor Q_0 at nominal gradient	–	6×10^9	1×10^{10}
$E_{\mathrm{pk}}/E_{\mathrm{acc}}$	–	2.63	1.99
$B_{\mathrm{pk}}/E_{\mathrm{acc}}$	[mT/(MV/m)]	5.12	4.20
Lorentz force detuning	[Hz/(MV/m)^2]	−1.6	−1.0
required tuning range	[kHz]	±300	±300
required field flatness	[%]	97.5	97.5
maximum rf duty cycle	[%]	8.5	8.4
Q_{ext} of input coupler at 40 mA beam current and −15 deg synchronous phase	–	1.2×10^6	1.2×10^6
number of HOM couplers	–	2	2

quency of 704.4 MHz was chosen for economical reasons. Older rf equipment, such as klystrons, waveguides and circulators, which was originally installed in LEP, is now reused in Linac4. Consequently, Linac4 operates at the same frequency of 352.2 MHz. The superconducting rf cavities of the SPL are designed for twice this frequency. Both families operate in pulsed mode at a duty cycle smaller than 10 %. Fig. 3.2 illustrates the electromagnetic field distribution of the fundamental mode in the high-β cavity. Qualitatively the same field distribution applies to the medium-β version. The first prototypes of the bare cavities are shown in Fig. 3.1. According to the experiences of the TESLA cavities [58], they are design for surface peak fields of $E_{\mathrm{pk}} = 50\,\mathrm{MV/m}$ and $B_{\mathrm{pk}} = 100\,\mathrm{mT}$ at nominal accelerating gradients. Further details about the designs and their fabrication are addressed in [19, 23, 89].

3.2 Eigenmodes of the SPL Cavities

This section provides detailed analyses on the HOM spectra of the medium-β and high-β SPL cavities based on eigenmode calculations. Modes with a frequency being closest to a harmonic of the bunch frequency as well as those with high (R/Q) values are of particular interest. All modes are cataloged, i. e. associated with radial, azimuthal and longitudinal indices using a somewhat improved method of [47] as described in the following.

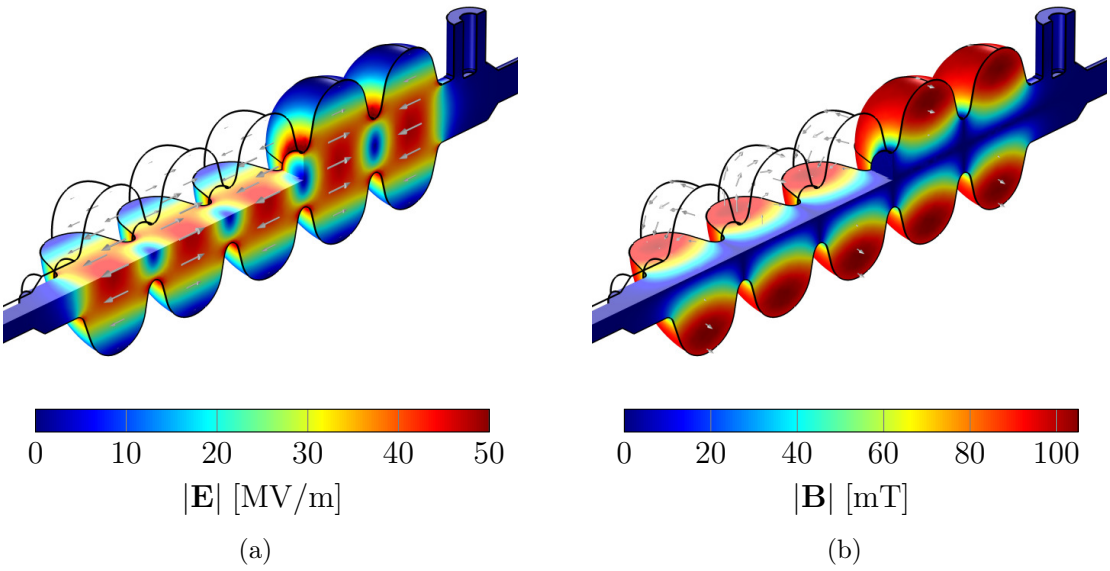

Fig. 3.2. Electric (a) and magnetic (b) field distributions for the fundamental mode of the high-β SPL cavity simulated using COMSOL Multiphysics® [90]. The field orientation is highlighted by gray arrows. The model including the fundamental power coupler is cut along the symmetry plane facing the viewer. Field magnitudes are scaled to the nominal accelerating gradient of 25 MV/m.

3.2.1 Automated Eigenmode Classification

The eigenmodes of accelerating structures are typically cataloged and compared by means of their electromagnetic field distribution regarding vanishing field components as well as the number of field nodes in each spatial dimension. Due to the rotational symmetry of the SPL cavities it is most appropriate to associate their numerically calculated eigenmodes with the analytic solutions of the pillbox cavity as described in Sec. 2.2.2. Modes are, thus, classified by the azimuthal, radial, and longitudinal indices m, n, and p. The algorithm to evaluate such mode indices based on the field distribution of the particular eigenmode follows to a large extent the work described in [47]. This applies in particular to the differentiation between TE, TM, and Hybrid modes and the evaluation of cell-to-cell phase advance. Likewise, the fields are probed along the cylindrical coordinate axes within one cavity cell. The choice of field components to count field nodes is, however, slightly modified. In case of TM monopole modes ($m = 0$), both azimuthal field components are considered whereas for multipolar modes ($m > 1$), independent off TM or TE, the azimuthal electric and radial magnetic field components are considered. The reason becomes obvious when observing the corresponding analytic solution of a pillbox cavity, here for the TM modes

$$E_\varphi^{(m)} = E_0 \frac{m k_z}{{k_r}^2 r} J_m(k_r r) \sin(m\varphi) \sin(k_z z), \tag{3.1}$$

$$H_r^{(m)} = j H_0 \frac{m\omega}{c_0 {k_r}^2 r} J_m(k_r r) \sin(m\varphi) \cos(k_z z), \tag{3.2}$$

$$H_\varphi^{(m)} = j H_0 \frac{\omega}{c_0 k_r} J'_m(k_r r) \cos(m\varphi) \cos(k_z z), \tag{3.3}$$

The azimuthal electric and radial magnetic field components must vanish at the radial extremity due to the boundary conditions, but the azimuthal magnetic field does not. Counting the zeros of the azimuthal magnetic field component along the radial direction may lead to wrong radial indices n due to numerical noise. The only practical cases where the azimuthal magnetic field component must be used are TM monopole modes since their radial magnetic field component vanishes. In contrast to the original algorithm, the evaluation of mode indices is done by sinusoidal fits of the field components along the cylindrical coordinate axes, which is less sensitive to numerical noise. The algorithm is implemented in VBSCRIPT and integrated as a post processing script into CST STUDIO SUITE® software [91].

3.2.2 Modal Analysis of the Medium-β SPL Cavity

The conceptional design of the SPL considers a total of 60 superconducting cavities for the medium-β section (Fig. 1.2), with ten cryomodules each incorporating six cavities. The section is about 130 m long and covers a particle velocity range of $\beta = 0.52$ to 0.84. The first prototype cavity has been fabricated by Research Instru-

ments (RI) between 2012 and 2013. The rf design including the fundamental mode coupler, taken from [19, 23] shall serve as the reference model for the subsequent analyses. Details of the geometrical parameters are listed in Appendix A.2. Note, these parameters differ slightly from those considered in previous studies [87] in 2011. This explains, in particular, the differing shunt resistances of some eigenmodes. The main rf parameters of the cavity are listed in Table 3.1.

Figure 3.3 shows the dispersion curves of the first monopole and dipole modes simulated using CST STUDIO SUITE® software [91]. The corresponding longitudinal and transverse geometric shunt resistances are given in Fig. 3.4 using (2.115)–(2.118). The beam pipe radius of 40 mm yields cutoff frequencies of 2.871 GHz and 2.198 GHz for the TM_{01} and TE_{11} waveguide modes, respectively. Consequently, some higher-order modes of the TM_{031} band are already strongly damped via the beam pipe ports. The dispersion curves are obtained by parameter fittings of (2.90). Poor fittings in Fig. 3.3(b) indicate coupling between corresponding TE and TM dipole modes causing hybridization.

According to Fig. 3.4(a), two SOMs provide the highest (R/Q) values besides the fundamental mode. The details of the fundamental passband are listed in Table 3.2, with the maximum and summation of the (R/Q) values being related to the entire

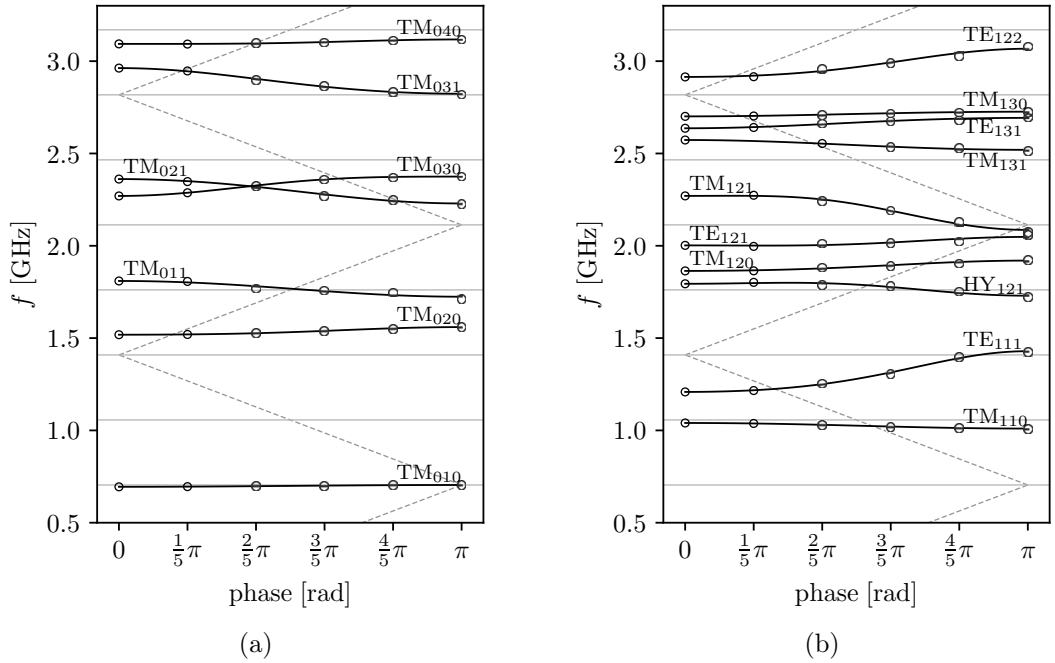

Fig. 3.3. Dispersion curves of (a) monopole and (b) dipole modes in the medium-β SPL cavity. The light line at $\beta = 0.65$ is dashed and machine lines are depicted as gray horizontal lines. The circles correspond to full structure simulations while the solid black lines connecting them result from a curve fitting based on the circuit model applied with periodic boundary conditions.

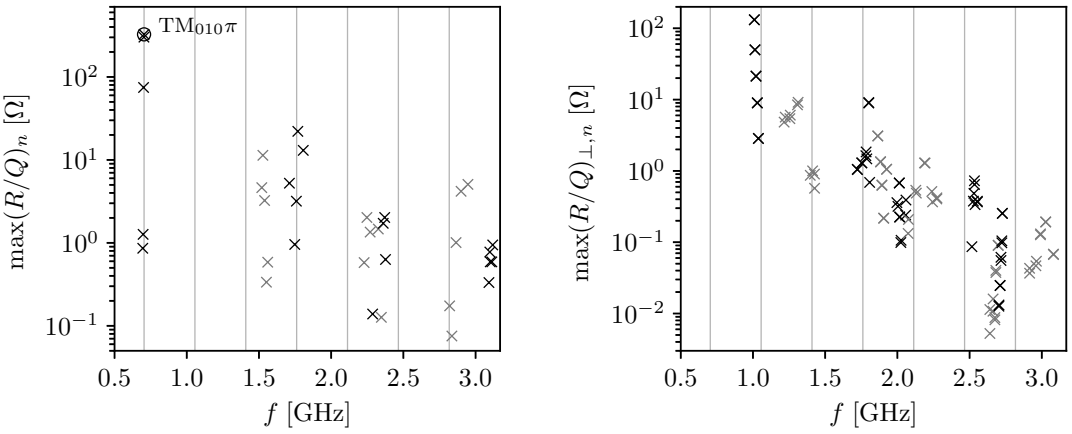

(a) (b)

Fig. 3.4. Maximum longitudinal and transverse geometric shunt resistances of (a) the first 35 monopole modes and (b) the first 60 dipole modes, respectively. The fundamental mode is highlighted by the circle. Machine lines are depicted as vertical gray lines.

SPL medium-β section. The variation of the (R/Q) value for each of these modes along this section is shown in Fig. 3.5(a). The TM_{010} $3/5\pi$ and TM_{010} $4/5\pi$ modes reveal shunt resistances comparable to the accelerating mode towards the start and end of the medium-β section. Despite high shunt resistances and frequencies being close to the second machine line, the impact of SOMs on emittance growth is marginal due to the relatively large band width of the fundamental power coupler with $Q_{\text{ext}} = 1.2 \times 10^6$. This was found in previous beam dynamic studies [87].

Table 3.3 lists the higher-order monopole modes with (i) the frequency being closest to a harmonic of the bunch frequency and (ii) the highest (R/Q) values. It is important to note that the frequencies of the TM_{011} $3/5\pi$ or TM_{031} $5/5\pi$ modes are by less than 3 MHz away from the fifth or eighth harmonic of the bunch frequency, respectively. Manufacturing errors and tuning may further reduce the particular distance in terms of frequency. For comparison, the ESS cavities are designed such that all HOM frequencies are more than 5 MHz away from the nearest harmonic of

Table 3.2. Modes in the fundamental passband of the medium-β SPL cavity.

mode n	f_n [MHz]	$(R/Q)_n(\beta_g)$ [Ω]	$\max(R/Q)_n$ [Ω]	$\sum(R/Q)_n$ [Ω]
TM_{010} $1/5\pi$	695.41	0.03	0.86	19.45
TM_{010} $2/5\pi$	697.89	0.15	1.27	14.53
TM_{010} $3/5\pi$	700.95	0.16	74.64	1175.56
TM_{010} $4/5\pi$	703.41	0.47	301.67	7877.24
TM_{010} $5/5\pi$	704.40	301.28	325.93	13446.22

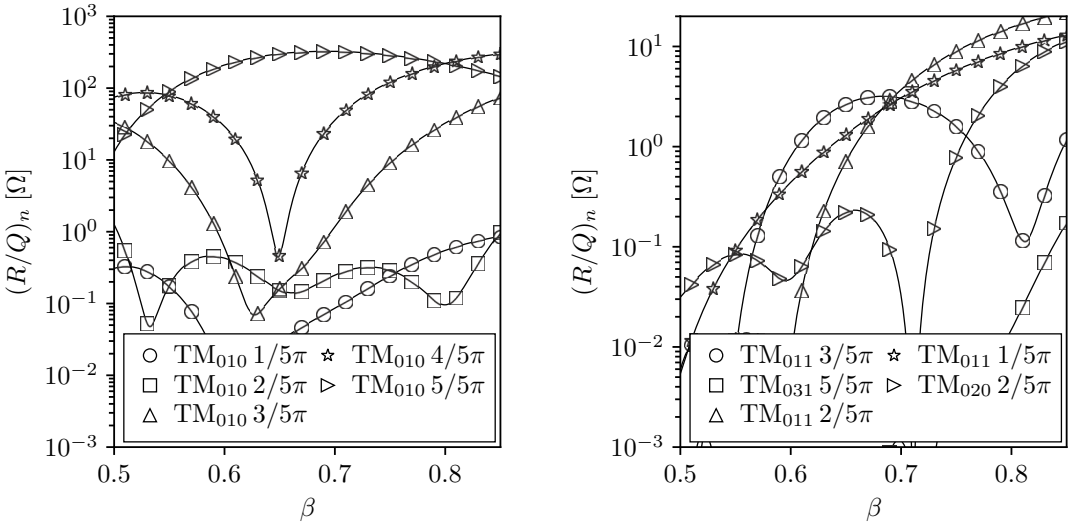

(a) (b)

Fig. 3.5. Longitudinal geometric shunt resistance as a function of the particle velocity for (a) modes in the fundamental passband and (b) some significant HOMs, both for the medium-β SPL cavity.

the bunch frequency [92]. Furthermore, the TM_{011} $2/5\pi$ provides the highest shunt resistance with respect to HOMs. In particular, this result is different to [87, p. 98] where a symmetric cavity design based on preliminary geometrical parameters was used to study the beam dynamics in the SPL. As a consequence, the dispersion relation of the TM_{011} band significantly differs between the present and previous studies. Shunt resistances were assumed to be partially twice as high as found here. The remaining HOMs in Table 3.3 provide comparably low (R/Q) values but might have significant impact in the presence of a particular bunch pattern as discussed

Table 3.3. Significant monopole HOMs in the medium-β SPL cavity.

mode n	f_n [MHz]	$\lvert f_n - f_{\mathrm{ML}}\rvert$ [MHz]	$\max(R/Q)_n$ [Ω]	$\sum(R/Q)_n$ [Ω]
Modes with frequencies closest to a machine line.				
TM_{011} $3/5\pi$	1759.21	1.79	3.18	63.37
TM_{031} $5/5\pi$	2820.44	2.84	0.17	0.94
TM_{011} $2/5\pi$	1769.17	8.17	22.09	515.65
Modes with the highest geometric shunt resistance.				
TM_{011} $1/5\pi$	1806.89	45.89	13.03	325.21
TM_{020} $2/5\pi$	1527.12	118.32	11.36	165.07
TM_{020} $1/5\pi$	1519.60	110.80	4.63	150.05
TM_{011} $5/5\pi$	1710.98	50.02	5.24	131.51
TM_{021} $4/5\pi$	2247.54	134.34	2.02	37.90

in Sec. 3.4.4. Figure 3.5(b) shows the variation of the longitudinal geometric shunt resistance along the medium-β section for the first five modes in Table 3.3. The highest shunt resistances are found towards the end of the section. A detailed conclusion on modes of concern in terms of beam dynamics is given in Sec. 3.4.

The higher-order dipole modes with largest transverse shunt resistances are listed in Table 3.3. As mentioned above, their impact on transverse emittance growth in the SPL is negligible but they might require additional considerations for a different application.

Table 3.4. Significant dipole HOMs in the medium-β SPL cavity.

mode n	f_n [MHz]	$(R/Q)_{\perp,n}(\beta_g)$ [Ω]	$\max(R/Q)_{\perp,n}$ [Ω]	$\sum(R/Q)_{\perp,n}$ [Ω]
TM_{110} $5/5\pi$	1009.59	1.38	132.13	2540.86
TM_{110} $4/5\pi$	1014.01	16.14	50.07	1798.40
TM_{110} $3/5\pi$	1020.87	20.60	21.46	483.47
TE_{111} $3/5\pi$	1312.69	0.95	9.16	300.68
TM_{110} $2/5\pi$	1030.21	5.22	8.94	269.30
TE_{111} $2/5\pi$	1258.53	4.83	6.05	186.19

3.2.3 Modal Analysis of the High-β SPL Cavity

The conceptional design of the SPL considers a total of 184 superconducting cavities for the high-β section (Fig. 1.2), with 46 cryomodules each incorporating four cavities. The section is about 370 m long and covers a particle velocity range of $\beta = 0.84$ to 0.99. Several Cu and Nb prototypes have been fabricated and tested in the recent years. The rf design including the fundamental mode coupler taken from [19, 88] shall serve as the reference model for the subsequent analyses. Details of the geometrical parameters are listed in Appendix A.2. The main rf parameters of the cavity are given in Table 3.1. The HOMs of this cavity have been studied to a large extend in [87, 93] in 2011. However, the shunt resistance of some HOMs was found to differ significantly from the correct values. This was verified by various simulations using CST STUDIO SUITE®, ANSYS® HFSS™, and COMSOL Multiphysics® software [90, 91, 94]. Furthermore, the mode notation presented here deviates in parts from that used in previous studies.

Figure 3.6 shows the dispersion curves of the first monopole and dipole modes calculated using CST STUDIO SUITE®. The corresponding longitudinal and transverse geometric shunt resistances are given in Fig. 3.7 using (2.115)–(2.118). The beam pipe radius of 40 mm yields cutoff frequencies of 2.871 GHz and 2.198 GHz for the TM_{01} and TE_{11} waveguide mode, respectively. Consequently, the TM_{040} modes are strongly damped via the beam pipe ports. The dispersion curves are obtained by parameter fittings of (2.90). Poor fittings such as for the TE_{111} and TM_{110} bands in Fig. 3.6(b) indicate coupling between corresponding dipole modes.

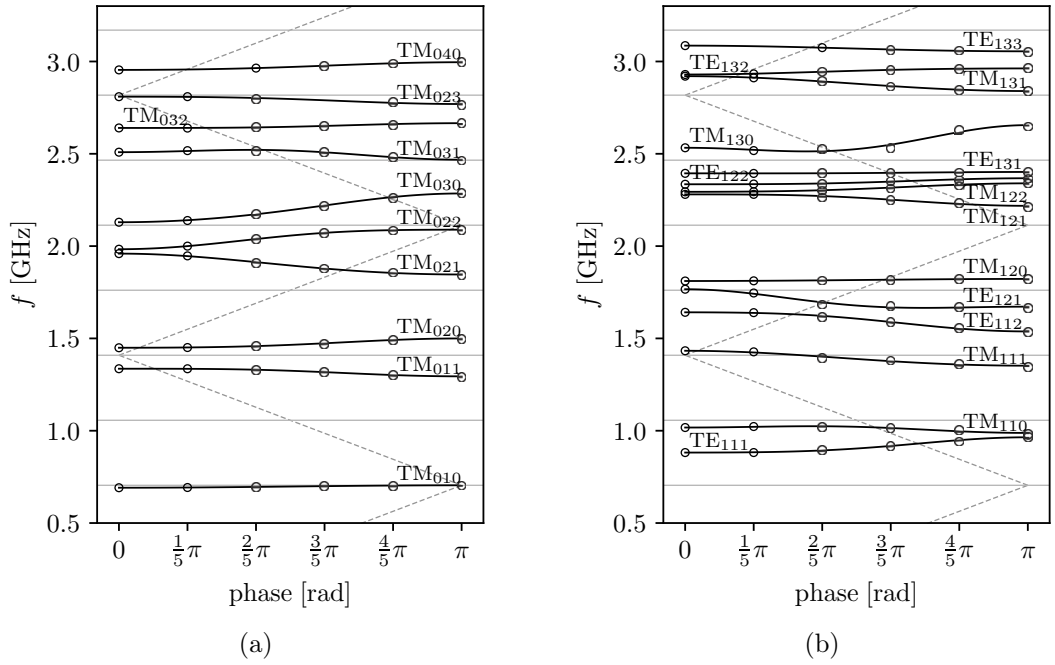

Fig. 3.6. Dispersion curves of (a) monopole and (b) dipole modes in the high-β SPL cavity. The light line at $\beta = 1.00$ is dashed and machine lines are depicted as gray horizontal lines. The circles correspond to full structure simulations while the solid black lines connecting them result from a curve fitting based on the circuit model applied with periodic boundary conditions.

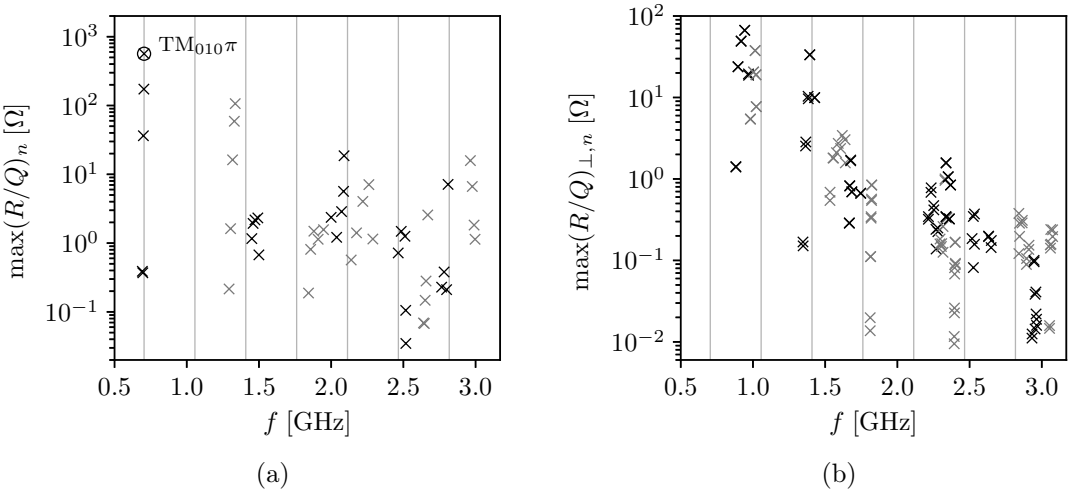

Fig. 3.7. Maximum longitudinal and transverse geometric shunt resistances of (a) the first 40 monopole modes and (b) the first 60 dipole modes, respectively. The fundamental mode is highlighted by the circle. Machine lines are depicted as vertical gray lines.

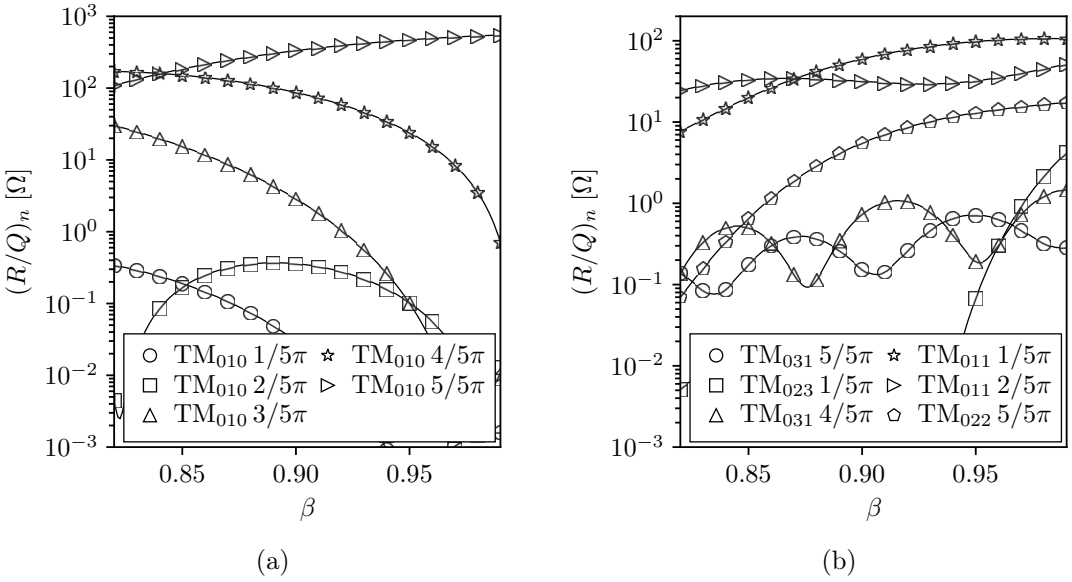

Fig. 3.8. Longitudinal geometric shunt resistance as a function of the particle velocity for (a) modes in the fundamental passband and (b) some significant HOMs, both for the high-β SPL cavity.

The details of the fundamental passband are listed in Table 3.5, with the maximum and summation of the (R/Q) values being related to the entire SPL high-β section. The variation of the (R/Q) value for each of these modes along this section is shown in Fig. 3.8(a). The TM_{010} $4/5\pi$ mode reveals a shunt resistance comparable to the accelerating mode towards the start of the high-β section. However, the situation is comparable to the SOMs in the medium-β cavity. The relatively large band width of the fundamental power coupler with $Q_{\mathrm{ext}} = 1.2 \times 10^6$ provides sufficient damping of the TM_{010} $4/5\pi$ mode in the high-β cavity. Hence, the expected longitudinal emittance growth in the SPL due to SOMs is marginal [87].

Table 3.6 lists the higher-order monopole modes with (i) the frequency being closest to a harmonic of the bunch frequency and (ii) the highest (R/Q) values. The design frequency of the TM_{031} π mode is about 1 MHz away from the seventh harmonic of the bunch frequency. Manufacturing tolerances may further reduce the

Table 3.5. Modes in the fundamental passband of the high-β SPL cavity.

mode n	f_n [MHz]	$(R/Q)_n(\beta_g)$ [Ω]	max $(R/Q)_n$ [Ω]	$\sum (R/Q)_n$ [Ω]
TM_{010} $1/5\pi$	692.45	0.002	0.39	3.33
TM_{010} $2/5\pi$	695.68	0.037	0.37	18.84
TM_{010} $3/5\pi$	699.75	0.010	36.34	276.11
TM_{010} $4/5\pi$	703.10	0.071	173.06	5973.75
TM_{010} $5/5\pi$	704.40	565.60	565.60	84957.47

Table 3.6. Significant monopole HOMs in the high-β SPL cavity.

mode n	f_n [MHz]	$\lvert f_n - f_{\mathrm{ML}} \rvert$ [MHz]	$\max{(R/Q)_n}$ [Ω]	$\sum{(R/Q)_n}$ [Ω]
Modes with frequencies closest to a machine line.				
TM_{031} $5/5\pi$	2464.35	1.05	0.72	73.57
TM_{023} $1/5\pi$	2809.48	8.12	7.13	212.54
TM_{031} $4/5\pi$	2485.27	19.87	1.48	151.52
Modes with the highest geometric shunt resistance.				
TM_{011} $1/5\pi$	1335.67	73.13	106.49	16721.78
TM_{011} $2/5\pi$	1329.51	79.29	59.03	7126.67
TM_{022} $5/5\pi$	2089.34	23.86	18.61	2339.15
TM_{011} $3/5\pi$	1317.33	91.47	16.23	945.51
TM_{030} $3/5\pi$	2219.33	106.13	4.03	487.98
TM_{022} $4/5\pi$	2085.83	27.37	5.65	351.82

distance in terms of frequency, which eventually favors a resonant buildup of the beam-induced HOM voltage despite the low shunt resistance. The remaining HOMs satisfy the minimum distance requirement of 5 MHz of the ESS cavities [92]. In comparison to the medium-β cavity, the high-β cavity provides HOMs with larger geometric shunt impedances. This applies, in particular, to the TM_{011} $2/5\pi$ and TM_{011} $3/5\pi$ modes. Figure 3.8(b) shows the variation of the longitudinal geometric shunt resistance along the high-β section for the first six modes in Table 3.6. The highest shunt resistances are found towards the end of the section. A detailed conclusion on modes of concern in terms of beam dynamics is given in Sec. 3.4.

The higher-order dipole modes with largest transverse shunt resistances are listed in Table 3.7. As mentioned above, their impact on transverse emittance growth in the SPL is negligible but they might require additional considerations for a different application.

Table 3.7. Significant dipole HOMs in the high-β SPL cavity.

mode n	f_n [MHz]	$(R/Q)_{\perp,n}(\beta_g)$ [Ω]	$\max{(R/Q)_{\perp,n}}$ [Ω]	$\sum{(R/Q)_{\perp,n}}$ [Ω]
TE_{111} $3/5\pi$	918.12	41.61	49.45	8416.31
TE_{111} $4/5\pi$	942.75	66.79	66.79	7773.75
TM_{110} $3/5\pi$	1015.06	37.71	37.71	5222.33
TM_{111} $2/5\pi$	1393.23	33.28	33.28	5012.94
TM_{110} $2/5\pi$	1020.73	8.97	19.00	2638.71
TM_{110} $4/5\pi$	1004.06	20.56	20.56	1576.87
TM_{111} $1/5\pi$	1427.24	9.97	9.97	1372.71
TE_{111} $5/5\pi$	968.88	19.48	19.48	1279.21

3.3 Impedance Analyses on the High-β SPL Cavity

In this section, a novel method is presented to derive the frequency, geometric shunt resistance and quality factor of trapped monopole and dipole modes based on truncated wake potentials. It is an alternative approach to the numerous eigenmode simulations required in Sec. 3.2 in order to deduce potentially harmful modes in the high-β SPL cavity. Note, the method is generally applicable to trapped modes excited by ultra-relativistic particle bunches (β=1).

It is well known that the properties of monopole and dipole modes can be accurately calculated from the longitudinal or transverse impedance, respectively, if the corresponding wake potential is simulated up to the point where it approximately vanishes according to (2.110) and (2.112). This often excludes a reasonable simulation time, particularly in the presence of very high quality factors as is typically the case for superconducting applications. Figure 3.9 shows the longitudinal and transverse beam coupling impedances of the high-β SPL cavity based on wake field simulations using CST STUDIO SUITE®, ABCI, and ECHO2D software [43, 63, 91]. There are no loss mechanisms present in the wake field simulations other than radiation into the beam pipe. This is a common consideration for wake field simulations in superconducting structures. The interesting trapped modes cause the wake potentials to not decay or to decay only very slowly. An arbitrarily defined truncation of the wake potentials that introduces artificial harmonics in the corresponding impedances is often unavoidable under these circumstances. Typically, a weighting

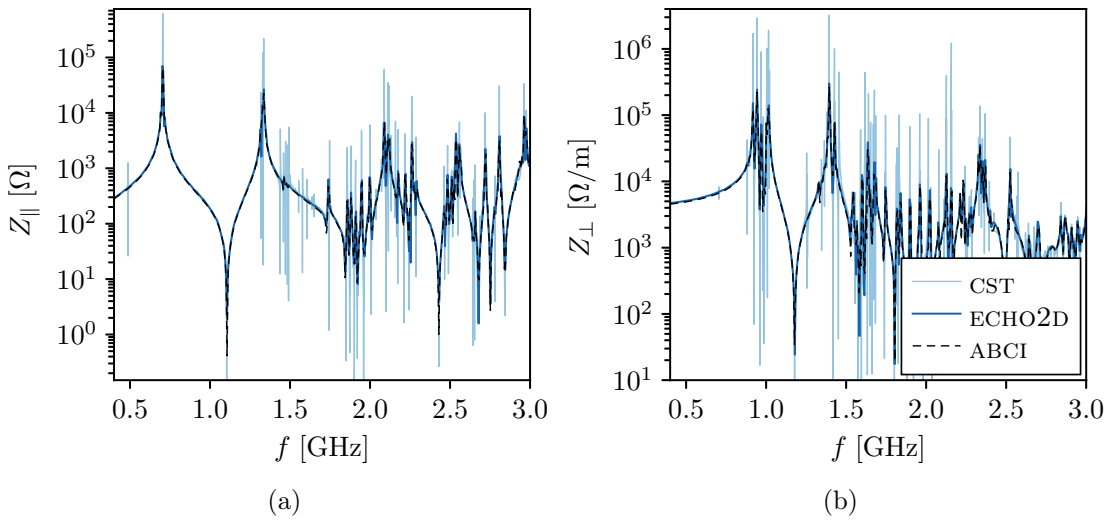

Fig. 3.9. (a) Longitudinal and (b) transverse beam coupling impedances of the high-β SPL cavity. The impedances are derived from wake potentials simulated using CST STUDIO SUITE®, ABCI, and ECHO2D software with an RMS bunch length of 25 mm. Wake potentials are truncated at 2000 ns and weighted by a Kaiser window to damp artificial harmonics in the resultant impedance spectra.

function is applied to the truncated wake potentials before calculating the Fourier transforms according to (2.110) and (2.112) in order to damp artificial fragments in the impedances. The frequencies of resonant modes can be calculated from such impedance spectra with very good precision using conventional fitting methods such as Cauchy distributions [12] or vector fitting [77]. However, the same methods, in general, fail to evaluate the geometric shunt resistances and quality factors of resonant modes independent of the use of the previously described weighting techniques to smooth the transition at the truncation point. An extended formulation of vector fitting is proposed to resolve this issue providing the desired accuracy in both frequency and geometric shunt resistance of trapped resonant modes within a predefined frequency interval. The method is further able to derive the corresponding loaded quality factors if at least 10 % of the full wake potential is calculated as measured by the time where the potential approximately vanishes.

In the following, it is shown that the classical and modified formulations of vector fitting from Sec. 2.3.3 are both eligible to fit the longitudinal and transverse beam coupling impedances of resonant structures in relation to trapped monopole and dipole modes. Three extended formulations of vector fitting are derived for the particular case that the impedance is calculated from a truncated wake potential. The consistency and convergence of these iterative methods is compared to the classical and modified vector fitting with the example of a circular cylindrical cavity with beam pipe apertures left open. Finally, the longitudinal and transverse impedances of the high-β SPL cavity are analyzed using vector fitting in the favored extended formulation. The results of potential harmful modes are compared to the eigenmode simulations of the last preceding section. It is worthwhile to note that the longitudinal and transverse impedances are significantly influenced by short range effects of the wake fields in the presence of particle bunches propagating at $\beta < 1$ due to static fields. It is generally very difficult to characterize resonant modes from such an impedance. For this reason, the medium-β SPL cavity is not addressed in this section.

3.3.1 Vector Fitting of the Narrow Band Resonator Impedance

Vector fitting has been applied in various fields to approximate frequency responses in terms of open-circuit impedance parameters, short-circuit admittance parameters, and scattering parameters [95–97]. A different algorithm likewise based on rational function approximation is proposed in [76, 98]. This scheme has been developed, in particular, to approximate scattering parameters in order to evaluate frequencies and quality factors of resonant modes in accelerating rf cavities. Similarly, the beam coupling impedances of rf cavities associated with trapped modes can be approximated by rational functions in order to characterize each mode individually as shown in the following.

The longitudinal wake function of a resonant cavity in the ultra relativistic limit

($\beta = 1$) can be written as [61, pp. 52,105]

$$w_{\parallel}^{\delta}(t) = \sum_{n=1}^{\infty} \frac{\omega_n R_n}{2Q_n} \exp\left(-\frac{\omega_n t}{2Q_n}\right) \cos(\omega_n t)\theta(t), \tag{3.4}$$

with the angular resonant frequency ω_n, shunt resistance R_n, and quality factor Q_n of the monopole mode n. The function θ represents the Heaviside step function using the half-maximum convention $\theta(0) = 1/2$. Equation (3.4) applies to narrow band resonances with $Q_n \gg 1$. Hence, the formulation is in particular valid for trapped modes which are typically of concern regarding beam instabilities. The corresponding impedance results from the Fourier transform of (3.4), which gives

$$Z_{\parallel}(s) = \int_0^{\infty} w_{\parallel}^{\delta}(t) e^{-st}\, dt, \tag{3.5}$$

$$= \sum_{n=1}^{\infty} \left(\frac{c_n}{s - a_n} + \frac{c_n}{s - a_n^*}\right), \tag{3.6}$$

with

$$c_n = \omega_n R_n/(4Q_n), \qquad a_n = -\omega_n/(2Q_n) + j\omega_n. \tag{3.7}$$

The superscript * accounts for the conjugated complex quantity. The properties of each resonant mode are represented by a pair of complex conjugated poles and a residue which is real. Typically, the sum is limited to modes within an interesting frequency range such that vector fitting is applicable, in principle. The same is true for the transverse beam coupling impedance since it can be expressed as a longitudinal impedance multiplied by the factor (c_0/ω) according to (2.113). Note, the frequency dependent factor is taken out from the calculated impedance data in order to apply vector fitting. In this case, the residues and poles in (3.7) are associated with the resonant frequency, quality factor, and transverse shunt resistance of a dipole mode n.

The calculation of longitudinal or transverse impedances with very high accuracy can be computationally intense and impractical as it requires the related wake potentials to be decayed to approximately zero. In particular, this is problematic if modes with high quality factors ($Q \geq 10^5$) are present in the structure. Thus, it is desirable to extract mode information likewise from the impedance of a truncated wake potential. The Fourier transform of a truncated time signal is characterized by artificial harmonics given by the period of the considered time window. These harmonics cannot be fitted by rational functions, hence the previously discussed method of vector fitting generally fails in case of beam coupling impedances that are derived from truncated wake potentials. It was found that the somewhat more relaxed vector fitting method using (2.159) as the helper function is able to converge robustly and consistently against the resonant frequencies, while the remaining mode

parameters associated with the residues and real part of the poles in (3.6) provide either large errors of $> 20\,\%$ or do not even converge. It is worthwhile to note that the same is true if the wake potentials are weighted by a window to provide a smooth transition at the truncation. The following section describes several modifications of vector fitting to overcome the problems of truncated wake potentials.

3.3.2 Resonator Impedance of Truncated Wake Potentials

A method to fit the impedance of a truncated longitudinal wake potential which can be described by (3.4) is presented in [99] along with an accurate derivation of the resonant frequency, quality factor, and geometric shunt resistance of various monopole modes in a circular cylindrical cavity. The algorithm is based on a non-linear approximation of a truncation time dependent impedance term, which is carried out for each mode individually. In the following, three alternative methods are presented. All of them are based on modifications of the classical vector fitting. Thus, the approximation problem is solved sequentially as a linear problem, where many modes are fitted simultaneously as described in Sec. 2.3.3. In contrast to the non-linear algorithm proposed in [99], these methods have the advantage of using the Fourier transform of only one single truncated wake potential.

Let $\tilde{Z}_\parallel(s,t')$ be the Fourier transform of the wake potential (3.4) truncated at the time $t = t'$. With the definition of poles and residues introduced in (3.6) and (3.7), the artificially compromised impedance can be written as

$$\tilde{Z}_\parallel(s,t') = \int_0^{t'} w_\parallel^\delta(t) e^{-st}\, dt, \tag{3.8}$$

$$= \sum_{n=1}^{\infty} \left(\frac{c_n}{s-a_n} w_n(s,t') + \frac{c_n}{s-a_n^*} w_n^*(-s,t') \right), \tag{3.9}$$

with the weighting function

$$w_n(s,t') = 1 - \exp\left[-(s-a_n)t'\right]. \tag{3.10}$$

The latter term introduces the artificial harmonics on the natural beam coupling impedance. A fitting method which is able to approximate a given impedance from a truncated wake potential with (3.9) and (3.10) over a finite number of resonances, in general, is eligible to derive the characteristic parameters of well separated modes, that is if $|\omega_{n+1} - \omega_n| \gg 1/t'$. Note, that the poles, residues, and harmonic weighting functions $\{a_n, c_n, w_n\}_{n=1}^{\infty}$ in (3.9) come in complex conjugated pairs, where the residues are actually real quantities. Moreover, it is important to remark that the harmonic weighting functions do not introduce any further poles since

$$\left|\exp\left[(s-a_n)t'\right]\right| = \exp\left(\frac{\omega_n t'}{2Q_n}\right) > 0. \tag{3.11}$$

The first modification of vector fitting follows instantly from the structure of (3.9) for the ansatz of the transfer function $H(s)$. With regard to a finite number of resonances, N, and a fixed truncation time t', an ansatz of

$$H^{(t')}(s) = \sum_{n=1}^{N} \left(\frac{c_n}{s - a_n} w_n(s,t) + \frac{c_n^*}{s - a_n^*} w_n^*(-s,t) \right)_{t=t'} \tag{3.12}$$

is chosen. Note, the index n is associated with one resonance, hence, with a pair of complex conjugated quantities, while the same index variable was used in Sec. 2.3.3 to declare a general pole or residue. Due to the harmonic weighting functions, the ansatz (3.12) is not anymore a rational function but rather a polynomial of infinite order. By Taylor expansion of the exponential term in (3.10), it can be shown that the pole of each partial fraction in (3.12) is canceled. Consequently, the quantities $\{a_n, a_n^*\}_{n=1}^{N}$ appear as poles and zeros in $H^{(t')}(s)$. In analogy to (2.156), the augmented least square problem is given by

$$\min_{\{\tilde{c}_n, c_n\}_{n=1}^{N}} \sum_{k=1}^{N_k} \left| \sigma(s_k) H^{(t')}(s_k) - \sigma(s_k) H_k^{(t')} \right|^2, \tag{3.13}$$

where $\{s_k, H_k^{(t')}\}_{k=1}^{N_k}$ are the sampled frequency and impedance values calculated from the wake potential that is truncated at the time $t = t'$. The parameters d and h in (2.154) can be optionally added to the approximation problem. However, they would account for artificial effects linear in frequency, which have not been observed in the calculated impedances. In order to obtain a linear approximation problem, the helper function $\sigma(s)$ with known poles but unknown residues $\{\bar{a}_n, \tilde{c}_n\}_{n=1}^{N}$ is chosen such that

$$\sigma(s) H^{(t')}(s) = \sum_{n=1}^{N} \left(\frac{c_n}{s - \bar{a}_n} w_n(s,t) + \frac{c_n^*}{s - \bar{a}_n^*} w_n^*(-s,t) \right)_{t=t'}. \tag{3.14}$$

Three different approaches for the helper function $\sigma(s)$ are investigated. The first two are identical with the ansatz of the classical and modified vector fitting. That is a fixed asymptotic behavior at very high frequencies according to

$$\sigma_1(s) = \sum_{n=1}^{N} \left(\frac{\tilde{c}_n}{s - \bar{a}_n} + \frac{\tilde{c}_n^*}{s - \bar{a}_n^*} \right) + 1, \tag{3.15}$$

and a more relaxed condition for the asymptotic behavior according to

$$\sigma_2(s) = \sum_{n=1}^{N} \left(\frac{\tilde{c}_n}{s - \bar{a}_n} + \frac{\tilde{c}_n^*}{s - \bar{a}_n^*} \right) + \tilde{d}. \tag{3.16}$$

In both cases, the zeros of $\sigma(s)$ used to correct the poles of $H_{t'}(s)$ in each iteration follow from (2.165). The third approach of the helper function is chosen in analogy to (3.12) using the harmonic weighting functions from (3.10). Together with the more relaxed condition for the asymptotic behavior at very high frequencies, the ansatz can be written as

$$\sigma_3^{(t')}(s) = \sum_{n=1}^{N} \left(\frac{\tilde{c}_n}{s - \bar{a}_n} w_n(s,t) + \frac{\tilde{c}_n^*}{s - \bar{a}_n^*} w_n^*(-s,t) \right)_{t=t'} + \tilde{d}. \tag{3.17}$$

As the transfer function, the ansatz (3.17) is not a rational function due to the exponential terms. Furthermore the quantities $\{\bar{a}_n, \bar{a}_n^*\}_{n=1}^N$ must appear as poles and zeros. The remaining zeros which cancel the poles of $H^{(t')}$, can be approximately derived from an eigenvalue problem based on a minimal state space representation of $\sigma_3^{(t')}(s)$. The latter one can be written as

$$s \begin{pmatrix} \mathbf{x}_1 \\ \mathbf{x}_2 \end{pmatrix} = \begin{pmatrix} \bar{\mathbf{A}} & 0 \\ 0 & \bar{\mathbf{A}} \end{pmatrix} \begin{pmatrix} \mathbf{x}_1 \\ \mathbf{x}_2 \end{pmatrix} + \begin{pmatrix} \mathbf{b} \\ \mathbf{W}^{(t')}(s)\mathbf{b} \end{pmatrix} u(s), \tag{3.18}$$

$$y(s) = \begin{pmatrix} \tilde{\mathbf{c}}^\mathsf{T} & -\tilde{\mathbf{c}}^\mathsf{T}\mathbf{W}^{(t')}(s) \end{pmatrix} \begin{pmatrix} \mathbf{x}_1 \\ \mathbf{x}_2 \end{pmatrix} + \tilde{d}u(s), \tag{3.19}$$

where the augmented poles and residues $\{\bar{a}_n, \bar{a}_n^*, \tilde{c}_n, \tilde{c}_n^*\}_{n=1}^N$ are contained in the diagonal matrix $\bar{\mathbf{A}}$ and vector $\tilde{\mathbf{c}}$, respectively. The elements of the vector $\mathbf{b}$ are again arbitrarily chosen to unity in conjunction to the residue vector $\tilde{\mathbf{c}}$ while the elements in the diagonal matrix $\mathbf{W}^{(t')}(s)$ are given by the exponential part of the harmonic weighting functions according to $\{1-w_n(s,t'), 1-w_n^*(s,t')\}_{n=1}^N$. Since the latter ones oscillate in frequency, the state space representation (3.18)–(3.19) can be linearized in the vicinity of each mode simultaneously by choosing the diagonal elements in $\mathbf{W}^{(t')}(s)$ according to

$$\hat{w}_n(t') = |1 - w_n(s,t')| = \exp(-\Re\{\bar{a}_n\}t'). \tag{3.20}$$

With this approach, the zeros of $\sigma_3^{(t')}(s)$ can be approximately calculated via an eigenvalue problem that is obtained in analogy to Sec. 2.3.3 by interchanging the input and output signals in the state space representation (3.18)–(3.19), and is given by

$$\operatorname{eig}\left\{ \begin{pmatrix} \bar{\mathbf{A}} & 0 \\ 0 & \bar{\mathbf{A}} \end{pmatrix} - \begin{pmatrix} \mathbf{b} \\ \hat{\mathbf{W}}^{(t')}\mathbf{b} \end{pmatrix} \tilde{d}^{-1} \begin{pmatrix} \tilde{\mathbf{c}}^\mathsf{T} & -\tilde{\mathbf{c}}^\mathsf{T}\hat{\mathbf{W}}^{(t')} \end{pmatrix} \right\}, \tag{3.21}$$

where the diagonal matrix $\hat{\mathbf{W}}^{(t')}$ contains the elements of (3.20) for each part of the complex conjugated pairs. It is important to remark that half of the resulting eigenvalues are identical to the poles $\{\bar{a}_n, \bar{a}_n^*\}_{n=1}^N$ as mentioned before, while the other half is used to correct the poles of $H^{(t')}(s)$.

3.3.3 Example of a Circular-Cylindrical Cavity

A circular-cylindrical cavity with beam pipe apertures left open similar to Fig. 2.11 shall serve as a first benchmark for impedance analyses based on the above derived vector fitting methods. The diameter and length of the cavity are chosen to be 153 mm and 100 mm, respectively. The equivalent parameters of the circular-cylindrical beam pipe are 10 mm and 15 mm, respectively, on either side of the cavity. Figure 3.10(a) shows the longitudinal wake potential of a Gaussian bunch of 15 mm RMS length passing the center of the cavity at the speed of light. A wall conductivity of 10^6 S/m is considered. This allows a numerical calculation of the entire wake potential and corresponding impedance in a relatively short time scale. The longitudinal beam coupling impedance shown in Fig. 3.10(b) reveals 16 trapped monopole modes between 1.5 GHz and 8 GHz. The details of these modes in terms of resonant frequency, geometric shunt resistance and quality factor are summarized in Table A.1. These values are calculated by eigenmode simulations using COMSOL and agree within 1 % with the results derived from the impedance in Fig. 3.10(b) using the classical vector fitting method and (3.7). The focus of this section is the accuracy of such mode parameters if the fitted impedance is obtained from a truncated wake potential. For this purpose all previously described methods are compared: (i) The classical vector fitting, denoted as VF, uses the ansatz (2.154) and (2.158) for the transfer and helper function, respectively. The starting poles are chosen according to [77], hence, the complex conjugated pairs are equidistantly distributed in the considered frequency interval. A small real part, such as 1 % of

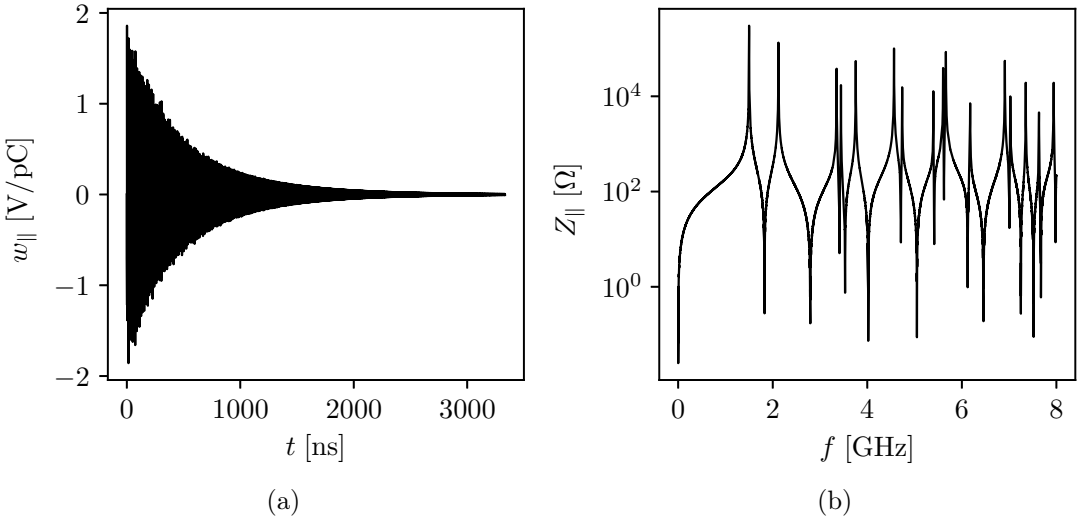

Fig. 3.10. (a) Wake potential of a Gaussian bunch of 15 mm RMS length passing the circular-cylindrical cavity with a wall conductivity of 10^6 S/m. The simulation is carried out using CST STUDIO SUITE® [91]. (b) Corresponding longitudinal beam coupling impedance.

the corresponding imaginary part, avoids an ill-conditioned least-square problem. Initially, two iterations are applied on a smoothed impedance which is obtained by the same truncated wake potential but weighted with a Kaiser window to damp artificial harmonics introduced by the truncation. This additional step significantly improves the convergence of the subsequent pole re-allocations. (ii) The modified vector fitting, denoted as MVF, uses the ansatz (2.154) and (2.159) for the transfer and helper function, respectively. The starting poles are equidistantly distributed in the considered frequency band with a small real part as in VF. The additional free parameter for the asymptotic behavior at very high frequencies of the helper function allows this fitting approach to be applied directly on the impedance of the truncated wake potential. Hence, no additional Fourier transform of the truncated wake potential weighted by a smoothing window is required. (iii) The first variant of impedance vector fitting, denoted as IVF1, uses the ansatz (3.12) and (3.15) for the transfer and helper function, respectively. Due to the fixed asymptotic behavior at very high frequencies of the helper function, the initial pole allocation succeeds as for VF. (iv) The second variant of impedance vector fitting, denoted as IVF2, combines the ansatz (3.12) and (3.16) for the transfer and helper function, respectively. The starting poles are allocated as for MVF. No additional smoothed impedance is required for the initial pole re-allocations. The same is true for (v) the third variant of impedance vector fitting using (3.12) and (3.17) for the ansatz of the transfer and helper function, respectively. This latter is denoted as IVF3 in the following.

A qualitative comparison of VF and IVF3 is shown in Fig. 3.11 where the imped-

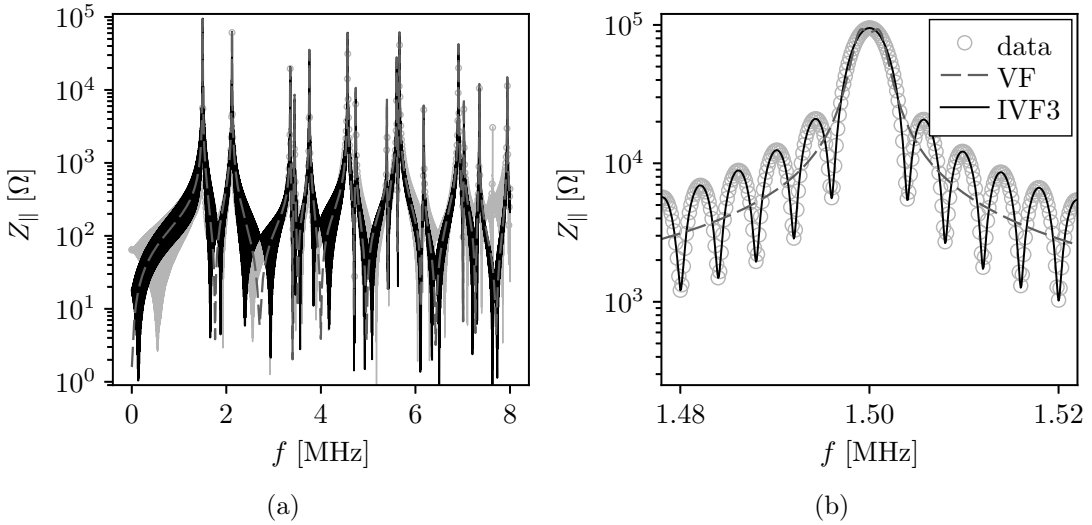

Fig. 3.11. In light gray, the impedance derived from the wake potential in Fig. 3.10 (a) truncated at the time $t' = 250\,\text{ns}$. The classical vector fitting (in dashed, dark gray) and a variant of the impedance vector fitting (black) are compared to each other, both, after 20 iterations. (a) The first sixteen trapped monopole modes below 8 GHz and (b) a zoom of the first mode at 1.5 GHz.

ance corresponds to the longitudinal wake potential in Fig. 3.10(a) truncated at the time $t' = 250\,\mathrm{ns}$, hence, when the potential is decayed by only approximately 40 %. The resonant frequencies in Fig. 3.11(a) are equally well resolved by both fitting methods. An exception is the fifteenth mode which requires a narrower frequency band to be resolved. For the sake of simplicity, this mode is excluded from the subsequent error studies related to frequency, geometric shunt resistance and quality factor. The harmonics in Fig. 3.11(b) introduced by the truncation are treated as noise in case of VF since the ansatz (2.154) cannot represent such behavior. The impedance obtained by the least-square problem is thus an average of the original data. In contrast, impedance vector fitting methods such as IVF3 can accurately reconstruct the impedance behavior of truncated wake potentials by use of the truncation time t'.

The more accurate reconstruction of impedance data by the impedance vector fitting methods is further underlined in Fig. 3.12(a) which compares the standard deviation of each fit from the given data as functions of the truncation time. The standard deviation is evaluated over 10 001 frequency samples from 0 GHz to 8 GHz. Note, the error below 100 Ω is dominated by the missing fifteenth mode in Fig. 3.11(a). There are two outliers at $t' = 217\,\mathrm{ns}$ and $t' = 350\,\mathrm{ns}$, which appear only for MVF, IVF2, and IVF3. This is due to at least one further mode being missed during the iterative pole re-allocations. The remaining methods are more

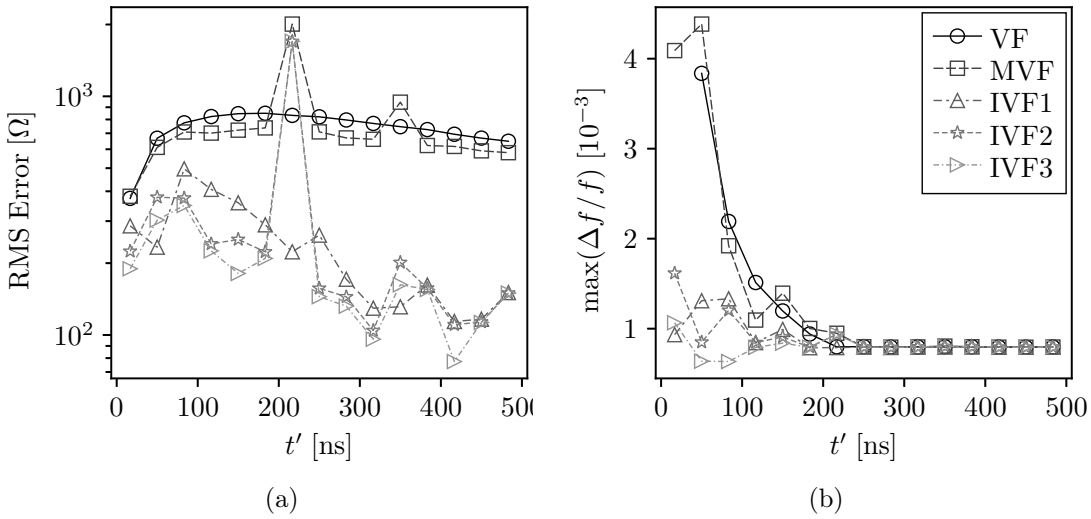

Fig. 3.12. (a) The RMS error of the impedance fits as a function of the truncation time of the corresponding longitudinal wake potential in Fig. 3.10 (a). The error is defined as the standard deviation of the individual fit from the calculated impedance over a frequency range from 0 GHz to 8 GHz. (b) Maximum relative error of the resonant mode frequencies in the same frequency regime where the fifteenth mode is excluded. The fitted frequencies are compared to the eigenmode results in Table A.1. Each fit is carried out with 20 iterations.

robust due to the use of few initial iterations on a smoothed impedance, which provides a more reliable set of starting poles. This approach is generally preferred for the impedance analyses of realistic structures in order to improve the performance of the particular vector fitting method. Furthermore, it is worthwhile to note that the relatively low error in Fig. 3.12(a) below $t' = 100\,\mathrm{ns}$ is due to the fact that the resonance peaks are significantly lowered and partially disappear. Consequently, the errors of resonant mode parameters are much higher in this regime. This is shown, for example, in Fig. 3.12(b) by means of the maximum error of the resonant frequency, considered over all monopole modes below 8 GHz except the fifteenth mode. The error converges against a systematic error of 0.08 % between the wake field and eigenmode results at a truncation of approximately $t' = 250\,\mathrm{ns}$. The overall error is below 0.5 % even if a truncation time of $t' = 5\,\mathrm{ns}$ is chosen. Figs. 3.13 and 3.14 show the corresponding errors of the geometric shunt resistance and quality factors, respectively, as functions of the truncation time. The calculations are carried out for an electric conductivity of the cavity wall of $10^6\,\mathrm{S/m}$ and $10^8\,\mathrm{S/m}$, each.

Though, the geometric shunt resistance is independent of material properties, the results in Figs. 3.13(a) and (b) are very different with an electric conductivity of $10^6\,\mathrm{S/m}$ and $10^8\,\mathrm{S/m}$, respectively. The maximum error of the geometric shunt resistance provided by VF is above $10\,\Omega$ in the considered range of truncation time. In the particular case $t' = 500\,\mathrm{ns}$ in Fig. 3.13(a), the geometric shunt resistance of the first mode at 1.5 GHz is estimated to approximately 18 % above the correct

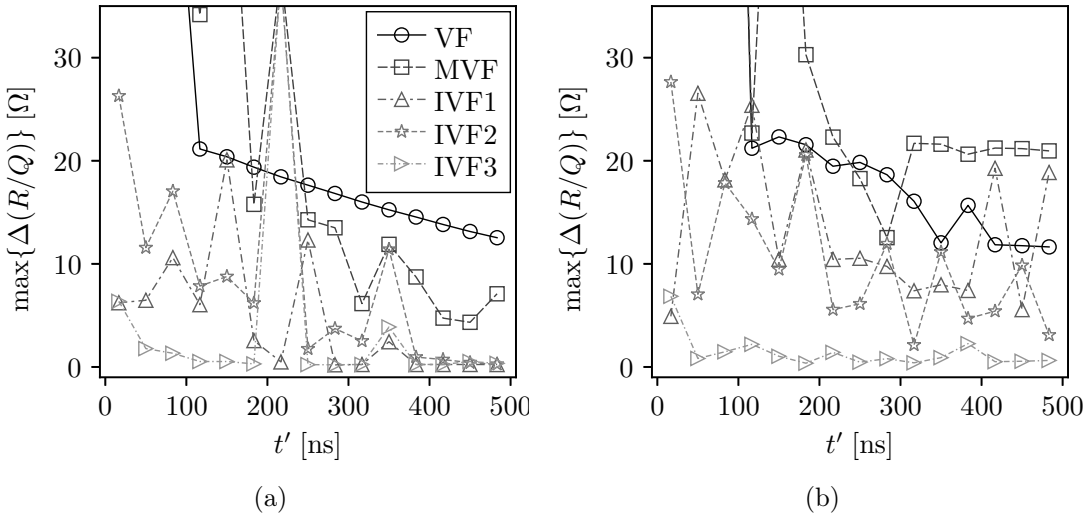

Fig. 3.13. Maximum error of the geometric shunt resistance over the considered resonant monopole modes below 8 GHz except the fifteenth mode. The fitted results are compared to the eigenmode results in Table A.1. The impedance is calculated from a truncated wake potential with varying truncation time t' where a wall conductivity of (a) $10^6\,\mathrm{S/m}$ and (b) $10^8\,\mathrm{S/m}$ is considered. Each fit is carried out with 20 iterations.

value. Thus, the results are unreliable as long as a truncated wake potential is taken as a base for the impedance calculations. The same conclusion applies to MVF which provides only slightly better results if the lower electric conductivity of $10^6\,\mathrm{S/m}$ is assumed. In contrast, the impedance vector fitting methods provide much lower maximum deviations from the correct geometric shunt resistances. The error decreases below $1\,\Omega$ for all methods if the corresponding wake potential is truncated at $t' \geq 400\,\mathrm{ns}$ and an electric conductivity of $10^6\,\mathrm{S/m}$ is assumed according to Fig. 3.13(a). This corresponds to a relative error below 1 % for all considered modes. It is remarkable that IVF3 provides this accuracy already for a truncation at $t' = 100\,\mathrm{ns}$. The outliers at $t' = 217\,\mathrm{ns}$ and $t' = 350\,\mathrm{ns}$ are present as in Fig. 3.12(a) and can be avoided by deriving an improved set of starting poles from an initial fit of the smoothed impedance as discussed before. The accuracy of IVF3 regarding the geometric shunt resistance is well preserved at higher electric conductivity as shown in Fig. 3.13(b) while IVF1 and IVF2 seem to diverge and may require a truncation above $t' = 500\,\mathrm{ns}$ for satisfying results. In fact, IVF1 and IVF2 converge much more slowly than IVF3, i. e. more than 20 iterations are necessary to achieve the same accuracy as IVF3. It was found that IVF3 correctly resolves the geometric shunt resistances within 1 % of all modes using less than 20 iterations even if perfect electric boundary conditions are assumed. Hence, this fitting approach is able to reflect the material independence of the geometric shunt resistance without adapting the number of iterations or truncation of the wake potential.

The deviation of the quality factor is strongly correlated to the truncation time as shown in Figs. 3.14(a) and 3.14(b) assuming an electric conductivity of the cavity wall of $10^6\,\mathrm{S/m}$ and $10^8\,\mathrm{S/m}$, respectively. Note, the ordinates are in logarithmic scale. For a truncation at $t' = 250\,\mathrm{ns}$ in Fig. 3.14(a), the maximum error over all considered modes provided by IVF3 is about 25 % while VF provides a maximum error of 60 %. In Fig. 3.14(b), the same errors increase to 60 % and a factor of ten, respectively. Though, impedance vector fitting methods provide much lower errors of the quality factors than VF and MVF, it is necessary to simulate at least 10 % of the full wake potential as measured by the time where the potential approximately vanishes. The error of 25 % that seems to persist in Fig. 3.14(a) is due to the fourth, ninth, and thirteenth mode in Fig. 3.11(a). These modes are within the vicinity of other, much stronger coupled modes. Their quality factors are compromised by an artificial coupling due to the harmonics introduced by the truncation. The consequence is an ambiguity in the solution of the least-square problem. Generally, a much longer wake potential must be considered for such modes in order to determine their quality factors correctly.

Finally, the convergence of each fitting scheme is shown in Fig. 3.15. The longitudinal wake potential is truncated at $t' = 250\,\mathrm{ns}$ and the electric conductivity of the cavity wall is $10^6\,\mathrm{S/m}$. IVF3 converges fastest within less than 10 iterations against a minimum standard deviation between the fit and the impedance data according to Fig. 3.15(a). Note, the minimum of roughly $100\,\Omega$ is caused by the missing fifteenth

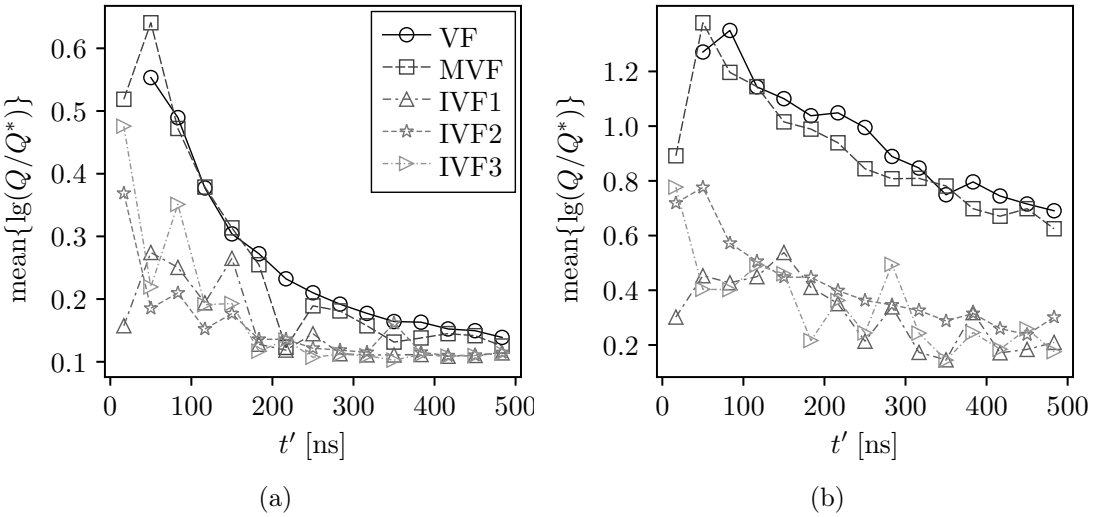

Fig. 3.14. Mean logarithmic error of the quality factor over the considered resonant monopole modes below 8 GHz except the fifteenth mode. The fitted results Q_n are compared to the eigenmode results Q_n^* in Table A.1. The impedance is calculated from a truncated wake potential with varying truncation time t' where a wall conductivity of (a) 10^6 S/m and (b) 10^8 S/m is considered. Each fit is carried out with 20 iterations.

mode in all fits. IVF1 and IVF2 converge much more slowly against the minimum standard deviation achieved by IVF3 while VF and MVF converge against a seven or, respectively, eight times larger standard deviation as the harmonics introduced by the truncation are averaged by these methods. The derived resonant frequencies in Fig. 3.15(b) converge similarly for all considered fitting schemes against a systematic error between the eigenmode and wake field simulations. The overall best accuracy of the geometric shunt resistance with respect to monopole modes below 8 GHz is achieved by IVF3 after 15 iterations as shown in Fig. 3.15(c). IVF1 and IVF2 provide slightly larger deviations which persist even after more than 20 iterations and are related to a single mode in the considered frequency band. The derived quality factors from IVF3 converge within 10 iterations to an error of less than 25 % averaged over the considered monopole modes below 8 GHz as shown in Fig. 3.15(d). IVF1 requires 20 iterations to converge against the same deviation on average. As mentioned above, this large error only applies to a few modes that are artificially coupled to other modes providing much higher shunt resistances.

It was found that the convergence of IVF3 can be further improved down to five iterations if the starting poles are derived from an initial fit of the smoothed impedance. The initial fit can be carried out by the classical vector fitting with two iterations, for example. The resulting set of starting poles must be slightly perturbed in order to improve the convergence. A perturbation of $\pm 10\pi/t'$ applied on the imaginary part is appropriate.

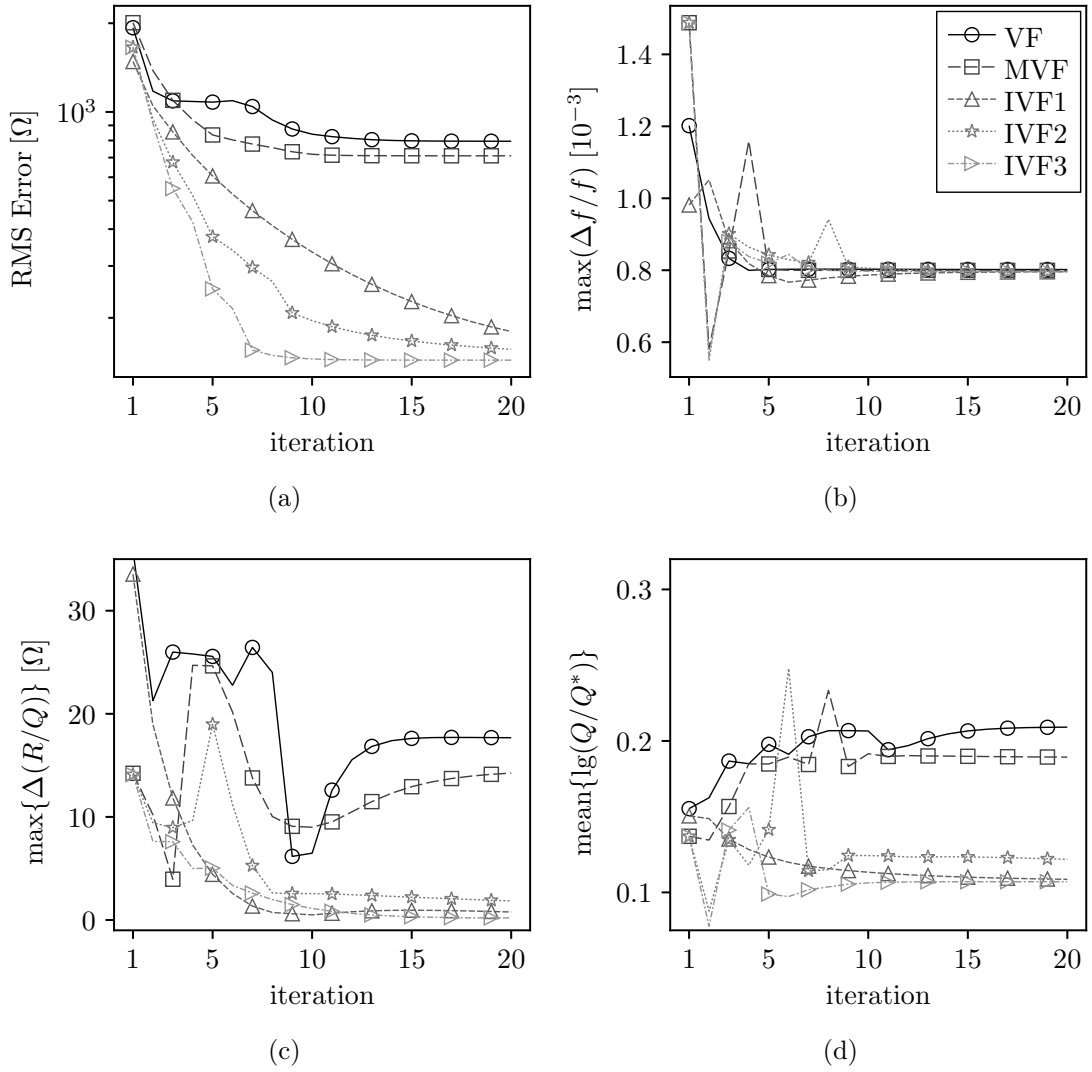

Fig. 3.15. (a) RMS error of the impedance fits versus number of iterations. The impedance corresponds to the wake potential in Fig. 3.10 (a) truncated at $t' = 250\,\mathrm{ns}$. The error is defined as the standard deviation of the individual fit from the calculated impedance over a frequency range from 0 GHz to 8 GHz. (b) Maximum relative error of the resonant mode frequencies, (c) maximum absolute error of the geometric shunt resistance and (d) mean logarithmic error of the quality factor, considered over all resonant monopole modes below 8 GHz except the fifteenth mode. The errors are based on comparisons with the corresponding eigenmode results in Table A.1.

3.3.4 Application on the High-β SPL Cavity

The longitudinal and transverse impedances shown in Figs. 3.16 and 3.17 are based on wake field simulations using CST STUDIO SUITE® [91] with a RMS bunch length of 25 mm. The resultant wake potentials were truncated after $t' = 2000\,\mathrm{ns}$ to obtain the particular impedances. The fitting is subdivided into two steps in order to

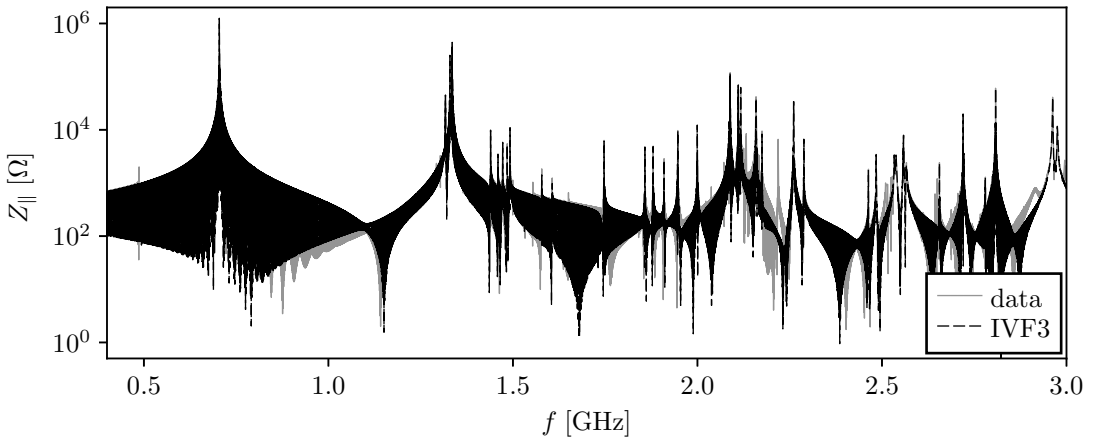

Fig. 3.16. Longitudinal beam coupling impedance obtained by the corresponding wake potential truncated at $t' = 2000\,\text{ns}$. The impedance is fitted by IVF3 using 160 poles.

improve the convergence: (i) Initial fits are applied on the smoothed impedances using VF with five iterations to provide a set of initial poles. (ii) The impedances as given in Figs. 3.16 and 3.17 are fitted using IVF3 with 20 iterations. A total of 160 poles is considered for each impedance in the frequency range below 3 GHz.

Tables 3.8 and 3.9 list the obtained resonant frequencies and geometric shunt resistances for all modes of concern along with the corresponding results of eigenmode simulations. Despite the very large frequency interval on which the fitting method is applied, the results of impedance and eigenmode analyses are in a very good agreement, particularly with respect to the monopole modes. It is worth noting that the accuracy can be further improved by reducing the frequency interval. Comparably

Table 3.8. Significant monopole HOMs in the high-β cavity.

	eigenmode simulations		wake field simulations	
mode n	f_n [MHz]	$(R/Q)_n(\beta_g)$ [Ω]	f_n [MHz]	$(R/Q)_n(\beta_g)$ [Ω]
Modes with frequencies closest to a machine line.				
TM_{031} $5/5\pi$	2464.35	0.39	2463.39	0.31
TM_{023} $1/5\pi$	2809.48	7.13	2807.82	7.07
TM_{031} $4/5\pi$	2485.27	1.35	2484.31	1.22
Modes with the highest geometric shunt resistance.				
TM_{011} $1/5\pi$	1335.67	104.60	1335.52	104.29
TM_{011} $2/5\pi$	1329.51	59.03	1329.37	59.07
TM_{022} $5/5\pi$	2089.34	18.61	2088.58	19.04
TM_{011} $3/5\pi$	1317.33	10.89	1317.20	11.08
TM_{030} $3/5\pi$	2219.34	1.66	2218.63	1.67
TM_{022} $4/5\pi$	2085.83	1.84	2085.13	1.94

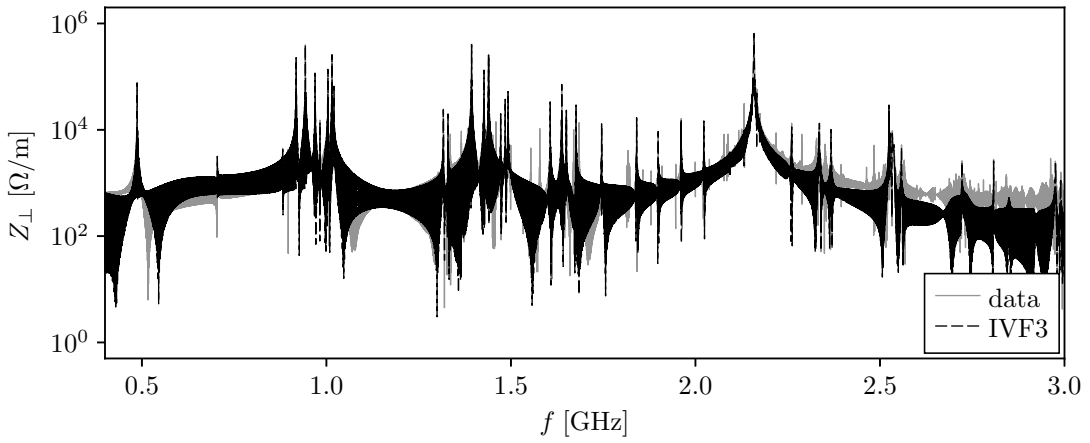

Fig. 3.17. Transverse beam coupling impedance obtained by the corresponding wake potential truncated at $t' = 2000\,\text{ns}$. The impedance is fitted by IVF3 using 160 poles.

large deviations observed for the geometric shunt resistance of some dipole modes listed in Table 3.9 are not yet fully understood. They occur despite the fact that the impedance spectrum is well approximated in the vicinity of these mode frequencies. Apart from this open problem, wake field simulations in combination with the proposed methods of vector fitting have proven to be a very suitable approach to investigate HOMs of resonant structures in great detail. Wake field simulations with appropriate truncation can be less computing-extensive than eigenmode simulations over the same frequency interval. Moreover, eigenmode simulations provide numerous multipolar modes which do not appear in the impedance spectra. Accordingly fewer modes need to be evaluated with regard to their frequency and geometric shunt resistance to conclude on potential harmful HOMs. The precise analyses of such modes, including the field distribution and particle velocity dependent geometric shunt resistance, are reserved for eigenmode simulations.

Table 3.9. Significant dipole HOMs in the high-β cavity.

	eigenmode simulations		wake field simulations	
mode n	f_n [MHz]	$(R/Q)_{\perp,n}(\beta_g)$ [Ω]	f_n [MHz]	$(R/Q)_{\perp,n}(\beta_g)$ [Ω]
TE_{111} $3/5\pi$	918.12	41.61	917.72	39.45
TE_{111} $4/5\pi$	942.75	66.79	942.62	66.43
TM_{110} $3/5\pi$	1015.06	37.71	1014.97	39.96
TM_{111} $2/5\pi$	1393.23	33.28	1392.94	48.85
TM_{110} $2/5\pi$	1020.73	8.97	1020.71	9.72
TM_{110} $4/5\pi$	1004.06	20.56	1004.06	21.64
TM_{111} $1/5\pi$	1427.24	9.97	1426.93	14.94
TE_{111} $5/5\pi$	968.88	19.48	968.77	19.89

3.4 Beam Dynamics

In circular machines, particle bunches repetitively excite HOMs in the accelerating cavities. A certain longitudinal and transverse bunch position modulation over drift spaces allows a resonant HOM build-up, in principle, at any mode frequency, and eventually leads to the longitudinal or transverse cumulative beam break up if a certain beam current threshold is reached [100]. Limiting the growth rate of the so-called coupled bunch instabilities is the fundamental reason for applying HOM damping in accelerating cavities of circular machines such as the LHC [101].

The situation in high-energy proton linacs is somewhat different. The impact of HOMs on the transverse beam dynamic is negligible as demonstrated in [50, 87] by means of the SPL and ESS linacs. However, HOM driven longitudinal instabilities may arise when the frequency of a higher-order monopole mode is close to a harmonic of the bunch frequency, which permits the HOM voltage to be resonantly built up. Moreover, pulse substructures introduce further but weaker resonant conditions as they are related to the repetition of the entire bunch pattern. The corresponding frequencies are denoted as chopping lines or chopping harmonics. The Linac4 houses a fast-switching electrostatic device to remove ultimately three out of eight bunches in order to provide the flexibility of the various chopping patterns.

This section focuses on the impact of beam-excited HOMs on the longitudinal beam dynamics of the SPL with the primary goal of defining HOM damping requirements by examining possible cumulative beam breakups in the longitudinal plane. The beam dynamics code SMD is adapted and refined to confirm and to extend the work performed by Schuh [87]. During this study, the implementation in ROOT [102] is modified to provide faster executions and parallel handling of different case studies. The statistical analyses comprise 10 to 100 times more samples than previous studies in order to provide the results with accordingly greater statistical significance. Furthermore, the simultaneous excitation of various modes listed in Tables 3.3 and 3.6, is included in the particle tracking simulations to compare their individual contribution to the power loss. Acceptance criteria are derived with regard to a feasible amount of dissipated and extracted HOM power. The corresponding tolerances are primarily related to the minimum acceptable distance between the resonant frequency of a particular mode and its nearest harmonic of the bunch or chopping frequency. The quality factor of HOMs is another crucial parameter. Ultimately, HOM damping by external coupling is required to ensure beam stability and to avoid excessive power dissipation on the cavity wall.

3.4.1 Implementation

Several pulses are tracked through the medium-β and high-β sections of the SPL, each containing 350 000 bunches considered as point-like macro particles. Typically, two pulses are launched to ensure a steady state. The simulation is based on a

drift-kick-drift model [50, pp. 165–166] where the momentum change is applied at the mid-plane of each cavity taking into account the velocity-dependent time of flight between subsequent cavities according to (2.131). The particle velocity inside the cavity is assumed constant. Along with the particle bunch propagation, energy and phase errors due to HOMs and errors in the main rf system are evaluated in each cavity using (2.129)–(2.130). A particle is defined as lost once it is outside the range [103, pp. 371]

$$2\phi_s < \phi < -\phi_s. \tag{3.22}$$

A detailed description on particle tracking in proton linacs including the interaction between the beam and HOMs is given in [100]. The original implementation in the beam dynamics code SMD [87, pp. 79–92] is considerably modified towards faster and parallel simulations in order to refine statistical analyses.

To obtain the statistical significance each simulation is repeated 1000 to 10 000 times, with Gaussian and uniform distributed error seeds being considered for (i) the energy and phase of the particle at the entrance of the linac, (ii) the rf amplitude and phase of the fundamental mode due to klystron errors, (iii) the frequency of the HOMs distributed over all cavities. While each cavity is tuned to the fundamental mode frequency, HOMs generally vary from cavity to cavity because of machining tolerances. To be consistent with previous studies [87], a Gaussian distributed frequency spread with a standard deviation of 1 MHz is chosen independent of the particular HOM. For comparison, an empirical study of HOM frequencies, which has been applied on cavities using deep drawing, states a maximum deviation of 0.38 % from the simulated mode frequencies [104]. Though slightly more conservative, this is fairly comparable to the frequency variations applied here. Furthermore, the amplitude and phase errors of the main rf system are anticipated for 0.5 % and 0.5 deg, respectively [19, p. 47-48]. For comparison, the low-level rf system of the superconducting cavities at ESS is designed to stabilize the amplitude and phase within 0.1 % and 0.1 deg, respectively. In addition to the energy and phase error, a bunch to bunch charge jitter of 3 % is considered [93]. All above mentioned quantities are summarized in Table 3.10 and are meant as default values which apply to

Table 3.10. Default parameters used for the particle tracking simulations [87].

parameter	unit	mean	σ	distribution
particle energy at insertion	[MeV]	160	0.078	Gaussian
particle phase at insertion	[deg at 704MHz]	−15	0.4	Gaussian
beam current I_B	mA	40	1.2	Gaussian
amplitude error of main rf	[%]	0	0.5	uniform
phase error of main rf	[deg at 704MHz]	0	0.5	uniform
bunch to bunch charge jitter	[%]	0	3	Gaussian
frequency spread of HOMs	[MHz]	0	1	Gaussian

the particular simulation if not stated differently.

Since transverse effects are expected to be marginal [50, 87], the longitudinal phase space can be assumed independently. Figure 3.18 shows the longitudinal phase space histogram of one pulse at the linac output in the presence of amplitude and phase errors in the rf system but without the excitation of HOMs. The effective phase space measured over one pulse, the so-called emittance ϵ, calculates as [19, p. 69]:

$$\epsilon = \pi \sqrt{\langle \Delta\mathcal{E}^2 \rangle \langle \Delta{\phi_s}^2 \rangle - \langle \Delta\mathcal{E}\, \Delta\phi_s \rangle^2}. \tag{3.23}$$

This quantity varies along the linac due to non-conservative forces, for instance, the accelerating and wake fields. The emittance ratio between linac output and input, denoted as ϵ/ϵ_0 in Fig. 3.18, reflects the growth of the longitudinal phase space along the structure. The phase space in Fig. 3.18(a) appears differently from [93, p. 99] because the linac configuration as well as field profiles of the cavity have changed since then. However, the emittance growth is nearly the same.

A major extension of the beam dynamics code SMD was the simultaneous excitation of arbitrarily many HOMs. Table 3.11 lists all HOMs considered in the following analyses. Their geometric shunt resistances are shown in Figs. 3.5(b) and 3.8(b) as functions of the particle velocity. Besides the nominal frequency in Table 3.11, the nearest harmonic of either the bunch frequency or the 50/80 bunch pattern frequency is provided, with the first one being chosen if the distance is smaller than 10 MHz. The association of individual modes with their nearest harmonics of the bunch or pattern frequency is of particular interest when estimating the maximum power dissipated in HOMs. It is worth noting that in addition to the manufacturing

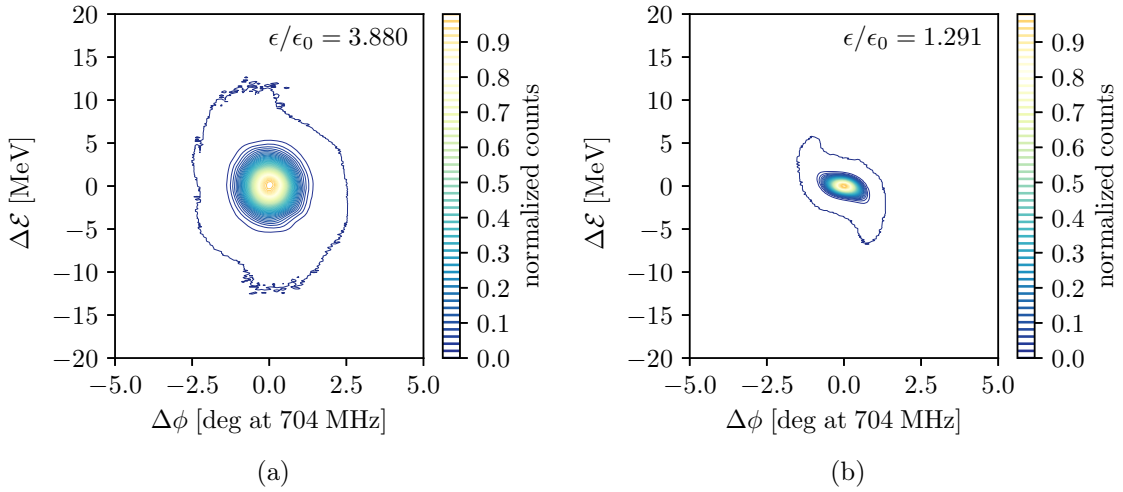

Fig. 3.18. Distrubution of the logitudinal phase space over one pulse at the linac output for 10 000 samples. Amplitude and phase errors of the main rf system are applied according to (a) 0.5 % and 0.5 deg, and (b) 0.1 % and 0.1 deg, respectively. No HOMs are considered.

Table 3.11. Monopole HOMs of concern.

mode n	f_n [MHz]	nearest harmonic [MHz]	
		bunch frequency	50/80 pattern
Medium-β cavity			
TM_{011} $3/5\pi$	1759.21	1761.0	–
TM_{011} $2/5\pi$	1769.17	1761.0	–
TM_{011} $1/5\pi$	1806.89	–	1805.0†
TM_{031} $5/5\pi$	2820.44	2817.6	–
High-β cavity			
TM_{011} $2/5\pi$	1329.51	–	1329.6
TM_{011} $1/5\pi$	1335.67	–	1334.0
TM_{022} $5/5\pi$	2089.34	–	2091.2
TM_{031} $5/5\pi$	2464.35	2465.4	–
TM_{023} $1/5\pi$	2809.48	2817.6	–

† harmonic of 5/8 bunch pattern.

tolerances which cause the frequency variation from cavity to cavity, the tuner is able to vary the frequency of HOMs at operation by several MHz.

3.4.2 HOM Frequency Spread

The impact of HOM frequency variations on the emittance growth along the SPL is illustrated in Fig. 3.19 at nominal DC beam current and at ten times larger current. The frequency errors are Gaussian distributed over the cavities, with the standard deviation f_σ being varied in a range from 10^3 Hz to 10^6 Hz. Moreover, the external coupling of HOMs, Q_{ext}, which determines the decay constant in (2.128), is varied between 10^5 and 10^8. The external quality factor is assumed to be the same for all considered HOMs. The amplitude and phase errors of the main rf system are excluded from the simulations. Each data point in Fig. 3.19 underlies a statistic of 1000 samples.

At the nominal beam current of 40 mA, the increase in longitudinal phase space is relatively small as shown in Fig. 3.19(a). Amplitude and phase errors of the main rf system would dominate the emittance growth independent of external coupling and frequency spread in the considered ranges. At considerably larger beam currents, a noticeable emittance growth can be induced by HOMs, in particular, at lower frequency spreads $f_\sigma < 0.1$ MHz. This is illustrated in Fig. 3.19(b) with a beam current as much as 400 mA. With additional HOM damping by external coupling in the order of $Q_{\text{ext}} \leq 10^5$, this effect completely vanishes. The reason why the emittance growth tends to increase for $f_\sigma > 0.2$ MHz is due to the fact that the TM_{011} $3/5\pi$ in the medium-β cavity becomes close to the fifth harmonic of the bunch frequency in some cavities. The same applies to the TM_{031} $5/5\pi$ in the

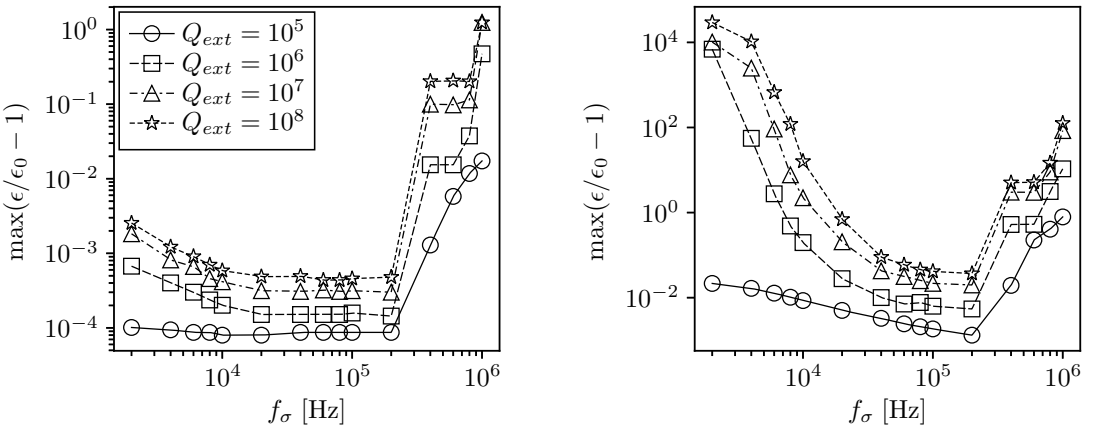

Fig. 3.19. Maximum emittance growth along the SPL as a function of frequency spread assumed for each HOM in Table 3.11. (a) $I_B = 40\,\mathrm{mA}$. (b) $I_B = 400\,\mathrm{mA}$. Statistics of 1000 samples are considered. Amplitude and phase errors of the main rf system are not considered.

high-β cavity with respect to the seventh harmonic. In both cases, the distance between the nominal resonant frequency and nearest harmonic of bunch frequency amounts to less than 2 MHz. It is worth noting that such large emittance growths at frequency spreads around $f_\sigma = 1\,\mathrm{MHz}$ were not observed in past studies [87, p. 102]. Due to design changes, the frequency of the TM_{011} $3/5\pi$ in the medium-β cavity became much closer to the fifth harmonic of the bunch frequency. In addition, not the TM_{031} $5/5\pi$ mode in the high-β cavity was considered in previous studies but the TM_{011} $1/5\pi$ mode which is by more than 70 MHz away from the nearest machine line (Table 3.6). Although the emittance growth at nominal beam current seems to be negligible within the considered resonant frequency variations, the situation changes significantly once a HOM frequency is close to a harmonic of the bunch frequency as demonstrated in the following.

3.4.3 Emittance Growth with Random Frequency Errors

In the previous section, it was already seen that the existence of parasitic modes near a harmonic of the bunch frequency essentially influences the longitudinal phase space. Following the approach in [50, pp. 185–187] the impact of such modes is further investigated in Fig. 3.20 for various predefined averaged distances between the HOM frequencies and their individually nearest harmonic of either the bunch frequency or 50/80 bunch pattern frequency according to Table 3.11. Hence, the nominal frequency of each HOM is defined by a common frequency shift Δf which varies from 0 MHz to 4 MHz. For comparison, the conceptional design of ESS specifies that all HOMs satisfy a minimum distance of 5 MHz from their nearest harmonic

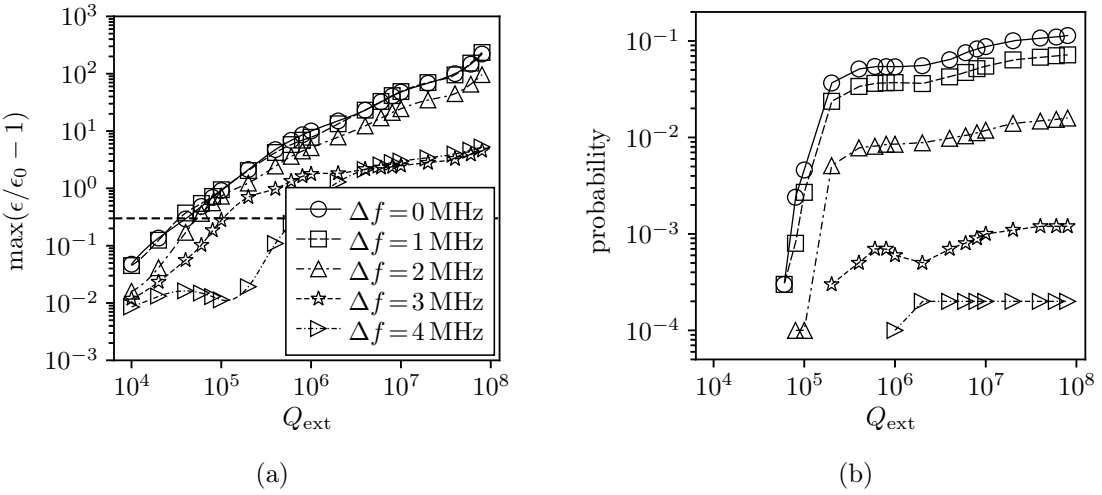

Fig. 3.20. (a) Maximum emittance growth along the SPL as a function of external coupling Q_{ext}. The frequency shifts Δf refer to the distance between the averaged frequency of the particular HOM and its nearest harmonic of either the bunch frequency or 50/80 bunch pattern frequency according to Table 3.11. The frequency spread is fixed to $f_\sigma = 1\,\mathrm{MHz}$. The nominal beam current of $I_B = 40\,\mathrm{mA}$ is assumed. Amplitude and phase errors of the main rf system are not applied. Statistics of 10 000 samples were carried out for each data point. The reference emittance growth in dashed corresponds to amplitude and phase errors of the main rf system of 0.1 % and 0.1 deg, respectively, and the absence of HOMs. (b) Probability to exceed the reference growth rate.

of the bunch frequency [92]. Furthermore, the frequency spread of all considered HOMs over the cavities is fixed to $f_\sigma = 1\,\mathrm{MHz}$. Each data point in Fig. 3.20 is derived from a statistic of 10 000 samples.

Figure 3.20(a) shows the maximum emittance growth as a function of the external coupling Q_{ext} commonly varied for all considered HOMs. The dashed reference line indicates the emittance growth in the presence of amplitude and phase errors of 0.1 % and 0.1 deg, respectively, and in the absence of HOMs as shown in Fig. 3.18(b). Figure 3.20(b) shows the corresponding probability that the particular emittance growth exceeds the reference value within a statistic of 10 000 samples. For example, if all considered HOMs lie on average 2 MHz away from the nearest harmonic of the bunch or pattern frequency, one out of 10 000 linac samples occurs where the emittance growth exceeds the threshold $\epsilon/\epsilon_0 = 1.291$ at $Q_{\mathrm{ext}} = 10^5$. For larger distances Δf, the probability of such a scenario is below 0.01 % and would require more extensive statistics to be resolved. The probability is apparently much smaller if a threshold of $\epsilon/\epsilon_0 = 3.880$ is considered, which corresponds to the nominal amplitude and phase errors of the main rf system according to Fig. 3.18(a). Even at $\Delta f = 0$, the probability to exceed this larger threshold is below 0.01 % as far as $Q_{\mathrm{ext}} \leq 2 \times 10^5$. This generally confirms the results of previous studies in [87, pp. 103–107] but with 100 times more samples per scenario, and multiple HOMs being excited in each cavity.

3.4.4 Sub-Structured Pulses

The same analysis as before was repeated for three different bunch patterns [19, p. 70]: (i) 5 out of 8 bunches, (ii) 50 out of 80 bunches, and (iii) 500 out of 800 bunches. The results of the first two cases are summarized in Fig. 3.21. The number of samples was reduced from 10 000 to 1000 to reduce the computational effort. This simplification was justified from previous analyses in Sec. 3.4.3 without sub-structured pulses, that is no significant differences in the maximum emittance growths were found between 1000 and 10 000 samples except that the probability to exceed a certain threshold cannot be resolved below 0.1 %.

Sub-structures in the pulse introduce further but weaker resonant conditions with a higher spectral density given by the bunch frequency divided by the maximum number of bunches within the pattern. Accordingly, the distance between harmonics of the 50/80 bunch pattern is 4.4025 MHz such that the maximum frequency shift between the particular mode frequency and its nearest harmonic of the bunch pattern frequency is at most 2.2012 MHz. Consequently, frequency shifts above 2 MHz in Fig. 3.21(b) apply only to those modes in Table 3.11, which are associated with harmonics of the bunch frequency. The remaining modes, such as the TM_{011} $1/5\pi$ mode in the medium-β cavity or the TM_{011} $1/5\pi$ mode in the high-β cavity, already approach the next harmonic of the 50/80 pattern frequency. This explains, in particular, the larger emittance growths at $\Delta f > 2$ MHz in Fig. 3.21(b) in comparison to Fig. 3.20(a) and 3.21(a). Note, the effect is less pronounced for the 500/800 bunch pattern which is not shown here. The maximum emittance growth at $\Delta f \leq 2$ MHz is

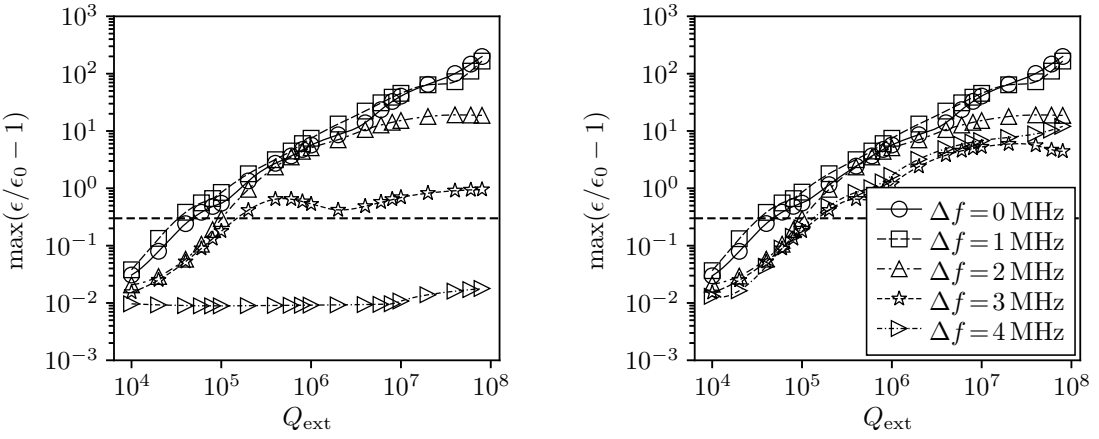

(a) bunch pattern: 5/8

(b) bunch pattern: 50/80

Fig. 3.21. Maximum emittance growth along the SPL as a function of external coupling Q_{ext} assuming different frequency shifts Δf. The same configuration is applied as described in Fig. 3.20 but for various bunch patterns. The statistics is reduced to 1000 samples for each data point. The dashed reference line indicates the emittance growth due to amplitude and phase errors of the main rf system of 0.1 % and 0.1 deg, respectively, if no HOMs are excited.

approximately the same independent of sub-structured or non-sub-structured pulses. It can be concluded that an external coupling of $Q_{\mathrm{ext}} \leq 2 \times 10^5$ sufficiently mitigates the impact of excited HOMs on the longitudinal emittance growth in the SPL.

3.4.5 Power Dissipation by HOMs

Previously, it was found that an external coupling of $Q_{\mathrm{ext}} \leq 2 \times 10^5$ must be ensured for the HOMs of concern not to enhance the longitudinal emittance growth along the linac. The corresponding fraction of power to be extracted from the n-th mode in the m-th cavity is given by

$$P_{\mathrm{ext},n}^{(m)} = \frac{|V_n^{(m)}|^2}{(R/Q)_n(\beta) Q_{\mathrm{ext},n}}, \tag{3.24}$$

where $P_{\mathrm{ext},n}$ is meant as the power averaged over the entire pulse. As before, the analysis is based on a statistical approach. The mean frequency of each HOM over all cavities is set at various predefined distances Δf from the nearest harmonic of either the bunch or pattern frequency according to Table 3.11. The frequency spread of all HOMs along the linac is fixed to $f_\sigma = 1\,\mathrm{MHz}$. Furthermore, the uncertainties of particle energy and phase at insertion as well as the spread of beam current according to Table 3.10 are taken into account for the statistic analyses, each comprising 1000 samples. Amplitude and phase errors of the main rf system are not considered. In addition, pulses with and without sub-structures are compared.

Figs. 3.22 and 3.23 show the maximum power to be extracted from individual modes in the medium-β or, respectively, high-β SPL cavity as a function of external coupling. The results are taken from those cavities compromised by the largest HOM voltages in the particular section. The amount of power rapidly reduces if the resonant frequencies are moved by more than 10 kHz away from the nearest harmonic of the bunch or pattern frequency. The total extracted power is dominated by those modes near a harmonic of the bunch frequency, for instance, the TM_{011} $3/5\pi$ mode in the medium-β cavity in Fig. 3.22 or the TM_{031} $5/5\pi$ mode in the high-β cavity in Fig. 3.23. Their nominal distance from the fifth or, respectively, seventh harmonic of the bunch frequency is less than 2 MHz. Note, the TM_{011} $2/5\pi$ mode in the medium-β cavity and the TM_{023} $1/5\pi$ mode in the high-β cavity are excited significantly more strongly than the previous discussed modes due to larger shunt impedances. However, their nominal frequency is about 8 MHz away from the fifth or, respectively, eighth harmonic of the bunch frequency, which is considered as a reasonable safety margin [92].

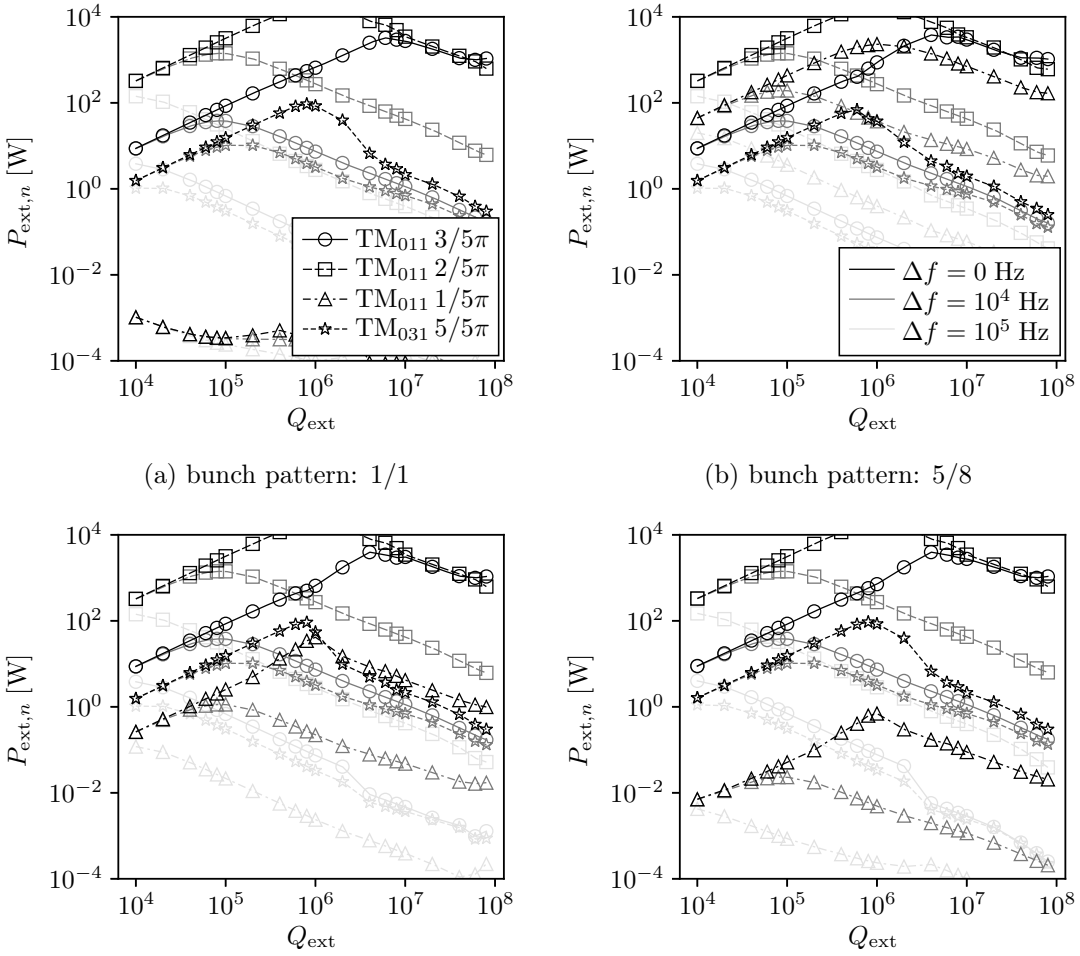

(a) bunch pattern: 1/1

(b) bunch pattern: 5/8

(c) bunch pattern: 50/80

(d) bunch pattern: 500/800

Fig. 3.22. Maximum mode specific extracted power in a medium-β cavity as a function of external coupling Q_{ext} assuming different frequency shifts Δf (gray scaled). The frequency shifts are related to the distance of the individual HOM mean frequency from its nearest harmonic of either the bunch frequency or 50/80 bunch pattern frequency according to Table 3.11. The frequency spread is fixed to $f_\sigma = 1\,\mathrm{MHz}$ for each mode. Four different bunch patterns are considered with the nominal beam current of $I_B = 40\,\mathrm{mA}$, each. Amplitude and phase errors of the main rf system are not applied. Statistic of 1000 samples were carried out for each data point.

In the presence of sub-structured pulses, the power to be extracted from the TM_{011} $1/5\pi$ mode in the medium-β cavity is substantially higher. This applies, in particular, to the 5/8 bunch pattern as illustrated in Fig. 3.22(b). In this scenario, the total extracted power is completely dominated by the TM_{011} $1/5\pi$ mode if the resonant frequency of the TM_{011} $2/5\pi$ mode is sufficiently separated from the fifth harmonic of the bunch frequency. This phenomenon does not appear for the high-β cavity since none of the considered modes is close enough to a harmonic of the 5/8

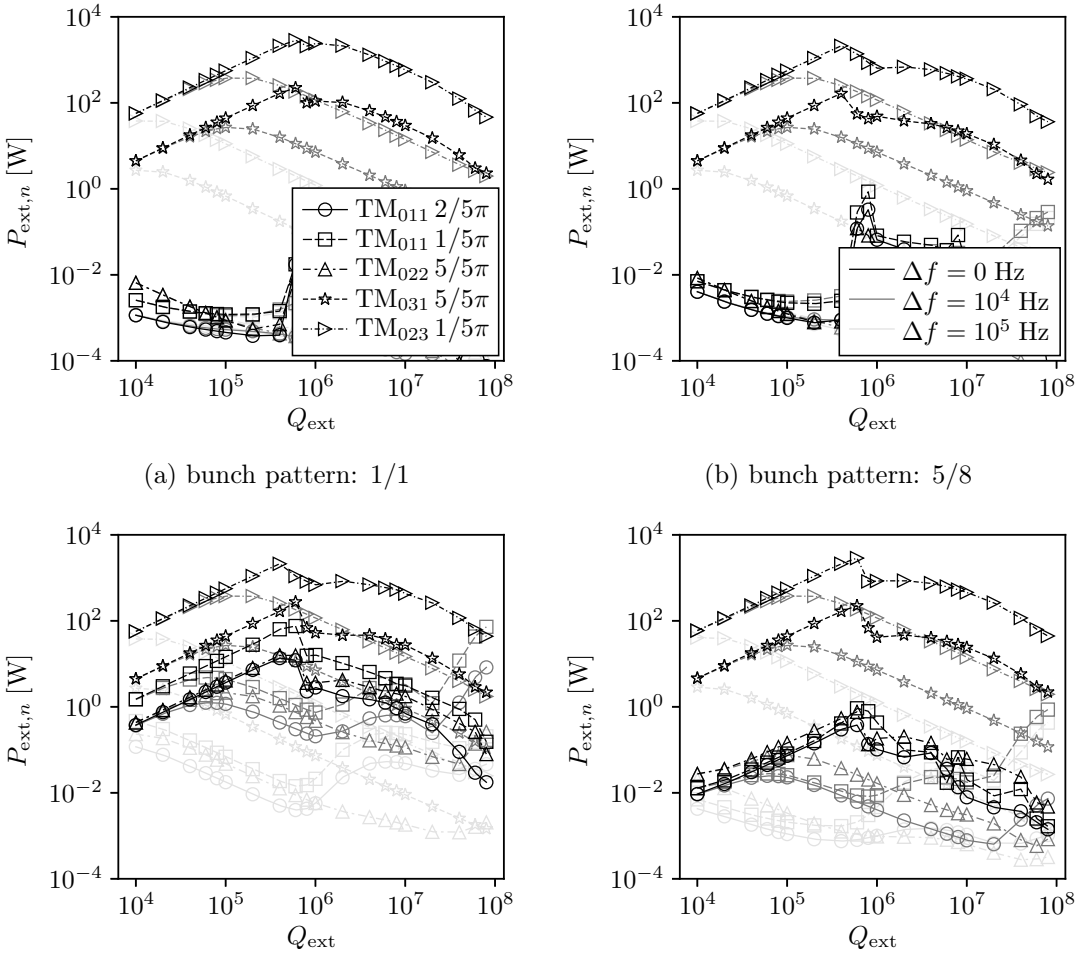

(a) bunch pattern: 1/1

(b) bunch pattern: 5/8

(c) bunch pattern: 50/80

(d) bunch pattern: 500/800

Fig. 3.23. Maximum mode specific extracted power in a high-β cavity as a function of external coupling Q_{ext} assuming different frequency shifts Δf (gray scaled). The frequency shifts are related to the distance of the individual HOM mean frequency from its nearest harmonic of either the bunch frequency or 50/80 bunch pattern frequency according to Table 3.11. The frequency spread is fixed to $f_\sigma = 1\,\mathrm{MHz}$ for each mode. Four different bunch patterns are considered with the nominal beam current of $I_B = 40\,\mathrm{mA}$, each. Amplitude and phase errors of the main rf system are not applied. Statistic of 1000 samples were carried out for each data point.

bunch pattern frequency. In case of the 50/80 bunch pattern in Fig. 3.23(c), the power required to extract from the TM_{011} $1/5\pi$ mode is comparable to the power required to extract from the TM_{031} $5/5\pi$ mode close to the seventh harmonic of the bunch frequency. Note, modes which have not been included in the simulation provide much smaller (R/Q) values and are considered as harmless. This conclusion is justified by observing Figs. 3.22 and 3.23 where the extracted powers vary partially by orders of magnitude between those modes which are accounted for.

The maxima in Figs. 3.22 and 3.23 appear for all considered modes with vanishing frequency shifts Δf in a range of $Q_{\text{ext}} = 10^6$ to 10^7. The reason why the power decreases at larger Q_{ext} is the fact that a significant fraction of the beam gets lost due to an unacceptable large growth of the longitudinal phase space as illustrated in Fig. 3.20(a). At a frequency shift of $\Delta f = 10\,\text{kHz}$, the maxima of extracted power appear in the vicinity of $Q_{\text{ext}} = 10^5$ while at a frequency shift of $\Delta f = 100\,\text{kHz}$, the corresponding maxima appear in the vicinity of $Q_{\text{ext}} = 10^4$. Depending on the frequency shift the power varies between a few tens of mW and 5 kW. However, a realistic amount of power, to be extracted by a single HOM coupler from a superconducting facility that is immersed in liquid helium at 2 K, ranges from a few tens of watts to 1 kW [16]. In the view of feasibility, quantity and costs, it was decided to restrict the maximum power extraction to 100 W per coupler [19]. This requires that the frequencies of the TM_{011} $2/5\pi$ mode in the medium-β cavity and the TM_{023} $1/5\pi$ mode in the high-β cavity are by far more than 100 kHz away from their nearest harmonics of the bunch frequency. In the presence of the 5/8 bunch pattern, the TM_{011} $1/5\pi$ mode in the medium-β cavity requires either a separation of at least 100 kHz from its nearest harmonic of the pattern frequency or a damping of $Q_{\text{ext}} \leq 10^4$ according to Fig. 3.22(b). The TM_{011} $3/5\pi$ mode in the medium-β cavity provides a power of almost 100 W at $Q_{\text{ext}} = 10^5$ if its frequency matches the fifth harmonic of the bunch frequency. A frequency shift of $\Delta f \geq 10\,\text{kHz}$ or a damping of $Q_{\text{ext}} \leq 5 \times 10^4$ should be considered. The damping option is preferred since this mode is by design less than 2 MHz away from the nearest machine line. The situation in the high-β cavity is slightly more relaxed. All considered modes other than the TM_{023} $1/5\pi$ mode provide in total less than 100 W to be extracted if an external coupling of $Q_{\text{ext}} \leq 10^5$ is ensured. This is true for any of the considered frequency separations Δf and bunch patterns.

It can be concluded that a damping of $Q_{\text{ext}} \leq 10^5$ is required for all HOM. Exceptions are the TM_{011} $3/5\pi$ and TM_{011} $1/5\pi$ mode in the medium-β cavity. Both modes must be stronger damped since a certain separation of their resonant frequencies from the nearest harmonics of the bunch or pattern frequency cannot be guaranteed during operating. The statement from [87, p. 123], that only moderate damping in the order of $Q_{\text{ext}} = 10^7$ is needed in the absence of any pulse substructures, does not apply to the current cavity designs since both the TM_{011} $3/5\pi$ mode in the medium-β cavity and the TM_{031} $5/5\pi$ mode in the high-β cavity provide nominal frequencies which differ by less than 2 MHz from their nearest harmonics of the bunch frequency as listed in Table 3.11. In the worst case, the particular mode coincides with the corresponding machine line due to manufacturing tolerances or tuner operations. A quality control and possible tuning with regard to these HOMs is recommended to ensure a minimum distance.

3.5 Low Power rf Measurements on High-β SPL Cavity

The first two prototypes of the high-β SPL cavity were fabricated out of Cu followed by four prototypes made of Nb. All of them were provided by RI Research Instruments. A fifth Nb prototype was fabricated at CERN but is not addressed in the present treatise. The measurements discussed in the following comprise (i) the resonant frequencies and frequency spreads of various monopole and dipole modes as measured over the four Nb prototypes, (ii) the field profile along the particle bunch propagation to identify selectively monopole and dipole modes as measured on a single Nb prototype, (iii) the frequency variation of resonant modes while cooling one of the Nb prototypes down to the operating temperature of 2 K, (iv) the frequency sensitivity and variation of HOMs due to plastic deformations as measured on one of the Cu prototypes, and (v) the frequency sensitivity of HOMs under the influence of elastic deformations during tuner operations as measured on one of the Nb prototypes. The results are compared to a large extent to simulations of preceding sections.

3.5.1 Frequency Spread

The resonant frequency of various monopole and dipole modes is measured at room temperature for high-β cavity prototypes. A Vector Network Analyzer (VNA) is used to analyze the rf transmission and reflection of the cavities from 0.5 GHz to 2.1 GHz. The reflected and transmitted signals are measured via two probe antennas. One of those is installed at the port foreseen for the fundamental mode coupler while the other one is installed on the pick-up coupler port. These ports are located at opposite cutoff tubes such that the transmitted signal passes through the cavity. The resonant frequencies are calculated from measured scattering functions using the method of vector fitting from Sec. 2.3.3. This is a convenient way to process many modes simultaneously without the lack of accuracy.

Figure 3.24 shows the frequency spread of various monopole and dipole modes measured over the four bulk Nb prototypes. Each mode is associated with its particular passband. The circuit model of Sec. 2.2.2 with (2.90) is used to approximate the dispersion relation for each pass band as illustrated by the solid black lines. Note, the hybridization of dipole modes due to coupling between TM and TE modes is not taken into account by (2.90), and yields partially poor approximations of the dispersion relation such as for the TM_{110} and TE_{121} bands in Fig. 3.24(b). The relative frequency spread of the considered HOMs ranges between 0.5 ‰ and 4 ‰ which corresponds to an absolute range of 0.5 MHz to 7 MHz. The measured monopole and dipole modes vary on average by 2.56 MHz and 2.45 MHz, respectively. Although the consideration of only four cavities is obviously not sufficient to quantify the frequency spread with statistical significance, the measurements provide a first estimate of realistic frequency spreads given by the mechanical tolerances during

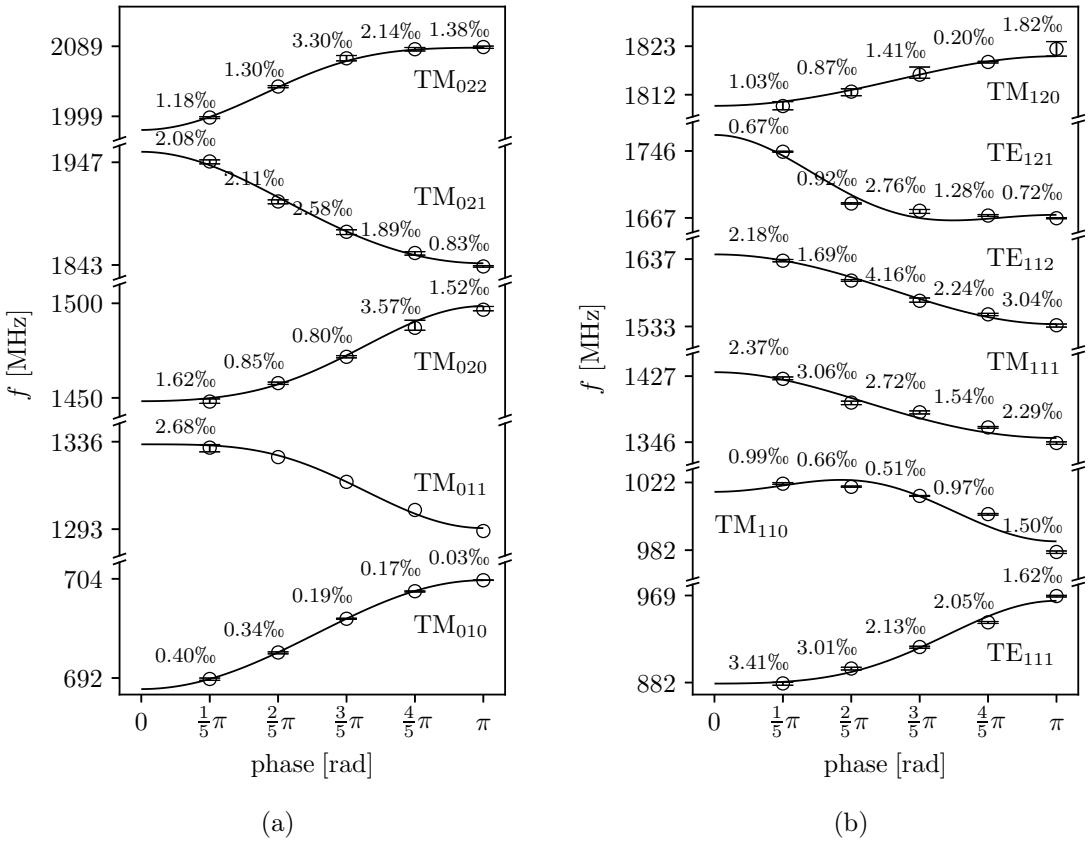

Fig. 3.24. Dispersion curves for (a) monopole and (b) dipole modes of the high-β SPL cavity with the relative frequency spread $\Delta f/f$ in ‰ measured over the first four bulk Nb prototypes as received from the manufacturer. Circles correspond to simulated values while the solid black lines result from a curve fitting based on the circuit model applied with periodic boundary conditions.

the fabrication and tuning. Due to the relatively large variations, it is absolutely necessary to examine in particular the TM_{031} $5/5\pi$ at 2464 MHz and the TM_{023} $1/5\pi$ mode at 2809 MHz within the cavity control as they are very close to harmonics of the bunch frequency according to Table 3.6. It is further recommended to examine the TM_{011} $1/5\pi$ mode at 1336 MHz as the power loss associated with this mode can be significant in the presence of substructured pulses as shown in Fig. 3.23(c).

3.5.2 Field Profile and Geometric Shunt Impedance

The measurement of the geometric shunt impedance requires knowledge about the field profile along the beam axis. In 1948, Hansen and Post [105] proposed a method which involves the interaction of the excited mode with a small metallic plunger guided along the center axis of the cavity. Since then, plungers of various shapes and compositions have been investigated in order to provide different effects on the

electric and magnetic field components. The perturbation of the resonant frequency $\delta\omega_n$ of mode n given by a small dielectric spherical bead with the radius δr in the vicinity of (r, φ, z) using cylindrical coordinates calculates as [106]

$$\frac{\delta\omega_n(r,\varphi,z)}{\omega_n} = -\frac{\pi\delta r^3}{\mathcal{U}^{(n)}}\left(\frac{\varepsilon_r-1}{\varepsilon_r+2}\varepsilon_0|\mathbf{E}^{(n)}(r,\varphi,z)|^2 + \frac{\mu_r-1}{\mu_r+2}\mu_0|\mathbf{H}^{(n)}(r,\varphi,z)|^2\right). \tag{3.25}$$

Typically, the perturbing bead is moved along the cavity axis, i. e. $r = \varphi = 0$ in order to evaluate the field profile of the particular mode along the nominal particle bunch propagation. The measurements presented in this section are carried out using a dielectric spherical bead with a relative permeability of $\mu_r = 1$ such that the magnetic field is, in general, not perturbed and variations of the resonant frequency are only correlated to the perturbation of the electric field according to

$$\frac{\delta\omega_n(z)}{\omega_n} = -\frac{\pi\delta r^3}{\mathcal{U}^{(n)}}\frac{\varepsilon_r-1}{\varepsilon_r+2}\varepsilon_0|\mathbf{E}^{(n)}(z)|^2. \tag{3.26}$$

It is worthwhile to note that the identification of resonant modes from scattering parameter measurements, as described in Sec. 3.5.1, can be problematic at higher frequencies where the mode spectrum becomes denser. In particular, this is the case when the variation of the resonant frequencies due to manufacturing tolerances is larger than the distance to adjacent modes. The measurement of the field profile by perturbation allows a unique identification of resonant modes. Figure 3.25 shows the simulated longitudinal and transverse electric field of significant monopole and dipole modes, respectively. It covers a small selection of modes that are examined by bead pulling in three bulk Nb prototypes. Note, the monopole and dipole modes provide only a longitudinal or, respectively, transverse electric field component on the beam axis such that the measurements of frequency variation along this axis correlates to the profile of the particular field components shown in Fig. 3.25. The remaining field components are either zero or not perturbed, so they are not measurable via the bead.

In general, it is desirable to reduce the measurement time since even minor changes in the environmental conditions such as temperature, humidity and pressure may affect the results. Therefore one usually evaluates the phase variation instead of the frequency variation while pulling the bead through the structure. The relationship between the perturbation of phase and frequency for a mode n with a quality factor $Q_n > 50$ is given by [106]

$$\delta\omega_n = \frac{\omega_n}{2Q_n}\tan\delta\phi_n. \tag{3.27}$$

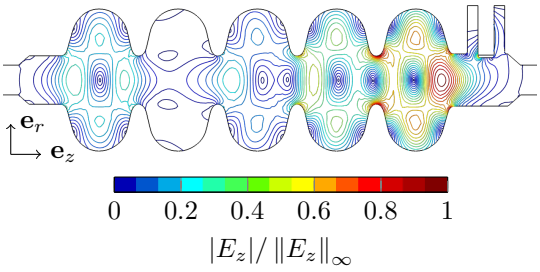

(a) TM_{011} $2/5\pi$ at 1328 MHz.

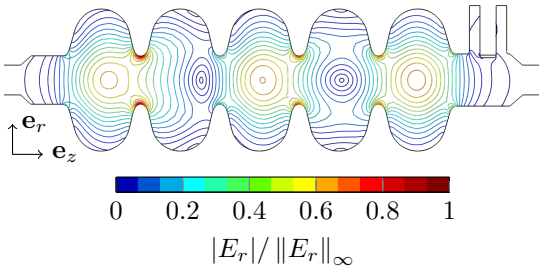

(b) TE_{111} $3/5\pi$ at 918 MHz.

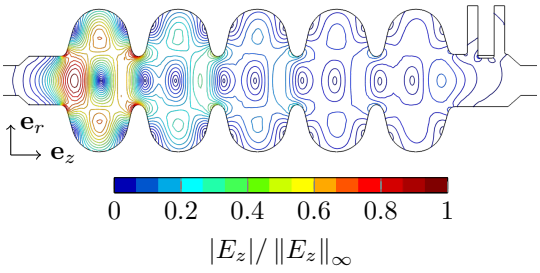

(c) TM_{011} $1/5\pi$ at 1335 MHz.

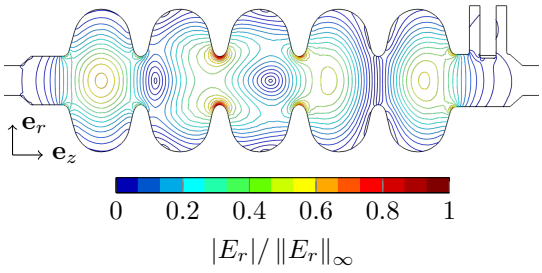

(d) TE_{111} $4/5\pi$ at 943 MHz.

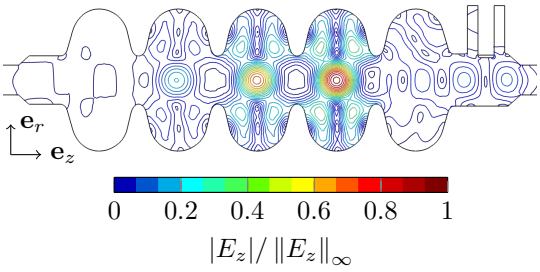

(e) TM_{022} $5/5\pi$ at 2088 MHz.

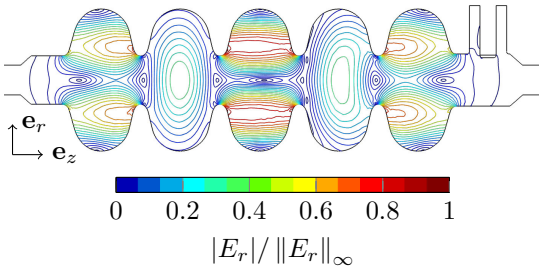

(f) TM_{110} $3/5\pi$ at 1014 MHz.

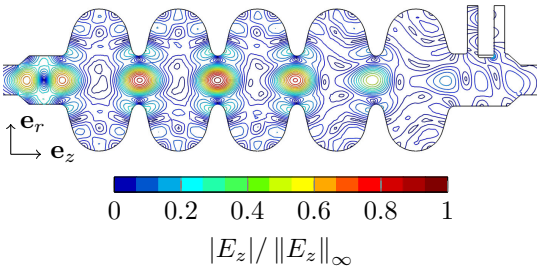

(g) TM_{031} $5/5\pi$ at 2463 MHz.

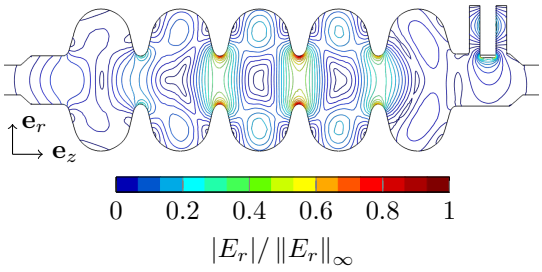

(h) TM_{111} $2/5\pi$ at 1395 MHz.

Fig. 3.25. Cross-sectional view of normalized electric field components for significant monopole (left) and dipole HOMs (right) simulated using COMSOL Multiphysics® software [90].

The phase and frequency are derived from scattering parameters measured between the fundamental mode coupler port and the port reserved for the pick-up antenna as described in Sec. 3.5.1. In case of the phase measurement, the VNA generates a harmonic signal with a frequency equal to the resonant frequency of the considered mode while the frequency measurement is based on a frequency sweep at each position of the bead with subsequent fitting of one or more resonant frequencies depending on the frequency interval. The latter approach does not require prior knowledge of the resonant frequency but is less accurate due to the longer measurement time.

In order to compare both methods, the field flatness from cell to cell was evaluated for three high-β SPL cavities made of Nb. The field flatness from cell to cell is a measure of the field quality related to the fundamental mode. It describes the maximum variation of the peak accelerating field over all cells along the center axis, and should be minimized during the tuning procedure of the cavity. Typically, it is measured via the phase variation while pulling a bead through the cavity. The results of phase and frequency measurements are compared in Table 3.12. Note, the definition of [107, p. 250] is used for the field flatness. Hence, a value of 100 % corresponds to a uniform distribution of the electric field maxima along the center axis. The errors of the phase measurements are based on five repetitions and are within ± 0.2 %. The errors of the frequency measurements are five to ten times larger, which is inappropriate for tuning the fundamental mode in terms of resonant frequency and field flatness. However, this accuracy is sufficient to identify HOMs, as shown in the following. The main advantage of the method based on frequency sweeps is the consideration of an entire frequency band over many modes without the need to know the exact resonant frequencies prior to the measurement.

Figs. 3.26 and 3.27 show the measured and simulated field profiles of various monopole and dipole modes along the particle bunch propagation. The measurements are carried out with a spherical bead made of Polyethylene with 6.2 ± 0.02 mm diameter and a relative permittivity of $\varepsilon_r = 2.35$. The ordinates of Figs. 3.26 and 3.27 correspond to the ratio of the longitudinal or, respectively, transverse electric field and the square root of the stored energy, which is proportional to the square root of the relative frequency variation according to (3.26). Note, the orientation of the electric field is deduced from simulations since the perturbation method provides only quantities that correlate to field magnitudes. The measured results agree fairly well with those of the simulations and permit a clear identification.

The particular case of TM monopole modes allows the calculation of geometric

Table 3.12. Field flatness of the first three high-β bulk Nb prototypes [%].

method	SPL1	SPL2	SPL3
phase measurement	98.3 ± 0.03	96.74 ± 0.18	98.01 ± 0.07
frequency measurement	98.05	95.98	97.74

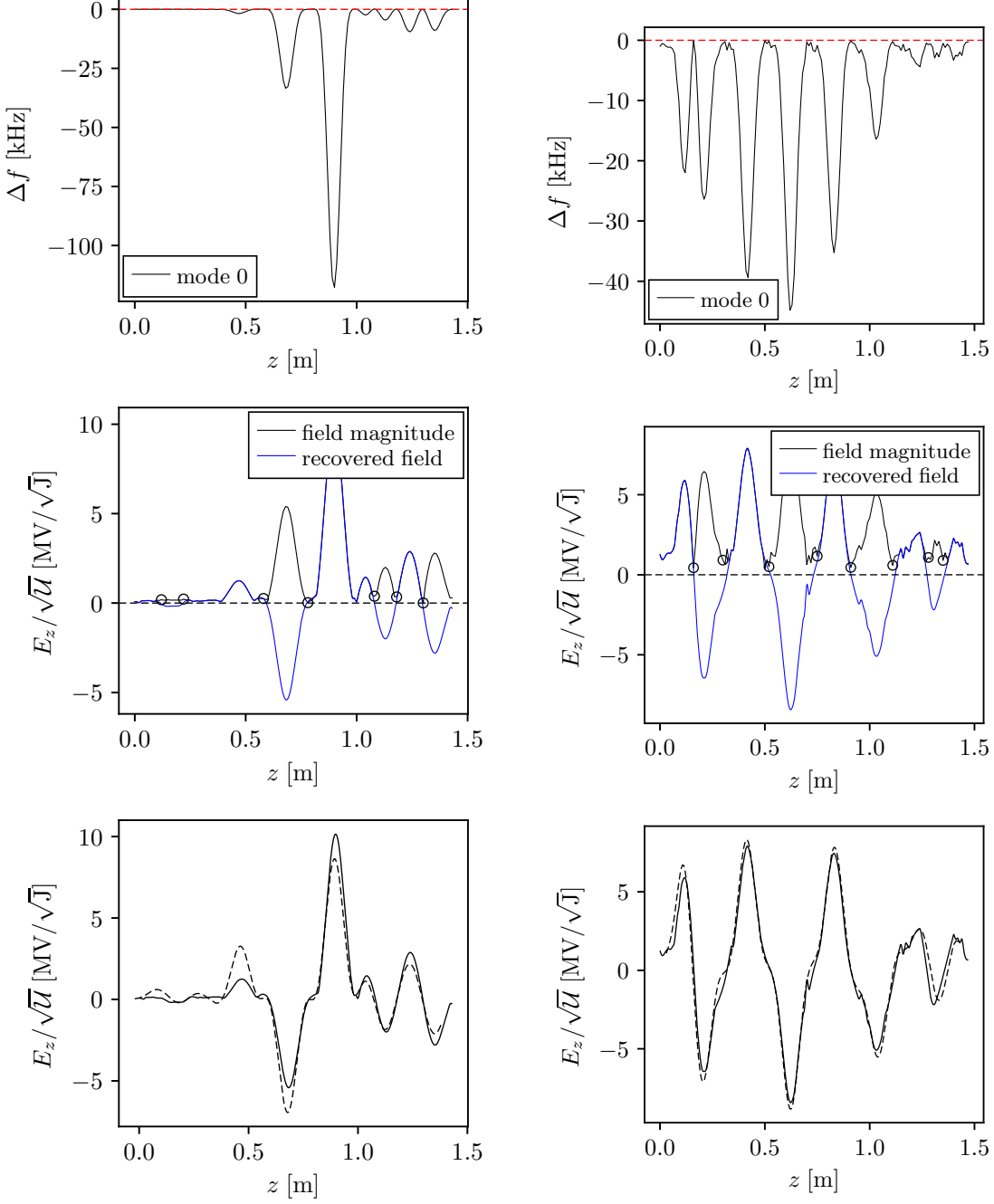

(c) TM_{022} $5/5\pi$ at 2088 MHz.

(d) TM_{031} $5/5\pi$ at 2463 MHz.

Fig. 3.26. Measured and simulated field profiles of higher-order monopole modes.

shunt impedances since the longitudinal electric field is the only contribution that needs to be integrated along the beam axis taking into account the phase advance according to (2.115). The error is relatively high, as shown in Table 3.13 for various monopole modes. This is mainly due to environmental changes that occurred during the measurements. The bead is moved in steps of 10 mm through the structure with the scattering functions being measured from 0.5 GHz to 2.5 GHz at each position. This procedure requires several minutes, which means that changes in the temperature, humidity and pressure are unavoidable, and can only partially be compensated in the case of slow drifts. Other well known problems are the slippage and vibrations of the wire which guides the bead through the cavity and causes distortions of the measured profiles [108, pp. 30–40]. Note, the simulated values in Table 3.13 slightly differ from Tables 3.5 and 3.6 as the cavity is considered at room temperature.

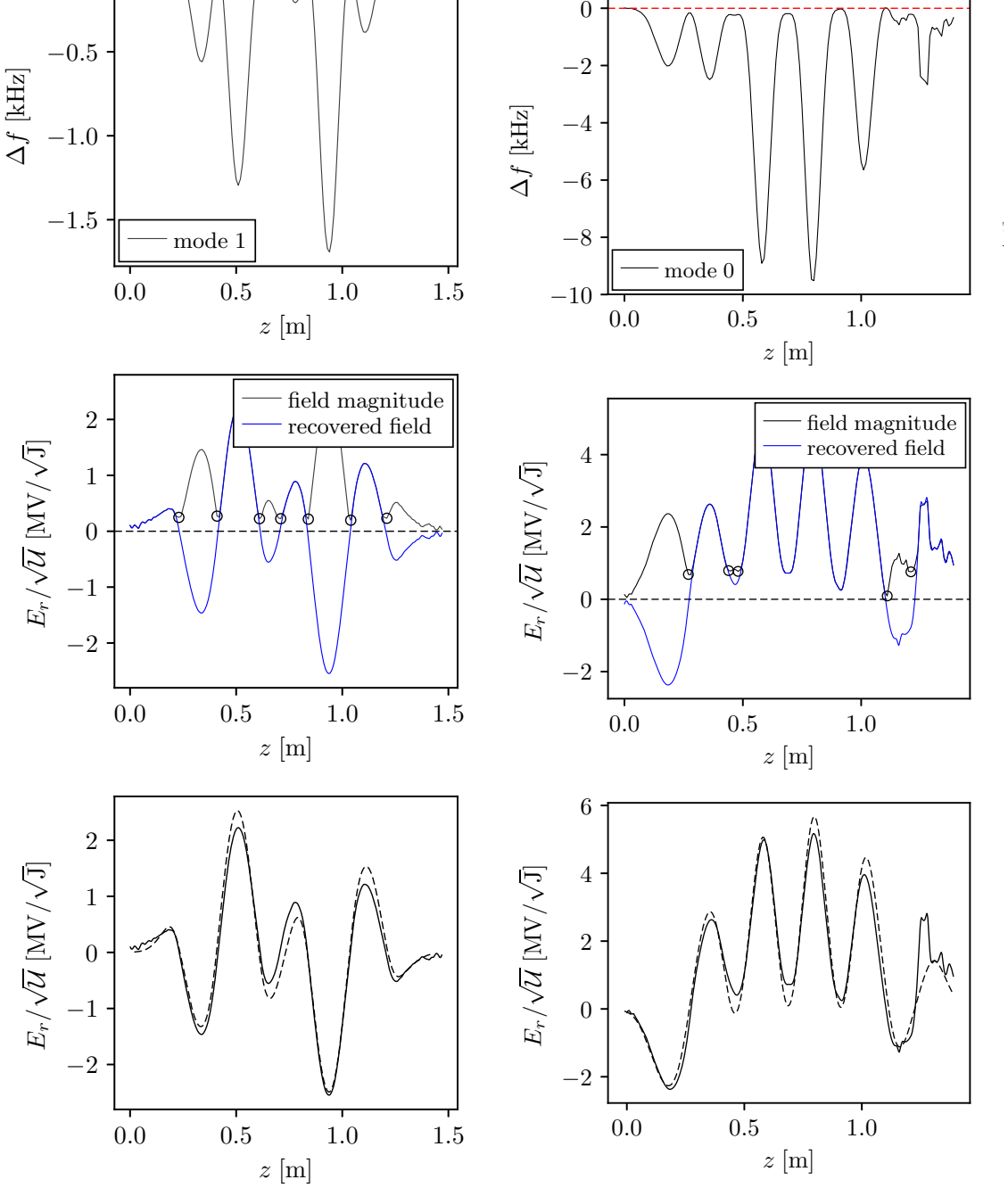

(c) TM_{110} $3/5\pi$ at 1014 MHz.

(d) TM_{111} $2/5\pi$ at 1395 MHz.

Fig. 3.27. Measured and simulated field profiles of higher-order dipole modes.

Table 3.13. Frequency and geometric shunt impedance at room temperature.

	simulation		measurement	
mode n	f_n [MHz]	$(R/Q)_n(\beta_g)$ [Ω]	f_n [MHz]	$(R/Q)_n(\beta_g)$ [Ω]
TM_{010} $5/5\pi$	703.82	565.50	703.82	501.82
TM_{011} $2/5\pi$	1328.45	59.05	1333.62	46.40
TM_{011} $1/5\pi$	1334.61	104.70	1337.86	122.86
TM_{022} $3/5\pi$	2070.75	0.27	2073.19	1.73
TM_{022} $4/5\pi$	2084.57	1.68	2088.11	6.17
TM_{022} $5/5\pi$	2088.04	19.21	2093.18	15.10
TM_{031} $5/5\pi$	2462.57	0.39	2463.08	0.62

3.5.3 Impact of Temperature

The focus of this section is the frequency shift of HOMs when cooling the cavity from room temperature down to the operating temperature of 2 K. The frequency change is mainly caused by the thermal contraction. Furthermore, the ambient environment changes from normal air at 293 K with 50 % humidity and atmospheric pressure to vacuum, which alters the relative permittivity ε_r and, thus, the frequency as well [109]. A third aspect is given by the abrupt change of the penetration depth in the transition from the normal conducting to superconducting state of Nb. This effectively alters the surface impedance, which is likewise related to a shift of the resonant frequency [110]. All three aspects are described in detail in [111].

Two bulk Nb prototypes are examined during high-gradient tests in a cryostat. Each cavity was installed vertically and equipped with temperature sensors as shown in Fig. 3.28(a). The measurements presented in the following refer to the prototype SPL2 and are carried out during the warming phase from 2 K to room temperature. The corresponding temperature profiles are shown in Fig. 3.28(b). Note, the Sensor TT844 is close to the heater to warm the structure, which explains the overall higher temperature. Also, the measurements are compromised by a temperature gradient in part about 40 K. Two separate measurements were evaluated with homogeneous temperature distribution at 2 K and 4 K.

The resonant frequencies are evaluated in a manner analogous to Sec. 3.5.1 or 3.5.2 using a VNA to measure the rf transmission and reflection between the fundamental mode coupler port and pick-up antenna port of the high-β SPL cavity. As a consequence of much longer rf cables and pressure fluctuations in the helium bath, the signal to noise ratio is significantly reduced. Figure 3.29 shows the example

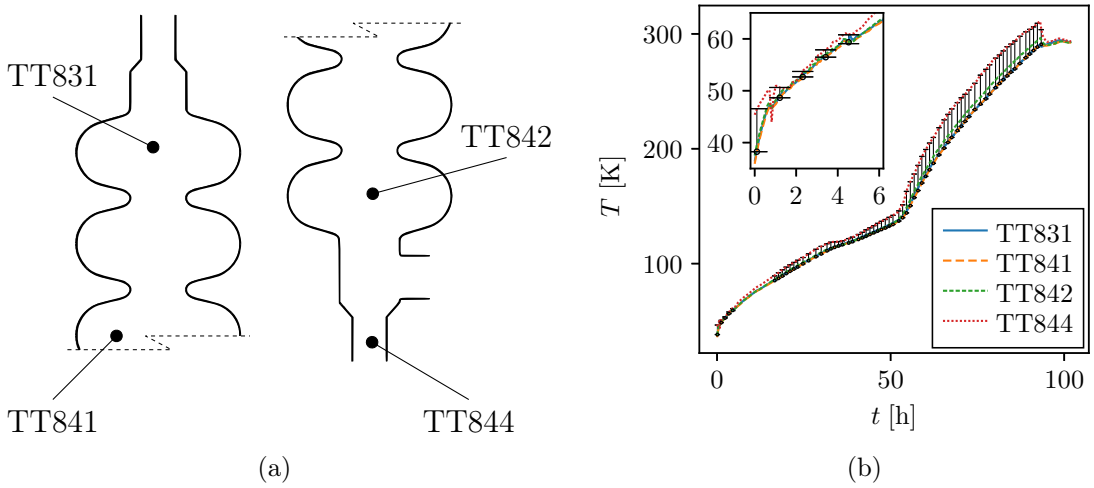

Fig. 3.28. (a) Sketch of the cavity equipped with four temperature sensors. (b) Temperature distribution measured over the cavity (SPL2) while warming from 2 K up to room temperature.

of the TM_{110} $2/5\pi$ dipole mode at 2 K and at room temperature. The measured transmission is shown in light gray while the dashed lines correspond to a fit of these data based on the method of classical vector fitting from Sec. 2.3.3. At both temperatures, the fitting procedure fails due to the high noise level, and the resonant frequencies are not resolved. Note, the modified vector fitting provides somewhat better results by using an additional free parameter for the asymptotic behavior at very high frequencies according to (2.159). It is more appropriate to filter or smooth the signal before applying the fitting procedure. There are several options to increase the signal to noise ratio without compromising the signal too much. For example, the VNA can be configured with a lower intermediate frequency bandwidth or averaging over several frequency sweeps may be applied. Both approaches reduce the noise level but increase the measurement time. Alternatively, filters such as a moving average or Savitzky-Golay filter [112] can subsequently be applied on the measured data, without the need of multiple frequency sweeps or a reduced intermediate frequency bandwidth of the VNA. A generic filter is implemented for the same purpose. It is analog to a low-pass filter but in time domain, and can be sketched as follows: (i) Transform the scattering parameters in time-domain. (ii) Apply a particular window, for instance, a Kaiser window to the obtained time signals such that components associated with the noise in the frequency spectrum are much reduced. These are, in general, the signal components at larger time and relatively low in amplitude. Thresholds are used to adapt the window parameters. (iii) Back-transform the filtered time signal in frequency domain. This approach is used to process measurements such as shown in Fig. 3.29 in a very robust way.

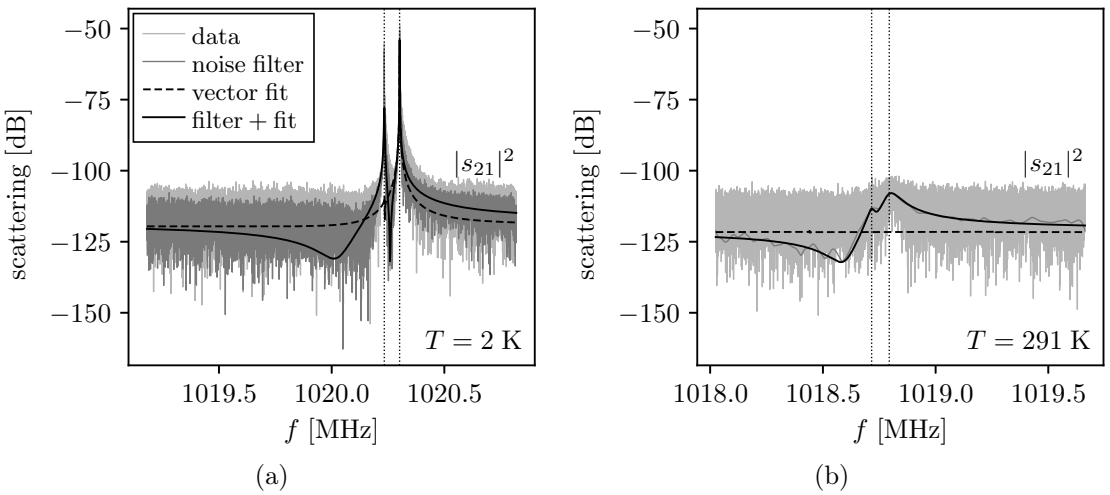

Fig. 3.29. Filtering and Fitting applied on the measured rf transmission around 1020 MHz at (a) 2 K and (b) room temperature. The plots show the two polarizations of the TM_{110} $2/5\pi$ dipole mode. The dotted vertical lines highlight the resonant frequencies. In dashed black, a vector fit applied on the pure data. In solid black, a vector fit applied on the filtered data.

Figure 3.30 depicts the measured frequency variation of various modes as a function of temperature. The dashed lines correspond to the frequency shift due to thermal contraction assuming a uniform temperature distribution at each measurement. It provides a rough estimate since neither the impact of temperature gradient nor changes in the environmental conditions are considered. In most cases the actual variation is larger. Figure 3.31 shows the total variation of all considered modes while warming the cavity from the operating temperature of 2 K to room temperature.

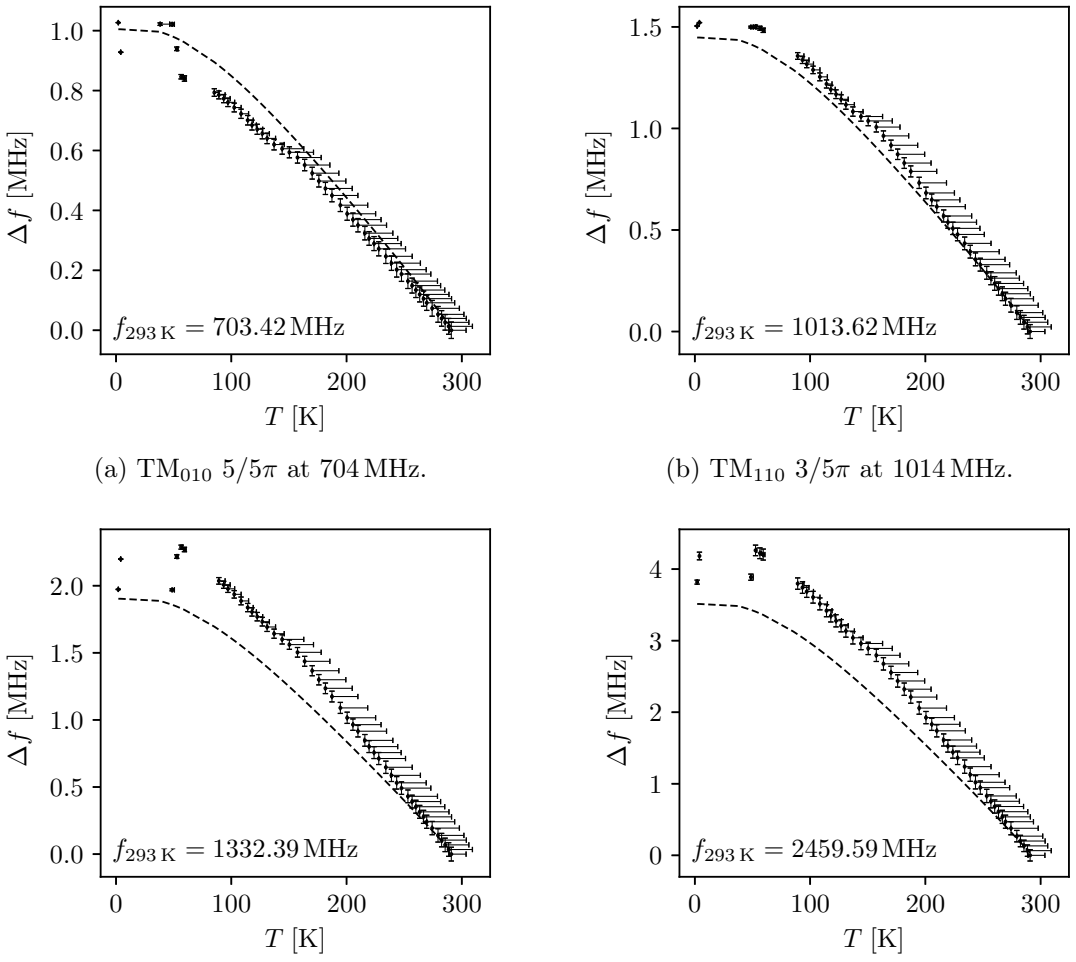

(a) TM_{010} $5/5\pi$ at 704 MHz.

(b) TM_{110} $3/5\pi$ at 1014 MHz.

(c) TM_{011} $1/5\pi$ at 1335 MHz.

(d) TM_{031} $5/5\pi$ at 2463 MHz.

Fig. 3.30. Frequency shift during warm up. The horizontal error bars correspond to the temperature gradient in the structure while the vertical error bars are associated with the 3 dB bandwidth. The dashed line corresponds to the analytic frequency shift due only to thermal contraction.

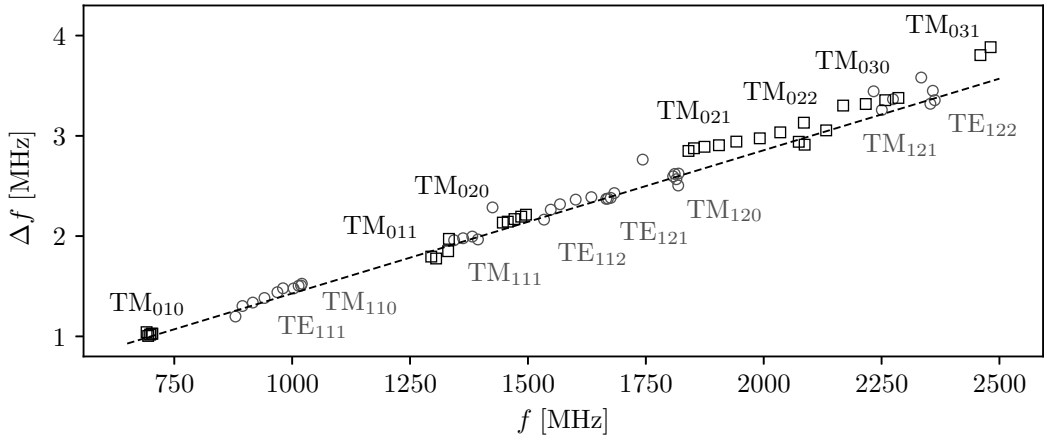

Fig. 3.31. Total variation of all considered modes while changing the temperature from 2 K to 293 K. Monopole modes are marked by squares while dipole modes are marked by circles. The dashed line corresponds to the analytic frequency shift due only to thermal contraction.

3.5.4 Plastic Deformation

After fabrication, it is imperative to tune the SPL cavities in terms of fundamental mode frequency and field flatness from cell to cell. This process is done by plastically deforming individual cells using a dedicated tuning bench as sketched in Fig. 3.32. A force is applied at the irises to squeeze or squash the particular cell, which alters the resonant frequency, cell-to-cell coupling, and eventually the field flatness of the fundamental mode.

In the interest of developing a method to shift the frequency of individual HOMs away from harmonics of the bunch or pattern frequencies, it is appropriate to study the influence of cavity detuning and retuning on HOMs of concern. The variation of various HOMs is evaluated for a bulk Nb mono-cell SPL cavity and a high-β SPL cavity made of bulk Cu. As previously described, the resonant frequencies are obtained by measuring the rf transmission and reflection using a VNA. The corresponding scattering parameters are fitted by the method of vector fitting in order to derive the resonant frequencies. In case of the mono-cell cavity, the two rf antennas to measure the scattering parameters are installed at both beam pipe ports. The measurements on the multi-cell cavity proceed in the same way as in Sec. 3.5.1 using one antenna at the input coupler port and the second antenna at the port foreseen for the pick-up antenna.

The tuning bench permits varying the length of individual cells in a range of approximately ± 1.5 mm. However, the limits depend on material conditions and history since the tuning bench is primarily limited by force. In order to squeeze the mono-cell cavity, the force is applied at the flanges as shown in Fig. 3.33(a). The setup to squeeze or squash one of the inner cells of the high-β SPL cavity prototype is shown in Fig. 3.33(b). The tuning walls are attached slightly above the irises. In

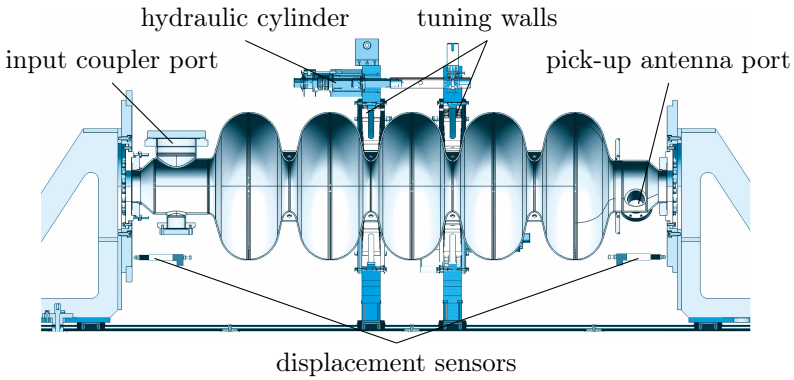

Fig. 3.32. Sketch of the tuning bench with mounted high-β SPL cavity. The tuning plates are attached slightly above the irises. The distance between the tuning walls is controlled by three hydraulic cylinders, which allows individual cells to be squeezed and squashed. In order to squeeze the outer cells, one of the tuning walls is fixed to the corresponding beam pipe flange. The overall cavity length and distance between the tuning walls is measured by displacement sensors. The left and right support as well as the tuning walls are on sliding bars.

addition, this setup is applied when squashing the mono-cell or the outer cells of the high-β SPL cavity. To squeeze the outer cells of the latter one, the tuning walls are attached to the corresponding iris and beam pipe flange, hence, a mixture of the setups shown in Fig 3.33 is used. The deformation is measured via the entire cavity length using displacement sensors as shown in Fig. 3.32. It is important to remark that the variation of the cavity length provides only an estimate of the considered cell deformation since the deformation of neighboring cells and cutoff tubes might be involved, depending on the setup.

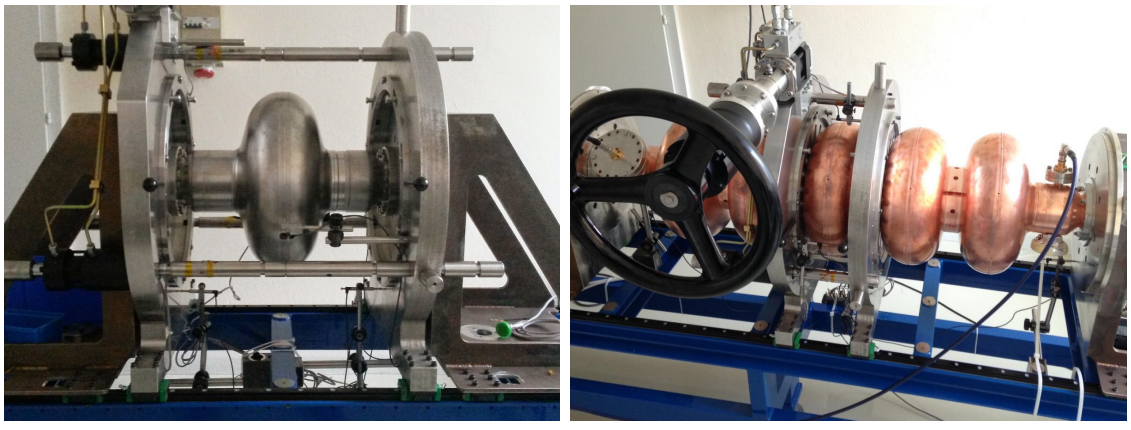

(a) (b)

Fig. 3.33. Setup of the tuning bench (a) to squeeze the bulk Nb mono-cell SPL cavity prototype and (b) to squeeze or squash the center-cell of a high-β SPL cavity prototype made of bulk Cu.

Figure 3.34 illustrates the impact of plastic deformations on various monopolar and dipolar HOMs in the mono-cell SPL cavity. The process of squeezing and squashing evolves very differently. This is primarily due to the fact that the force does not exactly act at the iris but rather slightly above the iris or at the beam pipe flanges. In a first step, the mono-cell cavity was plastically squashed by 0.23 mm, with the tuning walls being attached to the irises as shown in Fig. 3.33(b). In a second step, the mono-cell cavity was plastically squeezed until the original frequency of the fundamental mode was restored, hence until the cavity was retuned. For this purpose, the tuning walls were attached to the beam pipe flanges as shown in Fig. 3.33(a). The force required to provide a certain plastic cell deformation was found to be significantly lower if applied at the flanges than if applied at the irises. The remaining frequency variation of considered HOMs ranges from 0.1 MHz to 1.6 MHz. It is particularly surprising that the resonant frequency of some HOMs changes significantly during the squashing process but almost remains at the same value during the squeezing process. This behavior applies, for instance, to the TM_{011} mode in Fig. 3.34(a) or the TM_{120} mode in Fig. 3.34(b).

The high-β SPL cavity prototype made of bulk Cu is studied for various such detuning and retuning cycles. The corresponding remaining frequency variations of several monopolar and dipolar modes are summarized in Figs. 3.35 and 3.36, with the inner three cells being subjected only to plastic deformations. Initially, the five-cell cavity is tuned according to the fundamental mode frequency of 703.8 MHz and a field flatness from cell to cell of 99 % using the method described by Padamsee [17,

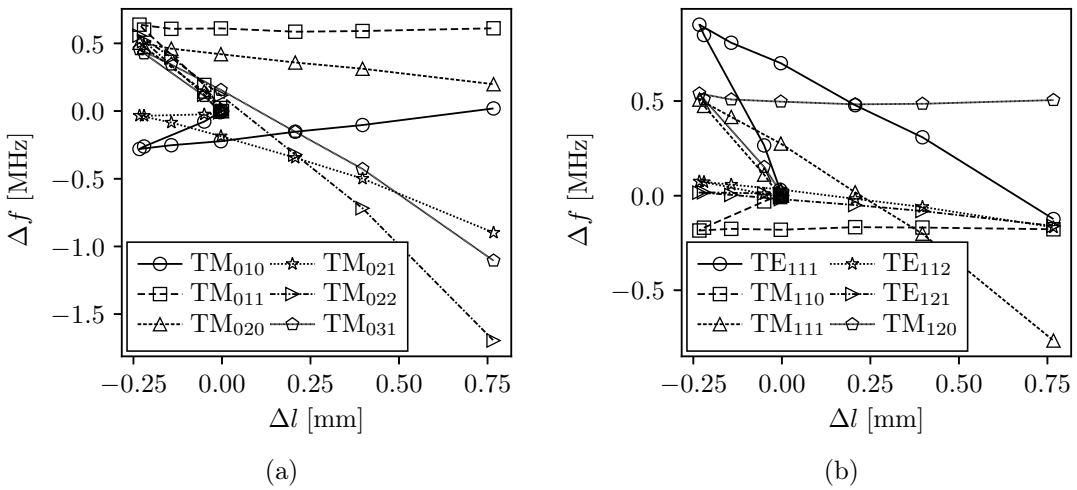

Fig. 3.34. Frequency variation of (a) monopolar and (b) dipolar HOMs in the mono-cell SPL cavity as a function of the variation in cavity length. The initial state of the cavity corresponds to $\Delta l = 0$ and $\Delta f = 0$ with respect to all modes. At first, the cavity was squashed by 0.23 mm. To retrieve the original frequency of the fundamental TM_{010} mode, the cavity was subsequently stretched by 1 mm such that $\Delta l = 0.77$. The remaining HOM variations range from 0.1 MHz to 1.6 MHz.

pp. 129–142]. After initial tuning, the impact of detuning and retuning on HOMs is studied for individual cells as well as for a combination of two cells. For this purpose, the cavity was firstly detuned by plastically deforming the particular cell or cells. The resulting variation in cavity length, Δl, is shown on the argument axes in Figs. 3.35 and 3.36, with negative and positive values being related to squashing and squeezing, respectively. Afterwards, the cavity was gradually tuned by deforming the considered cell or cells in the opposite way until the original frequency of the fundamental mode was restored within 10 kHz. The remaining frequency variation

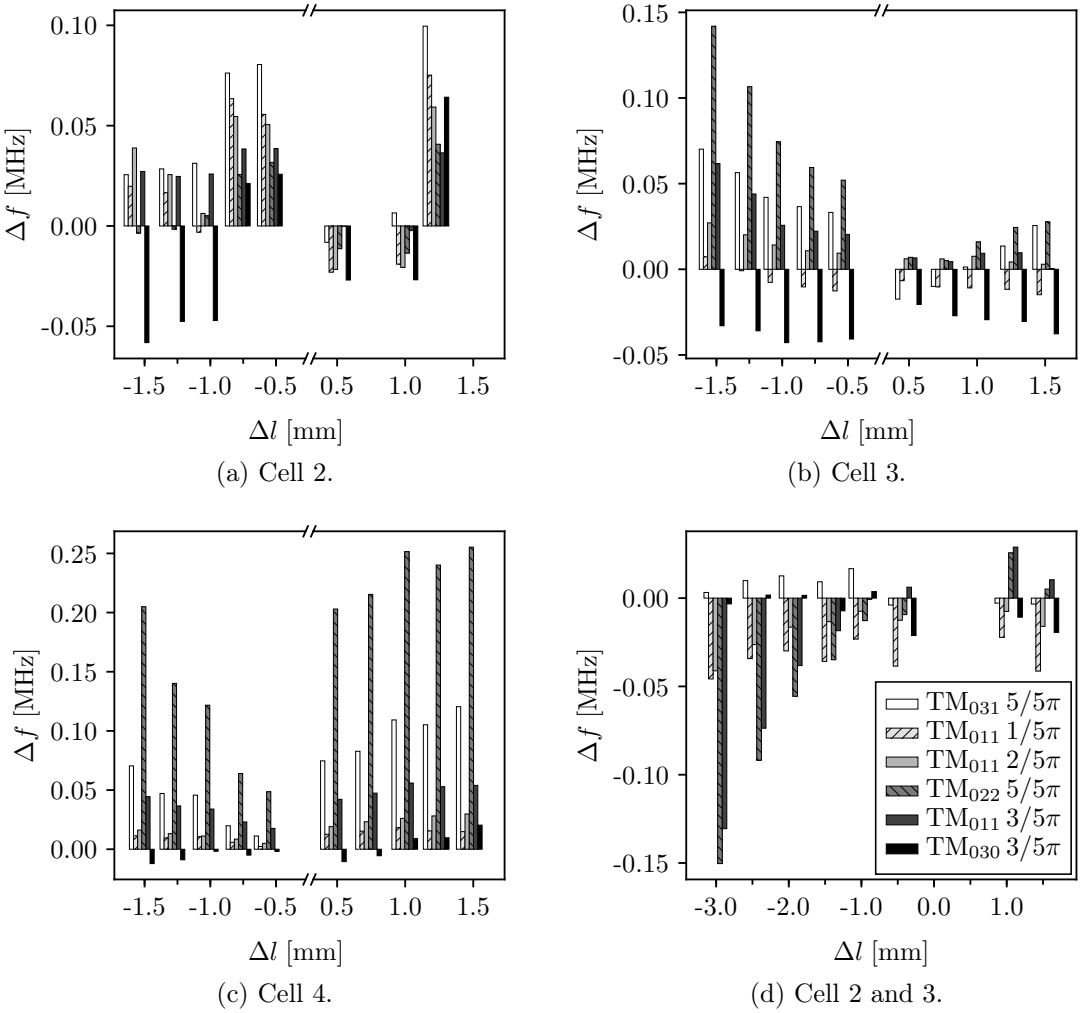

(a) Cell 2. (b) Cell 3.

(c) Cell 4. (d) Cell 2 and 3.

Fig. 3.35. Remaining frequency variation of monopolar HOMs after detuning and retuning the high-β SPL cavity made of bulk Cu. The deformations are applied to individual cells. The cell number is counted from the left to the right in Fig. 3.32. The cases (a)-(c) are related to the plastic deformation of the particular inner three cells while in (d), the deformation was applied on two neighboring cells. The remaining frequency variation after retuning, Δf, is shown as a function of the cavity length variation Δl measured after the previously applied detuning process.

of HOMs is illustrated as bars in Figs. 3.35 and 3.36. During the measurements, the field flatness from cell to cell was recorded above 96.5 % in each retuned state.

The variation of HOMs by detuning and retuning the high-β SPL cavity was found to be much less than observed for the mono-cell cavity. This is partially due to the fact that modes such as the TM_{011} $1/5\pi$ and TM_{011} $2/5\pi$ are mainly concentrated in the outer cells whose deformation is not considered here. However, even the TM_{022} $5/5\pi$ mode which is concentrated at two inner cells according to Fig. 3.25(e) does not provide larger variations than 250 kHz within the considered detuning range of

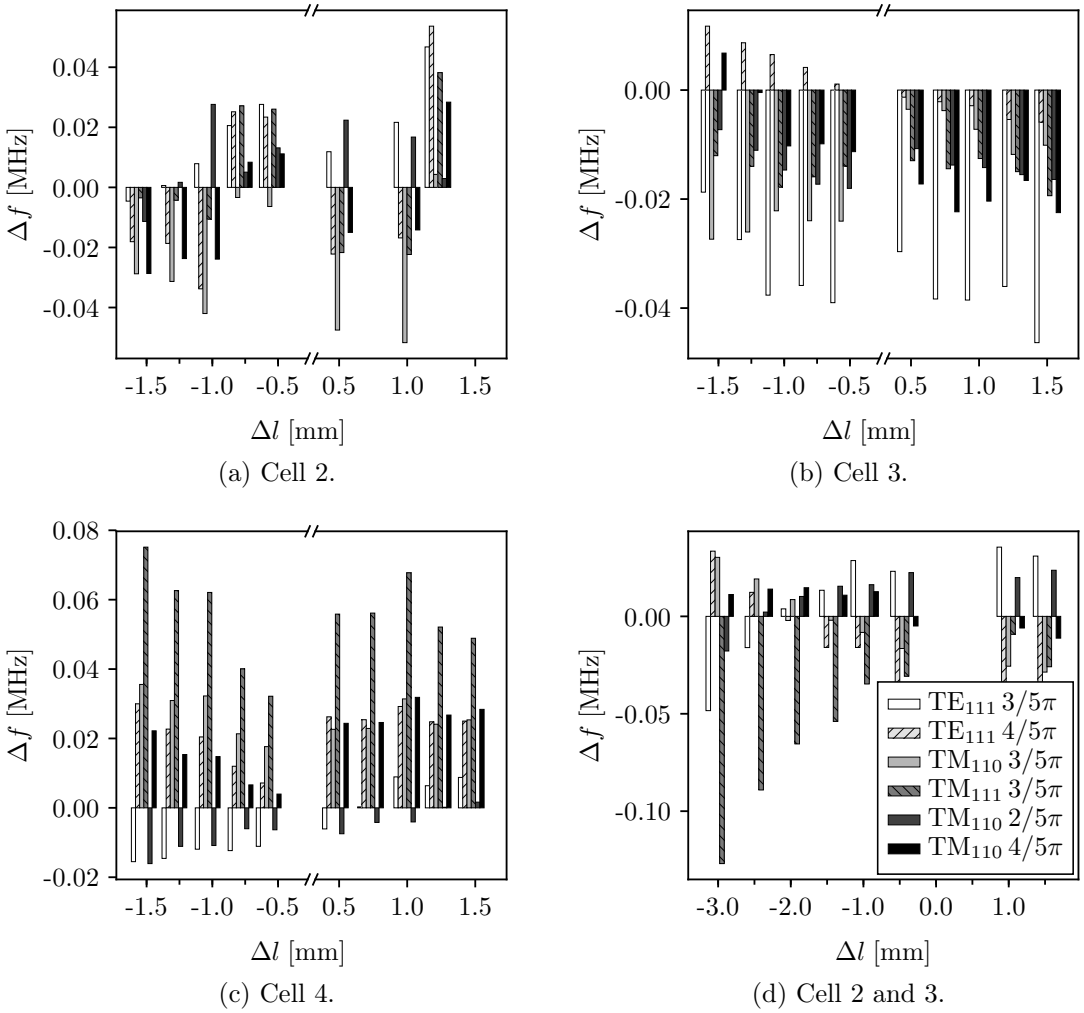

(a) Cell 2. (b) Cell 3.

(c) Cell 4. (d) Cell 2 and 3.

Fig. 3.36. Remaining frequency variation of dipolar HOMs after detuning and retuning the high-β SPL cavity made of bulk Cu. The deformations are applied to individual cells. The cell number is counted from the left to the right in Fig. 3.32. The cases (a)-(c) are related to the plastic deformation of the particular inner three cells while in (d), the deformation was applied on two neighboring cells. The remaining frequency variation after retuning, Δf, is shown as a function of the cavity length variation Δl measured after the previously applied detuning process.

$\Delta l = \pm 1.5\,\mathrm{mm}$. This is about six times smaller than the frequency variation achieved for the corresponding mode in the mono-cell cavity in Fig. 3.34(a). Comparing Figs. 3.35 and 3.36, the variations of the considered dipolar HOMs appear somewhat lower than the variations of the considered monopolar HOMs.

The present tuning bench permits only a moderate change of the particular HOM frequency in the order of a few hundreds of kHz at most. This is sufficient to avoid excessive power dissipation by HOMs with a frequency being too close to a harmonic of the bunch frequency, as studied in Sec. 3.4.5. However, the frequency variations of HOMs during operation due to the tuner may retune to this worst case scenario. The impact of elastic cavity deformations on HOMs caused by the tuner is discussed in the following.

3.5.5 Elastic Deformation during Operation

In order to compensate frequency drifts of the fundamental mode frequency during operation, each cavity is equipped with a tuner as sketched in Fig. 3.37. It is also required to compensate remaining unpredictable frequency errors occurring during the cryomodule assembly and cool down [19]. The tuner has been developed at CEA Saclay and is able to squeeze the entire cavity at 2 K within a range of approximately 3 mm. This range is considered as the elastic regime of the high-β SPL cavity and allows the fundamental mode frequency to be adjusted in a range of about 500 kHz. The tuner is attached to the tuning plate of the cavity and the helium vessel which is replaced by an experimental frame in Fig. 3.37. The same setup with the experimental frame is used in order to investigate the variation of HOM frequencies during the tuner operation at room temperature.

The measurements shown in Fig. 3.38 are carried out for one of the bulk Nb prototypes (SPL4). Since the deformations are elastic and relatively small, the resonant frequencies vary linearly with the displacement according to the perturbation theory. Therefore, the results are given as frequency variation per 1 mm cavity length

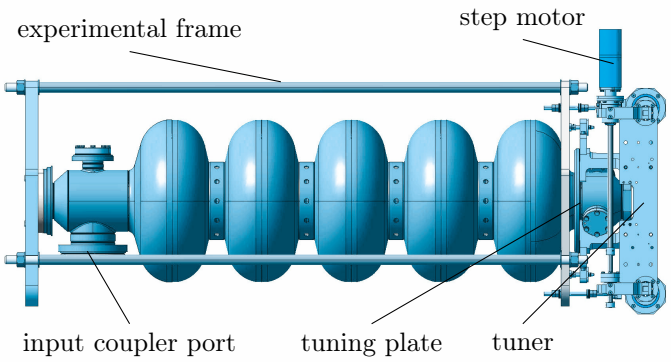

Fig. 3.37. Sketch of the high-β SPL cavity equipped with the tuner in an experimental frame.

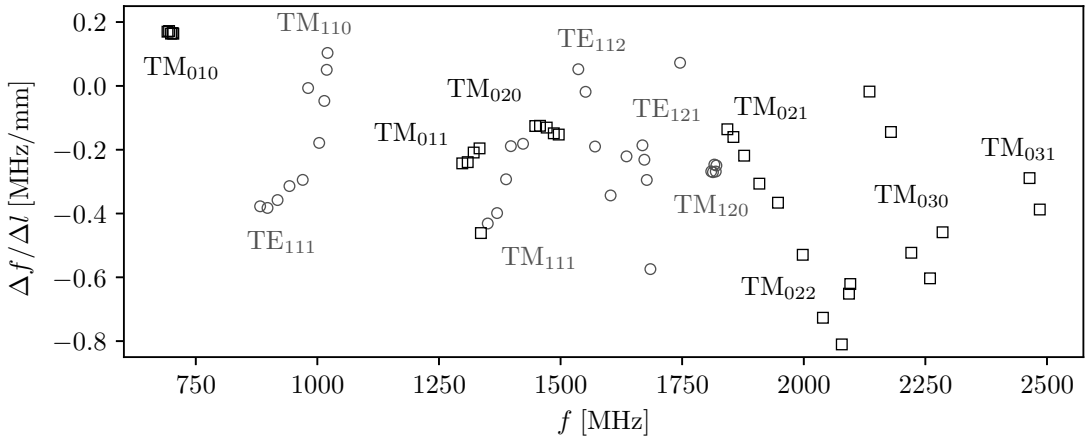

Fig. 3.38. Sensitivity of modes during tuner operation as a function of the mode frequency. The ordinate is given in frequency variation per 1 mm cavity length increase. Monopole modes are highlighted by squares while dipole modes are highlighted by circles.

increase. Depending on the considered mode the resonant frequency may vary up to ±2.4 MHz. The TM$_{031}$ $4/5\pi$ and TM$_{023}$ $1/5\pi$ in Table 3.6 provide sufficient distance from the seventh and eights harmonic of the bunch frequency, respectively. Note, this applies only if manufacturing errors or other unpredictable effects do not push these modes significantly closer to the particular harmonics of the bunch frequency. However, the TM$_{031}$ $5/5\pi$ mode with a nominal distance of 1.05 MHz from the seventh harmonic of the bunch frequency may vary in a range of about 0.9 MHz. According to Fig. 3.23, the extracted power rises by several tens of watts as this mode approaches the seventh harmonic of the bunch frequency. An HOM coupler intended to provide an external quality factor of $Q_{\mathrm{ext}} = 10^5$ for the TM$_{031}$ $5/5\pi$ mode is required to extract about 60 W in the worst case, only for this mode. A lower quality factor further increases the extracted HOM power to more than 100 W. It is important to remark that the TM$_{031}$ $5/5\pi$ is only moderately influenced by detuning and retuning individual cells, as shown in Fig. 3.35 by the black bars. It is due to the fact that this mode is concentrated in the irises and one cutoff tube according to Fig. 3.25(g). A deformation of the outer cell together with the corresponding cutoff tube is recommended.

3.6 Summary of the Results

Potentially dangerous higher-order modes have been identified for both the medium-β and high-β SPL cavity. A survey of extensive studies on the basis of simulations and measurements has been presented to characterize these modes not only in terms of resonant frequency, geometric shunt impedance, and field patterns but also by their influence on eventual emittance growth in the longitudinal phase space, sensitivity on plastic or elastic cavity deformations, as well as their frequency variations while cooling the cavity from room temperature, i. e. 293 K down to the operating temperature of 2 K.

The influence on the beam, which manifests first and foremost in an increased longitudinal phase space, strongly depends on the distance between the resonant frequency of the particular mode and its nearest harmonic of the bunch or chopping frequency. A minimum distance of 10 kHz is necessary to keep the operation feasible. Since the tuner allows for frequency shifts in the order of 2 MHz, the situation may become very problematic with respect to the TM_{011} $3/5\pi$ mode at $\sim$1759 MHz in the medium-β cavity and the TM_{031} $5/5\pi$ mode at $\sim$ 2464 MHz in the high-β cavity. Likewise, manufacturing tolerances may cause frequency variations in the order of few megahertz as measurements on four prototype cavities have shown. For comparison, the frequency shifts of individual HOMs achieved by plastic deformation using the tuning bench are very moderate and possibly not sufficient to provide the necessary distance from the nearest harmonic of the bunch or chopping frequency. Consequently, the frequencies of both HOMs need to be carefully revised and monitored during the cryomodule assembly and operation.

Moreover, a damping of $Q_{\mathrm{ext}} \lesssim 10^5$ is required for the HOMs concerned while the extracted power is specified to 100 W in the worst case. Besides the mode frequencies, these parameters provide the basic conditions for the design of appropriate HOM couplers. The distinct field patterns found for the various concerned high-order modes underline the need for these couplers on either cutoff tube of the cavity, as already defined in the SPL specification.

By deriving extended formulations of the classical vector fitting, a novel approach has been established to quantify the frequency and geometric shunt impedances of many modes simultaneously given the spectrum of a truncated wake potential. It provides an alternative to eigenmode simulations in order to characterize monopole and dipole modes. An open question asks why the geometric shunt impedance obtained for some dipole modes notably deviates from the predicted value provided by an eigenmode simulation, though the impedances spectrum is well approximated in the vicinity of the particular resonant frequency.

4 Coaxial Couplers and the Synthesis of Filter Functions

The understanding of obstacles in coaxial guides and the way they influence the frequency response and resonance properties is fundamental for the design of coaxial waveguide filters. Numerical simulations permit the precise evaluation of scattering properties associated with individual discontinuities in such waveguides. But their capabilities for the design of an entire filter are limited to exhaustive parameter variations on a particular topology of discontinuities. Often, it remains unclear whether the topology, as chosen prior to the numerical analyses, indeed is suitable for the given problem. Even for a specified topology, the applied numerical optimization scheme may not be able to converge against the best solution, given a certain set of requirements, as too many variables may be involved.

To answer these questions, it is instructive to investigate the scattering properties of basic discontinuities in coaxial guides. Section 4.1 provides various studies on this topic. Prior to these studies is a general method to evaluate equivalent microwave networks composed of transmission lines and lumped elements. It permits a highly simplified algebraic representation of the three-dimensional boundary value problem within frequency ranges that are limited but often practically the most relevant.

In order to complete the picture of coaxial HOM couplers which are typically mounted on cutoff tubes or sometimes even directly on the cavity, Sec. 4.2 discusses several aspects of electromagnetic field coupling which are particularly important for the antenna design. The problem is again represented by equivalent circuits. Novel work undertaken by the author comprises the investigations of frequencies at which the coupling to specific waveguide modes nearly vanishes.

Section 4.3 focuses on systematic procedures to design the waveguide filter of coaxial HOM couplers. At first, a method based on reactance-coupled $\lambda/2$ resonators proposed by Haebel and Gerigk [24, 101] is reviewed followed by detailed discussions on the topology of appropriate coaxial microwave filters. Finally, a combination of the insertion loss method and equivalent networks fitted to numerically simulated data is studied with the intention to develop a generally applicable design procedure for coaxial microwave filters; this further implies the most suitable topology for the given problem described by a filter or transfer function. This approach rests on the idea that scattering properties of discontinuities in coaxial waveguides are well described by lumped elements within the interesting frequency range. The principle of equivalent microwave circuits introduced by Montgomery [27] will be essential

for the proposed synthesis of filter functions. Two examples are presented, a third-order and fifth-order elliptic high-pass filter, both adapted to the requirements of the high-β SPL cavity. To the author's best knowledge there is no comparable systematic procedure to design the filter component of coaxial HOM couplers on the base of filter functions. Throughout this chapter, various existing HOM couplers are discussed with the focus on their equivalent networks and potential lacks in the filter approximation.

4.1 Components and Equivalent Circuits

Marcuvitz [40] provides a very comprehensive overview on equivalent microwave circuits for numerous discontinuities in waveguides, with the circuit parameters being derived from analytical or semi-analytical approaches. Such methods provide only approximate results for the frequency response of individual discontinuities. In contrast, numerical simulations are not subjected to these constraints. In particular, scattering properties of multiple discontinuities relatively close to each other, so that evanescent modes may interact, are partially unexplored. The subsequent studies rest on a more generic approach which is based on (i) numerical field calculations to obtain the full scattering matrix of the considered rf structure and (ii) a subsequent parameter fit of an appropriate microwave network such that nearly the same scattering matrix is achieved over a certain frequency range. It is important to note that the same scattering matrix can always be approximated by different equivalent circuits. However, these circuits will not, in general, be equally simple. Thus, it is preferable to choose the option with the simplest association between geometrical design parameters of the rf structure, such as lengths and radii, and equivalent circuit parameters, for instance, capacitances and inductances.

The microwave structures to be described in the following are composed of an input and output region.[1] Each corresponds to a coaxial guide, with the dimensions being, in general, different. Between these two sections resides the obstacle of interest, which ranges from a single discontinuity to a cascade of discontinuities. It is assumed that only the TEM mode propagates, so that the microwave structure may be described by equivalent two-port networks. These models are restricted to the frequency range below the cutoff frequency of the first HOM propagating through the coaxial guide. Note, this is the most important condition in practice [27, p. 60].

The coaxial waveguides at the input and output region are described by transmission lines, each taking into account the length and characteristic impedance according to the propagation of the TEM mode. While the impedance can be readily derived from the radii of the inner and outer conductor using (2.67), the length can only be estimated from the distance between the particular terminal plane and

[1] The notation 'input' and 'output' are only chosen for convenience. There is no preference direction for any of the considered rf structures.

obstacle due to the finite thickness of the latter one. For this reason, the waveguide lengths are involved in all subsequent fitting procedures as free parameters. It is important to note that the terminal planes must not be located too close to the obstacle in order not to compromise the resulting scattering matrix by evanescent modes. In other words, the coaxial waveguides representing the input and output region are a means to analyze scattering properties of the concerned obstacles.

4.1.1 Inductive Post in Coaxial Guide

A fixing between the inner and outer conductor of a coaxial waveguide can be modeled by a shunt inductance between two transmission lines according to Fig. 4.1. Matthaei [113, p. 362] provides an analytical expression for the inductance, however, with relatively large errors as later shown. Qualitatively the same behavior of a shunt inductance in a coaxial waveguide can be achieved by a small aperture [40, pp. 246]. The following procedure derives the inductance from the simulated scattering matrix of the entire structure and a non-linear model fit. It is assumed for the moment that the topology of the microwave network in Fig. 4.1(b) is appropriate for the given rf structure. Later in this section, it will be shown that this is indeed the case over a certain frequency range.

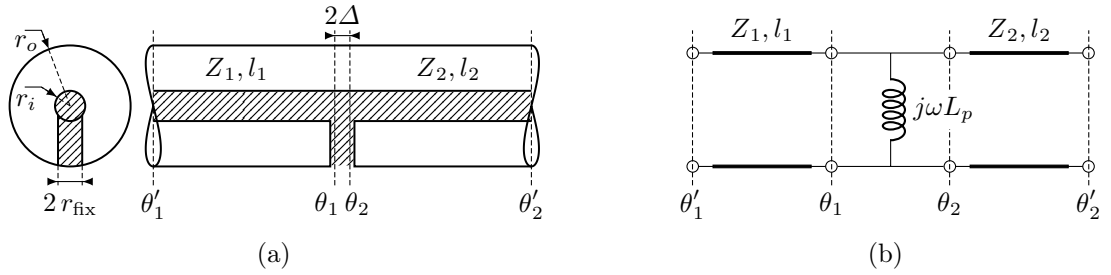

Fig. 4.1. (a) Cross-sectional and side view of a coaxial structure with a cylindrical fixing of radius r_{fix} between the inner and outer conductor. (b) Equivalent circuit model.

Referring to Fig. 4.1(a), at first, the scattering matrix $\mathbf{S}'$ of the microwave structure between the terminal planes θ_1' and θ_2', is obtained by numerical simulations.[2] It is assumed that the scattering matrix is normalized to the characteristic impedances Z_1 and Z_2 at the corresponding ports. As previously mentioned, the terminal planes must not be located too close to the obstacle in order to not compromise the results by artificial reflections associated with evanescent modes. A subsequent transformation provides the scattering matrix $\mathbf{S}$ at the obstacle between the terminal planes θ_1 and θ_2 according to [29, p. 250]

$$\mathbf{S}^{(l_1,l_2)} = \mathbf{w}^{(l_1,l_2)}\mathbf{S}'\,\mathbf{w}^{(l_1,l_2)}, \tag{4.1}$$

[2]Numerical simulations are mostly carried out using CST STUDIO SUITE® [91] for the present chapter. In part, they are verified with COMSOL Multiphysics® software [90].

where the diagonal matrix

$$\mathbf{w}^{(l_1,l_2)} = \mathrm{diag}\{e^{j\beta_1 l_1}, e^{j\beta_2 l_2}\} \tag{4.2}$$

invokes the inward phase shifts along each terminal translation given by the propagation constants $\beta_{1,2}$ and lengths $l_{1,2}$ according to (2.73). Note, a pure phase shift of the scattering functions assumes that no losses are present. Furthermore, the propagation constants are equal in both regions since the field propagation only in vacuum shall be considered. Thus, it is $\beta_1 = \beta_2 = \beta$. The exact values for the lengths l_1 and l_2 are per se not known due to the finite thickness of the obstacle. Consequently, the elements of the scattering matrix $\mathbf{S}$ are considered as functions of these lengths. Let $l_{1,2} + \Delta$ be the distance from the particular terminal plane $\theta'_{1,2}$ to the center of the obstacle, which is a priori known. Linear transforms $l_{1,2} \mapsto \Delta$ are introduced to reduce the number of length variables and to confine their variations to the vicinity of the fixing. In other words, the variable Δ represents half the *electric thickness* of the obstacle.

Furthermore, it is appropriate, to transform the scattering matrix $\mathbf{S}$ into a form which is a somewhat simpler association with the shunt inductance L_p, for instance, the open-circuit impedance matrix introduced in Sec. 2.1.2. Using (2.49), it may be written as

$$\mathbf{Z}^{(\Delta)} = \mathbf{P}^{\frac{1}{2}} \left[\mathbf{I} + \mathbf{S}^{(\Delta)}\right] \left[\mathbf{I} - \mathbf{S}^{(\Delta)}\right]^{-1} \mathbf{P}^{\frac{1}{2}}, \tag{4.3}$$

where

$$\mathbf{P} = \mathrm{diag}\{Z_1, Z_2\} \tag{4.4}$$

accounts for the normalization to the characteristic impedances of the coaxial guides, Z_1 and Z_2, while $\mathbf{I}$ refers to the identity matrix. Taking into consideration that only the TEM mode propagates through the structure, the characteristic impedances calculate as (Sec. 2.1.5)

$$Z_{1,2} = \frac{1}{2\pi}\sqrt{\frac{\mu}{\varepsilon}} \ln \frac{r_o}{r_i}\bigg|_{1,2}, \tag{4.5}$$

with the inner and outer radii r_i, r_o, of the particular coaxial waveguide region. Apart from the obstacle, Fig. 4.1(a) sketches a uniform coaxial guide, such that $Z_1 = Z_2$. According to (2.27), all open-circuit impedance functions in (4.3) must be approximated by the expression $j\omega L_p$ over a certain frequency range, so that the microwave network sketched in Fig. 4.1(b), may be considered as equivalent. Indeed, this is true for one solution of Δ, which consequently defines a unique shunt inductance as shown in Fig. 4.2(a) by means of a symmetric example. Though the shunt inductance was calculated at a single frequency point of 960 MHz, the reflection factor depicted in Fig. 4.2(b) is well approximated by the two-port network for $f < 1.5\,\mathrm{GHz}$ with residuals in the order of 10^{-2}. Referring to Fig. 4.2(a), the resultant value for Δ is by an order of magnitude smaller than the radius of the

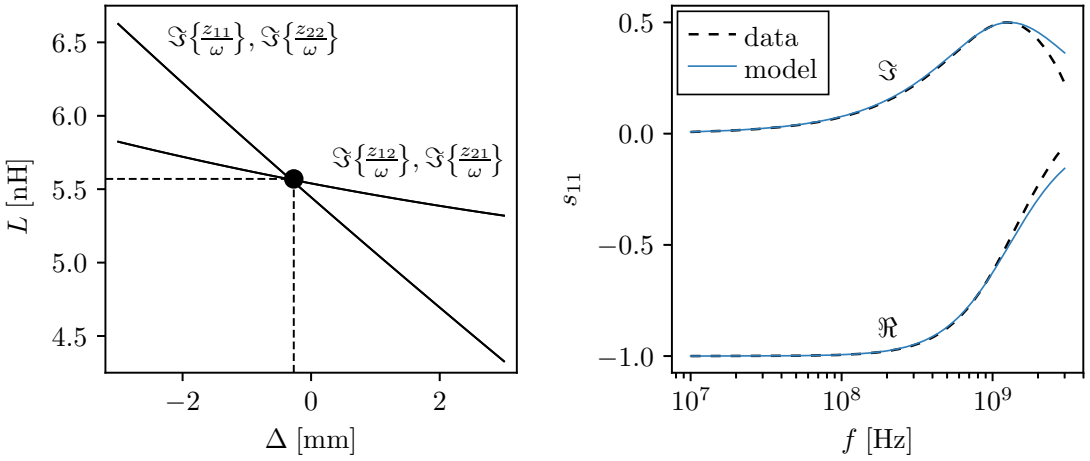

(a) (b)

Fig. 4.2. (a) Open-circuit impedance parameters as functions of the distance between the terminal planes $\theta_{1,2}$, and center of the obstacle according to the rf structure and equivalent circuit shown in Fig. 4.1. The structure is assumed to be symmetric, hence, $Z_1 = Z_2$ and $l_1 = l_2$. Furthermore, it is $r_i = 5\,\text{mm}$, $r_o = 22.5\,\text{mm}$, and $r_{\text{fix}} = 3\,\text{mm}$. The open-circuit impedance parameters are calculated at a frequency of 960 MHz. At $\Delta = 0.27\,\text{mm}$, all of them coincide and yield unique inductance of 5.566 nH which corresponds to the shunt inductance L_p of the equivalent circuit. (b) Reflection coefficient at the terminal plane θ_1 obtained from the simulated data and equivalent circuit model using the result of (a) over a larger frequency range.

cylindrical fixing, r_{fix}, for the considered example. Hence, it is important to distinguish between the geometric and electric size of the obstacle, with the latter being implied by the effective lengths l_1 and l_2 of the transmission lines representing the coaxial waveguide sections of the input and output region, respectively. It is worth noting that the electric thickness of the obstacle may alternatively be accounted for by additional lumped elements in the equivalent circuit [40].

By referring to (2.35), the formulation as transmission matrix allows an equally simple association with the shunt inductance L_p as previously described for the open-circuit impedance matrix. The relationship between the elements of both matrices is given in (2.29)–(2.32). Using the notation of (4.3), the transmission matrix may be written as

$$\mathbf{T}^{(\Delta)} = \frac{1}{z_{21}^{(\Delta)}} \begin{pmatrix} z_{11}^{(\Delta)} & z_{11}^{(\Delta)} z_{22}^{(\Delta)} - z_{12}^{(\Delta)} z_{21}^{(\Delta)} \\ 1 & z_{22}^{(\Delta)} \end{pmatrix}. \tag{4.6}$$

The advantage of this formulation emerges in the presence of multiple discontinuities in the rf structure as it will be seen later. The short-circuit admittance matrix of a shunt two-port is not defined. Hence, this formulation is not suitable to solve the equivalent circuit. However, the singularity can be used to identify the lengths l_1 and l_2. Another approach rests on the analytical expression for the scattering matrix

of a shunt two-port characterized by a general admittance function Y_p according to Fig. 2.5(b). The scattering functions satisfy [29, pp. 250]

$$s_{11} = {s_{11}}' e^{j2\beta l_1} = \frac{Y_1 - (Y_2 + Y_p)}{Y_1 + (Y_2 + Y_p)}, \tag{4.7}$$

$$s_{12} = {s_{12}}' e^{j\beta(l_1+l_2)} = \frac{2\sqrt{Y_1 Y_2}}{Y_1 + (Y_2 + Y_p)} = s_{21}, \tag{4.8}$$

$$s_{22} = {s_{22}}' e^{j2\beta l_2} = \frac{Y_2 - (Y_1 + Y_p)}{Y_2 + (Y_1 + Y_p)}, \tag{4.9}$$

with $Y_{1,2} = 1/Z_{1,2}$. Note, These formulas for a two-port junction have been used in [101] to estimate the shunt inductance of LHC HOM couplers.

Figure 4.3(a) shows the shunt inductance for reasonable dimensions of SPL HOM couplers. The radius r_{fix} of the cylindrical fixing is varied between 2 mm and 10 mm. Likewise, the radius r_i of the inner conductor is varied from 5 mm to 10 mm while the radius of the outer conductor is fixed to $r_o = 22.5$ mm according to specifications. The

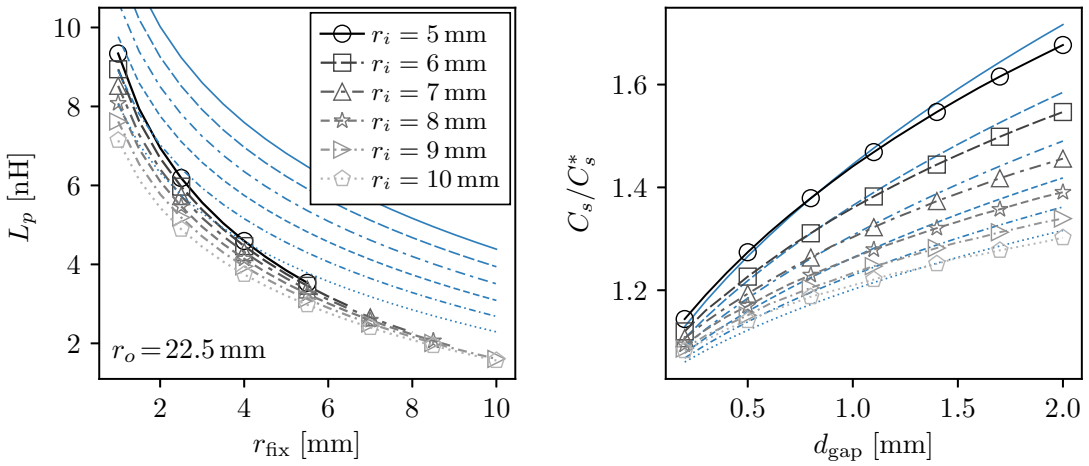

(a) (b)

Fig. 4.3. (a) Shunt inductance for various parameter configurations of the microwave structures shown in Fig. 4.1. In gray scaled and highlighted by markers, the inductance derived from the impedance formulation of the simulated scattering matrix (4.3). In blue, the estimated inductance obtained from (4.10). The radius r_{fix} of the cylindrical fixing is varied along with different radii r_i of the inner conductor. The radius r_o of the outer conductor is specified by the coupler ports of the SPL cavities. The equivalent network is valid for $f \leq 1.5$ GHz. (b) Series capacitor normalized to the expression (4.16) for various parameter configurations of the microwave structures shown in Fig. 4.4. In gray scaled and highlighted by markers, the capacitance derived from the admittance formulation of the simulated scattering matrix (4.11). In blue, the estimated capacitance obtained from (4.17). The gap distance d_{gap} is varied assuming the same configurations for r_i and r_o, as used in (a). The equivalent network is valid for $f \leq 3$ GHz.

inductances found by the impedance formulation (4.3) are highlighted by markers, and ranges approximately from $8.1 \pm 1.0\,\mathrm{nH}$ down to $2\,\mathrm{nH}$. Throughout all geometric variations, the frequency response of the microwave structure is well approximated by its equivalent circuit for $f < 1.5\,\mathrm{GHz}$ with residuals in the order of 10^{-2} as measured by scattering functions. The blue curves in Fig. 4.3(a) are obtained from an analytical expression provided by Matthaei [113, p. 362] according to

$$L_p \approx 0.3666\,\mu_0(r_o - r_i)\lg 2\frac{r_o - r_i}{r_{\mathrm{fix}}}. \tag{4.10}$$

The error is relatively large with respect to the considered dimensions. In particular, the expectation that the impact of r_i reduces as r_{fix} becomes larger is not satisfied.

According to the equivalent circuit in Fig. 4.1(b), the fixing between the inner and outer conductor of a coaxial guide may be denoted as *inductive post*. It provides a transmission zero at the frequency of zero. Hence, it is generally suitable for the design of coaxial high-pass and band-pass filters. Notwithstanding, this does not exclude that a shunt inductance may behave parasitically in a high-pass filter as further explained in Sec. 4.3.2. Low-pass and band-stop filters are, in general, unsuitable applications for a shunt inductance. It is worth noting that in spite of the characteristic frequency response, the inductive post is required in most coupler designs to hold the inner conductor in a vacuum environment. Depending on the power requirements, it may further provide the supply with a coolant for the antenna [101].

4.1.2 Capacitive Gap in Coaxial Guide

An interruption of the inner conductor in a coaxial waveguide can be modeled by a series capacitance between two transmission lines according to Fig. 4.4. In an analogous way to the previous section, the equivalent circuit parameters are found by associating the series capacitance C_s with the simulated scattering matrix at the terminal planes $\theta_{1,2}$.

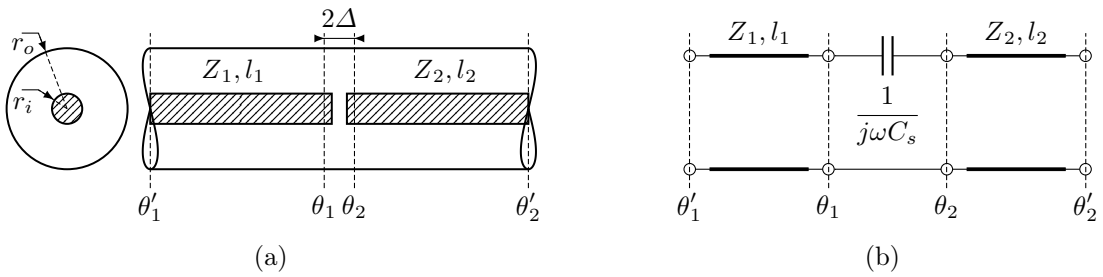

Fig. 4.4. (a) Cross-sectional and side view of a coaxial structure, with the inner conductor being interrupted by a distance d_{gap}. (b) Equivalent circuit model.

The open-circuit impedance matrix of a series two-port is singular, so the formulation (4.3) is not appropriate to solve the problem. Instead, the short-circuit admittance matrix can be used, whose elements must equal $\pm j\omega C_s$ according to (2.26), so that the microwave network sketched in Fig. 4.4(b) may be considered as equivalent. Similar to the previous section, this equality requires the correct choice for the lengths l_1 and l_2, which implies a nonzero distance Δ between the terminal planes $\theta_{1,2}$ and the center of the obstacle. According to (2.50), the relationship between admittance and scattering matrix may be written as

$$\mathbf{Y}^{(\Delta)} = \mathbf{P}^{-\frac{1}{2}} \left[\mathbf{I} - \mathbf{S}^{(\Delta)}\right] \left[\mathbf{I} + \mathbf{S}^{(\Delta)}\right]^{-1} \mathbf{P}^{-\frac{1}{2}}, \tag{4.11}$$

using the same definitions as in Sec. 4.1.1. Considering (2.34), the formulation as transmission matrix allows an equally simple association with the series capacitance C_s as the short-circuit admittance matrix. The relationship between the elements of both matrices is given in (2.29)–(2.32). Using the notation of (4.11), the transmission matrix may be written as

$$\mathbf{T}^{(\Delta)} = -\frac{1}{y_{21}^{(\Delta)}} \begin{pmatrix} y_{22}^{(\Delta)} & 1 \\ y_{11}^{(\Delta)} y_{22}^{(\Delta)} - y_{12}^{(\Delta)} y_{21}^{(\Delta)} & y_{11}^{(\Delta)} \end{pmatrix}. \tag{4.12}$$

Finally, the series capacitance C_s may be directly derived from the scattering matrix of a series two-port characterized by a general impedance function Z_s according to Fig. 2.5(a). The scattering functions of such a two-port junction satisfy [29, pp. 250]

$$s_{11} = {s_{11}}' e^{j2\beta l_1} = \frac{(Z_2 + Z_s) - Z_1}{(Z_2 + Z_s) + Z_1}, \tag{4.13}$$

$$s_{12} = {s_{12}}' e^{j\beta(l_1+l_2)} = \frac{2\sqrt{Z_1 Z_2}}{(Z_2 + Z_s) + Z_1} = s_{21}, \tag{4.14}$$

$$s_{22} = {s_{22}}' e^{j2\beta l_2} = \frac{(Z_1 + Z_s) - Z_2}{(Z_1 + Z_s) + Z_2}. \tag{4.15}$$

Figure 4.3(b) shows the series capacitance for reasonable dimensions of SPL HOM couplers. The gap distance d_{gap} is varied between 0.2 mm and 2 mm assuming different radii of the inner conductor, r_i. The capacitances obtained from the admittance formulation (4.11) are highlighted by markers. They are normalized to the definition

$$C^* = \varepsilon_0 \frac{\pi {r_i}^2}{d_{\mathrm{gap}}}, \tag{4.16}$$

to illustrate the impact of fringe fields. Referring to Fig. 4.3(b), such fringe fields contribute between 10 % and 40 % to the total capacitance. It is worthwhile to note that a variation by less than 10 % suffices to notably impact the frequency

response of microwave filters. Consequently, stray phenomena in the vicinity of capacitive gaps must be taken into account for the design of coaxial microwave filters, particularly with larger gap distances. Throughout all geometric variations, the frequency response of the microwave structure is well approximated by its equivalent circuit for $f < 3\,\mathrm{GHz}$ with residuals in the order of 10^{-2} as measured by scattering functions. The blue curves in Fig. 4.3(b) are obtained from an analytical expression provided by Matthaei [113, p. 363] according to

$$C_s \approx \varepsilon_0 \frac{\pi {r_i}^2}{d_{\mathrm{gap}}} + 1.9653\,\varepsilon_0 r_i \ln 2 \frac{r_o - r_i}{d_{\mathrm{gap}}}. \tag{4.17}$$

Like the inductive post of Sec. 4.1.1, the capacitive gap provides a transmission zero at a frequency of zero. Thus, it is generally suitable for the design of coaxial high-pass and band-pass filters. The counterpart, that is the transmission function of a low-pass or band-stop filter, cannot be realized by this element. Apart from the characteristic frequency response, the capacitive gap in some coupler designs is required for the thermal isolation, particularly in superconductive applications as demonstrated in Sec. 5.3.2.

4.1.3 Change of Radius in Coaxial Guide

The frequency response of a series inductance and shunt capacitance can be approximated by coaxial waveguides with varying radii of the inner or outer conductor [40, pp. 310]. Figs. 4.5 and 4.6 show two examples, with the discontinuity being applied only on the inner conductor. By referring to the equivalent circuits of a transmission line as illustrated in Fig. 2.9, a short coaxial section with reduced radius, given a small phase advance βl_0 and high characteristic impedance Z_0, can be approximated by a series two-port with an impedance function $Z_s = jZ_0\beta l_0 = j\omega L_s$. In contrast, a short coaxial section with increased radius, given a small phase advance βl_0 and low characteristic impedance Z_0, can be approximated by a shunt two-port with an admittance function $Y_p = jY_0\beta l_0 = j\omega C_p$.

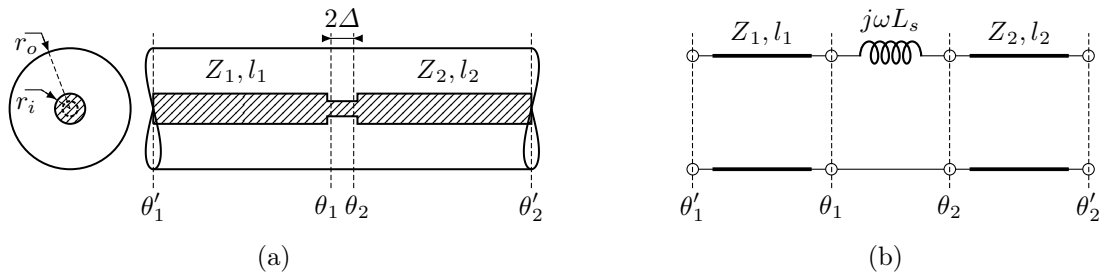

Fig. 4.5. (a) Cross-sectional and side view of a coaxial structure, with the radius of the inner conductor being decreased over a short distance. (b) Equivalent circuit model.

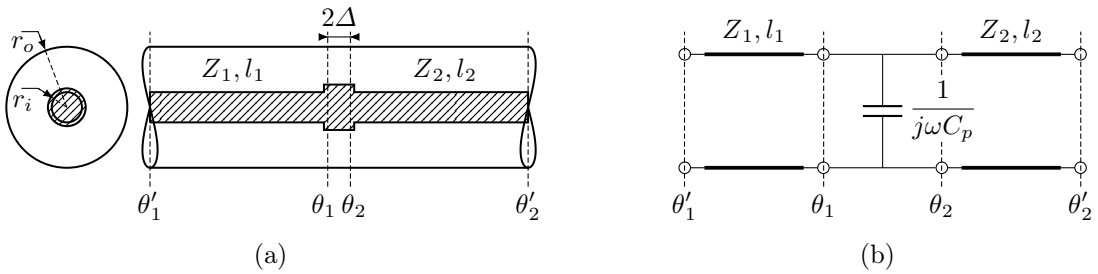

Fig. 4.6. (a) Cross-sectional and side view of a coaxial structure, with the radius of the inner conductor being increased over a short distance. (b) Equivalent circuit model.

The precise evaluations of the series inductance and shunt capacitance proceeds as for the series capacitance in Sec. 4.1.2 or the shunt inductance in Sec. 4.1.1, respectively. According to the equivalent circuits, both structures in Figs. 4.5(a) and 4.6(a) provide frequency responses with transmission zeros at infinite frequency. Hence, they are suitable for the design of low-pass filters, the so-called stepped impedance low-pass filters [41, pp. 422]. Both components are not of primary interest for the design of HOM couplers which, in general, aim for high-pass characteristics. However, they might be included in the design process for practical needs. For example, ceramic windows as vacuum barriers are typically considered for coaxial couplers in superconducting applications, where they introduce a notable shunt capacitance.

4.1.4 Two Uncoupled Inductive Posts in Coaxial Guide

The previously considered microwave structures where characterized by single discontinuities. A natural question arising from these studies is, how such obstacles may influence each other in a cascade similar to a ladder network. It is expected that coupling mechanisms between multiple discontinuities, which rest on the excitation of evanescent modes, modify parameters of equivalent circuits, assuming the discontinuities are close enough to each other. A first example is the combination of two inductive posts, each represented by a shunt inductance, and separated by a waveguide section according to Fig. 4.7. Note, the equivalent circuit does not account for coupling by explicit elements. Hence, the contribution of possible coupling mechanisms resides only in the shunt inductances $L_{1,2}$ and impedance Z_0. This way the results can be directly compared with those of Sec. 4.1.1.

In order to calculate the equivalent circuit parameters, it is not sufficient to consider the scattering matrix at a single frequency point as in the previous examples. The resulting problem formulation would be under determined yielding inconsistent results with varying frequency. Instead, a minimization problem over discrete samples in the interesting frequency range is proposed to solve the equivalent circuit model. At first, the scattering matrices $\mathbf{S}'_k$ between the terminal planes θ'_1 and θ'_2 of the rf structure, sketched in Fig. 4.7(a), are evaluated at discrete frequency samples

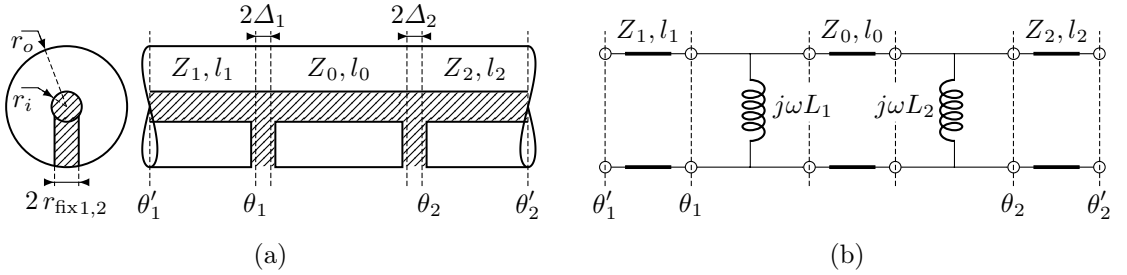

Fig. 4.7. (a) Cross-sectional and side view of a coaxial structure with two cylindrical fixing of radii $r_{\mathrm{fix}1}$ and $r_{\mathrm{fix}2}$ between the inner and outer conductor. (b) Equivalent circuit model.

$\{\omega_k\}_{k=1}^{N_k}$ using numerical simulations. The transform (4.1) provides the corresponding scattering matrices at the terminal planes θ_1 and θ_2, with the lengths l_1 and l_2 being unknown. Let $l_1+\Delta_1$ be the distance from the terminal plane θ_1' to the center of the left fixing in Fig. 4.7(a), which is a priori known. Similarly, let $l_2+\Delta_2$ be the distance from the terminal plane θ_2' to the center of the right fixing, which is likewise a priori known. Since Δ_1 and Δ_2 define half the electric thickness for the individual fixing, the sum $l_0+\Delta_1+\Delta_2$ must correspond to the distance between the centers of both fixings. Linear transforms $\{\Delta_1, \Delta_2\} \mapsto \{l_0, l_1, l_2\}$ are introduced to reduce the number of length variables and to confine their variations to the vicinity of the corresponding fixing.

The equivalent circuit between the terminal planes θ_1 and θ_2 in Fig. 4.7(b) allows for a relatively simple formulation of the short-circuit admittance matrix. Using the $\sqcap$ equivalent network of transmission lines as shown in Fig. 2.9(b), the admittance functions satisfy

$$y_{11} + y_{12} = \frac{1}{j\omega L_1} + jY_0 \tan\frac{\beta l_0}{2}, \tag{4.18}$$

$$y_{12} = jY_0 \csc \beta l_0 = y_{21}, \tag{4.19}$$

$$y_{22} + y_{12} = \frac{1}{j\omega L_2} + jY_0 \tan\frac{\beta l_0}{2}, \tag{4.20}$$

with $Y_0 = 1/Z_0$ being the effective admittance of the waveguide section between both fixings. A necessary condition for the frequency response of the rf structure being approximated by the equivalent circuit can be formulated as a minimization problem using (4.11) and (4.18)–(4.20) according to

$$\min_{\boldsymbol{\Delta}, Y_0, L_1, L_2} \sum_{k=1}^{N_k} \left\| \begin{array}{c} \omega_k L_1 \Im\{y_{11_k}^{(\boldsymbol{\Delta})} + y_{12_k}^{(\boldsymbol{\Delta})}\} - \omega_k L_1 Y_0 \tan\dfrac{\beta l_0^{(\boldsymbol{\Delta})}}{2} + 1 \\ \Im\{y_{12_k}^{(\boldsymbol{\Delta})}\} \sin \beta l_0^{(\boldsymbol{\Delta})} - Y_0 \\ \omega_k L_2 \Im\{y_{22_k}^{(\boldsymbol{\Delta})} + y_{12_k}^{(\boldsymbol{\Delta})}\} - \omega_k L_2 Y_0 \tan\dfrac{\beta l_0^{(\boldsymbol{\Delta})}}{2} + 1 \end{array} \right\|, \tag{4.21}$$

with $\mathbf{\Delta} = \{\Delta_1, \Delta_2\}$. The admittance parameters $y_{ijk}^{(\mathbf{\Delta})}$ are obtained from the simulated and phase shifted scattering matrix between the terminal planes $\theta_{1,2}$, which is sampled at the frequencies $\{\omega_k\}_{k=1}^{N_k}$. A suitable norm $\|.\|$ is given by the L^2 norm yielding a non-linear least-square problem. Furthermore, the model parameters must be normalized to precondition the problem and avoiding differences by orders of magnitude. In filter approximation theory, a common normalization of the frequency and lumped circuit elements ω, R, L, C is given by

$$\omega = \omega_{\text{ref}}\Omega, \qquad R = R_{\text{ref}}\widetilde{R}, \qquad L = \frac{R_{\text{ref}}}{\omega_{\text{ref}}}\widetilde{L}, \qquad C = \frac{1}{\omega_{\text{ref}}R_{\text{ref}}}\widetilde{C}, \tag{4.22}$$

where ω_{ref} is a reference angular frequency, typically, the cutoff frequency of a filter, and R_{ref} is a reference resistance, for instance, the characteristic impedance at one of terminal planes, $Z_{1,2}$.

An alternative and slightly more elegant approach to derive the model parameters succeeds via the transmission matrix. The equivalent circuit between the terminal planes θ_1 and θ_2 in Fig. 4.7(b) admits a transmission matrix whose elements satisfy

$$A = \cos\beta l_0 + \frac{Z_0}{\omega L_2}\cos\beta l_0 \tag{4.23}$$

$$B = jZ_0 \sin\beta l_0 \tag{4.24}$$

$$D = \cos\beta l_0 + \frac{Z_0}{\omega L_1}\cos\beta l_0. \tag{4.25}$$

Note, the remaining transmission parameter of the linear passive network may be calculated from the reciprocity condition according to (2.33). The network is characterized by only three independent transmission parameters according to the three independent short-circuit admittance parameters in (4.18)–(4.20). A necessary condition for the frequency response of the rf structure being approximated by the equivalent circuit follows from (4.6) and (4.23)–(4.25), and may be formulated as

$$\min_{\mathbf{\Delta}, Z_0, L_1, L_2} \sum_{k=1}^{N_k} \left\| \begin{array}{c} \Im\{B_k^{(\mathbf{\Delta})}\} + \omega_k L_2 \left(\cos\beta l_0^{(\mathbf{\Delta})} - \Re\{A_k^{(\mathbf{\Delta})}\}\right) \\ \Im\{B_k^{(\mathbf{\Delta})}\} - Z_0 \sin\beta l_0^{(\mathbf{\Delta})} \\ \Im\{B_k^{(\mathbf{\Delta})}\} + \omega_k L_1 \left(\cos\beta l_0^{(\mathbf{\Delta})} - \Re\{D_k^{(\mathbf{\Delta})}\}\right) \end{array} \right\|, \tag{4.26}$$

with the transmission parameters $A_k^{(\mathbf{\Delta})}, B_k^{(\mathbf{\Delta})}$, and $D_k^{(\mathbf{\Delta})}$ being derived from the simulated and phase shifted scattering matrix between the terminal planes $\theta_{1,2}$. They are sampled at the frequencies $\{\omega_k\}_{k=1}^{N_k}$. Again, using the L^2 norm a nonlinear least-square problem is obtained which can be solved by iterative minimization schemes, such as a constrained BFGS algorithm[3]

[3]Broyden-Fletcher-Goldfarb-Shanno algorithm, a hill-climbing optimization technique.

Figs. 4.8(a) and (b) show the results for a coaxial waveguide structure with two identical fixings based on the stort-circuit admittance or transmission matrix formulation, respectively. The dimensions are identically to those of the previously considered single inductive post in Fig. 4.2(b). The reflection coefficient is well approximated over the entire considered frequency range, which justifies the network sketched in Fig. 4.7(b) being an equivalent circuit model. It applies to a notably larger frequency range than found for the model of a single inductive post in Sec. 4.1.1, with residuals again in the order of 10^{-2}. The resulting circuit parameters slightly differ by less than 5 % between the two approaches. Generally, it was found that the formulation provided by the transmission matrix (4.26) leads to a more robust and consistent behavior of the applied minimization scheme. Despite this small variation between the results, the shunt inductances of each fixing appear somewhat larger than for the single inductive post. Furthermore, the impedance obtained for the central waveguide section, Z_0, is significantly below the characteristic impedance according to (4.5). Both effects are studied in further detail in Fig. 4.9 by varying the distance between the cylindrical fixings, d_{fix}, and the radii $r_{\text{fix}1,2}$ assuming a symmetric rf structure. The resulting circuit parameters vary smoothly and consistently according to the geometrical parameter changes. The waveguide

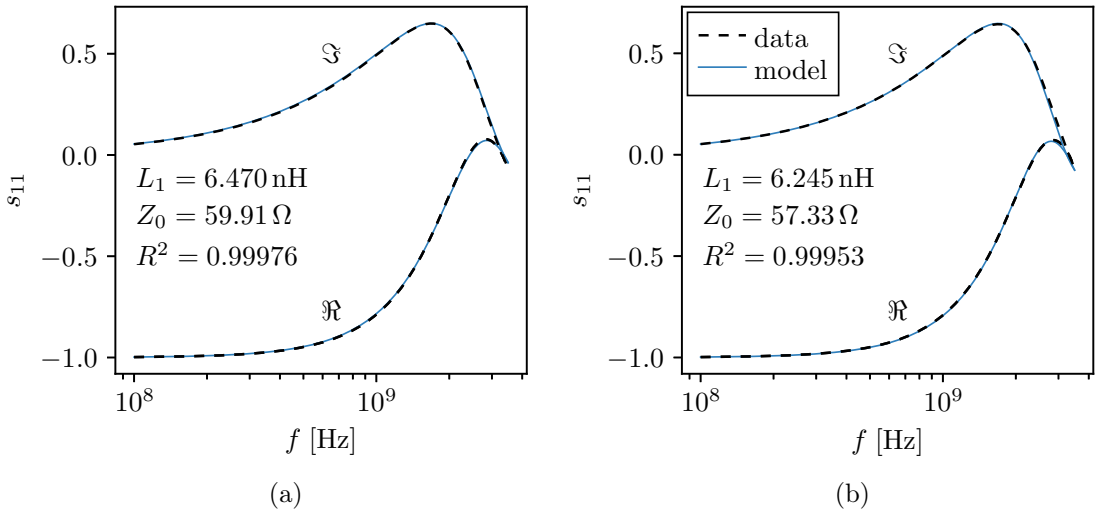

Fig. 4.8. Approximation of the numerically simulated rf reflection from the rf structure at the terminal plane θ_1 by means of the equivalent circuit model according to Fig. 4.7. The structure is assumed to be symmetric, hence, $Z_1 = Z_2$, $l_1 = l_2$, and $r_{\text{fix}1} = r_{\text{fix}2}$, with $r_i = 5\,\text{mm}$, $r_o = 22.5\,\text{mm}$, and $r_{\text{fix}1} = 3\,\text{mm}$. The cross section of the coaxial waveguide in between the fixings is identically to those of the input and output regions. The fixings are separated by a distance of 10 mm. The circuit parameters L_1, Z_0 are derived from the minimization problem given by (a) the admittance matrix formulation according to Eq (4.21) and (b) the transmission matrix formulation according to (4.26). The fits are characterized by R^2 values, each, revealing very good approximation in the considered frequency range $f \leq 3.5\,\text{GHz}$.

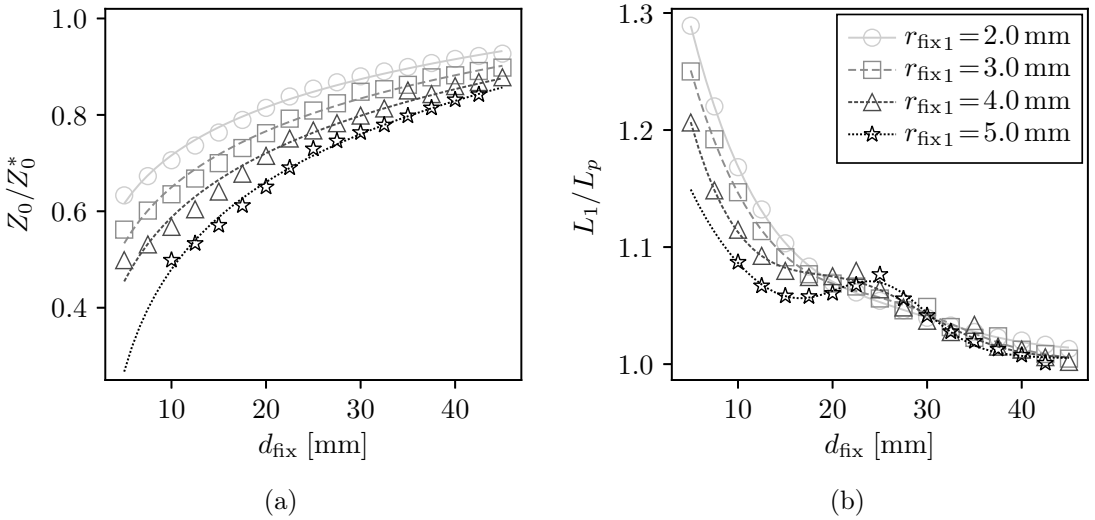

Fig. 4.9. Parameters of the equivalent circuit model as shown in Fig. 4.7, with the quantities being derived from the minimization problem (4.26). The inner and outer radii of the symmetrically assumed coaxial rf structure are 5 mm and 22.5 mm, respectively. The same cross section applies to the waveguide region between the identical fixings whose distance d_{fix} and common radius $r_{\mathrm{fix}1} = r_{\mathrm{fix}2}$ are varied. (a) Effective impedance of the central waveguide section normalized to the characteristic impedance of $Z_0^* = 90.24\,\Omega$ according to (4.5). (b) Shunt inductance of each fixing normalized to the corresponding value of the single inductive post in Fig. 4.3(a).

section between the fixings reveals effective impedance which is throughout below the characteristic impedance as calculated by (4.5). The curves shown in Fig. 4.9(a) correspond to the ratio of the effective and characteristic impedances, and follow approximately an exponential trend according to $\propto [1 - \exp(-d_{\mathrm{fix}}/d_0)]$, where d_0 is a constant. The ratio further reduces with increasing fixing radii $r_{\mathrm{fix}1,2}$. Figure 4.9(b) shows the shunt inductance of the identical fixings normalized to the solution for the corresponding single inductive post of Sec. 4.1.1, which is denoted as L_p. It exponentially decreases as the distance d_{fix} between the fixings becomes larger, and approaches unity. At a distance of $d_{\mathrm{fix}} = 10\,\mathrm{mm}$, the inductance ranges from 8 % to 15 % above the corresponding value of a single inductive post, depending on the considered fixing radii $r_{\mathrm{fix}1,2}$. The impact of the latter parameters becomes marginal for $d_{\mathrm{fix}} > 20\,\mathrm{mm}$ which corresponds to a tenth of the wavelength at 1.5 GHz, while the solution of the single inductive post may be considered for a distance $d_{\mathrm{fix}} > 40\,\mathrm{mm}$.

The equivalent circuit in Fig. 4.7(b) provides qualitatively a very similar frequency response as the single inductive post in Sec. 4.1.1. This can be seen already from the scattering functions depicted in Figs. 4.2(b) and 4.8. Approximating the transmission line in between the shunt inductances by a series inductance, the resulting two-port network barely provides a single transmission zero at the frequency of zero. Since this property is likewise achieved by the much simpler single inductive post, the combination of two inductive posts according to Fig. 4.7(a) does not appear of

particular interest for designing coaxial microwave filters with high-pass characteristics. Nevertheless, the structure is widely used, for instance, in the design of the TESLA HOM coupler and numerous of its derivatives [1, 58, 114]. This is primarily due to mechanical and thermal reasons as two connected fixings significantly facilitate the implementation of a cooling circuit. From the rf point of view, multiple inductive posts arranged to a cascade along the coaxial lines become reasonable for the implementation of reactance-coupled $\lambda/2$ resonators to provide band-pass characteristics as discussed in Sec. 4.3.1.

4.1.5 Two Coupled Inductive Posts in Coaxial Guide

Although the equivalent circuit in Fig. 4.7(b) allows for a fair approximation of the scattering properties of the microwave structure in the interesting frequency range, the effective impedance of the waveguide section between the two fixings is significantly lower than the expected characteristic impedance. It is an abstract rather than physical quantity to account for possible coupling effects. Figure 4.10(b) illustrates an alternative equivalent microwave network for the same coaxial rf structure. It describes inductive coupling between the particular fixing and inner conductor of the central coaxial waveguide by using additional inductances before and after the central transmission line.

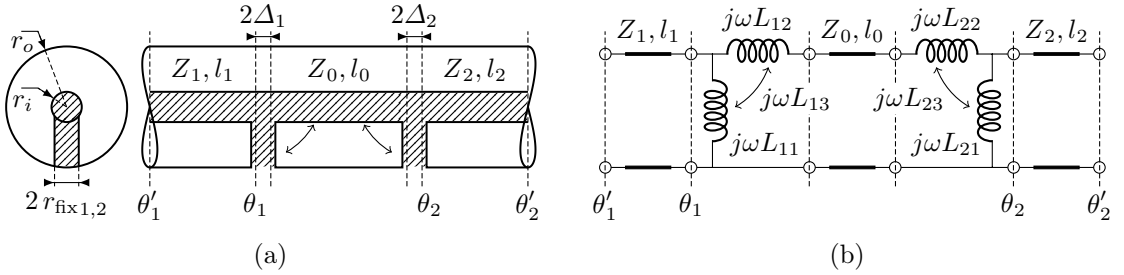

Fig. 4.10. (a) Cross-sectional and side view of a coaxial structure with two cylindrical fixing of radii $r_{\mathrm{fix}1}$ and $r_{\mathrm{fix}2}$ between the inner and outer conductor. (b) Equivalent circuit model.

Despite the fact that the equivalent circuit model introduces four further unknowns in comparison to the model of Sec. 4.1.4, the minimization problem can be written in a very similar form as before provided the coupled shunt and series inductances are described by transformers. To illustrate this, consider the circuit segment in Fig. 4.11(a), which is taken from the original microwave network in Fig. 4.10(b). By deriving its open-circuit impedance parameters and comparing with Fig. 2.4(a), it can be shown that the circuit depicted in Fig. 4.11(b) corresponds to an equivalent form. Such a T-network behaves like a transformer if and only if the canonical form of inductances vanishes [26, p. 118], that is if

$$-L_3(L_1+L_3)+(L_1+L_3)(L_2+L_3)-L_3(L_2+L_3)=0. \tag{4.27}$$

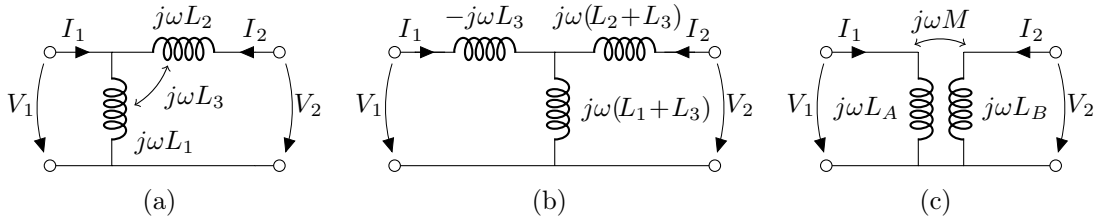

Fig. 4.11. (a) Two-port consisting of a series and shunt inductance which are coupled to each other. (b) T equivalent circuit of (a). The two-port in (c) describes a transformer which is likewise equivalent to the others provided $L_1L_2 = L_3^2$. This condition also known as *unity coupling*, leads to $M = L_1 + L_3,\ L_A = L_1,\ L_B = L_1 + L_2 + 2L_3$. A transformer is typically characterized by the mutual inductance M and the voltage or inverse current transform ratio $N = L_A/M = M/L_B$.

Hence, the inductances are not independent of each other. In fact, they are related as $L_1L_2 = L_3^2$. Figure 4.11(c) shows the network of a transformer which is likewise equivalent to the original one in Fig. 4.11(a), provided condition (4.27) holds. The advantage of the representation as transformer is the elegant expression of the transmission matrix which is given by

$$\begin{pmatrix} V_1 \\ I_1 \end{pmatrix} = \begin{pmatrix} N & 0 \\ \dfrac{1}{j\omega M} & \dfrac{1}{N} \end{pmatrix} \begin{pmatrix} V_2 \\ -I_2 \end{pmatrix}, \tag{4.28}$$

where N is the voltage or inverse current transform ratio while M corresponds to the coupling inductance. Using this notation and comparing with (2.36), N^{-1} may be interpreted as the turns ratio of an equivalent transformer. Following the notation in Fig. 4.11, both quantities are related to the inductances of the original circuit segment as

$$L_1 = MN, \qquad L_2 = \frac{M(1-N)^2}{N}, \qquad L_3 = M(1-N). \tag{4.29}$$

Using the equivalence of a transformer, the entire transmission matrix of the microwave network in Fig. 4.10(b) between the terminal planes θ_1 and θ_2 admits parameters which satisfy

$$A = \frac{N_1}{N_2}\cos\beta l_0 + \frac{N_1}{\omega M_2} Z_0 \sin\beta l_0 \tag{4.30}$$

$$B = jN_1N_2Z_0 \sin\beta l_0, \tag{4.31}$$

$$D = \frac{N_2}{N_1}\cos\beta l_0 + \frac{N_2}{\omega M_1} Z_0 \sin\beta l_0, \tag{4.32}$$

with the coupling inductance and voltage or inverse current transform ratio M_1, N_1, being related to L_{11}, L_{12}, L_{13} while M_2, N_2 are associated with L_{21}, L_{22}, L_{23},

each according to (4.29). A necessary condition for the frequency response of the rf structure being approximated by the equivalent circuit follows from (4.6) and (4.30)–(4.32), and may be formulated as

$$\min_{\boldsymbol{\Delta},Z_0,M_1,N_1,M_2,N_2} \sum_{k=1}^{N_k} \left\| \begin{array}{c} \Im\{B_k^{(\boldsymbol{\Delta})}\} + \omega_k M_2 \left(N_1 \cos \beta l_0^{(\boldsymbol{\Delta})} - N_2 \Re\{A_k^{(\boldsymbol{\Delta})}\} \right) \\ \Im\{B_k^{(\boldsymbol{\Delta})}\} - N_1 N_2 Z_0 \sin \beta l_0^{(\boldsymbol{\Delta})} \\ \Im\{B_k^{(\boldsymbol{\Delta})}\} + \omega_k M_1 \left(N_2 \cos \beta l_0^{(\boldsymbol{\Delta})} - N_1 \Re\{D_k^{(\boldsymbol{\Delta})}\} \right) \end{array} \right\| . \quad (4.33)$$

Again, the quantities $A_k^{(\boldsymbol{\Delta})}, B_k^{(\boldsymbol{\Delta})}$, and $D_k^{(\boldsymbol{\Delta})}$ are obtained from the simulated and phase shifted scattering matrix between the terminal planes θ_1 and θ_2 of the rf structure in Fig. 4.10(a). They are sampled at the frequencies $\{\omega_k\}_{k=1}^{N_k}$.

In order to investigate possible coupling phenomena solely by inductances, let the effective impedance Z_0 be fixed to the characteristic impedance according to the geometrical parameters of the coaxial waveguide section. Figs. 4.12 and 4.13 show the resulting network parameters for the symmetric example of Sec. 4.1.4 as functions of the distance d_{fix} between cylindrically shaped fixings whose common radius $r_{\text{fix1}} = r_{\text{fix2}}$ is likewise varied. Throughout all geometric variations, the frequency response of the microwave structure is well approximated by the equivalent circuit for $f < 3\,\text{GHz}$ with residuals in the order of 10^{-2} as measured by scatter-

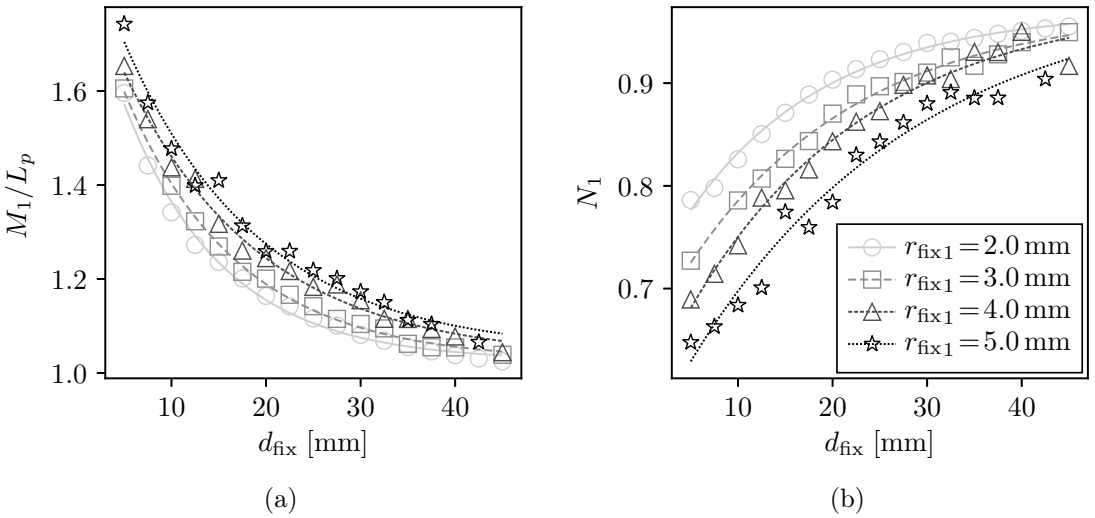

Fig. 4.12. Parameters of the transformers as a result of the minimization problem (4.33) given by the transmission matrix formulation of the equivalent circuit in Fig. 4.10. The inner and outer radii of the symmetrically assumed coaxial rf structure are 5 mm and 22.5 mm, respectively. The same cross section applies to the waveguide region between the identical fixings whose distance d_{fix} and common radius $r_{\text{fix1}} = r_{\text{fix2}}$ are varied. (a) Coupling inductance normalized to the corresponding inductance of the single inductive post as shown in Fig. 4.3(a). (b) Voltage transform ratio.

ing functions. Although the applicable frequency range is slightly lower than for the equivalent circuit of the previous section, it is a suitable network to represent scattering properties of the rf structure shown in Fig. 4.10(a).

Referring to Fig. 4.12(a), the coupling inductance of the equivalent transformers exponentially decreases with the distance d_{fix} and approaches the inductance L_p of the single inductive post discussed in Sec. 4.1.1. Furthermore, the value slightly decreases with decreasing radius of the cylindrical fixings. In Fig. 4.12(b), the voltage or inverse current transform ratio approaches unity towards larger distances as the coupling between the fixings reduces. Except for the largest fixing radius of $r_{\text{fix}} = 5\,\text{mm}$, both quantities M_1, N_1, vary smoothly and consistently according to the geometrical parameter changes of the rf structure, which gives confidence in the solutions of the minimization problem (4.33). This is not necessarily true for the derived shunt inductance L_{11} in Fig. 4.13(a) indicating relatively large errors. Nevertheless, the shunt inductance seems to behave very similarly to Fig. 4.9(b). Hence, a direct evaluation via the simpler equivalent circuit of Sec. 4.1.4 seems more appropriate as sufficient to provide the shunt inductances L_{11} and L_{21} of the extended model in Fig. 4.10(b). Since shunt inductances are not independent of the distance d_{fix}, it can be deduced that the equivalent circuit is not able to fully represent field coupling between the fixings by explicit lumped elements. The series inductance L_{12} in Fig. 4.13(b), likewise derived from the coupling inductance and voltage transform ratio, varies very consistently with geometrical parameter changes. The quantity reflects very clearly some fraction of coupling between the inductive posts. For a very short distance of $d_{\text{fix}} = 2.5\,\text{mm}$ and depending on the radius of

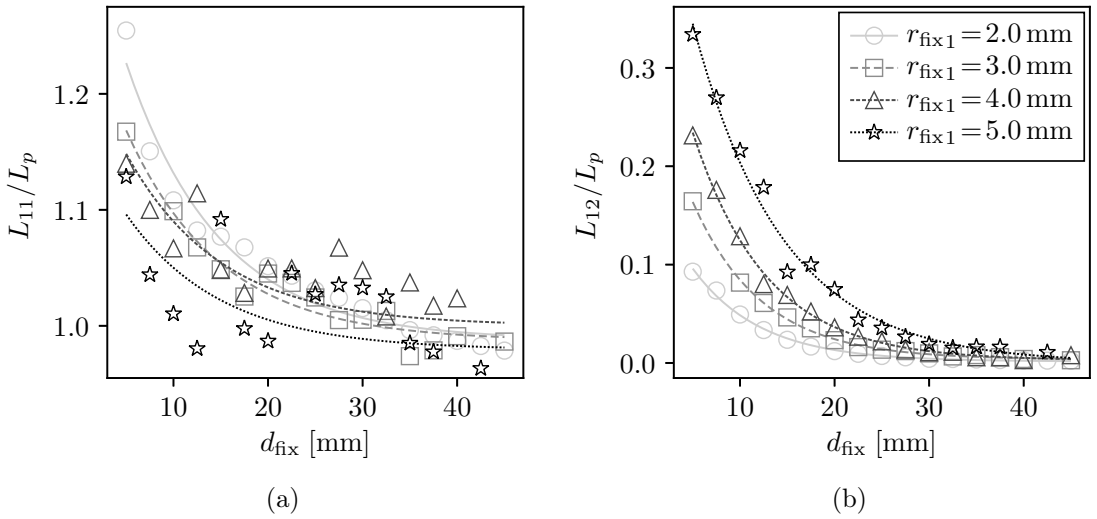

Fig. 4.13. (a) Shunt and (b) series inductances of the equivalent circuit model in Fig. 4.10 derived from the parameters of the transformer in Fig. 4.12 using (4.29). Both quantities are normalized to the corresponding inductance of the single inductive post as shown in Fig. 4.3(a).

the cylindrical fixings, the series inductance amounts between 10 % to 35 % of L_p provided by the single inductive post in Sec. 4.1.1.

To conclude, the equivalent circuit model in Fig. 4.10(b) is able to represent some fraction of eventual coupling between the two fixings by introducing inductive coupling between shunt and series inductances. It allows for a fair approximation of the frequency response of the rf structure in the interesting frequency range, although the accuracy is slightly lower than for the model discussed in the previous section. Furthermore, the equivalent circuit provides a more physical meaning, in that the effective impedance of the coaxial waveguide section in between the fixings corresponds to the characteristic impedance given by (2.67). However, the resulting shunt inductances of the circuits in Figs. 4.7(b) and 4.10(b) are approximately the same. Regarding numerical accuracy, it is more appropriate to consider the simpler equivalent circuit of Sec. 4.1.1 without dedicated coupling elements.

4.1.6 Mid-Shunt Ladder between Inductive Posts in Coaxial Guide

Although it is barely found in existing designs of HOM couplers, the following rf structure will be fundamental for the design of coaxial high-pass filters. It provides the key component for the synthesis method discussed in Sec. 4.3.3. Figure 4.14(a) illustrates the somewhat modified rf structure of Secs. 4.1.4 and 4.1.5, with the inner conductor of the central waveguide section in between the fixings being interrupted by a small distance d_{gap}, similar to Sec. 4.1.2. Interestingly, Xu [115] proposed a similar structure already in 2011 for his design of the so-called *two-stage HOM coupler with double notch frequency*. The design was based purely on numerical simulations. However, the equivalent circuit was misinterpreted, so the remarkable resonance behavior remained unnoticed. Likewise, Ainsworth [116, pp. 120] used this structure in one of his HOM coupler designs without giving attention to the consequences of an equivalent microwave network. The work of both essentially motivated the present studies.

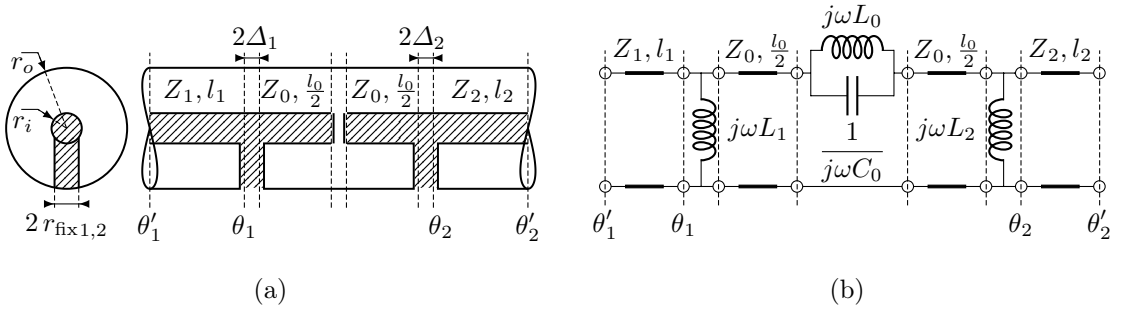

Fig. 4.14. (a) Cross-sectional and side view of a coaxial structure with two fixings between the inner and outer conductor. The fixings are modeled as cylinders with the radii $r_{\mathrm{fix}1}$ and $r_{\mathrm{fix}2}$. The inner conductor between the fixings is interrupted by a distance d_{gap}. (b) Equivalent circuit.

Following the results of Sec. 4.1.2, the gap which separates the inner conductor in Fig. 4.14(a) ought to be represented by a series capacitor. This together with the shunt inductances of the fixings would provide a typical network of a high-pass filter disregarding the transmission lines in between the lumped elements. A corresponding ladder network, which comprises the equivalent circuits of Secs. 4.1.1 and 4.1.2 in an alternating manner, provides multiple transmission zeros at the frequency of zero. However, numerical simulations of the rf structure reveal a transmission zero at finite, nonzero frequency as shown in Fig. 4.15(a) by means of $|s_{21}|^2$. In order to achieve this behavior for a ladder network, either the admittance function of a shunt arm or the impedance function of a series arm must provide a pole at finite, nonzero frequency. Since the inductive posts remained unchanged from Secs. 4.1.4 and 4.1.5, the focus will be on the series arm. The simplest one-port revealing an impedance function with one pole at finite, nonzero frequency, is given by the parallel LC resonator as shown in the circuit model of Fig. 4.14(b). Indeed this network enables the scattering properties of the considered microwave structure to be approximated over a large frequency range. The two-port consisting of a parallel LC resonator connected in series is denoted as *mid-shunt ladder* [39]. Though, the additional inductance L_0 is literally not seen in the coaxial rf structure, the subsequent

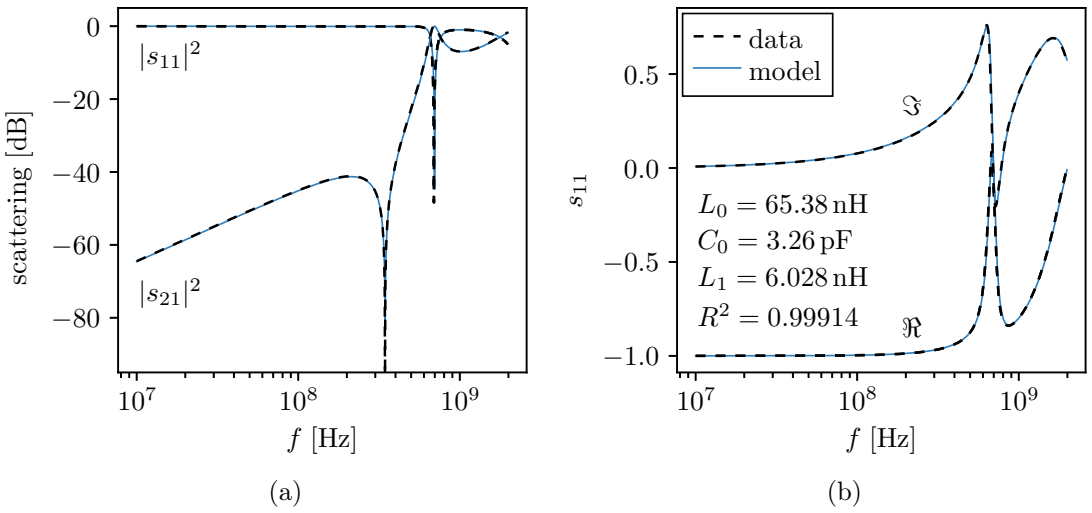

Fig. 4.15. Approximation of the numerically simulated rf reflection and transmission with respect to the terminal planes θ_1 and θ_1 by means of the equivalent circuit model according to Fig. 4.14. The structure is assumed to be symmetric, hence, $Z_1 = Z_2$, $l_1 = l_2$, and $r_{\mathrm{fix1}} = r_{\mathrm{fix2}}$, with $r_i = 5\,\mathrm{mm}$, $r_o = 22.5\,\mathrm{mm}$, and $r_{\mathrm{fix1}} = 3\,\mathrm{mm}$. The cross section of the coaxial waveguide in between the fixings is identical to those of the input and output regions. The fixings are separated by a distance of $d_{\mathrm{fix}} = 22.5\,\mathrm{mm}$ while the inner conductor is separated by a distance of $d_{\mathrm{gap}} = 0.3\,\mathrm{mm}$. The circuit parameters L_0, C_0, L_1 are derived from the minimization problem. (a) Magnitude of the rf transmission and reflection. (b) Real and imaginary part of the reflection at the terminal plane θ_1. The R^2 value reveals very good approximation in the considered frequency range $f \leq 2\,\mathrm{GHz}$.

investigations provide empirical evidence of its existence. Similar to Sec. 4.1.4, the circuit of Fig. 4.15(b) does not account for coupling between inductive posts and the inner conductor by dedicated elements. The contribution of possible coupling mechanisms resides in the shunt inductances $L_{1,2}$ and effective impedance Z_0.

The equivalent circuit is solved in a way analogous to the previous case studies. The microwave network in Fig. 4.14(b) between the terminal planes θ_1 and θ_2 admits a transmission matrix whose parameters may be written as

$$A = \frac{B}{j\omega L_2} + \cos\beta l_0 - \frac{1}{2Z_0C_0}\frac{\omega}{\omega_0^2-\omega^2}\sin\beta l_0 \tag{4.34}$$

$$B = j\frac{1}{C_0}\frac{\omega}{\omega_0^2-\omega^2}\cos^2\frac{\beta l_0}{2} + jZ_0\sin\beta l_0 \tag{4.35}$$

$$D = \frac{B}{j\omega L_1} + \cos\beta l_0 - \frac{1}{2Z_0C_0}\frac{\omega}{\omega_0^2-\omega^2}\sin\beta l_0, \tag{4.36}$$

where $\omega_0 = 1/\sqrt{L_0C_0}$ corresponds to the resonant frequency of the parallel LC resonator. A necessary condition for the frequency response of the rf structure being approximated by the equivalent circuit follows from (4.6) and (4.34)–(4.36), and may be formulated as

$$\min_{\substack{\mathbf{\Delta},Z_0,\\ C_0,L_1,L_2}} \sum_{k=1}^{N_k} \left\| \begin{matrix} C_0Z_0\delta_k^2\Im\{B_k^{(\mathbf{\Delta})}\} + C_0Z_0\delta_k^2\omega_kL_2\left(\cos\beta l_0^{(\mathbf{\Delta})} - \Re\{A_k^{(\mathbf{\Delta})}\}\right) - \dfrac{\omega_k^2L_2}{2}\sin\beta l_0^{(\mathbf{\Delta})} \\ C_0\delta_k^2\Im\{B_k^{(\mathbf{\Delta})}\} - \omega_k\cos^2\dfrac{\beta l_0^{(\mathbf{\Delta})}}{2} - C_0Z_0\delta_k^2\sin\beta l_0^{(\mathbf{\Delta})} \\ C_0Z_0\delta_k^2\Im\{B_k^{(\mathbf{\Delta})}\} + C_0Z_0\delta_k^2\omega_kL_1\left(\cos\beta l_0^{(\mathbf{\Delta})} - \Re\{D_k^{(\mathbf{\Delta})}\}\right) - \dfrac{\omega_k^2L_1}{2}\sin\beta l_0^{(\mathbf{\Delta})} \end{matrix} \right\|, \tag{4.37}$$

with $\delta_k^2 = \omega_0^2 - \omega_k^2$. The quantities $A_k^{(\mathbf{\Delta})}, B_k^{(\mathbf{\Delta})}$, and $D_k^{(\mathbf{\Delta})}$ are obtained from the simulated and phase shifted scattering matrix between the terminal planes θ_1 and θ_2 of the rf structure in Fig. 4.14(a). They are sampled at the frequencies $\{\omega_k\}_{k=1}^{N_k}$. Note, the resonant frequency ω_0 is readily available from the simulated frequency response as illustrated in Fig. 4.15(a). Consequently, only one parameter of the parallel LC resonator is involved in the minimization problem.

Figs. 4.16 and 4.17 show the resulting microwave network parameters of symmetric structures. Hence, the input and output waveguide regions as well as the cylindrically shaped fixings are identically such that $Z_1 = Z_2$ and $L_1 = L_2$. Throughout all geometric variations, the frequency response of the coaxial guide, expressed by scattering functions, is well approximated for $f \leq 3\,\mathrm{GHz}$ with residuals in the order of 10^{-2} by solving the minimization problem (4.37). Moreover in most cases, the resulting circuit parameters change very smoothly and consistently according to the geometric changes of the rf structures. The possibility of approximation and the consistency of the parameter variations both justify the microwave network in Fig. 4.14(b) as an equivalent circuit model.

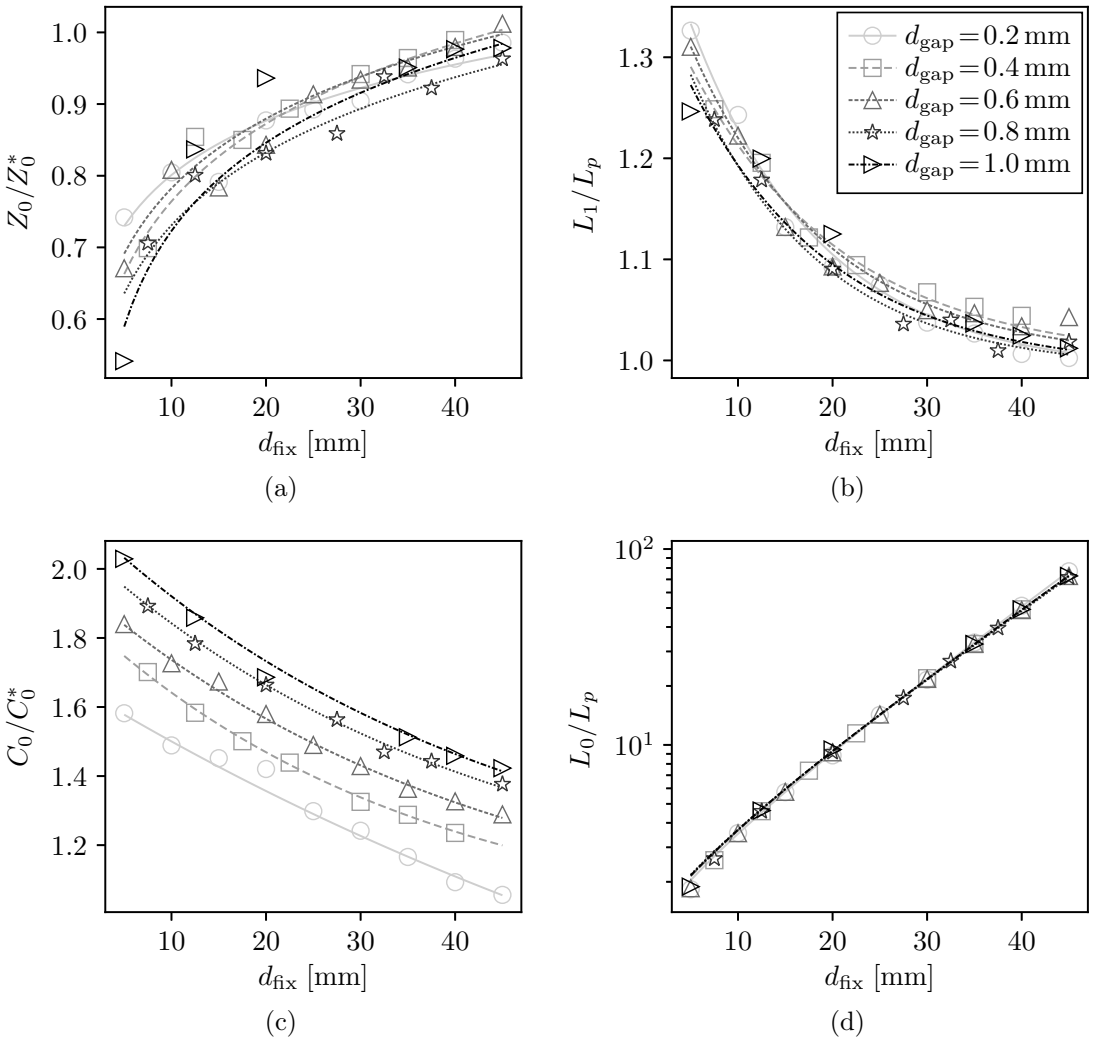

Fig. 4.16. Circuit parameters of the equivalent microwave network which represents the rf structure according to Fig. 4.14. The inner and outer radii of the symmetrically assumed coaxial geometry are 5 mm and 22.5 mm, respectively. The same cross section applies to the waveguide between the identical fixings whose distance d_{fix} is varied while their common radius $r_{\mathrm{fix}1} = 3\,\mathrm{mm}$. Moreover, the gap distance d_{gap} which separates the inner conductor is varied. (a) Effective impedance of the coaxial waveguide between the fixings normalized to the characteristic impedance of $Z_0^* = 90.24\,\Omega$ according to (4.5). (b) Shunt inductance of each fixing normalized to the corresponding value of the single inductive post in Fig. 4.3(a). (c) Capacitance of the parallel LC resonator normalized to the definition (4.16). (d) Inductance of the parallel LC resonator normalized as (b).

The first case study illustrated in Fig. 4.16 focuses on the impact of the gap distance d_{gap} which intuitively defines the capacitance of the parallel LC resonator. Furthermore all circuit parameters are shown as functions of the distance d_{fix} between the fixings while $r_{\mathrm{fix}1} = r_{\mathrm{fix}2} = 3\,\mathrm{mm}$. The effective impedance Z_0 and shunt inductance L_1, respectively, shown in Figs. 4.16(a) and 4.16(b), only marginally vary

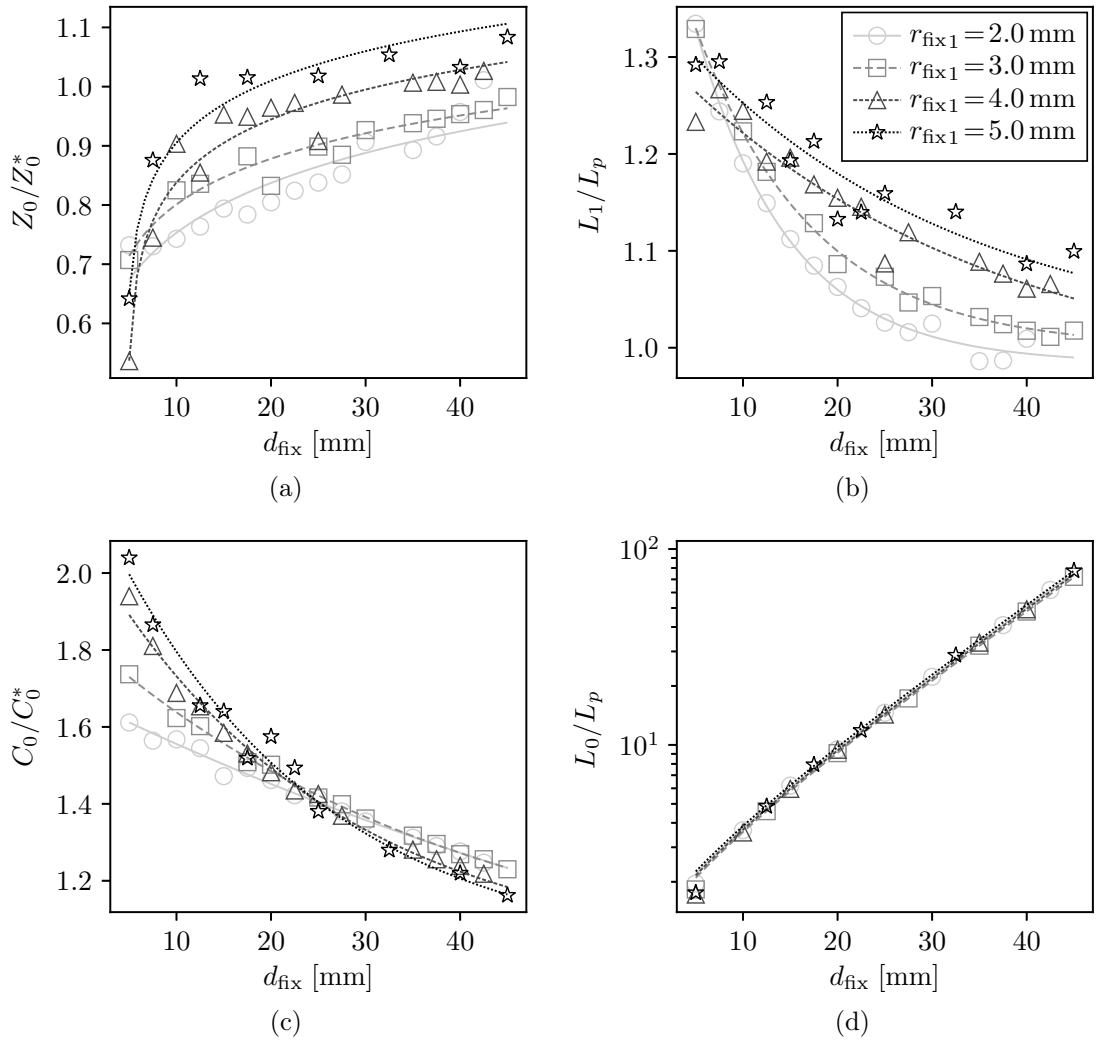

Fig. 4.17. Circuit parameters of the equivalent microwave network which represents the rf structure according to Fig. 4.14. The inner and outer radii of the symmetrically assumed coaxial geometry are 5 mm and 22.5 mm, respectively. The same cross section applies to the waveguide between the identical fixings whose distance d_{fix} and common radius $r_{\mathrm{fix}1}$ are varied. The gap distance which separates the inner conductor is fixed to $d_{\mathrm{gap}} = 0.3\,\mathrm{mm}$. (a) Effective impedance of the coaxial waveguide between the fixings normalized to the characteristic impedance of $Z_0^* = 90.24\,\Omega$ according to (4.5). (b) Shunt inductance of each fixing normalized to the corresponding value of the single inductive post in Fig. 4.3(a). (c) Capacitance of the parallel LC resonator normalized to the definition (4.16). (d) Inductance of the parallel LC resonator normalized as (b).

with the gap distance. The results are similar to those of Secs. 4.1.4 and 4.1.5 which consider the same microwave structure except for the capacitive gap. Likewise, the inductance L_0 of the parallel LC resonator does not depend on the gap distance as depicted in Fig. 4.16(d). However, it varies by an order of magnitude within the considered variation of d_{fix}. Notice, the inductance L_0 can be notably larger than

the shunt inductances L_1 and L_2. For the capacitance of the parallel LC resonator shown in Fig. 4.16(c), a similar dependency on the gap distance is observed as in Sec. 4.1.2. To illustrate the contribution of fringe fields, the capacitance is normalized to the definition (4.16). Interestingly, the capacitance reduces as the distance d_{fix} between the fixings becomes larger, and seems to approach the corresponding solution of Fig. 4.3(b). In other words, the presence of inductive posts increases the contribution of fringe fields to the total capacitance.

The second case study illustrated in Fig. 4.17 considers the impact of the common fixing radius $r_{\text{fix}1} = r_{\text{fix}2}$. All circuit parameters are given as functions of the distance d_{fix} between the inductive posts while a fixed gap distance of $d_{\text{gap}} = 0.3\,\text{mm}$ is assumed. Slight fluctuations of the circuit parameters along geometric variations of the coaxial rf structure indicate larger errors than for the previous case study. This applies, in particular, to the effective impedance Z_0 in Figs. 4.17(a) and shunt inductance L_1 in Fig. 4.17(b), each at a radius of $r_{\text{fix}1} = 5\,\text{mm}$. By comparing with Fig. 4.9, both circuit parameters behave similar as for the coaxial structure without capacitive gap. However, the presence of the mid-shunt ladder notably modifies the decay of the shunt inductance as the distance d_{fix} becomes larger. The capacitance of the parallel LC resonator depicted in Fig. 4.17(c) reduces with increasing distance d_{fix}, and approaches the solution of Sec. 4.1.2. Furthermore for $d_{\text{fix}} < 20\,\text{mm}$, the capacitance notably varies with the radius of the cylindrical fixings, i. e. in parts by 20 %. In contrast, the inductance L_0 of the parallel LC resonator shown in Fig. 4.17(d), only marginally depends on the radii $r_{\text{fix}1,2}$.

To further characterize the mid-shunt ladder, a new geometrical parameter will be introduced, the rotation angle α_{fix} between the two fixings in the transverse plane according to Fig. 4.18(a). It was found that the additional modification does not require a different equivalent microwave network than previously considered. Furthermore, the symmetry of the network is preserved even for $\alpha_{\text{fix}} \neq 0\,\text{deg}$ provided the input and output waveguide regions as well as inductive posts are identical.

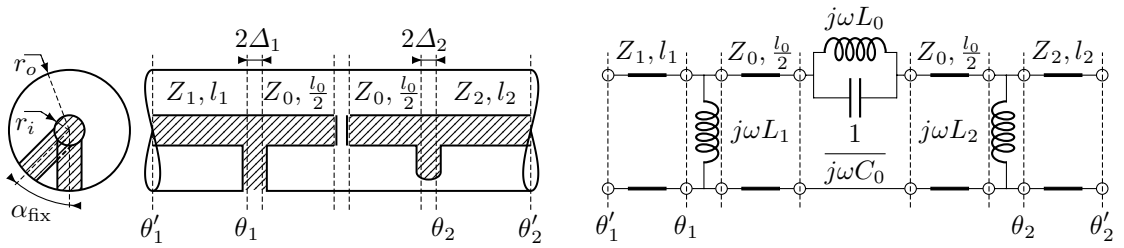

Fig. 4.18. (a) Cross-sectional and side view of a coaxial structure with two fixings between the inner and outer conductor. The fixings are modeled as cylinders with the radii $r_{\text{fix}1}$ and $r_{\text{fix}2}$. They are rotated against each other in the transverse plane by the angle α_{fix}. The inner conductor of the central waveguide section is interrupted by a distance d_{gap}. (b) Equivalent circuit model.

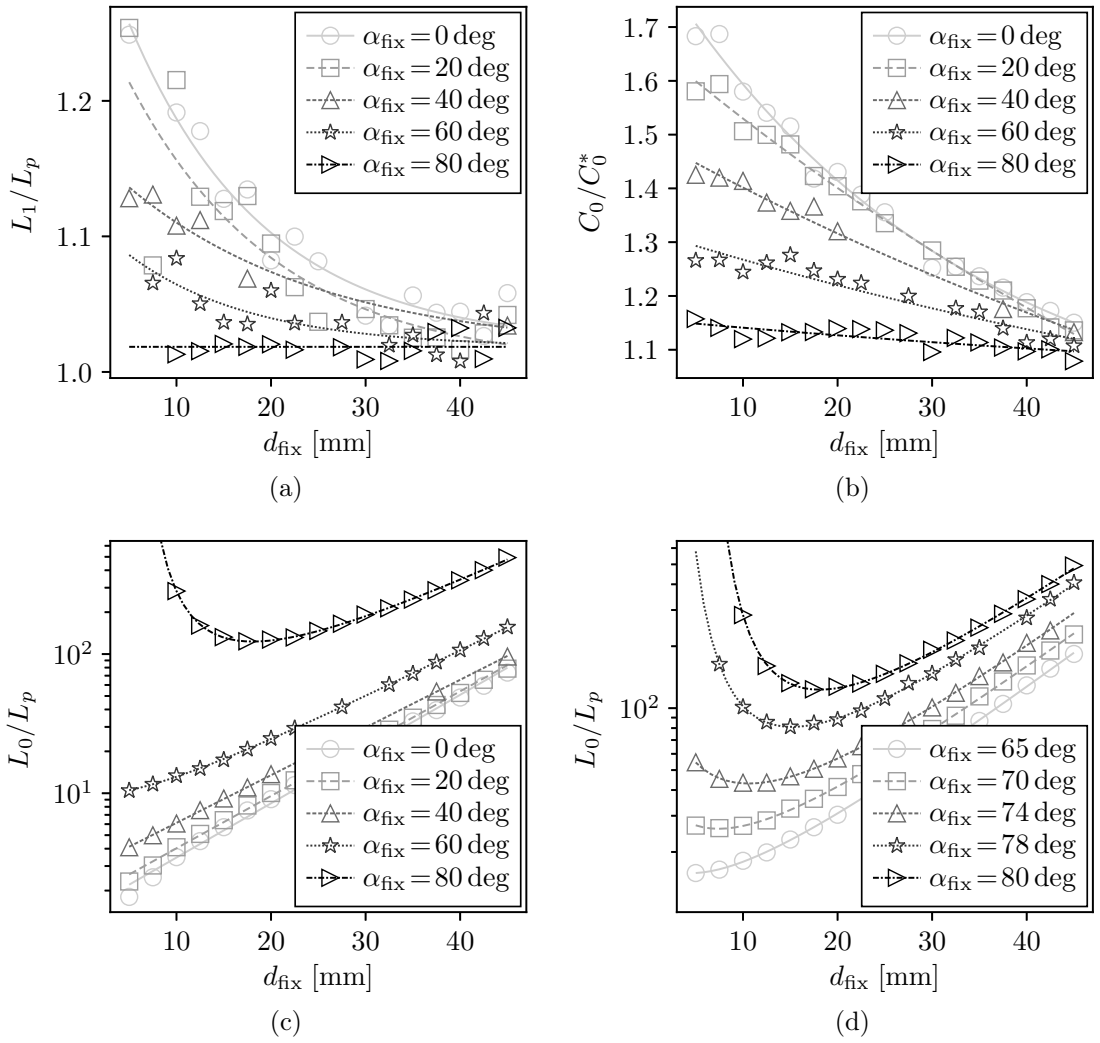

Fig. 4.19. Circuit parameters of the equivalent microwave network which represents the rf structure according to Fig. 4.18. The inner and outer radii of the coaxial geometry are 5 mm and 22.5 mm, respectively. The same cross section applies to the waveguide between the identical fixings whose distance d_{fix} is varied while their common radius $r_{\mathrm{fix1}} = 3\,\mathrm{mm}$. Moreover, the gap distance $d_{\mathrm{gap}} = 0.3\,\mathrm{mm}$ and the angle between the fixings in the transverse plane is varied. (a) Effective impedance of the coaxial waveguide between the fixings normalized to the characteristic impedance of $Z_0^* = 90.24\,\Omega$ according to (4.5). (b) Capacitance of the parallel LC resonator normalized to the definition (4.16). (c) and (d) Inductance of the parallel LC resonator normalized to the corresponding value of the single inductive post in Fig. 4.3(a).

The third case study illustrated in Fig. 4.19 considers the impact of the rotation angle α_{fix} assuming a symmetric microwave structure. Circuit parameters are given as functions of the distance d_{fix} between the inductive posts while the gap distance $d_{\mathrm{gap}} = 0.3\,\mathrm{mm}$ and common radius of the cylindrical fixings, $r_{\mathrm{fix1}} = r_{\mathrm{fix2}} = 3\,\mathrm{mm}$. In Fig. 4.19(a), the enhancement of shunt inductances due to coupling mechanisms,

significantly reduces as the rotation angle becomes larger, and nearly vanishes for $\alpha_{\text{fix}} \geq 80\,\text{deg}$. A similar behavior provides the capacitance of the parallel LC resonator shown in Fig. 4.19(b). As the rotation angle rises, the contribution of fringe fields to the total capacitance C_0 becomes less. The inductance L_0 of the parallel LC resonator shown in Figs. 4.19(c)–(d) rises partially by orders of magnitude with increasing rotation angle. The exponential dependency on the distance d_{fix} between the fixings is well preserved for $\alpha_{\text{fix}} \leq 60\,\text{deg}$. Note, this range is characterized by a relatively moderate variation of the inductance with the rotation angle. For $\alpha_{\text{fix}} > 60\,\text{deg}$, the inductance drastically increases as the angle becomes larger. Moreover, an asymptotic behavior due to a singularity appears for relatively small values of d_{fix} while the angle approaches 90 deg. This property will be very important for the synthesis of filter functions since it allows for practically any reasonable inductance of the LC resonator while the impact of transmission lines can be reduced as desired. Significant alterations of L_0 with the rotation angle α_{fix}, in particular, at small distances d_{fix}, provide evidence for the mid-shunt ladder being related to evanescent higher order multipole modes of the coaxial guide. It is remarkable that the corresponding frequency response of such a problem is fairly well represented by a simple resonator in between transmission lines and shunt inductances. However, a proof by means of analytical field calculations remains an open problem.

Disregarding the transmission lines, the equivalent circuit sketched in Fig. 4.18(b) corresponds to a canonical form of a third-order high-pass filter with one transmission zero at finite, nonzero frequency and another one at zero. For this reason, the considered coaxial microwave structure is an ideal candidate for the design of HOM couplers independent of the approximation type which may range from relatively simple *maximally flat* to computationally more ambitious *elliptic filters*. It is worth noting that the coaxial structure provides only three discontinuities, i. e. the inductive posts and capacitive gap, while the equivalent microwave network requires four lumped elements. Thus, the number of obstacles in a coaxial filter may be lower than the number of lumped elements in a canonical circuit of equivalent behavior.

4.1.7 Mid-Series Ladder between Inductive Posts in Coaxial Guide

The *mid-series ladder* refers to a two-port network consisting of a series LC resonator connected in shunt [39]. Enclosed by transmission lines and shunt inductances, it constitutes the counterpart to the equivalent circuit of the previous section. The realization as coaxial microwave structure is shown in Fig 4.20 together with the equivalent circuit. Other than the left and right fixings represented by the shunt inductances $L_{1,2}$, the center post is separated by a small distance from the outer conductor of the coaxial structure in order to introduce a capacitive gap. Alternatively, a mid-series ladder may be approximately achieved by a coaxial waveguide terminated with a shunt capacitance as applied for the TESLA HOM coupler. It is important to note that the latter approach provides only a certain inductance L_0 in

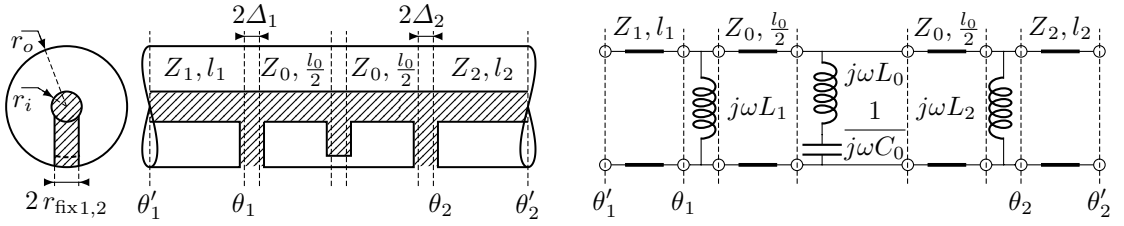

Fig. 4.20. (a) Cross-sectional and side view of a coaxial structure with two fixings between the inner and outer conductor. The fixings are modeled as cylinders with the radii $r_{\mathrm{fix}1}$ and $r_{\mathrm{fix}2}$. At the center, a cylindrical post of the radius $r_{\mathrm{fix}0}$ is attached to the inner conductor. It is separated from the outer conductor by a small gap of the size d_{gap}. (b) Equivalent circuit model.

the vicinity of the resonant frequency $\omega_0 = 1/\sqrt{L_0 C_0}$ due to the frequency dependent impedance transformation of the transmission line representing the waveguide. Both implementations of mid-series ladders are very common for the design of coaxial HOM couplers in order to provide transmission zeros at finite, nonzero frequency. A particular advantage is the simple and flexible frequency adjustment of the transmission zero by slightly modifying the distance of the capacitive gap [101, p. 29]. However, in contrast to the mid-shunt ladder of Sec. 4.1.7, the inductance of the series resonator, if any, is very constrained in practice. This is, in particular, unfavorable for the synthesis of certain filter functions which require distinct values for both the capacitance C_0 and inductance L_0.

The equivalent circuit for the coaxial rf structure according to Fig. 4.20 is solved in an analogous way to previous sections, by fitting the simulated and phase shifted scattering matrices over discrete frequency samples. Again, the transmission matrix of the equivalent circuit permits an elegant formulation of the non-linear minimization problem to derive circuit parameters. Between the terminal planes θ_1 and θ_2, the microwave network in Fig. 4.20(b) admits a transmission matrix whose parameters can be written as

$$A = \frac{B}{j\omega L_2} + \cos\beta l_0 - \frac{Z_0}{2L_0}\frac{\omega}{\omega_0^2 - \omega^2}\sin\beta l_0 \tag{4.38}$$

$$B = -j\frac{Z_0^2}{L_0}\frac{\omega}{\omega_0^2 - \omega^2}\sin^2\frac{\beta l_0}{2} + jZ_0\sin\beta l_0 \tag{4.39}$$

$$D = \frac{B}{j\omega L_1} + \cos\beta l_0 - \frac{Z_0}{2L_0}\frac{\omega}{\omega_0^2 - \omega^2}\sin\beta l_0, \tag{4.40}$$

where $\omega_0 = 1/\sqrt{L_0 C_0}$ corresponds to the resonant frequency of the series LC resonator. The remaining element of the transmission matrix results from the reciprocal condition (2.33).

Despite the different network topologies, the transmission functions given in (4.38)–(4.40) are very similar to (4.34)–(4.36) of the previous section. Let L_{0s} be denoted as the inductance of the series resonator in the microwave network of Fig. 4.20(b) while C_{0s} denotes the capacitance of the shunt resonator in the microwave network of Fig. 4.14(b). Then, both networks become equivalent if

$$\beta l_0 = \pi/2, \tag{4.41}$$

$$L_{0s} = -Z_0^2 C_{0p}. \tag{4.42}$$

The first condition strictly applies only for a certain frequency and is characteristic for a $\lambda/4$ transformer. Note, in the vicinity of this frequency, the scattering matrix of both circuits remain approximately the same. The second requirement yields a negative inductance which is not reasonable either for networks or microwave structures, provided they are linear, passive and time-invariant. It can be deduced that the microwave networks of Figs. 4.14(b) and 4.20(b) are not equivalent to each other. Consequently, the simplest and most reasonable model to describe the scattering properties of the coaxial microwave structure shown in Fig. 4.14(a) is given by the equivalent circuit of Fig. 4.14(b). The same conclusion applies for the structure and equivalent circuit depicted in Fig. 4.20. It provides pseudo-high-pass characteristics which are further discussed in Sec. 4.3.2.

4.2 On the Excitation of Waveguide Modes

The preceding section has dealt with the rf behavior of coaxial structures comprising one or more discontinuities and their corresponding equivalent microwave circuits. In order to complete the picture of coaxial couplers, it is necessary to further consider certain aspects of the coupling to modes in the attached waveguide, cutoff tube, or cavity. By reciprocity, this topic is closely related to the excitation of waveguide modes, which is extensively covered in the literature [27, 29, 42]. This section reflects, in parts, the theory developed in [29, pp. 276]. Qualitative results are discussed in the context of HOM couplers as well as consequences for the antenna design.

4.2.1 Probe and Loop Coupling in a Waveguide

Figure 4.21 illustrates common coupling types between a coaxial line and waveguide. The probe and open-loop antennas are particularly interesting for superconducting applications due to the simpler design and easier manufacturing. The power transfer essentially depends on the field distribution of the considered waveguide mode. Referring to Fig. 4.21(a), any mode providing nonzero electric field components along the probe antenna will excite currents on the probe. In contrast, loop antennas primarily couple to the magnetic field of the particular waveguide modes as further explained in Sec. 4.2.2.

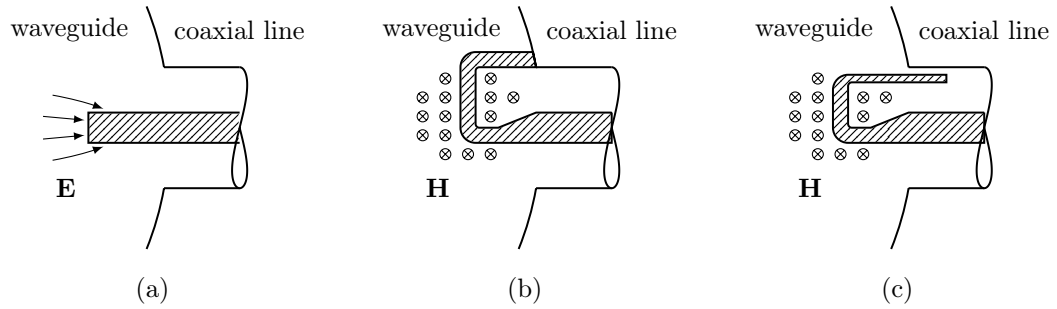

Fig. 4.21. Transition between a circular waveguide and coaxial line using (a) a probe antenna, (b) closed-loop antenna, and (c) open-loop antenna. The propagation direction of the circular waveguide faces the viewer. Electric and magnetic field lines correspond to a TE-like mode.

By referring to the examples in Fig. 4.21, let the volume V be imagined completely exterior and bounded by the surface S, with the coaxial line and waveguide being cut perpendicular to their particular axes at some arbitrarily chosen plane called terminal plane or port. Since vacuum is considered inside the coaxial line and waveguide, Maxwell's equations for harmonic fields yield a symmetric behavior of the solution, which may be expressed by the following form of the *reciprocity theorem* [29, p. 278]

$$\oiint_S (\mathbf{E} \times \mathbf{H}_n - \mathbf{E}_n \times \mathbf{H}) \cdot \mathbf{n}\, dA = \iiint_V \mathbf{E}_n \cdot \mathbf{J} dV, \tag{4.43}$$

where $\mathbf{n}$ refers to the local normal vector of the surface element dS. The electromagnetic field $\mathbf{E}$, $\mathbf{H}$, may be considered as the field being radiated by the current $\mathbf{J}$ on the antenna. Likewise, $\mathbf{J}$ may be considered as the current being induced by the same electromagnetic field. Equation (4.43) further accounts for the coupling to the n-th mode in the circular waveguide whose electric and magnetic fields are given by $\mathbf{E}_n$ and $\mathbf{H}_n$, respectively. By reciprocity, if the originally considered probe or loop currents are driven by a TEM mode incident from the coaxial line, the same waveguide modes will be excited, which were previously considered to be the source. Note, the circular waveguide in the examples of Fig. 4.21 may be the cutoff tube of an accelerating cavity. The considerations above equally apply if the coaxial line directly terminates into a cavity. In this case, the field quantities $\mathbf{E}_n$ and $\mathbf{H}_n$ correspond to the n-th resonant mode.

The antenna of an HOM coupler should be designed and placed such that coupling to the fundamental mode of the cavity is significantly reduced while the power transfer to concerned HOMs is as high as desired. Often, these requirements are contradictory and cannot be achieved by solely changing the shape or location of the antenna due to the given modal field distributions. This is true for the SPL cavities where both the fundamental and higher order modes of concern belong to the same category of transverse magnetic modes without azimuthal dependency.

Thus appropriate microwave filters are inevitable. If coaxial HOM couplers are considered, such a filter may be constructed from several of the components discussed in Sec. 4.1. In contrast, deflecting type cavities operating with multipole modes may be equipped with simple probe or loop antennas without additional filters in order to suppress undesired HOMs [8, 85].

4.2.2 Radiation from Current Elements

To illustrate the coupling of an antenna to modes in a waveguide or cavity, let a one-dimensional current source $\mathbf{J}$ be located between the terminal planes θ_1 and θ_2 of an infinitely long cylindrical waveguide. The current source may be arbitrarily formed by an open or closed path C describing the antenna shape as shown in Fig. 4.22(a) or 4.22(b), respectively. The electromagnetic field radiated from the left terminal

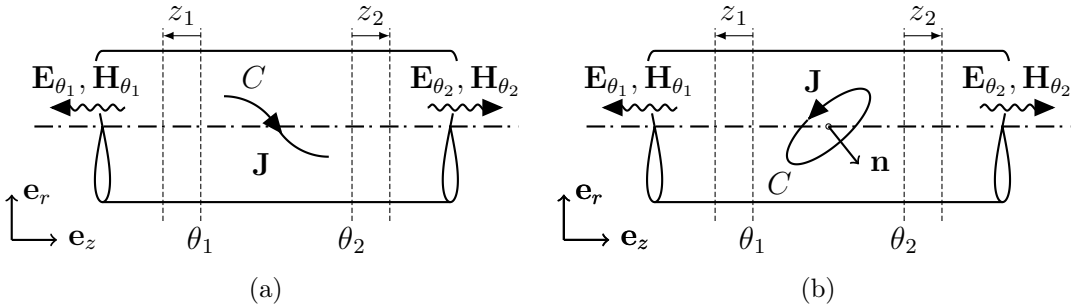

Fig. 4.22. Different current sources in an infinitely long waveguide. (a) Current segment and (b) current loop, each described by the corresponding path C. The loop is further characterized by the enclosed surface normal vector $\mathbf{n}$.

plane θ_1 where $z_1 > 0$ is source free and may be expressed as sum over all transverse electric and magnetic waveguide modes according to

$$\mathbf{E}_{\theta_1} = \sum_n c_{\theta_1,n}(\tilde{\mathbf{E}}_{\perp,n} + \tilde{\mathbf{E}}_{\parallel,n})e^{-j\beta_n z_1}, \tag{4.44}$$

$$\mathbf{H}_{\theta_1} = \sum_n c_{\theta_1,n}(-\tilde{\mathbf{H}}_{\perp,n} + \tilde{\mathbf{H}}_{\parallel,n})e^{-j\beta_n z_1}, \qquad z_1 > 0, \tag{4.45}$$

where $\tilde{\mathbf{E}}_{\parallel,n}$, $\tilde{\mathbf{H}}_{\parallel,n}$ are longitudinal and $\tilde{\mathbf{E}}_{\perp,n}$, $\tilde{\mathbf{H}}_{\perp,n}$ are transverse field components of the n-th waveguide mode with arbitrary normalization. The electric and magnetic fields radiated from the right terminal plane θ_2 where $z_2 > 0$ may be expressed in

the analogue way by the superposition of infinitely many waveguide modes as

$$\mathbf{E}_{\theta_2} = \sum_n c_{\theta_2,n}(\tilde{\mathbf{E}}_{\perp,n} - \tilde{\mathbf{E}}_{\parallel,n})e^{-j\beta_n z_2}, \tag{4.46}$$

$$\mathbf{H}_{\theta_2} = \sum_n c_{\theta_2,n}(\tilde{\mathbf{H}}_{\perp,n} + \tilde{\mathbf{H}}_{\parallel,n})e^{-j\beta_n z_2}, \qquad z_2 > 0, \tag{4.47}$$

Again, the index n involves all possible transverse electric and magnetic waveguide modes. Note, the coordinates z_1 and z_2 refer to the distance from the particular terminal plane as shown in Fig. 4.22. The coefficients $c_{\theta_1,n}$, $c_{\theta_2,n}$ can be derived from (4.43), with the volume V being confined by waveguide walls and both terminal planes $\theta_{1,2}$. In the lossless case, that is the electric conductivity of the waveguide walls becomes infinite and (2.77) holds, the surface integral of the reciprocity formula (4.43) reduces to the waveguide cross sections at the terminal planes. By choosing the n-th mode to be of the form (4.46)–(4.47) such that

$$\mathbf{E}_n = (\tilde{\mathbf{E}}_{\perp,n} - \tilde{\mathbf{E}}_{\parallel,n})e^{-j\beta_n z}, \tag{4.48}$$

$$\mathbf{H}_n = (\tilde{\mathbf{H}}_{\perp,n} + \tilde{\mathbf{H}}_{\parallel,n})e^{-j\beta_n z}, \tag{4.49}$$

the coefficient $c_{\theta_1,n}$ becomes [29, pp. 278]

$$c_{\theta_1,n} = \frac{1}{P_{\theta_1,n}} \iiint_V (\tilde{\mathbf{E}}_{\perp,n} - \tilde{\mathbf{E}}_{\parallel,n}) \cdot \mathbf{J} e^{-j\beta_n z}\, dV, \tag{4.50}$$

where $P_{\theta_1,n}$ is a measure of the modal power flow through the terminal cross section and is given by

$$P_{\theta_1,n} = 2 \iint_{\theta_1} (\tilde{\mathbf{E}}_{\perp,n} \times \tilde{\mathbf{H}}_{\perp,n}) \cdot \mathbf{e}_z\, dA = 2 \iint_{\theta_2} (\tilde{\mathbf{E}}_{\perp,n} \times \tilde{\mathbf{H}}_{\perp,n}) \cdot \mathbf{e}_z\, dA = P_{\theta_2,n}. \tag{4.51}$$

Note, due to the lossless consideration, this power flow is the same everywhere along the waveguide left from the terminal plane θ_1 or right from the terminal plane θ_2. A similar expression can be found for the coefficients $c_{\theta_2,n}$ by choosing the n-th mode in (4.43) to be of the form (4.44)–(4.45) that is

$$\mathbf{E}_n = (\tilde{\mathbf{E}}_{\perp,n} + \tilde{\mathbf{E}}_{\parallel,n})e^{j\beta_n z}, \tag{4.52}$$

$$\mathbf{H}_n = (-\tilde{\mathbf{H}}_{\perp,n} + \tilde{\mathbf{H}}_{\parallel,n})e^{j\beta_n z}. \tag{4.53}$$

Inserting into the reciprocity relation (4.43) yields

$$c_{\theta_2,n} = \frac{1}{P_{\theta_2,n}} \iiint_V (\tilde{\mathbf{E}}_{\perp,n} + \tilde{\mathbf{E}}_{\parallel,n}) \cdot \mathbf{J} e^{j\beta_n z}\, dV. \tag{4.54}$$

Though numerical simulations are generally required to evaluate waveguide modes and field integrals for realistic problems, expressions (4.50) and (4.54) already provide important qualitative information about the nature of mode excitation in a waveguide using probe or loop antennas. Let a linear current element $\mathbf{J}_\perp$ be located at $z = 0$ and directed perpendicular to the wave propagation. Note, this configuration is similar to the example of a probe antenna in Fig. 4.21(a). A current source of this type provides identical field amplitudes at both terminal planes since

$$c_{\theta_1,n} = \frac{1}{P_{\theta_1,n}} \int_C \tilde{\mathbf{E}}_{\perp,n} \cdot I d\mathbf{l} = \frac{1}{P_{\theta_2,n}} \int_C \tilde{\mathbf{E}}_{\perp,n} \cdot I d\mathbf{l} = c_{\theta_2,n}, \tag{4.55}$$

where the quantity I corresponds to the current flow in the predefined direction. By referring to (4.44)–(4.47), the electric field across the terminal planes θ_1 and θ_2 appears to be continuous while the transverse magnetic field is not. This behavior may equivalently be described by a shunt voltage source between two transmission lines which represent the propagation of a single mode in the waveguide. If more than one propagating mode is present, several such equivalent circuits may be considered independently due to the mode orthogonality. For the second configuration, let the center of a linear current element again be located at $z = 0$ but directed parallel to the wave propagation. If the line current density $\mathbf{J}_\parallel$ is symmetric in z, the modal field coefficients of such an axial current source obey the relationship

$$c_{\theta_1,n} = -\frac{1}{P_{\theta_1,n}} \int_C \tilde{\mathbf{E}}_{\parallel,n} \cdot I e^{-j\beta_n z} d\mathbf{l} = -\frac{1}{P_{\theta_2,n}} \int_C \tilde{\mathbf{E}}_{\parallel,n} \cdot I e^{j\beta_n z} d\mathbf{l} = -c_{\theta_2,n}, \tag{4.56}$$

since $\tilde{\mathbf{E}}_{\parallel,n}$ is independent of the longitudinal position z. As in the previous example, the coupling is governed by the electric field. Observing (4.44)–(4.47), the transverse magnetic field is equal at both terminal planes θ_1 and θ_2 while the transverse electric field provides a discontinuity here. This behavior may equivalently be described by a voltage source connected in series between two transmission lines taking into account the single mode propagation through the waveguide.

Similar conclusions on equivalent circuit models follow for the current loop shown Fig. 4.22(b). The coupling mechanism of this configuration which is representative for loop antennas as depicted in Fig. 4.21(b), is dominated by the magnetic flux traversing the loop. Given a homogeneous current flow I_0 around the contour C, this can be shown by reformulating the right hand side of the reciprocity formula (4.43) according to

$$\begin{aligned} \iiint_V \mathbf{E}_n \cdot \mathbf{J}\, dV &= \oint_C \mathbf{E}_n \cdot I_0 d\mathbf{l} \\ &= I_0 \iint_S \nabla \times \mathbf{E}_n \cdot d\mathbf{A} = -j\omega\mu_0 I_0 \iint_S \mathbf{H}_n \cdot d\mathbf{A} \end{aligned} \tag{4.57}$$

Here, the surface S is bounded by the closed path C. Consequently, the coupling is determined by the contribution of magnetic field that crosses the loop antenna. Using (4.57), the field amplitude of (4.44)–(4.47) may be written as

$$c_{\theta_1,n} = -\frac{j\omega\mu_0 I_0}{P_{\theta_1,n}} \iint\limits_S (\tilde{\mathbf{H}}_{\perp,n} + \tilde{\mathbf{H}}_{\parallel,n}) \cdot e^{-j\beta_n z} d\mathbf{A}. \tag{4.58}$$

$$c_{\theta_2,n} = -\frac{j\omega\mu_0 I_0}{P_{\theta_2,n}} \iint\limits_S (-\tilde{\mathbf{H}}_{\perp,n} + \tilde{\mathbf{H}}_{\parallel,n}) \cdot e^{j\beta_n z} d\mathbf{A}. \tag{4.59}$$

Again via continuity and discontinuity considerations of selected field components, the purely transverse current loop may be interpreted as a voltage source connected in shunt between two transmission lines which account for the propagation of a single mode through the waveguide. It is important to note that the choice of voltage or current source for the equivalent circuit model is arbitrary since any voltage source of a network may be replaced by an equivalent current source and vice versa according to Tévenin's theorem as introduced in Sec. 2.1. Nonetheless, a magnetic field may intuitively be associated with electric currents while the electric field may intuitively be associated with potential differences, hence, voltages.

4.2.3 Impedance Matching and Reactance Compensation

The previous considerations provide some preliminary ideas of how an equivalent microwave network may look in order to describe the coupling of waveguide modes with an antenna. Though illustrative, the simplified representation of the antenna by current elements located in the waveguide is unsuitable with respect to design and optimization tasks. Referring to the original problem in Fig. 4.21, that is a probe or loop antenna inserted into a circular waveguide and connected to a coaxial line, let the volume V be imagined completely exterior and bounded by the surface S, with the coaxial line and waveguide being cut perpendicular to their particular axes at some arbitrarily chosen terminal planes. The energy conservation for harmonic fields may be expressed using the complex Poynting vector as

$$\frac{1}{2} \oiint\limits_S \mathbf{E} \times \mathbf{H}^* \cdot \mathbf{n}\, dA = P_V + 2j\omega(\mathcal{U}_m - \mathcal{U}_e), \tag{4.60}$$

where P_V is the power dissipated in the volume V. Since the considered domain is source free and filled with vacuum, let this contribution to the energy balance be disregarded, thus $P_V = 0$. The second term on the right hand side accounts for the reactive power which is owed by the excitation of evanescent modes being present in the vicinity of the antenna. As no real power is carried by such modes, the contribution to the stored energy appears parasitic. Furthermore, let the electric conductivity of the waveguide walls and antenna be infinite such that (2.77) holds.

Then, the surface integral in (4.60) reduces to the circular and coaxial waveguide cross sections at the particular terminal planes. It may be split according to the direction of the power flow as

$$\frac{1}{2}\oiint_S \mathbf{E}\times\mathbf{H}^*\cdot\mathbf{n}\,dA = \frac{1}{2}V_{\text{in}}I_{\text{in}}^* - P, \tag{4.61}$$

with the first term on the right hand side being the inward power flow at the coaxial port and P is the power radiated in both directions through the infinitely long circular waveguide. The inward power flow represented by an equivalent voltage and current in (4.61) yields the connection between impedance and dissipated or stored energy, and is given by [27, pp. 130]

$$Z_{\text{in}} = \frac{P + 2j\omega(\mathcal{U}_m - \mathcal{U}_e)}{\frac{1}{2}I_{\text{in}}I_{\text{in}}^*} = R_0 + jX \tag{4.62}$$

The real part of this input impedance seen from the coaxial port,

$$R_0 = \frac{2P}{I_{\text{in}}I_{\text{in}}^*}, \tag{4.63}$$

is the *radiation resistance* of the antenna [29, p. 281]. Both quantities, the radiation resistance R_0 and parasitic reactance X, must be considered individually for each excited waveguide mode according to the modal power flow (4.51). Likewise, the input power and corresponding equivalent terminal current I_{in} must be projected onto the field distribution of the individual mode according to the reciprocity formula (4.43) and derived results for the field amplitudes (4.50) and (4.54). The radiation resistance and parasitic reactance are determined by various geometrical parameters that are not only related to the antenna shape and insertion depth but also to the waveguide cross section and aperture for the coaxial line. Eventually, discontinuities along the waveguide will have a notable impact as well.

Let a single mode be excited by an antenna in a circular waveguide through which it propagates. Now the problem may be simplified and described by one of the microwave networks shown in Figs. 4.23. According to Sec. 4.2.2, they constitute ideal cases, in that either the electric or magnetic field across the coupling region, between θ_1' and θ_2', behaves as continuous. The mode propagation in the circular waveguide is represented by the horizontal transmission lines at the terminal planes θ_1 and θ_2 while the skewed transmission line at the terminal plane θ_3 accounts for the propagation of the TEM mode through the coaxial line. The ideal transformer provides a means of adjusting the coupling such that the same amount of power radiates into the circular waveguide as delivered by the coaxial line. Equation (4.62) represents the input impedance at the terminal plane θ_3, which is given by the transformation of the wave impedance $Z_1 = Z_2$ and reactance jX. In order to avoid reflections at

the imagined terminal plane θ'_3 and to achieve the maximum power transfer, the radiation resistance (4.63) must equal the characteristic impedance of the coaxial line Z_3 given by (2.67). Note, the evaluation of scattering parameters provided by numerical simulations or measurement always refers to the rf transmission or reflection with respect to the terminal planes θ_1, θ_2, and θ_3. The radiation resistance allows the internal impedance mismatch to be quantified. Furthermore, it is important to minimize the amount of reactive energy stored in evanescent modes in order to maximize the power transfer to the desired mode. This is typically done by introducing a suitable reactance to compensate jX. Referring to the equivalent circuit models in Fig. 4.23, let the circular waveguide at the terminal plane θ_2 be shorted while the length l_2 is chosen such that the impedance at the terminal plane θ'_2 seen towards the short equals $-jX$. Though the equivalent circuits represent in both cases very idealized coupling, this approach of reactance compensation is common for realistic problems, for instance, the waveguide-coax transition of coaxial fundamental mode couplers [107, pp. 263]. The concept of reactance compensation may be involved in the design of HOM couplers with the additional complexity that multiple modes are considered. According to the previous considerations, the design task must not be restricted to the antenna and its penetration depth into the waveguide. It should also include the entire coupling region, that is, the circular waveguide with eventual discontinuities towards the cavity or beam pipe as well as the aperture to the coaxial line. A trade-off must be defined between modes of concern for achieving overall acceptable damping. In this context, the analysis of transmission zeros,

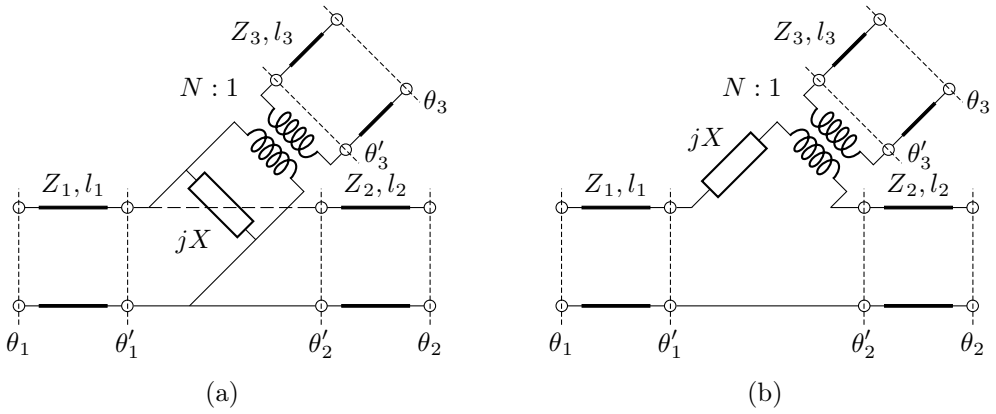

Fig. 4.23. Equivalent circuit models to describe the excitation of a single mode propagating through an infinitely long waveguide by an antenna which is inserted in the same and connected to a coaxial line. The mode propagation in the circular waveguide is represented by the horizontal transmission lines at the terminal planes θ_1 and θ_2 while the skewed transmission line at the terminal plane θ_3 accounts for the propagation of the TEM mode through the coaxial line. The field coupling is described by an ideal transformer for impedance conversion and a reactive component taking into account the energy stored by evanescent modes. Across the terminal planes θ'_1 and θ'_2, continuity of the transverse (a) electric and (b) magnetic field component is respected.

hence, frequencies at which no or very moderate power is transmitted, becomes very important, and is further discussed in Sec. 4.2.4.

Regarding HOM couplers, there is one case where the reactance X may be desired, that is for the fundamental mode of the cavity. According to the results of Sec. 4.2.2, the probe and transverse loop antennas may equivalently be described in a very simplified manner by the microwave network shown in Fig. 4.23(a) characterized by a shunt reactance. The open-loop antenna sketched in Fig. 4.21(c) is particularly interesting since its reactance corresponds to a series LC resonator similar to Sec. 4.1.7, given the inductive behavior of the loop combined with a capacitive gap between the antenna and outer conductor of the coaxial line. Various existing HOM couplers comprise such open-loop antennas in order to suppress the transmission of the fundamental mode by adjusting the resonant frequency of the equivalent LC resonator accordingly [101, 117].

In the literature, various interpretations of HOM couplers by equivalent circuits lack a very important component: the ideal transformer. As previously mentioned, this means is required to ensure energy conservation, and enables the radiation resistance to be distinguished from the characteristic impedance of a propagating mode in a waveguide or the resistance associated with the power dissipation of a resonant mode in a cavity. Figure 4.24(a) sketches the equivalent circuit of an HOM coupler with probe antenna as proposed in [17, pp. 361] and formerly discussed in [11, 24, 101] among others. The electromagnetic field inside the waveguide or cavity is represented by a current source according to the displacement currents picked up by the probe. The reactive part of the antenna, given by the stray capacitance at the probe tip, is connected in shunt similar to the equivalent circuit model in Fig. 4.23(a). Consequently the antenna is assumed to be infinitesimally thin to respect continuity of the transverse electric field components across the coupling region. The fact that the source does not provide any resistance is in contradiction to the physical meaning of power transfer. To illustrate this discrepancy, let the

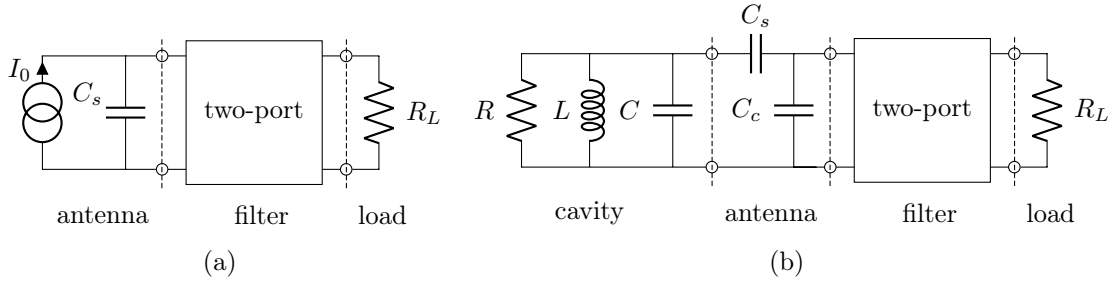

Fig. 4.24. Equivalent circuit models to describe the coupling of a resonant mode in a cavity to an HOM coupler. The electromagnetic field in the vicinity of the antenna is represented by (a) the current source I_0 [11, 101] and (b) an RLC circuit excited at the resonant frequency of the considered cavity mode [118]. The two-port ought to provide optimum power transmission with respect to dangerous HOMs while the fundamental mode is greatly rejected.

stray capacity be completely compensated for a selected mode. Then the extracted amount of power could be arbitrarily high by choosing a correspondingly high load resistance R_L. A wrong conclusion may be deduced from Fig. 4.24(a), for instance, the maximum power provided from the source is given by [17, pp. 363]

$$P_{\max} = \frac{I_0^2}{4\omega C_s}, \tag{4.64}$$

which applies if the resistance seen from the left side of the two-port is

$$R = \frac{1}{\omega C_s}. \tag{4.65}$$

Though correct for the given network, this result misses the fact that the current source must provide a resistance in order to allow for any power transmission and not to keep the energy stored in only evanescent or resonant modes. This resistance is exactly the radiation resistance derived from (4.62), and may be considered in parallel to the stray capacitance C_s in Fig. 4.24(a). Note, if the characteristic impedance of a propagating mode in a waveguide is considered instead of the radiation resistance, an ideal transformer must be inserted between the antenna and filter part in order to ensure energy conservation.

Likewise, the second example shown in Fig. 4.24(b) leaves out the ideal transformer in order to convert the resistance R associated with the power dissipation of a resonant mode in the cavity into the radiation resistance R_0. In contrast to the previous example, the reactive component of the antenna is described by an additional capacitance connected in series as proposed in [118] and likewise discussed in [116, pp. 98]. The interpretation of C_s and C_c is debatable, whether related to the stray capacitance or fringe field of the coaxial line in the region of the antenna tip. Nonetheless, the separation into two capacitances is not in contradiction to the model shown in Fig. 4.24(a), which considers merely one capacitance connected in parallel to a current source. The excited RLC resonant circuit may be imagined as a voltage source with the internal impedance given by the resistance R and capacitance C_s. By applying Tévenin's theorem as introduced in Sec. 2.1, this voltage source may equivalently be described by a current source with the resistance and capacitance each connected in shunt. Therefore, both circuits in Fig. 4.24 represent the coupling between a resonant mode and probe antenna in equivalent manner. A differentiation between C_s and C_c as depicted in Fig. 4.24(b) is not reasonable.

The equivalent circuits in Fig. 4.24 intuitively illustrate the principle of how a fraction of power is extracted from a resonant mode in a cavity. However, they do not represent power transmission in the strict sense. The first model lacks the source resistance while the second is a pure impedance consideration. Eventual reflections due to impedance changes are not accounted for, which implies perfect matching from the cavity up to the load. Though very illustrative, complex systems

consisting of a cavity, antenna, filter, and load are unfavorable for the initial design phase of HOM couplers. Nonetheless, the derived results (4.64) and (4.65) yield two important conclusions to achieve an optimum power transmission: (i) The effective reactance of the coupling must be minimized, for instance, by compensation. (ii) The optimal radiation resistance directly depends on the effective coupling reactance.

The two-ports in Fig. 4.24 allow for the specific filter characteristics of HOM couplers using components as presented in Sec. 4.1. They ought to provide the desired power transfer of concerned HOMs while the fundamental mode is greatly rejected. Furthermore, they need to be matched to the radiation resistance R_0 and load R_L. Since the first generally varies for different modes, a trade-off must be defined. Moreover, the two-port may be considered for partial compensation of the antenna reactance, though the impact is significantly lower than provided by geometric variations of the antenna, aperture or cutoff tube. A phenomenon which cannot be influenced by the filter component is subsequently discussed.

4.2.4 Frequencies of Field Cancellation

Often HOM couplers are not directly mounted on accelerating cavities. Instead, they couple to resonant modes through a cutoff tube which is located right before or after the cavity as in the case of the SPL. These tubes are essentially waveguides and provide the transition between the cavity and beam pipe as illustrated in Fig. 4.25(a). The cavity and beam pipe are, respectively, imagined left from the terminal plane θ_1 and right from the terminal plane θ_2 while the coaxial microwave filter of the HOM coupler is located above the terminal plane θ_3. Independent of the considered mode propagating through the circular waveguide, the frequency response at θ_1 with the TEM mode being excited at θ_3, is characterized by frequencies at which no or very

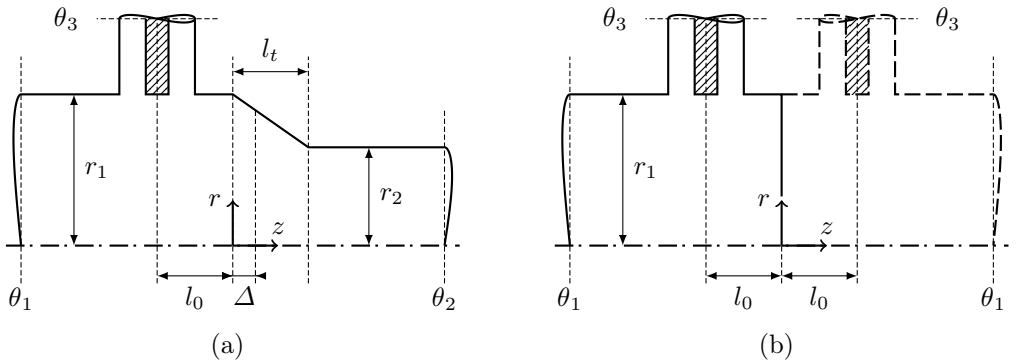

Fig. 4.25. (a) Probe antenna applied on a cylindrical waveguide which is tapered at a distance l_0 from the center of the antenna. This configuration corresponds to the cutoff tubes of the SPL cavities, with the cavity at the terminal plane θ_1. (b) Probe and its image (dashed) to model the field coupling between a coaxial line and cylindrical waveguide shortened at a distance l_0 from the center of the antenna. The z-axis coincides with the center axis of the circular waveguide.

low power transmission is observed. This is, in particular, problematic if the cavity provides potentially dangerous higher-order modes at such frequencies, as they may not sufficiently be damped no matter how the coupler is designed. The following theory is based on the superposition of propagating fields in the circular waveguide, in a way that they cancel out each other exactly at the antenna position.

Given an electromagnetic wave being able to propagate through the circular waveguide section of larger aperture in Fig. 4.25(a), it is assumed that the same mode is asymptotically damped within the waveguide section of smaller aperture, hence, it behaves evanescent after the taper. This is true if the considered frequency ω satisfies the relation

$$\omega_1 < \omega < \omega_2, \tag{4.66}$$

where ω_1 and ω_2 are the angular cutoff frequencies associated with the larger or smaller waveguide cross section, respectively. Referring to the cylindrical waveguides of radii r_1 and r_2 in Fig. 4.25(a), the cutoff frequency of transverse magnetic modes can be deduced from (2.87) according to

$$\omega_{1,2} = c_0 \frac{j_{mn}}{r_{1,2}}, \qquad \text{if TM}_{mn} \text{ mode}, \tag{4.67}$$

where j_{mn} is the n-th root of the Bessel function of first order and m-th mode. A similar expression follows for transverse electric modes, that is [29, p. 197]

$$\omega_{1,2} = c_0 \frac{j'_{mn}}{r_{1,2}}, \qquad \text{if TE}_{mn} \text{ mode}, \tag{4.68}$$

where j'_{mn} is the n-th root of the first derivative of the corresponding Bessel function. To begin with, let the coupling problem be simplified such that the circular waveguide is shortened in one direction at the distance l_0 from the center of the probe antenna as depicted in Fig. 4.25(b). The short circuit is motivated by the fact that no wave propagation occurs in the corresponding direction of the original problem. Though not accounting for the evanescent field contribution, this simplification is very illustrative to derive the condition under which a transmission zero between the terminal planes θ_1 and θ_3 occurs. The short-circuit is equivalent to an image of the entire structure, indicated by dashed lines in Fig. 4.25(b). Similar to Sec. 4.2.2, the probe antenna and its image may be considered as line current elements with opposite directions in order to fulfill the boundary condition at the longitudinal position $z = 0$. It is worthwhile to note that the same problem is discussed in [29, pp. 276] but in a different context. Due to the reverse directions of the current sources, the fields radiated from the probe and its image differ by a phase shift of π. Field cancellation occurs if the wavelength of the considered mode equals $\lambda = 2l_0$. This is equivalent to the condition

$$\beta_{0,n} 2l_0 = 2\pi n, \tag{4.69}$$

where the integer n imposes the periodicity with 2π and $\beta_{0,n}$ is the corresponding propagation constant. Under this condition, there is no net power transmitted towards the terminal plane θ_1 by the particular mode. The circumstance may be interpreted as a transmission zero between the considered mode at the terminal plane θ_1 and TEM mode at terminal plane θ_3. Condition (4.69) provides the counterpart of reactance compensation, that is the compensation of the radiation resistance.

Other, than for the TEM mode considered in Sec. 4.1, the propagation constant of a transverse magnetic or electric mode in a circular waveguide is determined by its cutoff frequency according to

$$\beta = \frac{1}{c_0}\sqrt{\omega^2 - \omega_1^2}, \qquad \omega > \omega_1. \tag{4.70}$$

Inserting in (4.69) yields the corresponding frequencies at which the transmission zeros occur,

$$\omega_{0,n} = \omega_1\sqrt{1 + \left(\frac{\pi n c_0}{\omega_1 l_0}\right)^2}. \tag{4.71}$$

The subsequent examples related to the dimensions of the SPL cutoff tubes, considering solely the case $n = 1$. Figure 4.26 shows the transmission power gain with respect to the propagation of either the TE_{11} or TM_{01} mode being considered at the terminal plane θ_1, and TEM mode propagation at the remaining terminal plane θ_3.

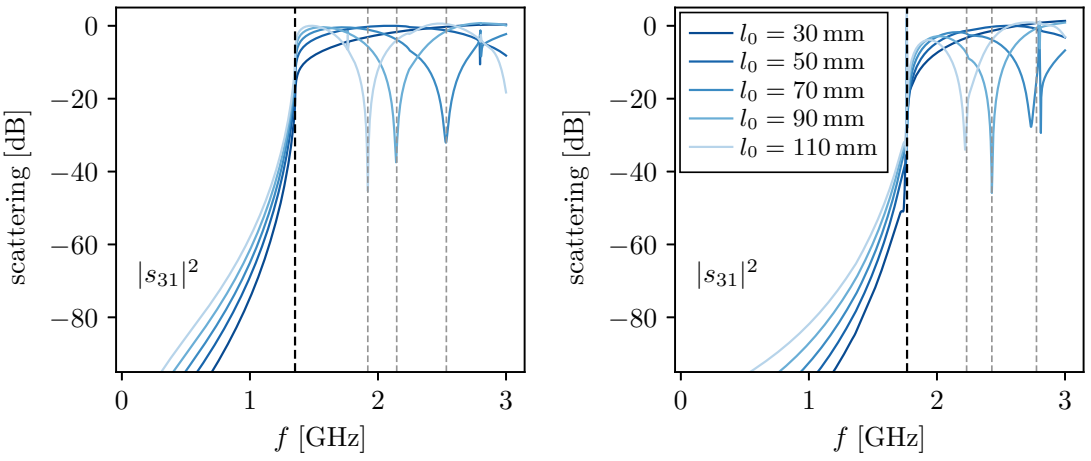

(a) TE_{11}-TEM transmission (b) TM_{01}-TEM transmission

Fig. 4.26. Transmission power gain between the circular and coaxial waveguide ports for the simplified problem depicted in Fig. 4.25(b), taking into account (a) the TE_{11} and (b) TM_{01} mode propagation at the terminal plane θ_1 while the remaining terminal plane θ_3 considers the TEM mode propagation, each. In dashed black, the cutoff frequency f_1 of the corresponding circular waveguide mode with radius $r_1 = 65\,\mathrm{mm}$. In dashed gray the transmission zeros given by (4.71).

Equation (4.71) precisely describes the transmission zeros for the simplified problem as shown by the dashed gray lines. The smaller the distance l_0 between the antenna and short-circuit, the larger is the corresponding frequency at which ideally no rf power is transmitted.

From (4.71), one may wrongly conclude that by sufficiently reducing the distance l_0 of a cutoff tube as depicted in Fig. 4.25(a), transmission zeros can be removed from any finite frequency range given by concerned HOMs. This is not observed for the original problem of a cutoff tube with tapered waveguide as shown in Fig. 4.27 by means of the transmission power gain for the same mode configuration as before. The transmission power gain shown in Fig. 4.27(a) refers to the coupling between the TE_{11} and TEM mode, respectively, at the terminal planes θ_1 and θ_3, and reveals transmission zeros at much lower frequencies in comparison to the previous case in Fig. 4.26(a). In particular, for the considered range of l_0, all transmission zeros appear below the cutoff frequency of the waveguide section with smaller radius ω_2.

A first attempt to describe the anticipated transmission zeros based on the above observation is motivated by a frequency transformation of even-order elliptic filter functions [31]. Let $\tilde{\omega}_{0,n}$ be defined by the linear dispersion relation of electromagnetic waves propagating in vacuum, $\tilde{\omega} = c_0\beta$, and the requirement (4.69) according to

$$\tilde{\omega}_{0,n} = \frac{\pi n c_0}{l_0 + \Delta}. \tag{4.72}$$

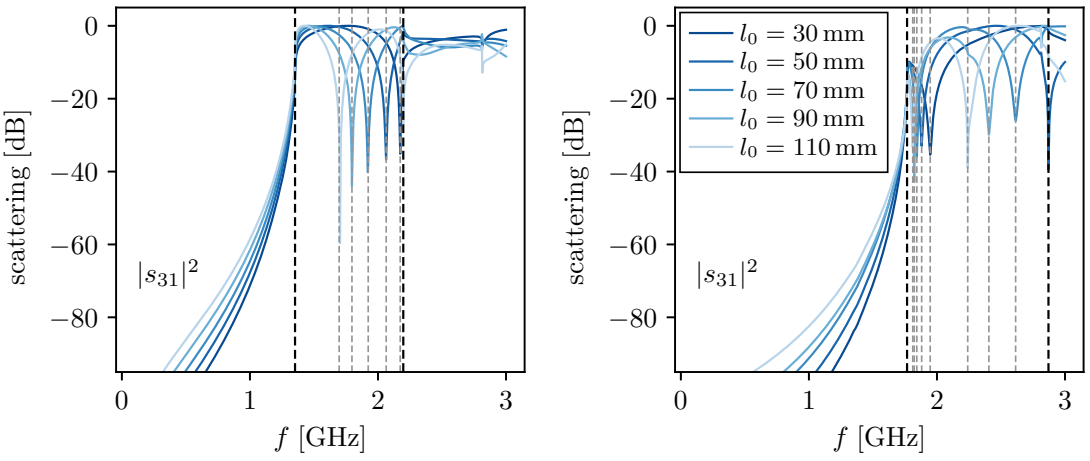

(a) TEM-TE_{11} transmission

(b) TEM-TM_{01} transmission

Fig. 4.27. Transmission power gain between modes at the terminal planes θ_1 and θ_3 of the problem depicted in Fig. 4.25(a). In dashed black, the cutoff frequencies f_1 and f_2 of the circular waveguide sections with corresponding radii $r_1 = 65\,\mathrm{mm}$ and $r_2 = 40\,\mathrm{mm}$. The dimensions refer to the cutoff tube of the high-β SPL cavity on tuner side, where the tapering is elongated over a distance of 28 mm. Transmission zeros are highlighted by dashed gray lines.

The quantity Δ introduces an additional distance as illustrated in Fig. 4.25(a). It accounts for the finite, nonzero transition region in which the considered waveguide mode is partially able to propagate. Its value is a-priori not known but can be approximated in different ways as later shown. To map the frequency $\tilde{\omega} \in (0, \infty)$ to $\omega \in [\omega_1, \omega_2]$, at first, a normalization is introduced, which ensures the resulting cutoff frequencies being reciprocal to each other. With the normalized frequencies given by

$$\tilde{\Omega} = \frac{\tilde{\omega}}{\sqrt{\omega_1 \omega_2}}, \tag{4.73}$$

$$\Omega = \frac{\omega}{\sqrt{\omega_1 \omega_2}}, \tag{4.74}$$

let the inverse transform be defined as

$$\tilde{\Omega}^2 = \left| \frac{\Omega^2 - \Omega_1^2}{1 - \Omega_1^2 \Omega^2} \right| = \frac{\Omega^2 - \Omega_1^2}{1 - \Omega_1^2 \Omega^2}, \tag{4.75}$$

with $\Omega \geq \Omega_1$ and $0 \leq \Omega_1 \Omega \leq 1$. Note, by replacing the frequency variables with their corresponding complex variables $p = j\Omega$ and $\tilde{p} = j\tilde{\Omega}$, the transformation used in [31] is restored. Equation (4.75) may also be expressed via the *Poincaré hyperbolic distance function* [25, p. 11] as $\tilde{\Omega}^2 = \rho(\Omega^2, \Omega_1^2)$ with the pseudo-hyperbolic metric being defined on the open disk of radius Ω_1^{-2}. Rearranging (4.75) for Ω, substitution according to (4.73)–(4.74), and invoking the condition for field cancellation (4.72) based on the propagation constant in free space yields the transformed transmission zeros as

$$\omega_{0,n} = \omega_1 \sqrt{\frac{1 + (\tilde{\omega}_{0,n}/\omega_1)^2}{1 + (\tilde{\omega}_{0,n}/\omega_2)^2}}. \tag{4.76}$$

It is important to note that the frequency map is entirely based on the observation that transmission zeros of the present problem seem to appear between the cutoff frequencies ω_1 and ω_2 given by the two apertures of the circular waveguide in Fig. 4.25(a). In the limit $\omega_2 \to \infty$ which applies if $r_2 = 0$, the expression (4.71) of the short-circuit problem is restored. It was found that (4.76) well describes transmission zeros with respect to the TE_{11} mode as shown in Fig. 4.27(a). The correction Δ is chosen such that the error of transmission zeros for all considered lengths l_0 is minimized. Table 4.1 shows the relative error of (4.76) by means of the SPL cutoff tube with radii $r_1 = 65\,\mathrm{mm}$, $r_2 = 40\,\mathrm{mm}$ and a tapered transition region of 28 mm elongation [88]. The values are likewise found in Fig. A.2. The length l_0 which describes the longitudinal distance from the center of the HOM coupler port to the position where the taper begins, is varied from 30 mm to 110 mm, where $l_0 = 30\,\mathrm{mm}$ corresponds to the actual value of the prototype geometry. Note, the dimensions apply to the cutoff tube of the high-β SPL cavity on the tuner side as sketched

Table 4.1. Approximation error of transmission zeros in the cutoff tubes.

	TE_{11}			TM_{01}		TM_{01}	
l_0 [mm]	ω_0 [GHz]	$\delta\omega^\dagger$ [%]	$\delta\omega^\ddagger$ [%]	ω_0 [GHz]	$\delta\omega^\S$ [%]	ω_0 [GHz]	$\delta\omega^\S$ [%]
30	2.1735	0.0003	–	1.9473	0.7153	–	–
50	2.0633	0.0413	0.0413	1.8806	0.3673	2.8695	0.1560
70	1.9212	0.1302	0.1687	1.8429	0.0083	2.6143	4.8981
90	1.7965	0.0148	0.9626	1.8226	0.0746	2.4055	0.4501
110	1.7037	0.4035	1.2446	1.8110	0.0444	2.2402	0.5608

† Relative error of (4.76) using a correction of the distance $\Delta = -17\,\text{mm}$.
‡ Relative error of (4.81) using the model in Fig. 4.28(a) with $L_t = 6.6\,\text{nH}$ and $\Delta = 33.7\,\text{mm}$.
§ Relative error of (4.81) using the model in Fig. 4.28(b) with $C_t = 0.81\,\text{pF}$ and $\Delta = 14\,\text{mm}$.

by the test assembly in Fig. 3.37. The second and third columns of Table 4.1, respectively, list the frequency of transmission zeros based on numerical simulations, ω_0, and corresponding relative errors provided by the approximation (4.76) if a distance correction of $\Delta = -17\,\text{mm}$ is considered. Errors below 0.5 % reveal fairly good approximations with respect to the TE_{11} mode. However, the analytic model fails in the view of the TM_{01} mode since the associated frequency response significantly differs between both mode types, as is apparent in Fig. 4.27.

The following more general approach for describing transmission zeros in cutoff tubes is based on equivalent circuits involving lumped and distributed elements. Referring to Fig. 4.25(a), the mode propagation or damping within the different waveguide sections of constant radius r_1, r_2, with $r_1 > r_2$, is represented by corresponding transmission lines of characteristic impedances $Z_{1,2}$ and lengths $l_{1,2}$. Here, transverse electric and magnetic modes naturally behave very differently. The characteristic impedances for a TM mode in the different waveguide sections may be written as [29, p. 197]

$$Z_1 = \frac{Z_0}{\omega}\sqrt{\omega^2 - \omega_1^2}, \tag{4.77}$$

$$Z_2 = j\frac{Z_0}{\omega}\sqrt{\omega_2^2 - \omega^2}, \qquad \text{if TM mode,} \tag{4.78}$$

taking into account (4.66) for the considered frequency range. The quantity Z_0 refers to the impedance of free space given by $\sqrt{\mu_0/\varepsilon_0}$. Regarding TE modes, an equivalent expression applies to the reciprocal of characteristic impedance, hence, to the admittance which may be written for the individual waveguide sections as

$$Y_1 = \frac{Y_0}{\omega}\sqrt{\omega^2 - \omega_1^2}, \tag{4.79}$$

$$Y_2 = j\frac{Y_0}{\omega}\sqrt{\omega_2^2 - \omega^2}, \qquad \text{if TE mode,} \tag{4.80}$$

where $Y_0 = 1/Z_0$. Furthermore, the tapered transition region in Fig. 4.25(a) can be approximated by a lumped element as well as a length correction Δ applied to the neighboring transmission lines in order to account for the electric size of the transition. The procedure is identical to the characterization of discontinuities in coaxial waveguides as extensively treated Sec. 4.1, with the difference that the characteristic impedances or admittances in (4.77)–(4.80) are frequency dependent. By testing various microwave networks on their equivalence to the tapered circular waveguide disregarding the coaxial line in Fig. 4.25(a), it was found that the transition region behaves for the TE_{11} mode as a shunt inductance but for the TM_{01} mode as a shunt capacitance, each within the frequency range given by (4.66). Consequently, the scattering properties of the tapered circular waveguide may equivalently be described by the microwave networks shown in Fig. 4.28. The lumped elements and length corrections are derived by fitting the simulated rf reflection s_{11} at the terminal plane θ_1 with the expression (4.7) over the predefined frequency range. With respect to the previously introduced dimensions applying to a cutoff tube of the high-β SPL cavity, the approximation error provided by the equivalent circuits is below 2×10^{-2} as measured by real and imaginary parts of the reflection coefficient assuming (4.66). Since the particular mode is asymptotically damped in the waveguide section of smaller aperture as a consequence of (4.66), the transmission line given by Z_2, l_2 may be imagined to be infinitely long, which corresponds to a termination by its characteristic impedance. On the basis of these equivalent circuits, the necessary and sufficient condition for a transmission zero being present in a cutoff tube according to Fig. 4.25(a) is a vanishing input impedance $Z_{\mathrm{in},1}$ at the position of the probe antenna. Thus, the corresponding frequencies may be written as

$$\omega_{0,n} = \arg\{Z_{\mathrm{in},1}(j\omega) = 0 : l_1 = l_0 + \Delta\}, \tag{4.81}$$

where n accounts for the periodic behavior of the transmission line. In analogy to

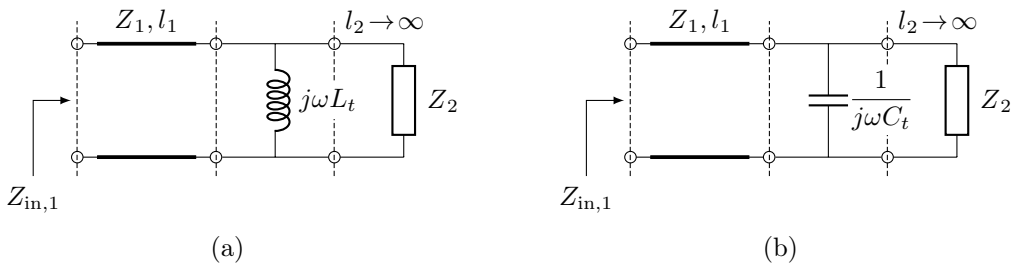

Fig. 4.28. Equivalent circuits describing (a) the TE_{11} and (b) TM_{01} mode propagation through the tapered circular waveguide as sketched in Fig, 4.25(a) disregarding the coaxial line. Both models are limited to the frequency range given by (4.66). Within the waveguide section of larger aperture, the input impedance $Z_{\mathrm{in},1}$ is defined on an internal terminal plane at given distance from the taper while the waveguide section of smaller aperture is matched at the terminal plane θ_2.

the previous approach based on frequency transformation, the problem (4.81) may be reformulated for the TE_{11} mode as

$$\tilde{\Omega}_h^2 = \rho(\Omega^2, \Omega_1^2), \tag{4.82}$$

and for the TM_{01} mode as

$$\tilde{\Omega}_e^{-2} = \rho^{-1}(\Omega^2, \Omega_1^2), \tag{4.83}$$

taking into account the frequency normalization given by (4.73)–(4.74). Those $\Omega = \Omega_{0,n}$ which solve (4.82) or (4.83) are the corresponding normalized frequencies being associated with transmission zeros. As previously introduced, ρ is the pseudo-hyperbolic distance function defined as

$$\rho(\Omega^2, \Omega_1^2) = \left| \frac{\Omega^2 - \Omega_1^2}{1 - \Omega_1^2 \Omega^2} \right| = \frac{\Omega^2 - \Omega_1^2}{1 - \Omega_1^2 \Omega^2}. \tag{4.84}$$

Its square root and the reciprocal of its square root as functions of Ω are shown in solid black in Fig. 4.29. Unlike (4.75), the left hand sides of (4.82) and (4.83) do not only depend on the distance l_0 and order n which is related to the periodic behavior of the transmission line. They are also functions of Ω according to

$$\tilde{\Omega}_h = \left(\frac{1}{\Omega_1} - \frac{1}{Y_0 \sqrt{\omega_1 \omega_2} L_t \sqrt{1 - \Omega_1^2 \Omega^2}} \right) \tan \beta (l_0 + \Delta), \tag{4.85}$$

$$\tilde{\Omega}_e^{-1} = \left(Z_0 \sqrt{\omega_1 \omega_2} C_t \sqrt{1 - \Omega_1^2 \Omega^2} - \Omega_1 \right) \tan \beta (l_0 + \Delta), \tag{4.86}$$

with the propagation constant β as defined in (4.70). Thus, the idea of a frequency transformation as previously considered for the TE_{11} mode, is generally not appropriate. Expressions (4.85) and (4.86) are likewise plotted as functions of Ω in 4.29(a) and 4.29(b), respectively, with the distance l_0 being varied from 30 mm to 110 mm. The intercepts of black and blue curves in Fig. 4.29 provide the normalized frequencies $\Omega_{0,n}$, hence the frequencies of transmission zeros, $\omega_{0,n}$, after applying (4.74). The corresponding relative approximation errors listed in Table 4.1 are below 1 % except for two cases. Although, slightly less precise than (4.76) for the TE_{11} mode propagation, the calculation of transmission zeros on the basis of equivalent circuits as shown in Fig. 4.28 yields a more general approach being suitable for different mode types. It allows the study of conditions under which transmission zeros disappear without the need of extensive numerical simulations. Referring to the example of the SPL cutoff tube, the transmission zeros with respect to the TM_{01} mode propagation vanish if the capacitance C_t provided by the taper is reduced to half while placing the probe antenna at a distance $l_0 = 15$ mm away from the taper. Although very abstract, particularly the requirement on C_t, these considerations may provide

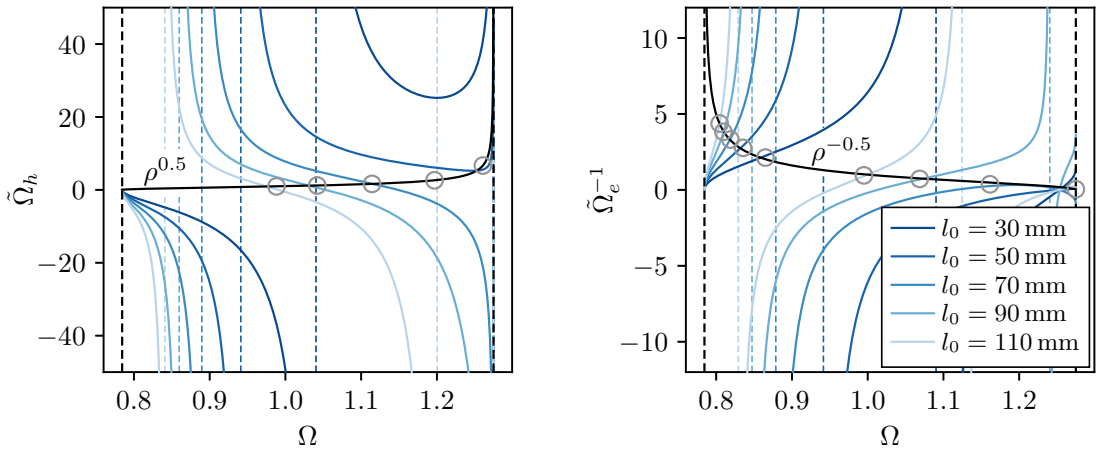

(a) Transmission zeros for TE_{11} mode

(b) Transmission zeros for TM_{01} mode

Fig. 4.29. Expressions (4.85) and (4.86) as functions of the normalized frequency Ω, with the distances l_0 being varied. The dashed blue lines represent poles of these functions. In dashed black, the normalized cutoff frequencies Ω_1 and $\Omega_2 = \Omega_1^{-1}$ resulting for the cutoff tube described in Fig. 4.27, with $r_1 = 65\,\mathrm{mm}$ and $r_2 = 40\,\mathrm{mm}$. In solid black, root expressions of the pseudo-hyperbolic distance function ρ according to (4.84). Gray circles refer to normalized frequencies of transmission zeros as simulated. The intercepts of black and blue curves provide the normalized frequencies of transmission zeros predicted by the equivalent circuit models according to Fig. 4.28 and derived conditions (4.82)–(4.83). In accordance with Table 4.1, the parameters accounting for the taper of $l_t = 28\,\mathrm{mm}$ length are (a) $L_t = 6.6\,\mathrm{nH}$, $\Delta = 33.7\,\mathrm{mm}$ and (b) $C_t = 0.81\,\mathrm{pF}$, $\Delta = 14\,\mathrm{mm}$.

general guidance for the design of cutoff tubes.

Finally, Table 4.2 compares the available cutoff tubes of high-β SPL cavities as designed by CEA Saclay [19, pp. 80]. Geometrical parameters such as the radii r_1, r_2 of the circular waveguide sections, taper elongation l_t, or distance between the coaxial line and taper, l_0, have significant impact on the frequency of transmission zeros in the considered cutoff tube. In addition, variations of the antenna shape provided by the HOM coupler may cause slight frequency shifts. The listed frequency ranges in Table 4.2 result from different HOM coupler designs considered in Chapter 5. It is important to note that transmission zeros with respect to the

Table 4.2. Transmission zeros of the high-β SPL cutoff tubes.

cutoff tube	r_1 [mm]	r_2 [mm]	l_t [mm]	l_0 [mm]	$\omega_0{}^{\dagger}$ [GHz]	$\omega_0{}^{\ddagger}$ [GHz]
tuner side	65	40	28	30	2.18–2.19	1.85–1.96
fundamental mode coupler side	70	40	34	59	1.93–1.94	1.68–1.74

† TE_{11} mode propagation through the circular waveguide.
‡ TM_{01} mode propagation through the circular waveguide.

TM_{01} mode propagation occur for both cutoff tubes at frequencies sufficiently far away from the TM_{011} frequency band of the cavity. Consequently, the damping of corresponding potentially dangerous HOMs, as listed in Table 3.8, is expected not to be compromised by field cancellation phenomena within the cutoff tubes.

4.3 Design Procedure of Coaxial Filters

The remaining part of this chapter focuses on the rf design of coaxial HOM couplers. The design process is understood as synthesis, that is the systematical approach to approximate a given frequency response by an appropriate microwave structure, typically being a combination of those components discussed in Sec. 4.1. It should not be confused with the design of HOM couplers, which is a more general task involving inter alia the thermal and structural behavior and will be assessed in Chapter 5. Thus, the filter synthesis constitutes the first step towards designing an HOM coupler. It is important to note that there is no generally applicable theory on the synthesis of coaxial microwave structures with multiple discontinuities. Little work has been published in this field, mostly based on frequencies of the fundamental mode and some HOMs [24, 101, 118]. This section presents initial studies towards an insertion loss method for coaxial high-pass filters given a transfer or corresponding filter function. To begin with, the procedure developed by Haebel and Gerigk [101] is reviewed. Results of Secs. 4.1 and 4.2 are used to point out limitations of this approach as well as some misinterpretations in this work.

4.3.1 Review of the Coupler Design by Haebel and Gerigk

The design procedure reported by Haebel [24] is a result of various ideas that had been developed and tested in the scope of HOM couplers for LEP and HERA. Later, the approach was refined by Gerigk [101], and eventually led to the HOM couplers being used for LHC cavities. The designs are closely related to synchronously tuned reactance-coupled $\lambda/2$ resonators [113, pp. 528]. Other than the insertion loss method, it is not a transfer function that is taken as the base but rather distinct frequencies associated with the fundamental mode, ω_0, and concerned higher-order modes denoted as $\omega_1, \omega_2, \ldots \omega_k$. The design procedure relies on the principal of reactance compensation over a possible large frequency range given by the HOMs of concern. It is illustrated in the following with the help of microwave networks shown in Fig. 4.30, disregarding the transmission behavior for the fundamental mode.

The antenna, either a probe or loop, is described by a current or voltage source which provides internal impedance seen left from the terminal plane θ_1. Note, the original references, such as [24], only consider a reactance. However, such models miss the definition of an internal resistivity to allow power flow as extensively discussed in Sec 4.2.3 by means of the probe antenna. Although the conditions under which power is extracted from a resonant mode must be rethought when introduc-

ing a source resistance R_1, the actual design procedure remains the same due to the focus on the reactive component. Referring to the microwave networks in Fig. 4.30, the maximum power transmission to the load R_2 occurs, if the source susceptance ωC_s or reactance ωL_s is compensated while matching the resistance seen from the terminal plane θ_1 towards the load with the source resistance R_1. The necessary impedance transformation can be achieved by a transmission line in combination with the shunt inductance L_p, however, only in the vicinity of distinct frequencies. This condition is sometimes referred to as *resonant coupling*. The shunt inductance L_p is considered of necessity in the view of coaxial filters. As discussed in Sec. 4.1.1 the connection between inner and outer conductor result in such an inductive behavior. In [24], some equivalent circuits further consider series and shunt capacitances which likewise have their practical meaning in the coaxial filter but the principle of resonant coupling is the same. It is important to note that the sources together with the internal impedance are, in general, fictive models to represent the antenna. Depending on whether a current or voltage source is considered, the equivalent circuit is referred to as *electric* or *magnetic coupling*, respectively [101]. However, this interpretation is somewhat misleading since the rf device provides a unique frequency response. In the presence of mode coupling into a waveguide or resonator, the impedance provided by the source in Fig. 4.30 acts as being connected in shunt following the considerations in Sec. 4.2.3 with the equivalent circuit shown in Fig. 4.23(a). This is equally achieved by replacing current and voltage source respectively by an open or short.

A weakness of the design procedure lies in the assumption that reactance compensation can be achieved by merely adjusting the filter part of HOM couplers. According to Sec. 4.2, the excitation of evanescent modes associated with reactive components is to some extent influenced by the waveguide or cavity geometry. The most obvious example is the observation of transmission zeros in cutoff tubes as dis-

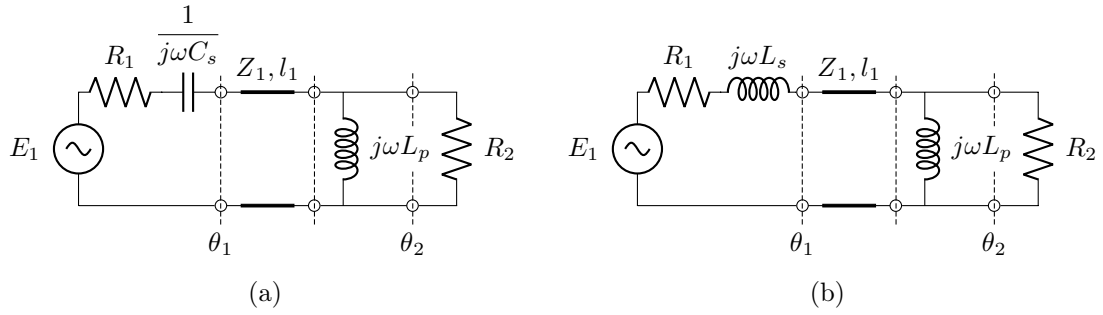

Fig. 4.30. Circuit models to describe mode coupling via (a) probe or (b) loop antenna. To maximize the power transmitted to the load R_2, the capacitive or inductive reactance of the source must be compensated while the resistance seen from the terminal plane θ_1 towards the right must be matched to the source resistance R_1. The required impedance transformation is realized by a transmission line in combination with the shunt inductance L_p for distinct frequencies.

cussed in Sec. 4.2.4. Consequently, the idea of reactance compensation and derived resonant coupling is not sufficient to elaborate a design procedure for HOM couplers. It is the matching between the source and load resistance R_1, R_2, via impedance transformation which completes the design strategy.

A practical difficulty results from the fact that the frequencies of maximum power transmission usually do not fit the spectrum of concerned HOMs [24]. More control of the passband behavior can be achieved using multiple transmission lines separated by shunt inductances as proposed in [101]. The obtained network shown in Fig. 4.31(a) disregarding the capacitances C'_ν corresponds to a coaxial waveguide structures which is essentially a cascade of the components discussed in Sec. 4.1.1 and 4.1.4. The approach is motivated from the band-pass characteristics of inductively coupled series resonators as depicted in Fig. 4.31(b). To achieve the desired behavior of series resonators in the microwave network, each transmission line in between shunt inductances is considered as $\lambda/2$ resonator terminating in a short [34, p. 26]. The latter implies that the impedance of each shunt arm is much smaller than the total impedance connected in parallel to it. Figure 4.32 illustrates the approximation between lumped circuit and transmission line model by means of an arbitrarily chosen example using three inductively coupled resonators. According to Sec. 2.1.5, the periodic behavior of transmission lines leads to infinitely many passbands, with the first being most relevant for the design of HOM couplers. Each further coupled resonator provides a new resonance in the passband of the resulting filter. However, for feasibility, coaxial HOM in superconductive applications are typically limited to two or three stages. The main problem when optimizing the rf design remains to fit the frequencies of maximum power transmission to the given HOM pattern, which is often characterized by conflicting goals.

Given the specific topology of a coaxial guide according to the equivalent circuit in Fig. 4.31(a), a systematic design procedure can be developed. Note, all considerations are solely focused on the transmission of HOMs, hence the passband characteristics of the corresponding coupler. A proposal for such a design procedure

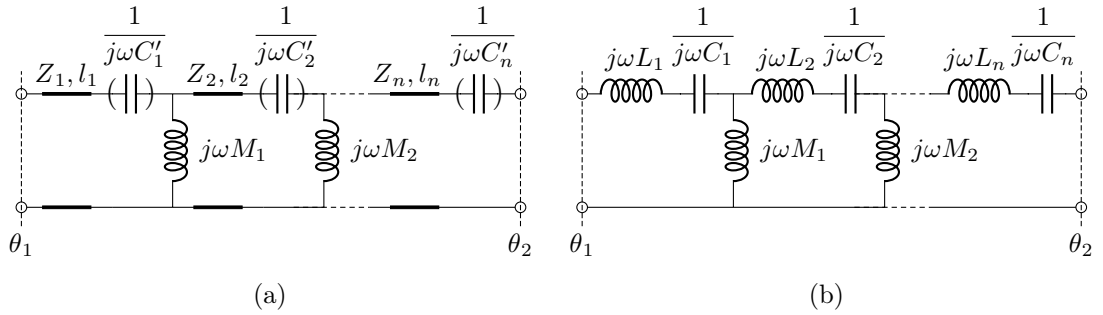

Fig. 4.31. (a) Band-pass filter using inductively coupled series resonators, with the capacitances being optional. (b) Lumped network to approximate the band-pass characteristics of (a).

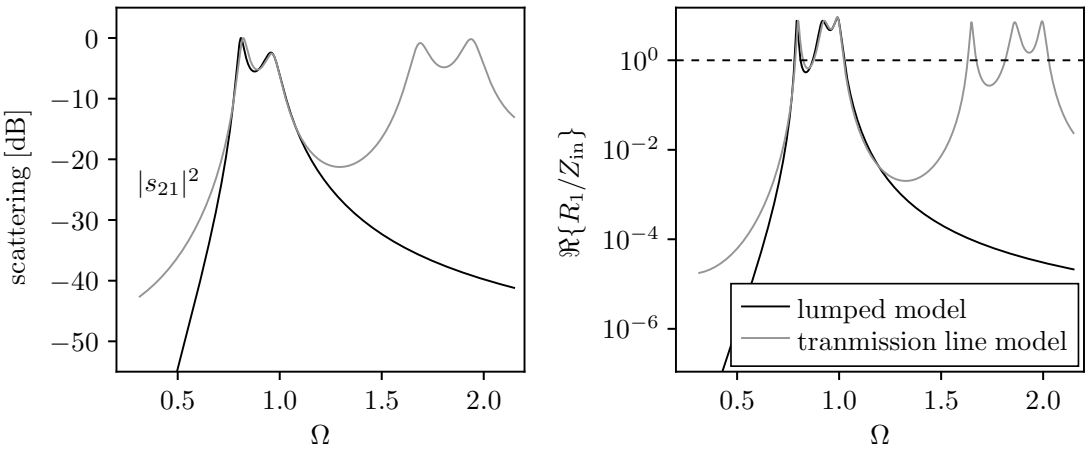

Fig. 4.32. Band-pass consisting of three inductively coupled resonators realized by lumped elements or $\lambda/2$ transformers assuming $C_i' = \infty$ according to Fig. 4.31. (a) Transmitted power gain between the terminal planes θ_1 and θ_2, and (b) real part of the normalized input admittance at the terminal plane θ_1, both as functions of the normalized frequency $\Omega = \omega/\omega_1$, where $\omega_1 = 1/\sqrt{L_1 C_1}$. The example is calculated for the values $L_1 = L_2 = L_3 = 10\,\text{H}$, $C_1 = C_2 = C_3 = 0.1\,\text{F}$, $M_1 = M_2 = 10\,\text{H}$ and reference resistances at the terminal planes θ_1 and θ_2 of $R_1 = 7\,\Omega$ and $R_2 = 1\,\Omega$, respectively. Lengths of the transmission lines correspond to half the wavelength at ω_1 while their characteristic impedances satisfy $Z_1 = Z_2 = Z_3 = R_1$.

is reported in [101] and briefly reflected in the following. Let the reference frequency ω_∞ be defined as the geometric mean of the lowest and highest considered HOM frequency according to

$$\omega_\infty = \sqrt{\omega_1 \omega_k}. \tag{4.87}$$

This will be the design frequency for each individual resonator. Furthermore, the bandwidth of the anticipated band-pass filter is defined as

$$\Delta\omega = |\omega_k - \omega_1|. \tag{4.88}$$

Coupled resonators are characterized by a coupling factor k which is given as ratio of the bandwidth and center frequency, that is

$$k = \frac{\Delta\omega}{\omega_\infty}. \tag{4.89}$$

It relates the shunt and neighboring series inductances in Fig. 4.31(b) according to

$$k\sqrt{L_\nu L_{\nu+1}} = M_\nu, \qquad \nu = 1\,2, \ldots n-1. \tag{4.90}$$

Weak coupling, that is $k \ll 1$, allows for the assumption that each transmission line in Fig. 4.31(a) terminates approximately in a short, and yields the equivalence between series LC resonator and $\lambda/2$ transformer. Strictly speaking, each transmission line terminates in small impedance dominated by the particular shunt inductance. Consequently, small corrections of the transmission line lengths are required. The impedance transformation for the ν^{th} shorted transmission line in the vicinity of the design frequency ω_∞ may be written as [101, p. 25]

$$Z_{\text{in},\nu}(\omega) = jZ_\nu \tan\left(\frac{\omega\pi}{\omega_\infty}\right) \underset{\omega\approx\omega_\infty}{\simeq} jZ_\nu \left(\frac{\omega\pi}{\omega_\infty} - \pi\right), \tag{4.91}$$

where the characteristic impedance Z_ν is given by the predefined cross section of the particular coaxial waveguide segment according to (2.67). A weak formulation is used to solve the lumped circuit elements in Fig. 4.31(b). It requires equal slope between the input reactance of the terminated transmission line and corresponding lumped circuit resonator at design frequency. For the first loop providing a resonator with inductances L_1, M_1 and the capacitance C_1, the condition is expressed as

$$\frac{\partial}{\partial\omega}\left(j\omega(L_1 + M_1) + \frac{1}{j\omega C_1}\right)\bigg|_{\omega=\omega_\infty} = \frac{\partial}{\partial\omega} Z_{\text{in},1}(\omega)\bigg|_{\omega=\omega_\infty}. \tag{4.92}$$

Similar expressions are obtained for the remaining loops of the ladder network depicted in Fig. 4.31(b). It is important to note that such weak conditions proposed in [101, p. 25] do not imply approximation between transmission line and lumped circuit model. Merely, a similar passband behavior is realized due to the identical resonant frequency ω_∞ considered in both models. Alternatively to (4.92), the reactance of the transmission line and corresponding lumped circuit resonator may be equated with each other at design frequency instead of their derivatives, in order to ensure approximation at least in a single frequency point. Evaluating (4.92) and corresponding conditions for the other loops of the ladder network yields a system of equations which satisfy

$$2\omega_\infty(L_1 + M_1) = Z_1, \tag{4.93}$$

$$2\omega_\infty(L_{\nu+1} + M_\nu + M_{\nu+1}) = Z_{\nu+1}, \qquad \nu = 1, 2 \ldots n-2 \tag{4.94}$$

$$2\omega_\infty(L_n + M_{n-1}) = Z_n. \tag{4.95}$$

Together with (4.90) it becomes a non-linear system of equations, in general, providing multiple solutions, some of which will not be feasible. Once a solution is found, the remaining capacitances C_ν are obtained via the resonant frequency ω_∞ and total inductance of each resonator. A subsequent manual tuning of the circuit elements is mandatory to adjust the frequency response of the band-pass filter before calculating the lengths of transmission lines. The latter again is based on the equivalence between the input reactance of transmission line and lumped cir-

cuit resonator at design frequency. Note, the assumption of weak coupling permits each resonator to be considered independently. In the process of finding appropriate transmission lines, series capacitances C'_ν as shown in Fig. 4.31(a) may optionally be added to reduce their lengths. Finally, the coaxial waveguide filter is constructed from the specific transmission line model. The shunt inductances M_ν are realized as fixings between the inner and outer conductor, and adjusted by the non-linear fitting approach described in Sec. 4.1.1. Similarly, the optional series capacitances C'_ν which correspond to interruptions of the inner conductor in the coaxial guide, may be adjusted according to the procedures discussed in Sec. 4.1.2.

Although the fundamental mode will, in general, be outside the passband of the above described band-pass filter, its rejection is usually not sufficient in practice, particularly not for superconducting applications. A band-stop filter is added to achieve the desired suppression, typically realized as a mid-series ladder with the resonant frequency ω_0 given by the fundamental cavity mode. The so-called notch filter is either implemented as open-loop antenna as shown in Fig. 4.33, or by replacing one of the shunt inductances M_ν in Fig. 4.31 with a series LC resonator such that

$$\omega_0 = \frac{1}{\sqrt{L_0 C_0}}, \tag{4.96}$$

$$j\omega_\infty L_0 + \frac{1}{j\omega_\infty C_0} = j\omega_\infty M_\nu. \tag{4.97}$$

The latter option yields coaxial filter structures of the type discussed in Sec. 4.1.7.

It is important to note that the design procedure according to Haebel and Gerigk provides merely an initial geometry due to the various assumptions made in this approach: (i) The frequency pattern of the concerned HOM is reduced to a single

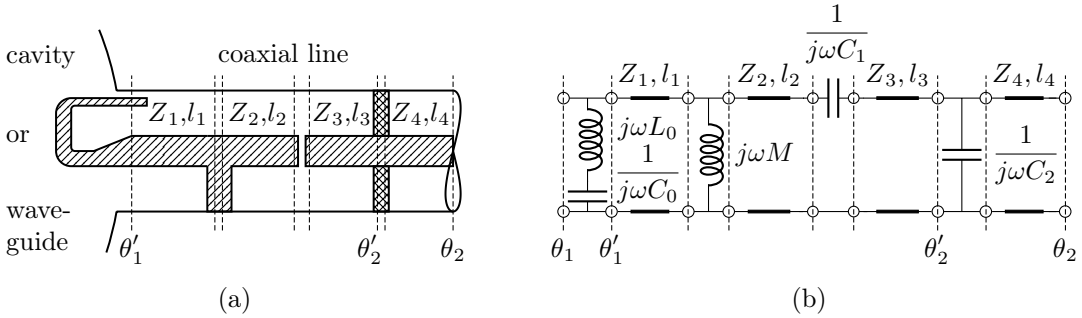

Fig. 4.33. Coaxial HOM coupler with an open-loop antenna to realize band-stop behavior at the fundamental mode frequency. (a) Longitudinal cross-sectional view of the waveguide filter and (b) equivalent circuit. The combination of shunt inductance M, series capacitance C_1, and transmission lines yields a band-pass filter adjusted to the concerned HOM frequency pattern. The shunt capacitance C_2 is introduced by the ceramic window at the terminal plane θ'_2.

frequency ω_∞ and coupling factor k to define the passband characteristics. Attenuation limits are not involved. (ii) The band-pass and band-stop filter for the high-order modes and fundamental mode, respectively, influence slightly. This interaction is not controlled during the design process. (iii) The resulting lengths l_ν are often too large for realistic implementations such that the assumption of weak coupling may get lost. (iv) As later discussed in Sec. 4.3.2, the combination of shunt inductance and mid-series ladder to provide a band-stop filter compromises the overall filter characteristics in both the stopband and passband. The resultant attenuation loss or increase within these frequency bands is not taken into account. (v) Weak conditions such as (4.92) do not imply approximation between the transmission line and lumped circuit model shown in Fig. 4.31. To conclude, subsequent rf design optimizations using numerical simulations are an essential addition to the method described above.

4.3.2 Topological Considerations

The design procedure of the previous section underlies a particular topology of the coaxial filter structure and associated equivalent circuit, that is a cascade of shunt inductances and transmission lines in combination with a mid-series ladder. Based on the observations in Sec. 4.1, a microwave filter which is given by a coaxial waveguide housing multiple obstacles, thus, providing various discontinuities, may equivalently be described by a generalized network as sketched in Fig. 4.34. It considers alternately uniform transmission lines and lumped lossless two-ports connected in a chain. Each discontinuity excites evanescent modes which correspond to the lumped lossless networks. Some of the evanescent modes will be able to extend their influence well to the neighboring obstacles. An example is the mid-shunt ladder between inductive posts, which is a result of the coupling between evanescent multipolar modes. Surprisingly, even in this case, the equivalent circuit is found to be a cascade of lumped lossless two-port networks and transmission lines in an alternating order according to Sec. 4.1.6. It is important to note that the topology depicted Fig. 4.34 is a result of the coaxial structures investigated in Sec. 4.1. It is by no means proven to be generally applicable. For instance, there has not yet been a study of the coupling between more than two inductive posts located relatively closely to each other so that evanescent modes may extend their impact over all discontinuities.

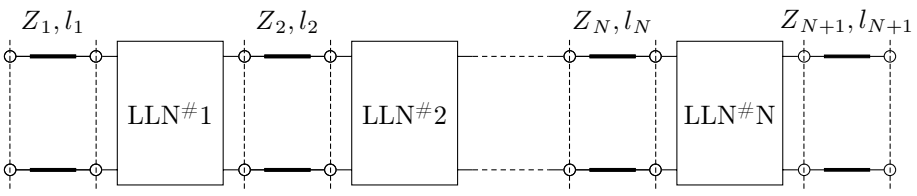

Fig. 4.34. Cascade of lossless lumped networks (LLN) and unit elements in alternating order.

Consequently, when combining the various discontinuities considered in Sec. 4.1, a sufficient distance must be assumed so that the particular equivalent circuits remain valid. Taking this restriction into account, the microwave structures introduced in Sec. 4.1 cover all basic reactive components which are important for the construction of high-pass filters on the basis of ladder networks.[4] The shunt inductance shown in Fig. 4.35(a) is realized as a fixing between the inner and outer conductor according to Sec. 4.1.1. The two-port network provides a transmission zero at the frequency of zero as the admittance function of the shunt arm provides a pole here. Likewise, the series capacitance shown in Fig. 4.35(b) is characterized by a transmission zero at vanishing frequency as the impedance function of the series arm provides a pole here. It is realized by a capacitive gap interrupting the inner conductor of the coaxial guide according to Sec. 4.1.2. The mid-series ladder shown in Fig. 4.35(c) may

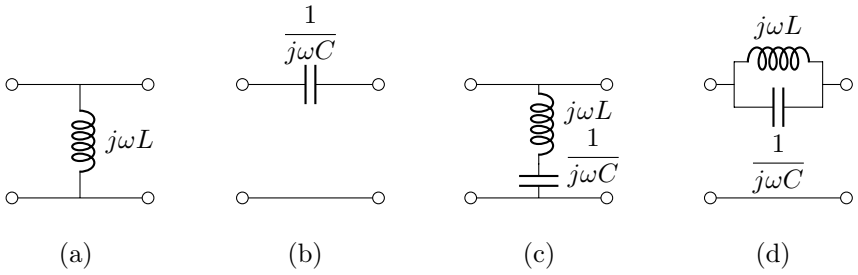

Fig. 4.35. Fundamental lumped two-port networks to construct high-pass filters in ladder configuration. The shunt inductance (a) and series capacitance (b) provide a transmission zero at the frequency of zero, each. The mid-series ladder (c) and mid-shunt ladder (d) reveal a conjugated complex pole pair of the shunt admittance or series impedance function, respectively. The associated transmission zero occurs at $\omega_0 = 1/\sqrt{LC}$, in both cases.

be realized by an inductive post in combination with a capacitive gap between inner and outer conductor of the coaxial guide. A combined consideration with shunt inductances as in Sec. 4.1.7 is not mandatory for the existence of a mid-series ladder. In contrast, the mid-shunt ladder shown in Fig. 4.35(d) occurs only in combination with enclosed shunt inductances regarding the coaxial microwave structure of Sec. 4.1.6. Note, an explicit implementation of a parallel LC resonator along the inner conductor of a coaxial line as proposed in [119] is not reasonable since shunt inductances are essential parts for the construction of high-pass filters. Similar to the mid-series ladder whose shunt arm yields an admittance function with a conjugated complex pole pair, the mid-shunt ladder provides an impedance function of the series arm with a conjugated complex pole pair. Consequently, the transmission zero occurs in both cases at finite nonvanishing frequency.

[4]HOM couplers may be realized as high-pass or band-pass filters with respect to concerned higher-order modes, or as band-stop filters with respect to the fundamental mode. For the same filter order, the first option yields the simplest of all networks with least number of lumped elements.

The literature offers numerous realizations of rational high-pass filter functions by lossless lumped networks [32–34]. It is important to note that these realizations only conditionally and approximately apply to coaxial microwave structures due to the presence of transmission lines in their equivalent circuits represented by Fig. 4.34. The shorter the transmission lines, the better is the approximation by a pure lossless lumped network. Nevertheless, the distance between discontinuities in the coaxial waveguide must be chosen sufficiently large so that equivalent circuits of individual sections remain valid. The following topologies of coaxial microwave filters and associated equivalent circuits are motivated by canonical realizations of rational high-pass filter functions by means of lumped lossless ladder networks. The synthesis of filter functions by lumped elements is outlined in Sec. 2.1.4 and further discussed in subsequent sections. It is worthwhile to note that there is no nearly complete theory on the synthesis of filter functions by general networks comprising lumped and distributed elements [25, p. 18]. However, some classes of lumped distributed ladder networks, mostly assuming unit elements of the same one-way delay, have been investigated significantly, in [38, 120, 121] among others.

The simplest form of a lossless lumped high-pass filter is realized by alternately applying shunt inductances and series capacitances in a chain [34, pp. 137, 151]. Each element introduces a transmission zero at the frequency of zero, thus increments the filter order by one. Typical examples are *maximally flat filters* also known as *Butterworth filters*, or the *Chebyshev filters* with equiripple behavior in the passband [31]. Approximate realizations of such rational filter functions may be achieved by coaxial microwave structures of the type sketched in Fig. 4.36 together with the equivalent circuits of each segment. Shunt inductances and series capacitances are, respectively, realized as inductive posts and capacitive gaps according to the studies of Secs. 4.1.1 and 4.1.2. Following the results of Sec. 4.1.6, subsequent fixings are

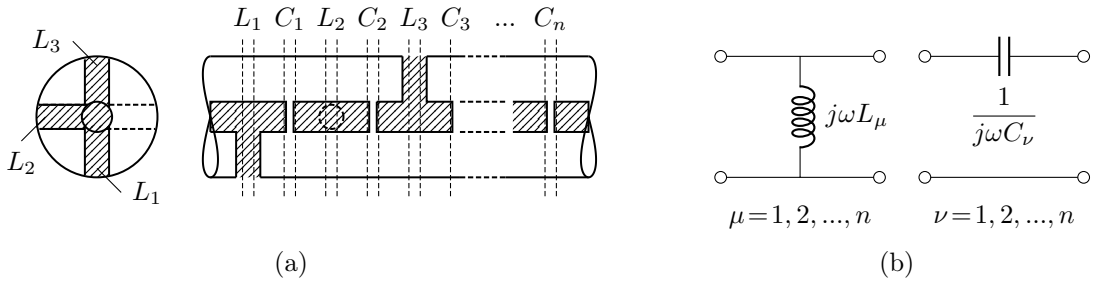

Fig. 4.36. (a) Cross-sectional and side view of a coaxial waveguide filter with high-pass characteristics using shunt inductances and series capacitances. (b) Equivalent circuits of the inductive posts and capacitive gaps, respectively, represented by a shunt inductance and series capacitance two-ports. They occur in alternating order according to the discontinuities in the coaxial guide, and are separated by transmission lines as illustrated in Fig. 4.34 to account for the waveguide sections in between discontinuities. Subsequent inductive posts are rotated by $\geq 90\,\text{deg}$ against each other in the transverse plane in order to suppress coupling between them.

rotated by $\alpha_{\text{fix}} \geq 90\,\text{deg}$ in the transverse plane in order to suppress possible coupling which may introduce a finite inductance connected in parallel to the capacitances C_ν. Note, for a sufficiently large rotation angle α_{fix}, the implied inductance becomes infinite as deduced from Sec. 4.1.6. However, these empirical studies are based on the presence of only two inductive posts. Indeed, the equivalent circuits in Fig. 4.36 apply well to the different sections of the microwave structure if it is terminated after the capacitance C_2, yielding the equivalent behavior of a fourth-order high-pass filter. The structure could likewise start with capacitive gap before L_1, to increase the order to five. However, if more than two inductive posts are applied, the frequency response, in particular, in the stopband is not well approximated by considering merely series capacitances and shunt inductances between uniform transmission lines for the equivalent circuit. Transmission zeros at finite, nonzero frequency may occur despite a rotating angle of $\alpha_{\text{fix}} = 90\,\text{deg}$ between subsequent inductive posts. Although they may be shifted to zero by increasing the angle to $\alpha_{\text{fix}} = 180\,\text{deg}$, the stopband characteristics of the resultant microwave structure notably differs from the asymptotic behavior of the anticipated rational filter function. As a consequence, the equivalent circuit, if any, will be applicable only in the vicinity of the cutoff frequency. In practice, appropriate filter functions should be restricted to the fifth-order to allow for a synthesis using the topology shown in Fig. 4.36(a), with the discontinuities being sufficiently represented by shunt inductances or series capacitance according to Fig. 4.36(b).

The selectivity[5] of high-pass filters can be further increased by placing some of the transmission zeros at finite, nonvanishing frequency below the cutoff. An example is the *elliptic filter* also known as *Cauer filter* which provides equiripple behavior in both the stopband and passband [31] by placing all but one transmission zeros at finite, nonzero frequencies. Two types of canonical realizations using lumped ladder networks are very common in the literature for such filter functions, and further discussed in the following with the focus solely on odd-order filter functions. The reason is that the associated transfer function of even-order filter functions according to (2.45) requires additional frequency mapping, so that an asymptotic damping towards vanishing frequency is ensured. Note, this is a necessary condition for a high-pass filter function to be realizable by lumped elements. Some frequency maps are discussed, for instance, in [31].

The first canonical realization of odd-order high-pass filter functions with all but one transmission zeros at finite, nonvanishing frequency, consists of shunt inductance two-ports and mid-shunt ladders as shown in Figs. 4.35(a) or (d), respectively. The elements connected in a chain occur in alternating order, with a shunt inductance being located at either extremity. One of them yields the transmission zero at the frequency of zero, and thus contributes to the filter order as stated by Property 2.1.2.

[5]Selectivity refers to the transition between stopband and passband. An increase in selectivity means that the frequency region of the transition becomes smaller. It is closely related to the quality factor of resonators (2.91).

The remaining shunt inductances shift zeros of partial admittance functions as described in Sec. 2.1.4 and referring to Property 2.1.4. The transmission zeros at finite, nonvanishing frequency are introduced by the mid-shunt ladders, each increasing the filter order by two according to Property 2.1.3. Such a lumped circuit realization may be translated into a coaxial microwave structure as sketched in Fig. 4.37(a). It is considered as an approximate realization of the original filter function within a limited frequency range. The latter is defined by the validity range of the equivalent circuits shown in Fig. 4.37(b) to represent discontinuities within the microwave structure. Remarkably, the difference to the previous topology shown in Fig. 4.36 is given by the rotating angle α_{fix} between subsequent inductive posts in the transfer plane. Empirically, they must be rotated by $\alpha_{\text{fix}} < 90\,\text{deg}$ so that evanescent multipolar modes excited by neighboring inductive posts may couple to each other. Note, this coupling is essential for the mid-shunt ladder being an equivalent circuit. In particular, its inductance $L_{0\nu}$ shown in Fig. 4.37(b) is significantly influenced by the rotating angle as Fig. 4.19(d) illustrates. Alternatively to the coaxial filter structure shown in Fig. 4.37(a), the chain may begin or end with a capacitive gap interrupting the inner conductor of the coaxial guide. This would correspond to a pure series capacitance yielding an additional transmission zero at vanishing frequency. Consequently, the resultant high-pass filter is of even order.

The second canonical realization of odd-order high-pass filter functions with all but one transmission zeros at finite, nonzero frequencies, consists of series capacitance two-ports and mid-series ladders as shown in Figs. 4.35(b) and (c), respectively. The elements connected in a chain occur in alternating order with a series capacitance located at either extremity. One of them yields the transmission zero at vanishing frequency, thus contributes to the filter order as stated by Property 2.1.2. The re-

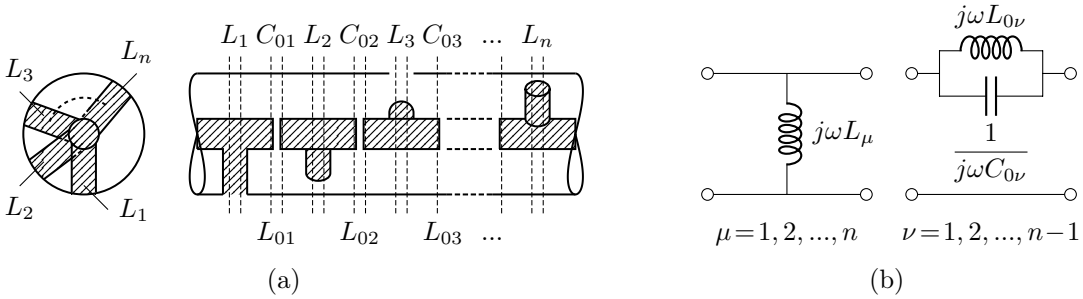

Fig. 4.37. (a) Cross-sectional and side view of a coaxial waveguide filter with high-pass characteristics using mid-shunt ladders. (b) Equivalent circuits of inductive posts and capacitive gaps in between inductive posts, respectively, represented by a shunt inductance two-port and mid-shunt ladder. The lumped networks occur in alternating order according to discontinuities in the coaxial guide and are separated by transmission lines as illustrated in Fig. 4.34 to account for the waveguide sections in between discontinuities. Subsequent inductive posts are rotated by specific angles against each other in the transverse plane in order to control the coupling of evanescent multipolar modes, and thus the inductances $L_{0\nu}$.

maining series capacitances shift zeros of partial impedance functions as described in Sec. 2.1.4 and referring to Property 2.1.4. The transmission zeros at finite, nonvanishing frequency are introduced by the mid-series ladders, each increasing the filter order by two according to Property 2.1.3. Such a lumped circuit realization may be translated into a coaxial microwave structure as sketched in Fig. 4.38(a). It is considered as an approximate realization of the original filter function within a limited frequency range. The latter is defined by the validity range of the equivalent circuits shown in Fig. 4.38(b) to represent discontinuities within the microwave structure. The capacitive gaps along the inner conductor of the coaxial guide correspond to the series capacitances while the characteristic transmission behavior of mid-series ladders results from inductive posts attached to the inner conductor. They are separated from the outer one by small capacitive gaps. Similar as for the first topology, the inductive posts are rotated against each other by $\alpha_{\text{fix}} \geq 90\,\text{deg}$ in the transverse plane in order to suppress coupling between them. Alternatively to the coaxial filter structure shown in Fig. 4.38(a), the chain may begin or end with an inductive post connecting inner and outer conductor of the coaxial guide. This would correspond to a pure shunt inductance yielding an additional transmission zero at vanishing frequency. The resultant high-pass filter is of even order.

The topologies of Figs. 4.36, 4.37 and 4.38 cover by no means all conceivable implementations of high-pass filters. They offer some conceptional ideas for coaxial structures with a minimal number of elements or discontinuities. It is obvious that microwave filters resting upon the third topology in Fig. 4.38(a) are not suitable for superconducting HOM couplers since the coaxial waveguide is not filled with solid dielectric material which can hold the electrically isolated pieces of the inner conductor. In contrast, microwave filters based on either of the topologies shown

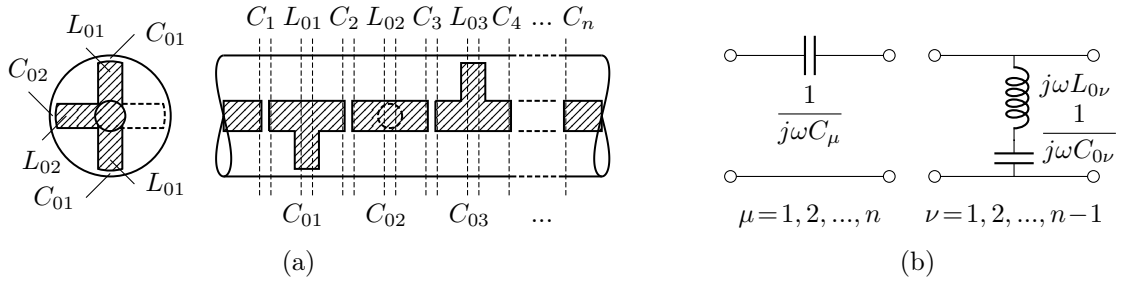

Fig. 4.38. (a) Cross-sectional and side view of a coaxial waveguide filter with high-pass characteristics using mid-series ladders. (b) Equivalent circuits of capacitive gaps along the inner conductor and inductive posts separated from the outer conductor of the coaxial guide, respectively, represented by a series capacitance two-port and mid-series ladder. The lumped networks occur in alternating order according to discontinuities in the coaxial guide and are separated by transmission lines as illustrated in Fig. 4.34 to account for the waveguide sections in between discontinuities. Subsequent inductive posts are rotated by 90 deg against each other in the transverse plane in order to suppress coupling between them.

in Figs. 4.36(a) and 4.37(a), are suitable candidates. Moreover, the explicit implementation of mid-series ladders in coaxial structures is very much restricted by reasonable dimensions of the inductive posts whereas both capacitance and inductance of the equivalent mid-shunt ladder may be varied over wide ranges according to the results of Sec. 4.1.6. It is worth noting that the microwave filters introduced above should not be confused with reactance-coupled $\lambda/2$ resonators using additional capacitance to reduce their lengths [113, pp. 528]. Such structures provide band-pass characteristics. They are not able to provide transmission zeros at finite, nonvanishing frequency.

Furthermore, it is possible to combine mid-shunt and mid-series ladders by inserting shunt inductance or series capacitance as demonstrated in [32, p. 243]. However, such combinations are likewise unsuitable candidates for the design of HOM couplers as they require solid dielectric material to hold electrically isolated pieces of the inner conductor. Some prototypes discussed in Chapter 5 indeed provide combinations of equivalent mid-shunt and mid-series ladders. However, additional fixings are introduced or capacitive gaps removed to avoid floating elements. These arrangements, in turn, compromise the filter characteristics which may be referred to as pseudo-high-pass behavior. Two examples are depicted in Fig. 4.39. Though it is common for designing HOM couplers, the implementation of a mid-series ladder in combination with a shunt inductance is unsuitable for the synthesis of high-pass filter functions. To illustrate this, the simplified circuit of Fig. 4.39(a) shall be considered. Its dual network shown in Fig. 4.39(b) is less relevant for HOM couplers, but is mentioned for completeness. The networks constitute the only two-combinations from the set of basic two-ports given in Fig. 4.35, which reveal pseudo-high-pass characteristics. Disregarding the transmission line, the network shown in Fig. 4.39(a) admits an open-circuit impedance matrix whose elements may be directly derived from (2.27), and are given as

$$z_{11} = z_{12} = z_{21} = z_{22} = j\omega L_1 \frac{\omega_\infty^2}{\omega_0^2} \frac{(\omega_0^2 - \omega^2)}{(\omega_\infty^2 - \omega^2)}, \tag{4.98}$$

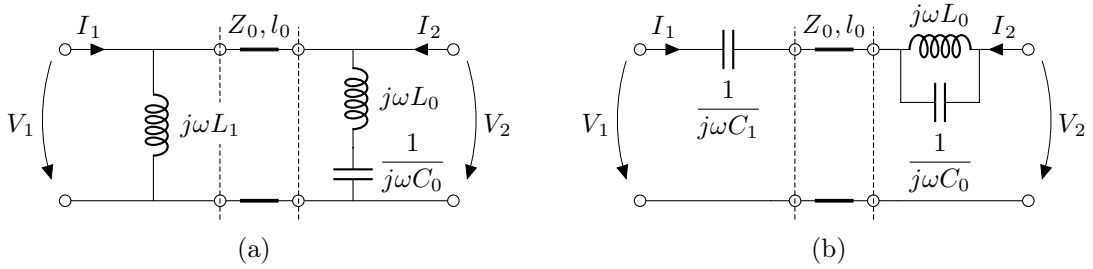

Fig. 4.39. (a) Cascade of a shunt inductance and mid-series ladder separated by a unit element of characteristic impedance Z_0 and length l_0. (b) Cascade of a series capacitance and mid-shunt ladder likewise separated by a unit element.

where $\omega_0 = 1/\sqrt{L_0 C_0}$ corresponds to the resonant frequency of the LC resonator which causes a transmission zero while $\omega_\infty = 1/\sqrt{(L_0 + L_1)C_0}$. Similarly, the network shown in Fig. 4.39(b) without transmission line admits a short-circuit admittance matrix whose elements may be derived from (2.26), and are given as

$$y_{11} = -y_{12} = -y_{21} = y_{22} = j\omega C_1 \frac{\omega_\infty^2}{\omega_0^2} \frac{(\omega_0^2 - \omega^2)}{(\omega_\infty^2 - \omega^2)}, \tag{4.99}$$

with the same expressions for ω_0 and ω_∞ as before. Note, the zeros of z_{21} and y_{21} generally equal the zeros of the scattering function s_{21}, provided they are rational as discussed in Sec. 2.1.4. Furthermore, from (2.49) and (2.50), it follows that the common pole of the impedance and admittance functions in (4.98) or (4.99), respectively, equals the frequency where s_{21} becomes unity. Hence, ω_∞ corresponds to the angular frequency of maximum power transfer. Such frequencies are also referred to as *transmission poles* [26, pp. 196]. It goes without saying that

$$\omega_0 > \omega_\infty. \tag{4.100}$$

This property contradicts the natural requirement of high-pass filter functions, that is all transmission zeros are above a desired cutoff frequency while the transmission poles remain below. The presence of the transmission line does not change the general validity of (4.100) as shown in Fig. 4.40 by means of an example for the shunt inductance in combination with a mid-series ladder. However, ω_∞ reduces with increasing length of the transmission line while $|s_{21}(\omega_\infty)| < 1$, though ω_∞ remains as a local maximum for the power transfer. Referring to the transmission power gain

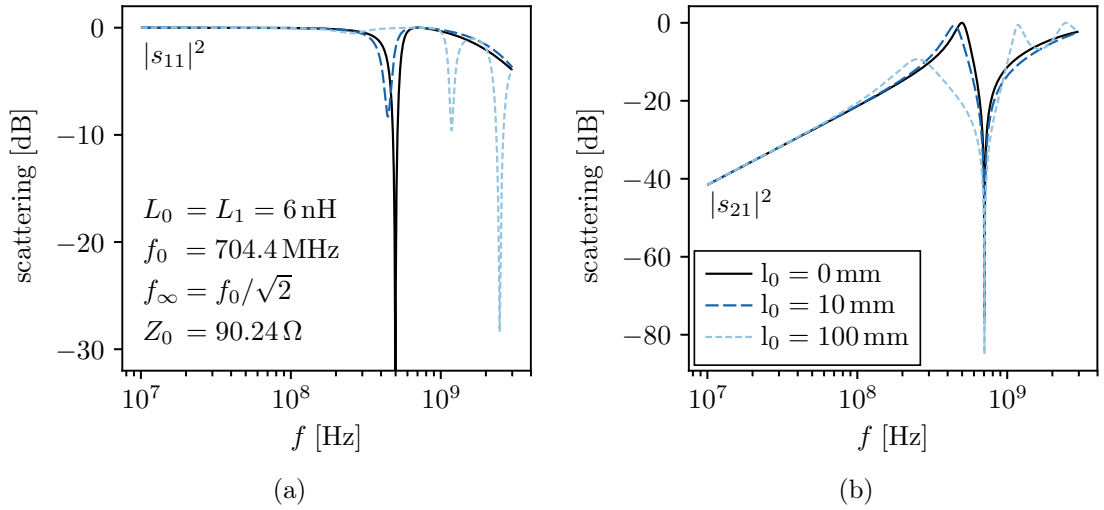

Fig. 4.40. (a) Reflected and (b) transmitted power gain for an example of the circuit in Fig. 4.39(a), with length of the unit element between shunt inductance and mid-series ladder being varied.

depicted in Fig. 4.40(b), the microwave network of Fig. 4.39(a) provides a similar behavior as a first order high-pass filter. This is seen from the asymptotic decrease of 20 dB per decade towards lower frequencies below 100 MHz. For comparison, a much simpler network merely consisting of a shunt inductance and series capacitance yields already a second order high-pass filter. The mid-series ladder in Fig. 4.39(a) introduces band-stop characteristics which, however, due to (4.100) reside in the passband of the original intended first order high-pass filter. The consequence is a sharp notch with very small bandwidth on one side and an increased insertion loss in the passband of the resultant pseudo-high-pass filter on the other side. In particular, the first property is often claimed as problematic for HOM couplers, since bad tuning of the notch frequency may cause too much coupling to the fundamental mode of the cavity, such that the coupler may overheat [115].

An example of pseudo-high-pass filters is the TESLA HOM coupler whose simplified equivalent circuit is shown in Fig. 4.41(a). Transmission lines are not included in the model which is taken from [116, p. 101]. The capacitance C_1 accounts for the capacitively coupled feedthrough and C_2 for the capacitance introduced by the ceramic window. The transmission power gain as measured from the antenna to load R_L appears very similar to Fig. 4.40(b). Merely the order of the pseudo-high-pass filter is increased, due to the presence of C_1 which introduces another transmission zero at vanishing frequency. Nonetheless, condition (4.100) is conserved. The same is true for the example shown in Fig. 4.33 and many other HOM coupler designs [101, 114, 122]. Likewise, the prototypes considered in Chapter 5 suffer from the combination of an equivalent mid-series ladder and shunt inductance. Note, the reason for implementing mid-series ladders is the ease to tune their resonant frequency while the shunt inductances are primarily a result of mechanical and thermal needs. Therefore, the combination of both parts often appears to be inevitable.

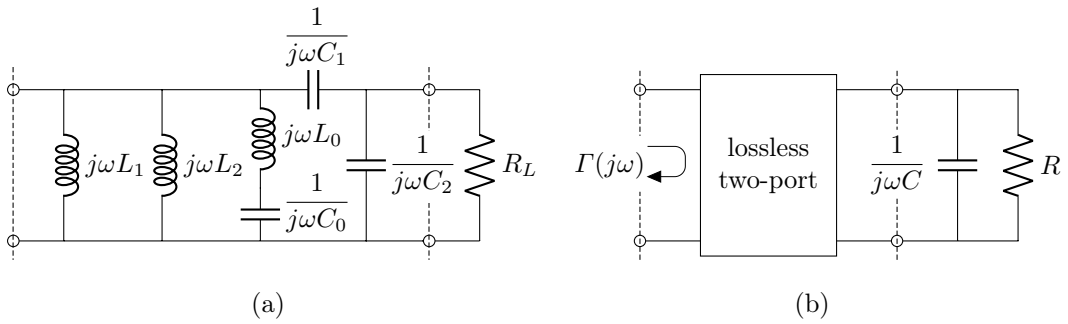

Fig. 4.41. (a) Simplified impedance model of the TESLA HOM coupler without transmission lines [116, p. 101]. The impedance seen from the left terminal pair towards the load R_L corresponds to the input impedance seen from the antenna towards the coaxial output. (b) Generalized impedance model for an HOM coupler. The high-pass characteristics is introduced by the lossless two-port which may contain any of the elements shown in Fig. 4.35 as well as transmission lines according to Fig. 4.34. The shunt capacitance of (a) is considered as part of the load.

Another undesired behavior in the frequency response of coaxial HOM couplers is due to the ceramic window used as a vacuum barrier [101, p. 41]. This part requires particular attention in the rf design as it may significantly impact the passband behavior. Typically, the dielectric material provides relative permittivity numbers of $\varepsilon_r > 9$, thus introduces a measurable capacitance between the inner and outer conductor of the coaxial guide, and is accounted by a shunt capacitance in the equivalent circuits as shown, for instance, in Figs. 4.41. However, a shunt capacitance is not appropriate for the implementation of high-pass filters as it involves a transmission zero at infinite frequency. Eventually, the shunt capacitance limits the bandwidth of the filter according to the *Bode-Fano Criterion* [123], [41, pp. 267]. By referring to Fig. 4.41(b), let the high-pass characteristics of the HOM coupler be described by a linear, lossless, passive, and time-invariant two-port without specifying its internal structure. It may contain any of the networks shown in Fig. 4.35 as well as unit elements according to Fig. 4.34. The shunt capacitance associated with the ceramic window is considered as part of the load. Assuming no other capacitance connected in parallel, the Bode-Fano criterion states that

$$\int_0^\infty \ln \frac{1}{|\Gamma(j\omega)|} d\omega \leq \frac{\pi}{RC} \tag{4.101}$$

where $\Gamma(j\omega)$ is the reflection coefficient seen from the input of the filter towards the load. Note, if the source impedance equals the reference impedance of the input port, the reflection coefficient becomes the scattering function $s_{11}(j\omega)$ according to (2.40). Condition (4.101) implies that the reflection cannot vanish over an arbitrarily wide frequency range in the passband of the high-pass filter. A larger shunt capacitance yields more reflection within the passband. Consequently, the goal must be to reduce the capacitance involved by the ceramic window as much as possible.

4.3.3 Equivalent Circuit Synthesis

Using the results of Sec. 4.1 and the topological considerations of the previous section, a first attempt of synthesis based on the insertion loss method is presented. Unlike the design approach by Haebel and Gerigk resting on two frequencies being independently treated in terms of transmission or rejection, a prescribed attenuation over the entire interesting frequency range is taken as the basis. Thus, the different treatments of the fundamental mode and high-order modes are covered by an approximation problem. In addition to these specific frequencies, the anticipated filter response may further be specified by attenuation limits for the stopband and passband. Referring to Fig. 2.6, let a linear, lossless, passive, and time-invariant two-port be inserted between a source and load characterized by the resistances R_1 or R_2, respectively. The first may correspond to a mode specific radiation resistance of the antenna while the latter may be considered as the characteristic impedance of the coaxial cable at the output of the HOM coupler. Then, the insertion loss given

in units dB is calculated as [34, p. 63],

$$\alpha = -10 \log |s_{21}(j\omega)|^2 = -10 \log 4 \frac{R_1}{R_2} |H(j\omega)|^2 \tag{4.102}$$

using either the transmission power gain $|s_{21}(j\omega)|^2$ or, via (2.44), the squared magnitude of the transfer function $|H(j\omega)|^2$. Both are defined on the imaginary axis in the complex s-plane introduced in (2.2). Note, the transfer function $H(s)$ defined in the entire complex plane is the analytic continuation of $H(j\omega)$ similar to (2.53). Likewise, $s_{21}(s)$ corresponds to the analytic continuation of $s_{21}(j\omega)$. Regarding the frequency response of a high-pass, attenuation thresholds may be defined as [26, pp. 197]

$$\alpha(\omega) \geq \alpha_{\min}, \text{ if } \quad 0 \leq \omega \leq \omega_s, \tag{4.103}$$

$$\alpha(\omega) \leq \alpha_{\max}, \text{ if } \omega_p \leq \omega \leq \infty, \tag{4.104}$$

where ω_s and ω_p are the edge frequencies of the stopband or passband, respectively, provided $\omega_s < \omega_p$ and $\alpha_{\min} > \alpha_{\max}$. Figure 4.42 illustrates the insertion loss of a transfer function with one transmission zero at finite, nonzero frequency, which corresponds to a conjugated complex pair, and two real zeros at $\omega = 0$. A more intuitive expression provides the filter function $D(s)$ according to the definition (2.45), since its zeros and poles are entirely located on the imaginary axis, and correspond to the frequencies at which the insertion loss becomes infinite or vanishes, respectively. Referring to the example in Fig. 4.42, the filter function may be written as

$$D(s) = c_1 \frac{(s^2 + \omega_{\infty 1}^2)(s^2 + \omega_{\infty 2}^2)}{s^2 (s^2 + \omega_{01}^2)}, \tag{4.105}$$

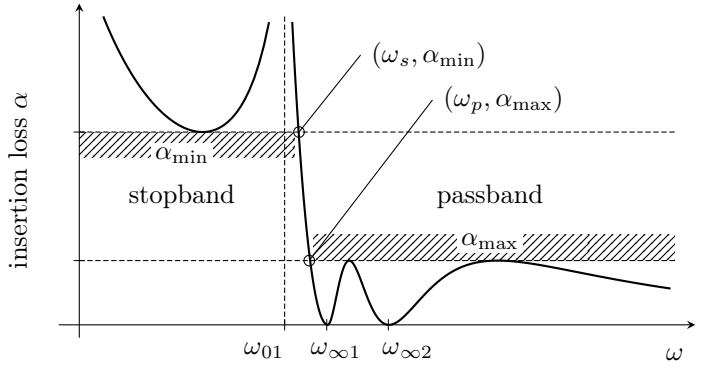

Fig. 4.42. Insertion loss of a high-pass filter as function of the angular frequency. The attenuation limits in the stopband and passband according to (4.103) and (4.104) are highlighted. The corresponding transfer function provides zeros at $s = \pm j\omega_{01}$ and twice at $s = 0$.

where c_1 is a real constant determined by the attenuation limit in the passband. For the design of an HOM coupler, it is obvious to choose ω_{01} as the fundamental mode frequency, so that the filter provides purely imaginary input impedance at this frequency and ideally no power is transmitted. In contrast, the frequencies $\omega_{\infty 1}$ and $\omega_{\infty 2}$ may be located in the vicinity of those HOMs which are particularly of concern. The transition region which refers to the distance between the stopband and passband edges ω_s, ω_p, depends on the attenuation thresholds according to (4.103)–(4.104), and order of the rational filter function in (4.105). In other words, the distance of the first concerned HOM from the fundamental mode frequency specifies the filter order as the transition region reduces with increasing order. The theoretical limit for the transition region at a given order is discussed in Sec. 4.3.4.

Following the procedure described in Sec. 2.1.4, the rational filter function is realized as a lumped lossless network whose structure is directly seen from the poles in (4.105). A suitable canonical network is shown in Fig. 4.43(a). Each real pole or conjugated complex pole pair corresponds to a transmission zero of the network. By referring to Property 2.1.3, the conjugated complex pole pair at $s = \pm j\omega_{01}$ is introduced by the mid-shunt ladder with $\omega_{01} = 1/\sqrt{L_{01}C_{01}}$. Prior to this, either of the shunt inductance L_1 or L_2 is considered to shift the zero of the particular partial admittance function to ω_{01} according to Property 2.1.4. The remaining shunt inductance as well as series capacitance C_2 yield the two transmission zeros at $s = 0$ according to Property 2.1.2. Consequently, the high-pass filter is of fourth order, as already expected from the filter function (4.105).

The idea is to approximate the frequency response of the derived lumped circuit by a generalized network which likewise serves as an equivalent circuit for a coaxial microwave structure. According to Sec. 4.3.2, shunt inductances, series capacitance, and mid-shunt ladder may be associated with certain discontinuities in a coaxial guide. However, they need to be separated by transmission lines in order to account for the waveguide sections in between. The resultant generalized network of the considered example is shown in Fig. 4.43(b). It may equally describe the scattering properties of a coaxial filter with the topology shown in Fig. 4.37, assuming that

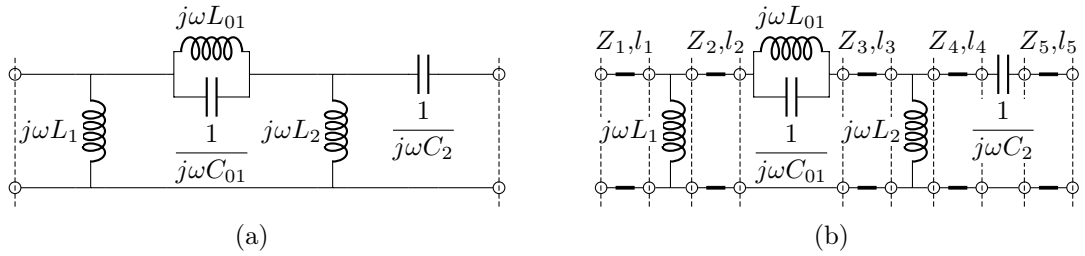

Fig. 4.43. (a) Lumped network realization of the filter function $D(s)$ as given in (4.105) with one transmission zero at finite, nonzero frequency and two at zero. (b) Equivalent circuit of a corresponding coaxial microwave structure as an approximate realization of the same filter function.

the cascade of discontinuities terminates after the second capacitive gap which provides C_{02}. Note, the inductance L_{02} becomes infinite due to the missing subsequent inductive post. Finally, the methods discussed in Secs. 4.1.2 and 4.1.6 are used to adjust all discontinuities in the coaxial guide. The characteristic impedance of each waveguide section is specified beforehand. In particular, the characteristic impedances of the first and last section must equal the source or load resistance R_1, R_2, respectively, to not introduce additional reflections due to impedance mismatch.

In the current stage of development, no systematic correction of the lumped circuit elements due to the presence of transmission lines is taken into account. This is beyond the present treatise. Notwithstanding, towards vanishing distances between discontinuities along the microwave structure, hence if $l_2, l_3, l_4 \to 0$, it is obvious that such corrections become marginal. The question is, how small these distances can be made, keeping in mind that the equivalent circuit must remain valid. To answer this question, the impact of transmission lines on the frequency response of some practical examples is analyzed in the subsequent section.

4.3.4 Elliptic Filters

Elliptic filters are based on rational functions with equiripple behavior in both the stopband and passband. Given a minimum required insertion loss in the stopband and a corresponding maximum acceptable value in the passband, equiripple rational functions yield the steepest transition, thus, filters with largest selectivity. It is important to note that this is true for rational functions of fixed order, being realized with a finite number of lumped circuit elements. Analytical methods to involve transmission lines in the realizations are limited to special cases, for instance, using unit elements of a unique one-way delay [121]. Disregarding transmission lines in the equivalent circuits of microwave filters as discussed in Sec. 4.3.2, the design procedure introduced in the previous section will be drawn by means of two examples, each providing quasi-elliptic filter characteristics. The impact of transmission lines is studied independently of the synthesis in order to discuss the needs for eventual improvements of the latter one.

As common in filter theory, the design originates from a normalized low-pass filter. For this purpose, let the complex frequency $s = \sigma + j\omega$ be transformed with respect to the geometric mean of the stopband and passband edges according to

$$p = \Sigma + j\Omega = \frac{\sqrt{\omega_p \omega_s}}{\sigma + j\omega} = \frac{\sqrt{\omega_p \omega_s}}{\sigma^2 + \omega^2}(\sigma - j\omega), \tag{4.106}$$

Note, the frequency mapping conserves the positive real characteristic of impedance and admittance functions as discussed in Sec. 2.1.1. Though, strictly speaking not

correct but more convenient, let the imaginary parts be related as

$$\Omega = \frac{\sqrt{\omega_p \omega_s}}{\omega}, \tag{4.107}$$

keeping in mind that the positive $j\omega$ axis maps onto the negative axis and vice versa. The filter function of a normalized elliptic low-pass of odd order n admits the form [31]

$$D(p) = c_1 p \prod_{\nu=1}^{(n-1)/2} \frac{p^2 + \Omega_{\infty\nu}^2}{\Omega_{\infty\nu}^2 p^2 + 1}, \tag{4.108}$$

where $n = 3, 5, 7, \ldots$. Apart from the zero at vanishing frequency, the reciprocal of each finite zero corresponds to a pole according to

$$\Omega_{0\nu} = \frac{1}{\Omega_{\infty\nu}}. \tag{4.109}$$

This relationship, also known from *Zolotarev functions*, is a necessary condition for the equiripple behavior [34, p. 65]. That is all minima of attenuation in the stopband are equal. Likewise, all maxima of attenuation in the passband are equal as shown in Fig. 4.44 by means of a fifth-order elliptic low-pass filter. The zeros are calculated by Jacobian elliptic sine functions as

$$\Omega_{\infty\nu} = k \,\mathrm{sn}\left(2\nu K/n, k\right), \tag{4.110}$$

where K is the complete elliptic integral of the first kind with the modulus $k = \Omega_s^{-2}$,

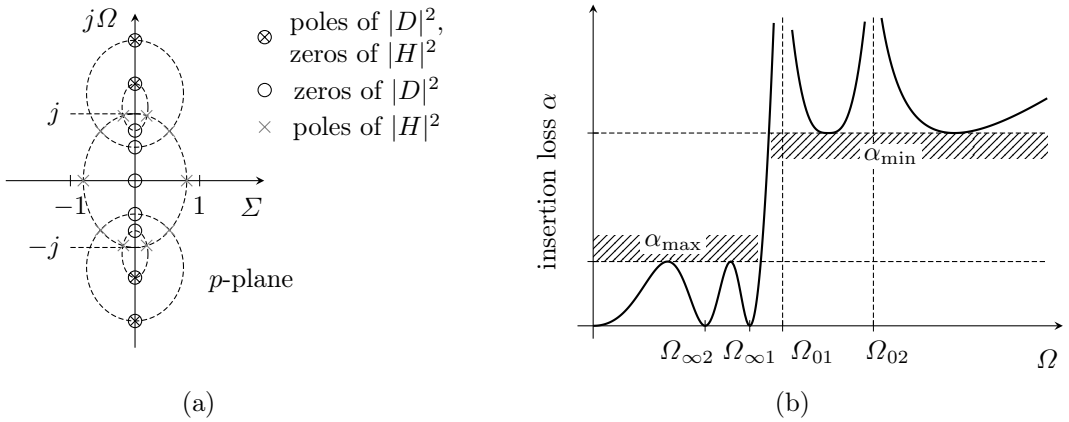

Fig. 4.44. Characteristics of a fifth-order elliptic low-pass filter. (a) The pole and zero distribution of the filter function D and corresponding transfer function H. (b) Sketch of the insertion loss with equiripple behavior in both, the pass- and stopband. Characteristic frequencies of zero and infinite attenuation $\Omega_{0\nu}, \Omega_{\infty\nu}$, are highlighted together with the maximum acceptable attenuation in the passband $\alpha_{\max}$ and the minimum required attenuation in the stopband $\alpha_{\min}$.

and may be written as

$$K = K(k) = \int_0^{\frac{\pi}{2}} \frac{d\vartheta}{\sqrt{1 - k^2 \sin^2 \vartheta}} \tag{4.111}$$

The factor c_1 in (4.108) is specified by the maximum acceptable insertion loss in the passband $a_{\max}$. Detailed design formulas as well as the minimum filter order to satisfy the predefined attenuation threshold in the stopband, $a_{\min}$, are given in A.3.

Two examples will be considered in the following. The first one, a third-order high-pass filter, is designed for an attenuation of at least 30 dB below 0.787 GHz. Above the passband edge frequency of 1.191 GHz, a maximum attenuation of 3 dB is tolerated. Note, the frequencies are chosen such that a transmission zero occurs at 0.704 GHz while the maximum power transfer is achieved at 1.331 GHz. The first corresponds to the frequency of the fundamental mode and the latter corresponds to the frequency of the dominant higher-order mode, both with respect to the high-β SPL cavity. With the same intention of having the minimum and maximum power transfer at the particular mode frequencies, a fifth-order high-pass filter is designed for an attenuation of at least 60 dB below 0.734 GHz. Above the passband edge frequency of 1.276 GHz, a maximum attenuation of 3 dB is tolerated. For convenience, the source and load resistances R_1 and R_2 are chosen to be equal. The value of 90.24 Ω results from the characteristic impedance of a coaxial line according to (2.67), provided the diameters of inner and outer conductor are 10 mm and 45 mm, respectively. Note, these are realistic dimensions for SPL HOM couplers.

As in the previous section, the topology of the lumped network is directly seen from the filter function given in (4.108). The frequency mapping according to (4.107) merely swaps and scales the passband and stopband frequency regions. Transmission zeros are transformed into transmission poles and vice versa. In particular, the pole at infinity in (4.108) becomes a transmission zero at $s = 0$. Figure 4.45 shows suitable canonical network realizations of the third- and fifth-order elliptic filter function $D(p)$, with the normalized complex frequency variable being mapped onto the s-plane according to (4.106). Each real pole or conjugated complex pole pair of $D(s)$

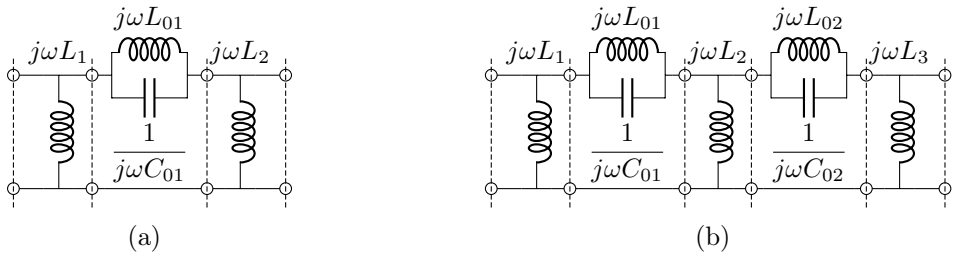

Fig. 4.45. Canonical lumped network realizations of filter functions each of the form (4.108) taking into account (4.106), i. e. the frequency map. (a) Third-order and (b) fifth-order high-pass filter.

corresponds to a transmission zero of the network. Only one shunt inductance yields the transmission zeros at $s = 0$ while the mid-shunt ladder tuned by remaining shunt inductances, causes the transmission zeros at finite, nonvanishing frequency. The resulting lumped circuit parameters are summarized in Table 4.3 for both examples. Calculations are outlined in Sec. A.4.

Table 4.3. Circuit parameters and approximations of different high-pass realizations.

parameter	unit	third-order elliptic filter[†]		fifth-order elliptic filter[‡]	
		lumped	equivalent	lumped	equivalent[§]
L_1	[nH]	4.190	4.274	3.680	3.698
L_{01}	[nH]	18.730	17.822	22.922	23.187
C_{01}	[pF]	2.727	2.761	2.228	2.232
L_2	[nH]	4.190	4.274	2.816	2.834
L_{02}	[nH]			61.474	61.074
C_{02}	[pF]			1.952	1.954
L_3	[nH]			3.388	3.369

[†] Specifications are $f_s = 0.787\,\mathrm{GHz}$, $\alpha_{\min} = 30\,\mathrm{dB}$, $f_p = 1.191\,\mathrm{GHz}$, $\alpha_{\max} = 3\,\mathrm{dB}$, $R_1 = R_2 = 90.24\,\Omega$.
[‡] Specifications are $f_s = 0.734\,\mathrm{GHz}$, $\alpha_{\min} = 60\,\mathrm{dB}$, $f_p = 1.276\,\mathrm{GHz}$, $\alpha_{\max} = 3\,\mathrm{dB}$, $R_1 = R_2 = 90.24\,\Omega$.
[§] Element values are derived from two partial networks, each consisting of one mid-shunt ladder and the neighboring shunt inductances according to Sec. 4.1.6.

By inserting a uniform transmission line at each dashed highlighted terminal pair in Fig. 4.45, the resulting networks may be considered as equivalent circuits of coaxial microwave structures, provided the topology sketched in Fig. 4.37 applies. Depending on the length and characteristic impedance, the impact of such distributed elements on the intended frequency response, that is the frequency response of the original lumped network, can be very different. Some arbitrary examples are shown in Fig. 4.46 assuming unit elements of identical characteristic impedance and length. It is difficult to predict the impedance of each coaxial section in between the discontinuities of the microwave structure without numerical simulations. The studies carried out in Sec. 4.1.6 reveal resistances which are generally below the analytical value obtained from (2.67). One explanation might be reactance coupling between the transmission line and adjoined inductive post as discussed in Sec. 4.1.5. From Figs. 4.16(a) and 4.17(a), it may be deduced that the effective impedance of the concerned unit elements approaches zero as their length becomes smaller.

In general, inserting unit elements in the lumped networks of Fig. 4.45 as described before will cause larger attenuation at some frequencies within the passband such that the intended threshold values $\alpha_{\max}$ cannot be guaranteed anymore. Characteristic in the presence of the distributed elements is the shift of transmission poles towards lower frequencies, that is where the insertion loss becomes zero. As these frequencies are typically associated with potentially dangerous HOMs, this property becomes particularly important for the synthesis. Already a length of 5 mm and

effective impedance of 40 Ω commonly considered for all unit elements in between the lumped elements of the networks sketched in Fig. 4.45 cause the frequency of transmission poles to be shifts by more than 100 MHz. This is shown in Fig. 4.46.

Figures 4.47 and 4.48 show approximate realizations of the third-order, or respectively, fifth-order elliptic filter function as coaxial microwave structures. The designs result from iterative simulations, with the geometry being gradually changed, so that fitted circuit parameters approximately match the desired ones in Table 4.3. The parameter model elaborated in Sec. 4.1.6 applies to one capacitive gap along the inner conductor which is enclosed by two inductive posts. This matches exactly the needs of the third-order filter whose equivalent circuit is well represented by (4.34)–(4.36) together with the reciprocity condition (2.33). Consequently, lumped and distributed elements of the equivalent circuit may be derived by solving the minimization problem (4.37). The corresponding values of the finalized geometry are listed in the fourth column of Table 4.3. The distance between inductive posts is much reduced to minimize the frequency shift of the transmission pole. Nonetheless, a remaining shift of 103 MHz is observed. The insertion loss is well within the predefined limits. The minimum attenuation in the stopband is slightly lower than for the lumped network but still above $\alpha_{\min} = 30\,\mathrm{dB}$.

For the fifth-order filter, it is proposed to consider each mid-shunt ladder combined with adjoined shunt inductances individually. Each subunit consisting of a capacitive gap along the inner conductor enclosed by two inductive posts is adjusted in order

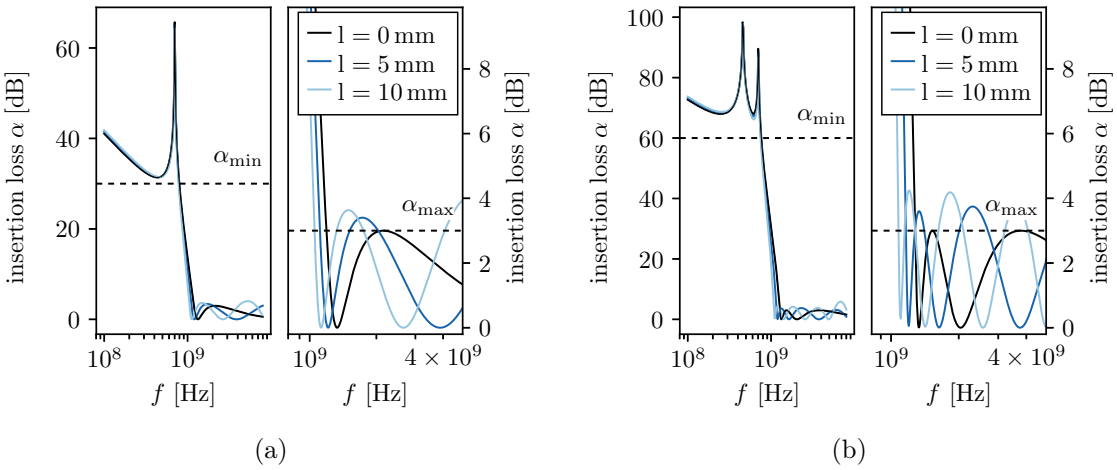

Fig. 4.46. Insertion loss as a function of frequency (a) for the third-order elliptic filter as shown in Fig. 4.45(a), and (b) for the fifth-order elliptic filter as shown in Fig. 4.45(b). The corresponding values of lumped elements are listed in the third or fifth column of Table 4.3, respectively. Different modifications are compared, with equal unit elements being inserted at each dashed highlighted terminal pair of the corresponding network. The length l of the unit elements is varied from zero which means the original network, to 10 mm while the characteristic impedance is fixed to 40 Ω.

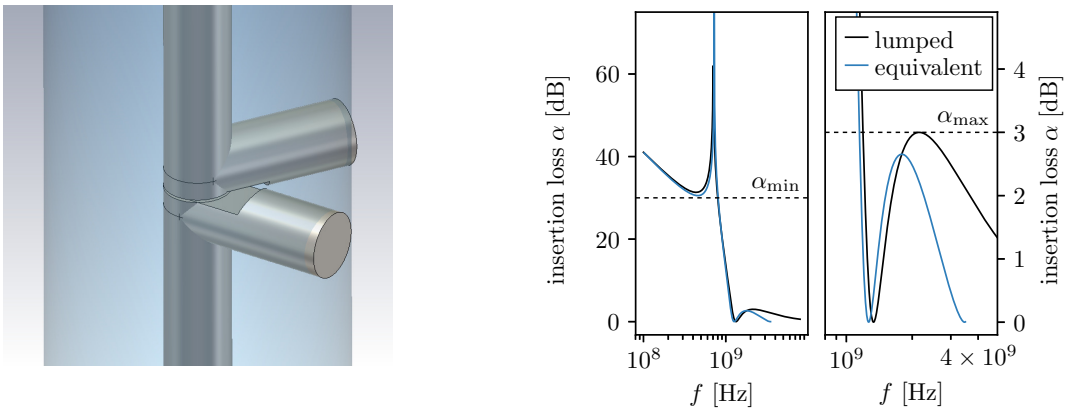

Fig. 4.47. (a) Microwave structure to approximate the frequency response of a third-order elliptic high-pass filter. (b) Attenuation as given by the lumped network in Fig. 4.45(a) in black and the approximation by the coaxial structure in blue. Deviations are caused by transmission lines.

to approximate element values of the lumped circuit as shown in Fig. 4.45(b). The fitted parameter values of both partial microwave structures are listed in the sixth column of Table 4.3. The subsequent connection required additional modification of the rotation angles between inductive posts in order to achieve the attenuation curve as shown in Fig. 4.48(b). In comparison to the previous example, it was found that the distance between neighboring fixings must be notably larger so that the equivalent circuits of Fig. 4.37, representing the discontinuities in the coaxial guide, remain valid as discussed in Sec. 4.3.2. The equiripple behavior is apparent.

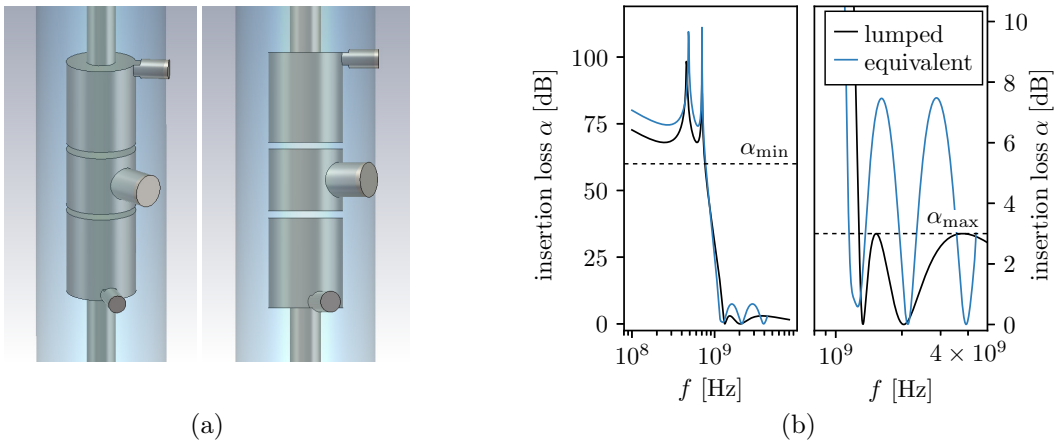

Fig. 4.48. (a) Microwave structure to approximate the frequency response of a fifth-order elliptic high-pass filter. (b) Insertion loss as given by the lumped network in Fig. 4.45(b) in black and the approximation by the coaxial structure in blue. Deviations are caused by transmission lines.

However, the insertion loss is increased by approximately 5 dB in both the stopband and passband. This example illustrated the limits of pure lumped networks for the design of coaxial microwave filters. A rigorous consideration of generalized networks involving lumped and distributed elements to ensure fair approximations of the anticipated microwave structures is essential even for relatively short transmission lines. For instance, the lumped elements of the equivalent circuit may be adjusted in the presence of predefined transmission lines prior to any electromagnetic field simulation and model fitting. This problem opens up another research topic not further discussed here: the synthesis of filter functions by means of generalized networks [38, 120].

4.4 Summary of the Results

The scattering properties of various discontinuities and obstacles in coaxial waveguides have been investigated, some of which provide unexpected behavior that is not documented in the literature. Particularly interesting for the implementation of high-pass filters is the microwave structure discussed in Sec. 4.1.6, due to the similarity of its equivalent circuit with a third-order canonical high-pass realization providing a transmission zero at finite, nonvanishing frequency, together with the fact that equivalent circuit parameters may be adjusted over a larger range of variation. Analyses of the mid-shunt ladder by means of analytical field calculations remain for future work.

A first attempt has been demonstrated to develop a generally applicable systematic procedure to design coaxial filters given a filter or transfer function. Unlike the design procedure developed by Haebel and Gerigk as outlined in Sec. 4.3.1, which rests on reactance-coupled $\lambda/2$ resonators being often very bulky, the aforesaid approach suggests reducing waveguide sections between the discontinuities as much as possible. The limit is given by the applicable range of the considered equivalent circuit, and might be very different as shown by the considered examples in Sec. 4.3.4. The examples direct to a new class of compact coaxial HOM couplers with minimum number of discontinuities. The design procedure requires further refinement, for instance, more control of the transmission poles, the prediction of effective impedance by which the transmission lines in the equivalent circuit are characterized, or the synthesis of generalized networks consisting of lumped and unit elements.

Another aspect important for the rf design of HOM couplers involves the antenna which is characterized by the radiation resistance and parasitic reactive components associated with the excitation of evanescent modes. In contradiction to standard literature about microwave engineering such as [29, 41], accessible tutorials on the design of HOM couplers [24, 101, 118] discount the important role of the radiation resistance, and thereby miss the possibility that the coaxial line may be mismatched to the antenna. Furthermore, the filter component of an HOM coupler should not be considered as a means of compensating the antenna reactance since the latter is

partially dominated by discontinuities in the circular waveguide on which the coupler is mounted. An example is the observation of field cancellation phenomena in cutoff tubes as discussed in Sec. 4.2.4. Thus, a proper design is not only restricted to the antenna shape of the HOM coupler but also involves careful considerations of the entire coupling region. Depending on the design, this may involve the cavity, cutoff tube, or eventual apertures. Referring to the cutoff tubes of high-β SPL cavities, it has been shown that transmission zeros with respect to the TM_{01} mode propagation occur at frequencies sufficiently far away from the TM_{011} frequency band. Certainly this circumstance permits the use of coaxial HOM couplers. The next chapter discusses various other design aspects on the way towards a first prototype.

5 Coupler Design and Testing

The previous chapter has dealt with fundamental design considerations of coaxial HOM couplers with the focus on scattering properties. In addition to this initial step, the particular design needs to optimize the multipacting behavior, allow the heat load to be investigated, minimize the mechanical complexity, and maximize the tolerances in order to keep the cost at a reasonable level. Due to this multi-physical problem, the topological approach to a coupler design is quite heuristic, and hence requires comparison with other topologies. Typically, the final design results from several iterations accounting for the different physical aspects. This chapter presents a total of six coaxial couplers applied to the high-β SPL cavity. Initially, they are optimized in terms of rf characteristics, also taking into account fundamental mechanical limitations. These designs were then assessed in terms of robustness and tunability, external quality factors of concerned HOMs, heat load, and multipacting. Simulation results for final designs are presented together with measurements carried out on three prototypes. Subsequent analyses belong to what is thought of as 'standard' considerations for the design of HOM couplers, and may similarly be found, for example, in [16, 116].

5.1 Conceptional Designs and Prototypes

Similar to the characterization of low-pass filters by a set of effective parameters [34, p. 137], coaxial HOM couplers may be classified by (i) the antenna type, (ii) the order of complexity disregarding unit elements in the equivalent circuits, and (iii) the number of transmission zeros at finite, nonvanishing frequency. The antenna can be either of the types sketched in Fig. 4.21, i. e. probe (P), closed loop (CL), or open-loop (OL). For example, the coupler denoted as P 05 02 combines a probe antenna with a fifth-order coaxial filter providing two transmission zeros at finite, nonvanishing frequency. Naturally, all couplers are intended to provide high-pass or pseudo-high-pass characteristics. Hence, a differentiation by the filter kind is not needed. Although the classification introduced above neither specifies attenuation limits in the stopband and passband nor allows a specific topology to be derived for the microwave structure, it is sufficient to distinguish between the design approaches introduced in the following. They serve as a basis for all subsequent analyses whose results for the most part are published in [117].

5.1.1 Topological Approaches

Figure 5.1 provides a survey of the various design approaches referred to in this chapter. It shows the longitudinal cross-section for each design, with the outer conductor being merely represented by a boundary. A perspective view of the P 06 02 coupler is illustrated in Fig. 5.2 together with the set of geometrical parameters. All designs underlie certain mechanical limitations and preferences: (i) The tube diameter of the outer conductor is fixed to 45 mm according to the specifications of the high-β SPL cavity. (ii) The diameter of the inner conductor should preferably be large in order to facilitate the fabrication, particularly if the antenna requires active cooling. That is, if a coolant such as liquid helium flows through it. However, a larger cross section of the inner conductor reduces the space inside the tube, and ultimately decreases the scope of shunt inductances associated with fixings as studied in Sec. 4.1.1. Thus, a trade-off must be defined. (iii) The HOM couplers are mounted on cutoff tubes using rotatable flanges. Referring to the drawing of the high-β SPL cavity in Fig. A.2, the distance between flange and cutoff tube amounts 41 mm on the fundamental mode coupler side and 46 mm on the tuner side. Consequently, any fixing of the inner conductor must be located above the flange connection. Note, the design approaches as sketched in Fig. 5.1 penetrate

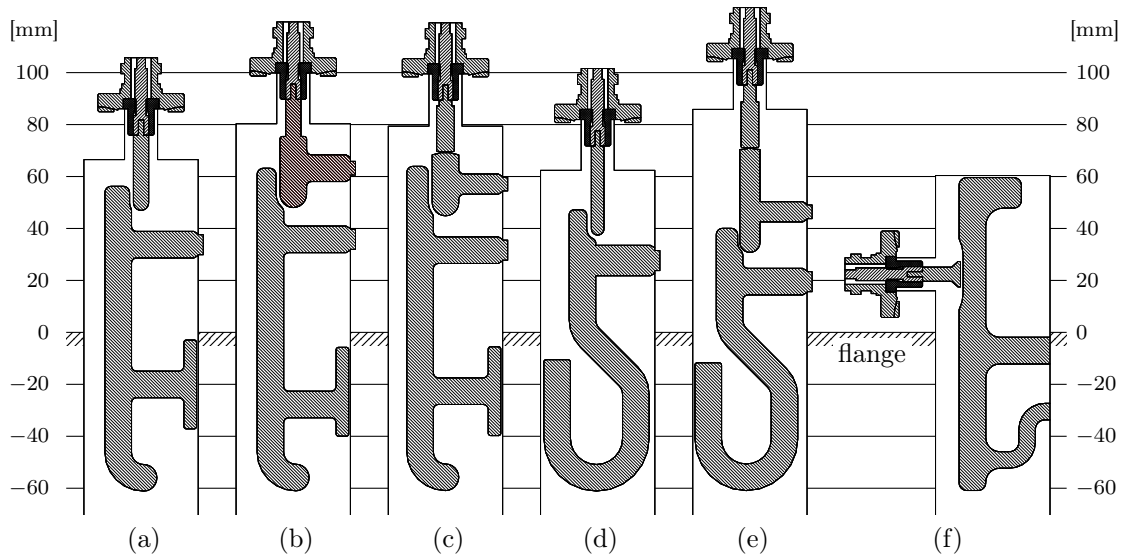

Fig. 5.1. HOM coupler design approaches for the high-beta SPL cavity. The dashed line indicates the flange. The designs are classified in accordance to (i) the antenna type which is either a probe (P), closed loop (CL), or open-loop (OL). (ii) The order of complexity disregarding unit elements in the equivalent circuits. (iii) The number of transmission zeros at finite nonvanishing frequency. Correspondingly, the notations are (a) P 04 01, (b) P 05 02, (c) P 06 02, (d) OL 04 01, (e) OL 06 02, (f) CL 04 01. Depending on the considered cutoff tube, the antennas penetrate by 15 mm or 20 mm, respectively, on the tuner or fundamental mode coupler side. The darker appearing parts highlighted in crosshatch correspond to the ceramic windows of the feedthroughs.

the cutoff tube by 15 mm or 20 mm, respectively, on the tuner or fundamental mode coupler side. (iv) The distance between the cutoff tube and coaxial output of the HOM coupler is constrained to 200 mm.

The topologies of the P 04 01 and OL 04 01 couplers shown in Figs. 5.1(a) and (d) are essentially redesigns of the LHC HOM couplers [101] adapted to the needs of the high-β SPL cavity. The frequency response of both designs is characterized by a single transmission zero at the cavity's fundamental mode frequency, which is caused by an equivalent mid-series ladder. Depending on the particular coupler, the latter is either realized as inductive post in combination with a capacitive gap to the outer conductor, or as open-loop antenna. Topological extensions of both coupler designs with increased order of complexity led to the microwave structures sketched in Figs. 5.1(b), (c), and (e). Particularly interesting is the combination of equivalent mid-series and mid-shunt ladder which causes two transmission zeros at finite, nonvanishing frequency for each of these designs. The implementation of mid-shunt ladders follows Sec. 4.1.6. Finally, the CL 04 01 coupler depicted in Fig. 5.1(f) with a closed loop antenna is originated from the TESLA HOM coupler [58]. A single transmission zero is introduced by the waveguide section above the feedthrough in combination with the capacitive gap between inner conductor and top plate. In the vicinity of the transmission zero an equivalent behavior of a mid-series ladder is approximately restored. The advantage of this design lies in the tunability of the frequency at which the transmission zero occurs [58, 124]. A closed loop antenna is only reasonable if the mounting point is close to the cutoff tube. In Fig. 5.1(f), both fixings are below the flange whose position is marked by the zero level. Shifting the fixings above this level would spoil the whole rf performance. For this reason the TESLA HOM coupler and its adaptations to other projects, for instance, SNS, CEBAF, and ILC, are directly welded onto the cutoff tube [1, 125, 126]. Although

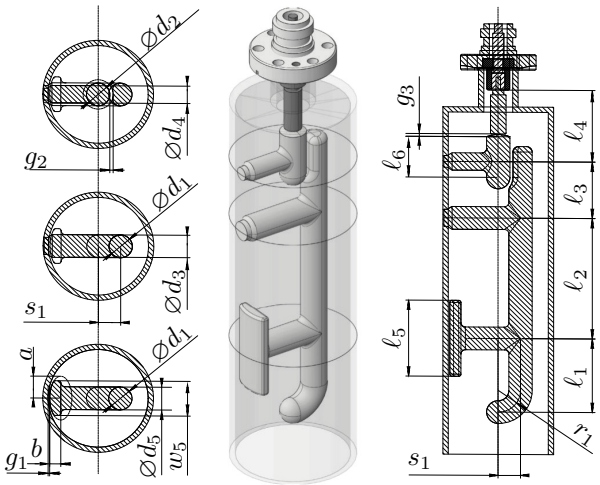

Fig. 5.2. Parameter set of the P 06 02 coupler [117]

the design shown in Fig. 5.1(f) is not an option for a mountable SPL HOM coupler, it extends the scope of different design approaches being studied and compared with respect to the various physical aspects.

5.1.2 Design Process for the Microwave Filter

To begin with, each coupler was initially designed on the basis of reactance coupled $\lambda/2$ resonators using the method of Haebel and Gerigk as outlined in Sec. 4.3.1. Strictly speaking, the procedure considers only the filter component of the particular HOM coupler which is illustrated in Fig. 5.3 by means of the P 06 02 design. Given the results of Sec. 4.1, it may equivalently be described by the network shown in Fig. 5.4, with the coaxial output at the terminal plane θ_2 being terminated by the characteristic impedance of the attached coaxial cable.

Initial values for the lengths and characteristic impedances of individual transmission lines, shunt inductances, and optional series capacitances are derived from a predefined design frequency ω_∞ related to concerned HOMs according to (4.87), and a parameter k given by (4.89) accounting for the coupling between adjacent $\lambda/2$ resonators. Referring to Fig. 5.2, the implied equivalent circuit parameters are related to various geometrical parameters, such as the diameters of inner conductor pieces, d_1, d_2, and their displacement from the center, s_1, lengths of waveguide segments, $\ell_1, ..., \ell_4$, the capacitive gap g_3, as well as diameters d_3, d_4 and corresponding lengths of both fixings. To allow for the desired band-stop characteristics in the vicinity of the fundamental mode frequency provided by the cavity, transmission zeros at finite, nonvanishing frequency are invoked using mid-series and mid-shunt ladders. Their capacitance and inductance are obtained from a predefined frequency of the intended transmission zero and earlier solved circuit parameters associated with the band-pass filter according to (4.96)–(4.97). Again by referring to Fig. 5.2, these parameters are implicitly related to the capacitive gaps g_1 and g_2, the length ℓ_5 and width w_5 of the capacitive plate, the diameters $d_3, ..., d_5$, and corresponding lengths of inductive posts. In addition, the equivalent circuits of all HOM couplers

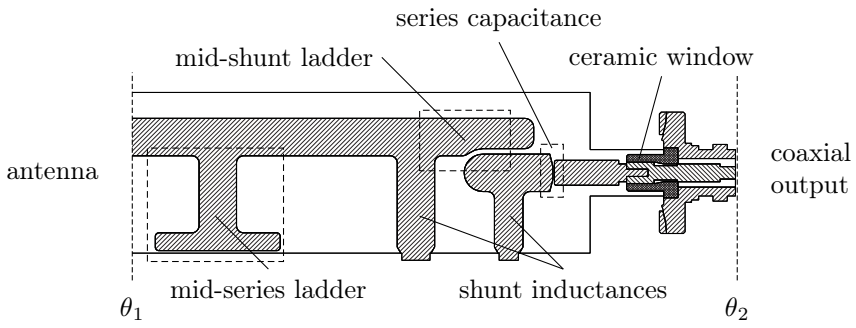

Fig. 5.3. Longitudinal cross-sectional view of the P 06 02 coupler. Only the filter part and feedthrough are considered. The antenna penetrating into the cutoff tube is not shown.

need to account for the relatively high shunt capacitance between the inner and outer conductor at the feedthrough, which is due to the ceramic window. Following the Bode-Fano criterion (4.101) in Sec. 4.3.2, this capacitance denoted as C_2 in Fig. 5.4, should be made as small as possible. Though, it may be adjusted within reasonable limits to fine tune the frequency response with respect to individual HOM frequencies.

After obtaining an initial set of geometrical parameters, the particular design is further refined on the basis of numerically calculated scattering functions for the three-dimensional problem. Given the example in Figure 5.3, the scattering matrix is evaluated with respect to the terminal planes θ_1 and θ_2, with the incident and reflected waves being normalized to the characteristic impedance associated with TEM mode propagation at the particular terminal plane. Figure 5.5 provides a qualitative comparison between the microwave structure sketched in Fig. 5.3 and its equivalent network shown in Fig. 5.4. The input impedance at the terminal plane θ_1 normalized to $1\,\Omega$ is illustrated for three parameter variations correspondingly applied to each model while assuming that the coaxial output at the terminal plane θ_2 is matched. The equivalent circuit model describes reasonably well the relationship between the coupler geometry and filter characteristics, so that it permits directing an iterative optimization process using numerical simulations. However, it is important to differentiate between the geometric lengths ℓ_1 and ℓ_2 related to waveguide sections in Fig. 5.2 and the length l_1 and l_2 which are associated with transmission lines in the equivalent circuit of Fig. 5.3. The latter do not include the electric thickness of adjacent inductive posts. Similarly, the gap distance g_2 in Fig. 5.2 may slightly impact the inductance of the mid-shunt ladder such that its impact on the frequency response is not exactly the same as the reciprocal of the capacitance C_3 in the equivalent circuit.

Taking into account the potentially dangerous HOMs listed in Table 3.6, the microwave filter is intended to provide a large transmission power gain in the vicinity of 1330 MHz, 2085 MHz, and 2464 MHz. Prior to this is the rejection of the fundamental cavity mode at 704.4 MHz, which requires an insertion loss in the order of $\alpha > 100\,\mathrm{dB}$. In the view of circular accelerators, it is further necessary to incorporate significant dipole modes as listed in Table 3.7. Corresponding microwave filters are intended to reveal passband edges already at around 920 MHz.

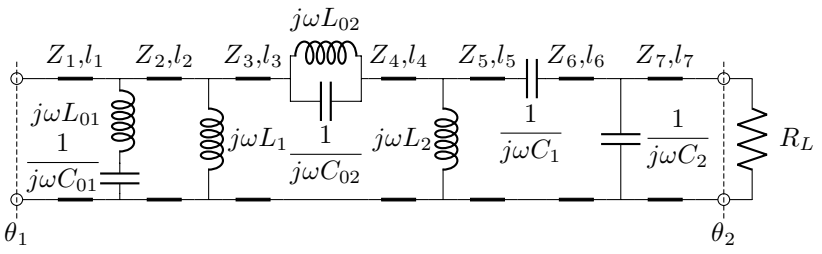

Fig. 5.4. Equivalent lumped circuit model of the P 06 02 coupler.

The optimization of filter characteristics involves numerous geometrical parameters which hinder applying exhaustive parameter variations for the particular microwave structure. In the following, some general design recommendations are drawn by referring to the example shown in Fig. 5.2 and the corresponding equivalent circuit of its filter part in Fig. 5.4. To begin with, it is preferable to adjust the diameters d_3, d_4, and corresponding lengths of the fixings which are related to the shunt inductances L_1 and L_2. For this purpose, the procedure outlined in Sec. 4.1.1 may be used. Note, a displacement of the inner conductor from the center described by the parameter s_1 allows for larger shunt inductances without greatly reducing the diameters d_3 and d_4. Afterwards, the lengths ℓ_1 and ℓ_2 may be adjusted to frequencies of concerned HOMs, since these parameters significantly influence the passband behavior of the filter. Components related to equivalent mid-series and mid-shunt ladders may initially be designed using the models introduced in Secs. 4.1.6 and 4.1.7. Subsequent adjustments for the capacitance or inductance of the particular LC resonator are necessary to ensure that the corresponding transmission zero occurs at the desired frequency.

To complete the HOM coupler design, the formerly evaluated model of a microwave filter is extended by an antenna penetrating into the cutoff tube. As discussed in Sec. 4.2, radiation resistances are adjusted to achieve the desired power

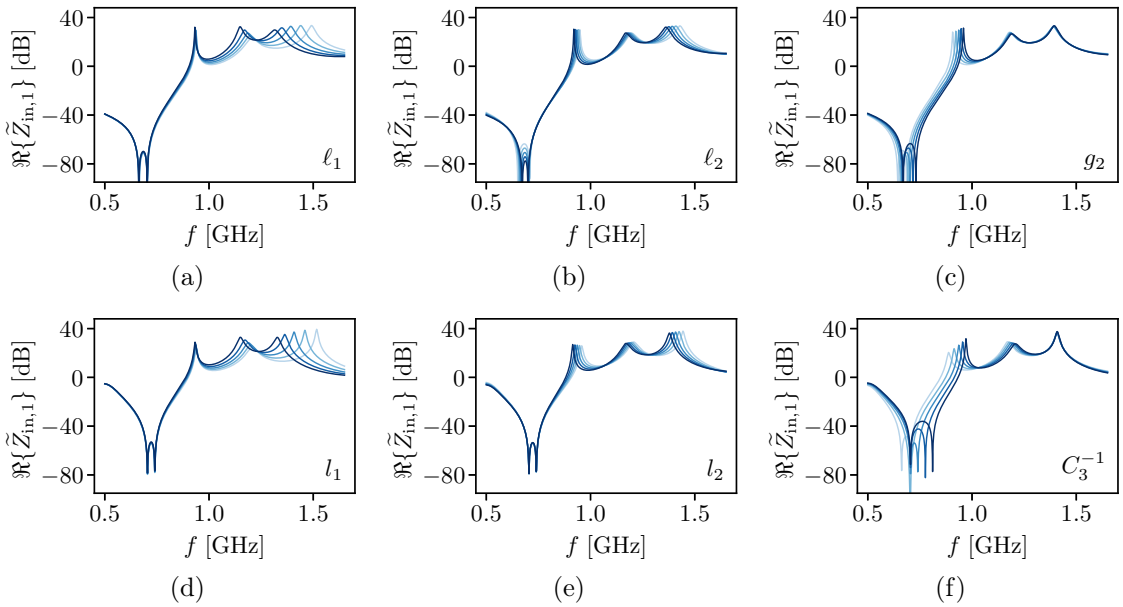

Fig. 5.5. Input impedance normalized to 1 Ω obtained from (a)-(c) numerical simulations for the microwave structure shown in Fig. 5.3 using ANSYS® HFSS™ [94], and (d)-(f) analytic calculations of the equivalent circuit shown in Fig. 5.4. The port at the coaxial output is assumed to be matched. Associated parameters are varied in the range from −20 % (light blue) to +20 % (dark blue) relative to their nominal values.

transfer between waveguide modes present in the cutoff tube and coaxial output of the HOM coupler. Since the entire design of the high-β SPL cavity was fixed in advance, only the antenna shape and its penetration depth into the cutoff tube are free to choose. Consequently, the possibilities to compensate any parasitic reactance provided by the antenna are very limited. Furthermore, eventual transmission zeros due to the cutoff tube are marginally influenced by the antenna shape. Note, the model extension implies moderate but important readjustments of the filter part, in particular, with respect to equivalent mid-series and mid-shunt ladders.

5.1.3 Prototypes

The finalized designs shown in Fig. 5.1 are a result of several design iterations intended to improve the monopole and dipole coupling, reduce the rf sensitivity against mechanical tolerances, to ensure stable operations under reasonable thermal and structural conditions, as well as to suppress multipacting barriers. The various aspects are discussed in subsequent sections mostly on the basis of numerical simulations and, in part, verified by measurements using the prototypes shown in Fig. 5.6. A preliminary version of the P 06 02 coupler depicted in Fig. 5.6(a) was fabricated as a three-dimensional print made of plastic and covered by a copper layer of approximately 0.1 mm thickness. The same technique applies to the OL 06 02 prototype shown in Fig. 5.6(c). Furthermore, a solid prototype of the finalized P 06 02 design was fabricated. It is made of copper and equipped with a rotatable stainless steel flange as illustrated in Fig. 5.6(b). Details of the mechanical design are given in Sec. A.5. Note, the printed prototypes provide a relatively high surface roughness

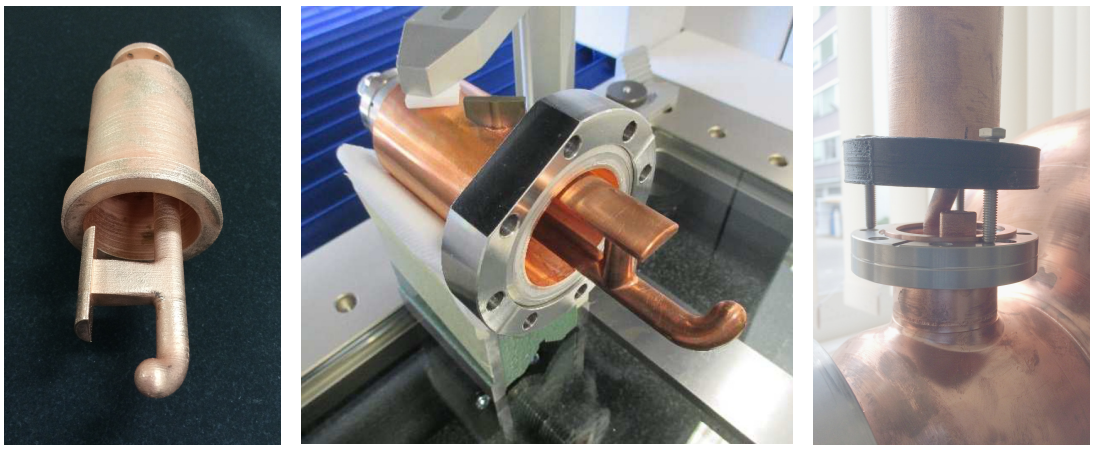

(a) (b) (c)

Fig. 5.6. Prototypes of HOM couplers for the high-β SPL cavity. (a) Preliminary three-dimensional printed version of the P 06 02 coupler. (b) Solid prototype of the finalized P 06 02 coupler made of copper. (c) Three-dimensional print of the OL 06 02 coupler while mounting on the cutoff tube.

of 240 µm as measured by the maximum height of the surface profile. Though, not being suitable for measurements under vacuum and cryogenic temperatures, these prototypes allow the characterization of scattering properties and external coupling factors at room temperature. The solid copper prototype of the P 06 02 further permits to analyze the rf behavior at different environment conditions.

5.2 Filter Characteristics and Mode Coupling

The following analyses refer to rf characteristics of the various designs introduced in Sec. 5.1, with the focus on modal transmission power gains, the frequency sensitivity of transmission zeros, as well as external quality factors associated with concerned HOMs of the high-β SPL cavity. The configuration shown in Fig. 5.7 serves as a reference for subsequent simulations and measurements. The latter were carried out using one of the SPL cavity prototypes fabricated out of copper. Probe antennas attached to the terminal planes θ_2 and θ_4 allow the evaluation of the power transmitted from the coaxial port of the HOM coupler at the terminal plane θ_3 through the cutoff tube to the beam pipe, or through the cavity to the fundamental mode coupler, respectively. The internally considered terminal plane θ_1 is useful for simulation studies and optimizations of the coupler geometry without involving the cavity. Unless otherwise stated, the HOM coupler is located on the tuner side as sketched in Fig. 5.7(a). Not shown in the sketch, the cavity provides an aperture across from the terminal plane θ_4, which is likewise foreseen for an HOM coupler. Note, the details of the cavity geometry including both cutoff tubes are provided in

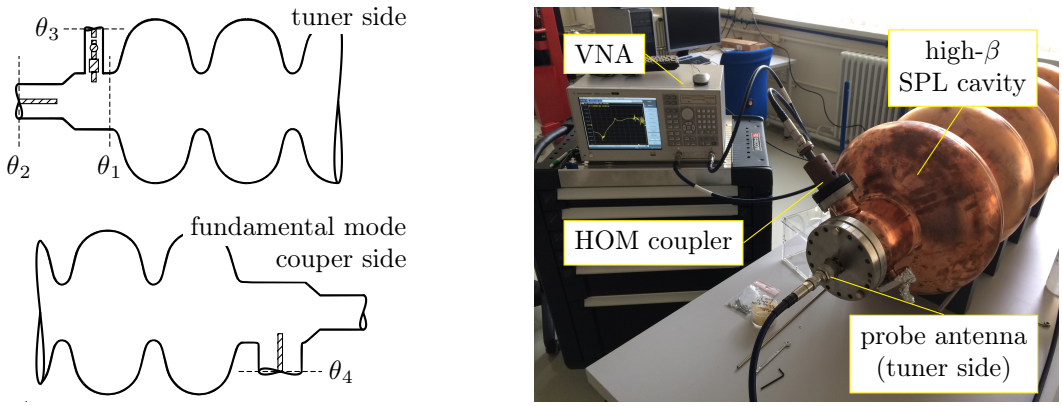

(a) (b)

Fig. 5.7. Configuration to characterize the frequency response of the HOM coupler as well as external quality factors for individual resonant modes. (a) Sketch of the set-up, with probe antennas being attached to the terminal planes θ_2 and θ_4. The HOM coupler is located at the terminal plane θ_3 on the tuner side. The internal terminal plane θ_1 is considered for simulations. (b) Measurement of the transmission power gain between the terminal planes θ_2 and θ_3.

Sec. A.2. In addition, all HOM couplers are oriented such that the capacitive plate of their mid-series ladder is perpendicular to the longitudinal axis of the cavity unless otherwise stated. That is, the capacitive plate faces the viewer in Fig. 5.7(a). Simulations are carried out using CST STUDIO SUITE® [91].

5.2.1 Frequency Response

Figs. 5.8(a) and 5.9(a) show the simulated transmission power gain with respect to the TM_{01} mode being considered at the terminal plane θ_1, and TEM mode propagation at the terminal plane θ_3 according to the configuration shown in Fig. 5.7. The particular frequency response provides a first impression of how efficient transverse magnetic monopole modes in the cavity may be damped by the different HOM couplers. The frequencies of concerned HOMs listed in Table 3.6 are highlighted in dashed gray. Not relevant for SPL but for the sake of completeness, Figs. 5.8(b) and 5.9(b) show the simulated transmission power gain assuming the TE_{11} mode at the terminal plane θ_1 while the TEM mode propagation at the terminal plane θ_3 remains. Figs. 5.8 and 5.9, respectively, refer to the designs with probe or loop antennas. Transmission zeros occurring in the vicinity of 2 GHz are caused by the cutoff tube following the studies of Sec. 4.2.4.

Apart from the antenna type, the previously introduced notations for the different design approaches become apparent from their frequency responses. The P 05 02 and P 06 02 couplers in Fig. 5.8(a) as well as the OL 06 02 design in Fig. 5.9(a) feature two finite transmission zeros close to the frequency of the fundamental cavity mode,

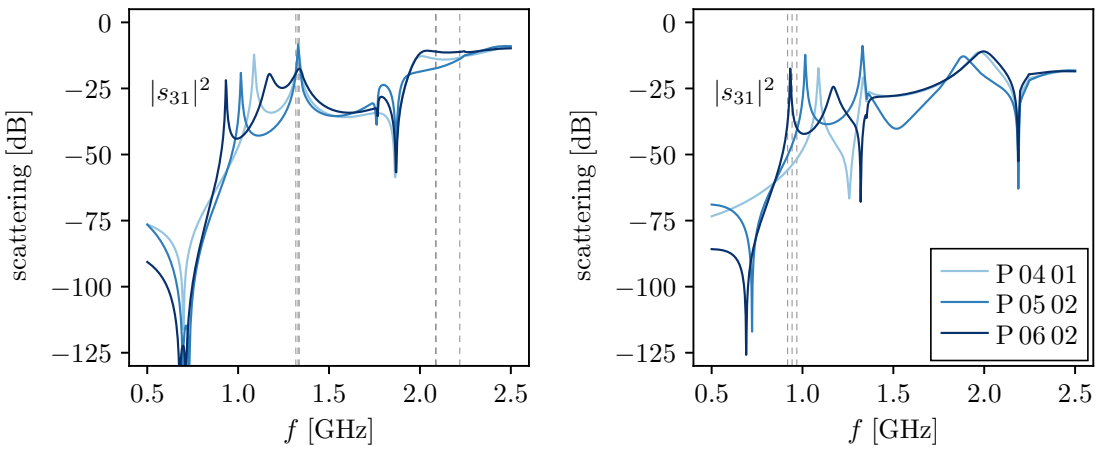

(a) TM_{01}-TEM transmission (b) TE_{11}-TEM transmission

Fig. 5.8. Transmission power gain between the circular waveguide ports of the cutoff tube towards the cavity and the coaxial output of the HOM coupler for different designs using probe antennas. In dashed gray, the frequency of concerned HOMs listed in Table 3.6 and 3.7. Shown are only those which provide (a) TM_{01X} or (b) TE_{11X} characteristics.

i. e. 704.4 MHz. This allows for a sufficiently high insertion loss over considerably larger frequency ranges than achieved by remaining designs. Quantitative predictions of the stopband region as measured by an insertion loss of $\alpha > 100\,\mathrm{dB}$ are listed in Table 5.1 for the different couplers. They range from few megahertz up to more than 200 MHz. Besides the better rejection, those couplers with higher filter order also show a steeper transition between stop- and passband, which possibly allows the inclusion of HOMs of the first dipole passband at around 930 MHz in the design process, as shown in Figs. 5.8(b) and 5.9(b). However, the combination of an equivalent mid-series and mid-shunt ladder to introduce two transmission zeros at finite, nonvanishing frequency forms a more complex microwave structure in comparison to those revealing merely one equivalent mid-series ladder. Consequently, the fabrication becomes more challenging. More welds are required which increases the risk of vacuum leaks. Likewise, the cleaning and surface preparation become more difficult.

The transmission power gain at frequencies of concerned monopole modes in the TM_{011}, TM_{022}, and TM_{031} bands around 1330 MHz, 2089 MHz, and 2464 MHz, respectively, is comparable between all designs as depicted in Figs. 5.8(a) and 5.9(a). Referring to Fig. 5.9(b), the designs involving open-loop antennas are characteristic for their dipole coupling, in particular, with respect to the TE_{111} band at around 930 MHz. The modified TESLA design CL 04 01, though providing the same filter order and number of finite transmission zeros as the OL 04 01 coupler, is not suitable to achieve equally good rf transmission in the frequency region associated with TE_{111} modes of the cavity.

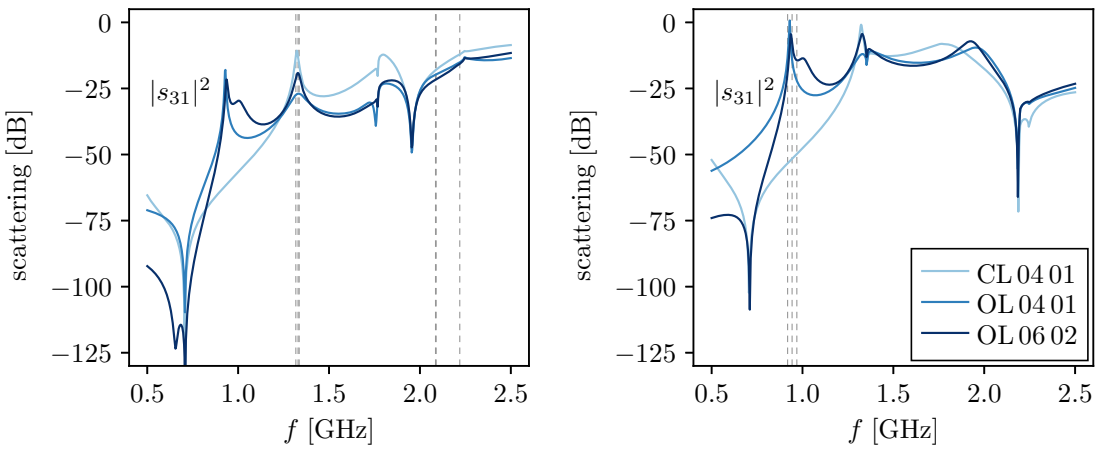

(a) TM_{01}-TEM transmission (b) TE_{11}-TEM transmission

Fig. 5.9. Transmission power gain between the circular waveguide ports of the cutoff tube towards the cavity and the coaxial output of the HOM coupler for different designs using loop antennas. In dashed gray, the frequency of concerned HOMs listed in Table 3.6 and 3.7. Shown are only those which provide (a) $\mathrm{TM}_{01\mathrm{X}}$ or (b) $\mathrm{TE}_{11\mathrm{X}}$ characteristics.

Table 5.1. Sensitivity of frequency responses referred to Figs. 5.8(a) and 5.9(a).

design	parameter	$\partial f_{01}/\partial x^{\dagger}$ [MHz/mm]	$\partial f_{02}/\partial x^{\dagger}$ [MHz/mm]	$\alpha_{\max}{}^{\ddagger}$ [dB]	$\Delta f_{100}{}^{\S}$ [MHz]
P 04 01	g_1	383.77			5 to 25
P 05 02	g_1	246.67	138.01	91.52 to 115.38	85 to 180
	g_2	129.29	7.08	84.67 to 111.42	85 to 172
P 06 02	g_1	180.74	177.71	121.93 to 98.71	135 to 215
	g_2	70.84	47.73	106.71 to 121.49	137 to 155
CL 04 01	g_1	692.53			5 to 17
OL 04 01	g_1	155.74			<1 to 5
OL 06 02	g_1	251.93	-5.27	101.86 to 122.84	130 to 220
	g_2	126.75	136.00	128.86 to 106.62	137 to 160

† Sensitivity of the transmission zero with respect to a change of the particular gap distance.
‡ Minimum insertion loss within the frequency range given by two transmission zeros.
§ Frequency span of the stopband as measure by a minimum insertion loss of $\alpha = 100\,\mathrm{dB}$.

The insertion losses seen in Figs. 5.8(a) and 5.9(a) appear throughout larger than 15 dB even in the passbands. This is due to the fact that corresponding monopole modes do not propagate through the larger waveguide section of the cutoff tube but rather behave evanescently. Consequently, the power extraction of concerned HOMs is significantly limited by the cutoff tube which eventually hinders achieving the required external coupling coefficients. This is further discussed in Sec. 5.2.3. In addition, it is worthwhile to mention that all design approaches reveal pseudo-high-pass behavior as outlined in Sec. 4.3.2. Though not shown in Figs. 5.8 and 5.9, each frequency response provides narrow-band band-pass characteristics below 500 MHz, which is parasitic.

Given the different frequency responses in Figs. 5.8(a) and 5.9(a), the P 06 02 and OL 06 02 couplers achieve the best rf performance also in terms of robustness later discussed in Section 5.2.2. Figure 5.10 shows the transmission power gain of corresponding rapid prototypes as measured between the terminal planes θ_2 and θ_3 according to the configuration shown in Fig. 5.7, with TEM mode propagation being considered at each port. The measurements agree reasonably well with the simulations. Unlike before, the simulation models involve the cavity. The insertion loss around 704.4 MHz was found well above 100 dB for both designs.

The preceding studies dealt with filter characteristics of individual HOM couplers mounted on the cutoff tube at the tuner side as sketched in Fig. 5.7(a). Similar results are obtained if the corresponding coupler is mounted on the opposite extremity of the cavity. The slightly different cutoff tube on the fundamental mode coupler side provides a transmission zero at somewhat lower frequency as listed in Table 4.2. In addition, the HOM coupler is placed 30 mm farther away from the cavity leading

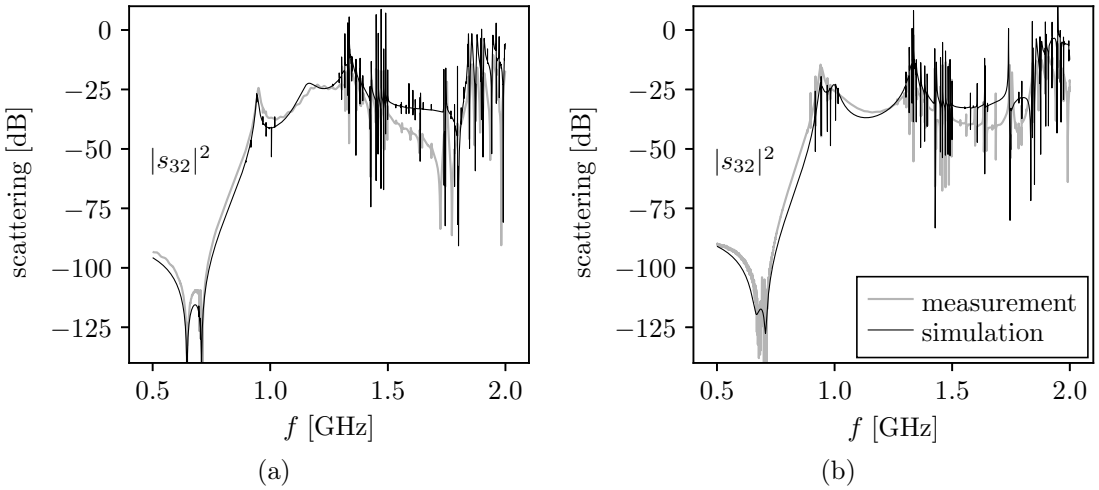

Fig. 5.10. Simulated and measured transmission power gain for different HOM coupler prototypes considered at the terminal plane θ_3 while applying a probe antenna at the terminal plane θ_2 following the configuration shown in Fig. 5.7. (a) P 06 02 coupler and (b) OL 06 02 coupler. The measurements were carried out using the rapid prototypes shown in Fig. 5.6(a) and (c).

to generally lower transmission power gains with respect to Figs. 5.8 and 5.9.

5.2.2 Sensitivity Analysis

The mechanical tolerances of HOM couplers should not be smaller than $\pm 0.2\,\mathrm{mm}$ to limit the cost of fabrication. By applying small perturbations on geometrical parameters of the various coupler designs, the impact on the specific frequency responses shown in Figs. 5.8(a) and 5.9(a) is studied. Most sensitive parts are related to the capacitances of equivalent mid-series and mid-shunt ladders due to relatively small gap distances partially being $< 1\,\mathrm{mm}$. Consequently, the rejection of the fundamental mode may be very sensitive to uncertainties in these parameters, in particular, for those designs providing only one transmission zero at finite, nonvanishing frequency to form the stopband. Important results of the sensitivity studies are listed in Table 5.1. The parameters g_1 and g_2, respectively, refer to the gap distance of the mid-series and mid-shunt ladder, if any, as illustrated in Fig. 5.2 for the P 06 02 design. The geometrical parameters are varied in a range of $\pm 0.3\,\mathrm{mm}$. Linear dependencies are found in all cases within $\pm 0.1\,\mathrm{mm}$. Referring to the stopband region Δf_{100} characterized by an insertion loss $> 100\,\mathrm{dB}$, couplers comprising more than one transmission zero at finite, nonvanishing frequency to form the stopband, are found to be very robust. In contrast, the rf reflections provided by the P 04 01, OL 04 01, and CL 04 01 couplers at 704.4 MHz appear highly sensitive to the gap distance g_1. Hence, a precise tuning during the installation is mandatory.

5.2.3 External Coupling Factors

The present section focuses on the damping of HOMs, which is quantified by the external quality factor following the definition (2.93). Studies on longitudinal beam dynamics presented in Sec. 3.4 recommend external quality factors of $Q_{\text{ext}} \leq 10^5$ for all concerned HOMs listed in Table 3.6. Figure 5.11(a) shows the corresponding values for modes of the TM_{011} and TM_{022} passbands obtained from eigenmode simulations, with the particular HOM coupler being mounted on both extremities of the high-β SPL cavity. The antenna is inserted by 20 mm into the cutoff tube on either side. Note, the relatively large insertion was found to be necessary in order to ensure $Q_{\text{ext}} \leq 10^5$ for all concerned HOMs. The results are comparable between all coupler designs with few exceptions. Referring to Fig. 5.11(b), the damping of some TE_{111} and TM_{110} dipole modes appears considerably larger in the presence of the OL 06 02 coupler than for the other designs.

External quality factors for modes up to 2.1 GHz are further measured at room temperature, i.e. 293 K, using the prototype cavity shown in Fig. 5.7(b). Given the configuration in Fig. 5.7(a), the probe antenna attached to the terminal plane θ_4 serves as a reference antenna. Scattering functions are evaluated between the terminal planes θ_3 and θ_4 using a VNA while the terminal plane θ_2 is shortened. The procedure adopted from [52, 127] may be drawn as follows: At first, the loaded quality factor Q_L is determined from the resonant frequency and 3 dB bandwidth of

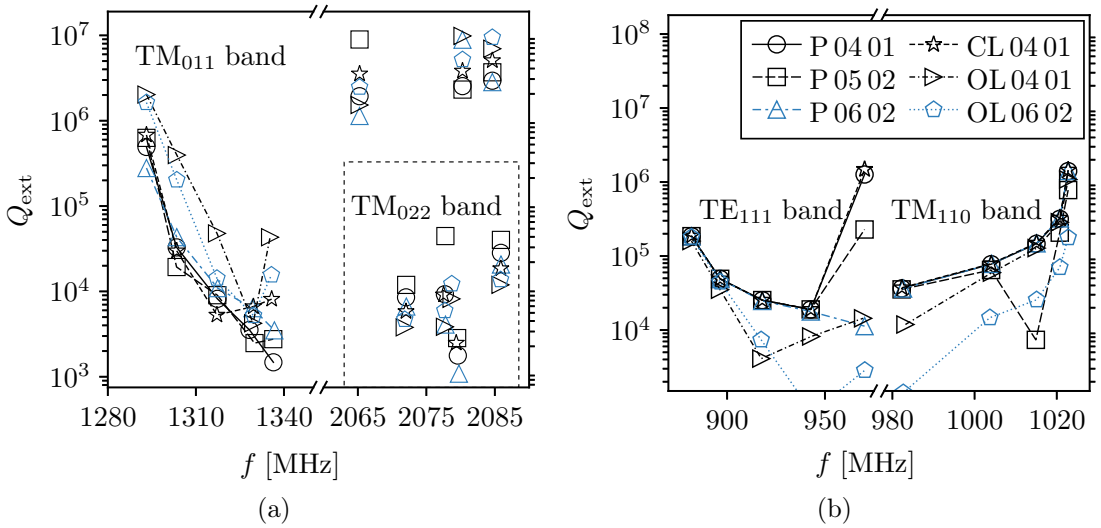

Fig. 5.11. Simulated external quality factors for selected modes of the high-β SPL cavity, with the particular HOM coupler being considered on either extremity. The antenna is inserted by 20 mm into the cutoff tube, each. (a) Modes of the TM_{011} and TM_{022} monopole bands. (b) Modes of the first two dipole bands. Those values highlighted in blue refer to designs which have been selected for the fabrication of prototypes according to Sec. 5.1.3.

the measured transmission power gain $|s_{34}|^2$. Next, the coupling coefficients of the reference antenna and HOM coupler κ_{ref}, κ_{hom}, are derived from the corresponding reflected power gains at resonance using (2.94). Alternatively, the coupling coefficients may be obtained from the diameter of the particular Q-circle in the Smith chart as described in [52]. The latter option is typically less sensitive to random errors. Finally, the intrinsic quality factor is obtained from (2.92) which allows evaluating the external quality factor implied by the HOM coupler using (2.93).

Resulting external quality factors for modes of the first four monopole passbands are shown in Fig. 5.12. Potentially dangerous HOMs of Table 3.6 are highlighted in blue. Deviations between measurements and simulations are primarily due to cavity imperfections. Note, the cavity was several times deformed and subsequently tuned in previous tests such as described in Sec. 3.5.4. Furthermore, in the case of a very low coupling, the error associated with the reflection type measurement becomes significant. This appears easily at room temperature. A possible way to bypass this problem and to achieve reliable results for those coupling factors requires a stronger coupled reference antenna. Rather than using the standing wave ratio as described before, the coupling coefficient provided by the HOM coupler is calculated as [128]

$$\kappa_{\mathrm{hom}} = \frac{|s_{34}|^2}{\dfrac{4\kappa_{\mathrm{ref}}}{(\kappa_{\mathrm{ref}}+1)^2} - |s_{34}|^2}, \tag{5.1}$$

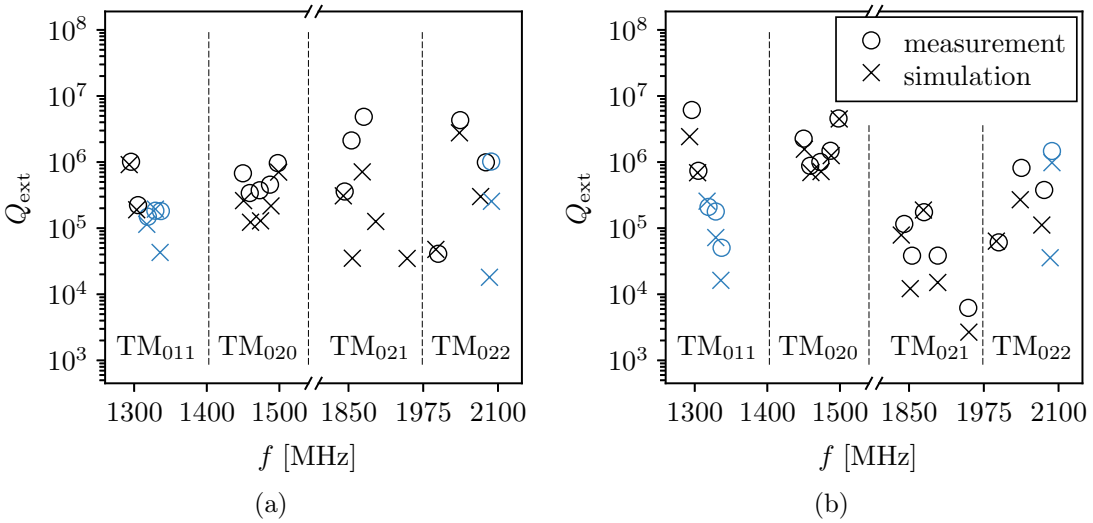

Fig. 5.12. Measured and simulated external quality factors for different HOM coupler prototypes mounted on the high-β SPL cavity according to Fig. 5.7. (a) Solid prototype of the P 06 02 design according to 5.6(b). (b) Rapid prototype of the OL 06 02 design according to 5.6(c). The HOM couplers are installed on the tuner side, each with an insertion depth of 15 mm into the cutoff tube. Potentially dangerous HOMs are highlighted in blue.

at the particular mode frequency. By referring to Fig. 5.12(a), concerned modes of the TM_{011} passband provide external quality factors slightly above the threshold of $Q_{ext} = 10^5$. Corresponding values for the OL 06 02 coupler highlighted in Fig. 5.12(b) range from 2×10^4 to 2×10^5. Although the simulations suggest somewhat lower values, the measured external quality factor of the TM_{022} $5/5\pi$ mode at 2089 MHz was found in the order of $Q_{ext} = 10^6$ for both couplers. The results underline the need of two couplers, one on each cutoff tube of the high-β SPL cavity with an insertion depth between 15 mm to 20 mm.

Finally, the dependency of external quality factors on the coupler orientation is investigated. The results for HOMs of concern are summarized in Fig. 5.13. An angle of $\alpha = 0$ means that the individually considered coupler is mounted on the cutoff tube such that the capacitive plate of its equivalent mid-series ladder is aligned perpendicular to the longitudinal axis of the cavity. This is according to the configuration sketched in Fig. 5.7(a) where the capacitive plate faces the viewer. At $\alpha = -90$ deg, the capacitive plate ought to face the cavity cells. Correspondingly, the plate faces the beam pipe at $\alpha = 90$ deg. For each angle, the capacitance of the equivalent mid-series ladder has to be readjusted to ensure nearly the same insertion loss at the frequency of the fundamental mode. Referring to Fig. 5.13, the P 06 02 and OL 06 02 couplers behave notably differently with respect to the angle α. Naturally, designs comprising a loop antenna are more sensitive to changes of the orientation. Surprisingly, even in case of the P 06 02 coupler, the external quality

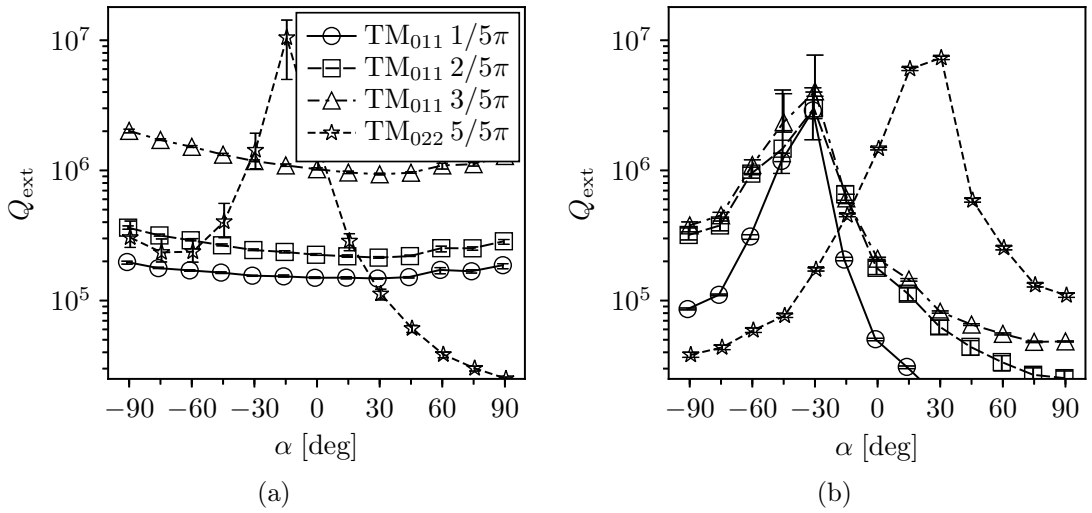

Fig. 5.13. Measured external quality factors of concerned HOMs listed in Table 3.6 as functions of the rotation angle. (a) Solid prototype of the P 06 02 design according to 5.6(b). (b) Rapid prototype of the OL 06 02 design according to 5.6(c). The HOM couplers are installed on the tuner side, each with an insertion depth of 15 mm into the cutoff tube. Error bars are related to the different methods used to evaluate coupling coefficients via (2.94) and (5.1). Markers correspond to the geometric mean of the solutions obtained from the different methods.

factor of the TM_{022} $5/5\pi$ modes at 2089 GHz varies strongly with the rotation angle. This is in part due to the transmission zero provided by the cutoff tube (Table 4.2), as well as due to the slightly bended probe antenna as shown in Fig. 5.6(b). The results may suggest optimal angles of 30 deg and −15 deg for the P 06 02 or OL 06 02 coupler, respectively. It is important to note that these conclusions apply only with respect to the considered HOMs.

5.3 Thermal Behavior

Thermal analyses are performed to evaluate the risk of thermal quenches on the surface of superconducting HOM couplers, and to define cooling requirements, eventually introducing additional thermalization loads which need to be taken into account for the thermal budget of the cryomodule. Figure 5.14 illustrates the assembled SPL cryomodule with the focus on the HOM coupler being mounted across from the fundamental mode coupler. Unlike the cutoff tube on the tuner side, the helium vessel houses the entire cutoff tube on the depicted extremity. Apart from the heat transferred to the helium bath at 2 K, the thermal loads for the HOM coupler are determined by the power deposition on the surface due to the presence of electromagnetic fields in combination with a finite, nonzero surface resistance, and the static thermal conduction through the coaxial cable intended to transmit rf power to a load outside the cryomodule. Both phenomena are studied in the following, in part, with additional thermalization loads being applied to the coupler as illustrated in Fig. 5.14(b) by the thermalization bar. In addition, the impact of thermal contraction on the stopband characteristics during the cool down is investigated.

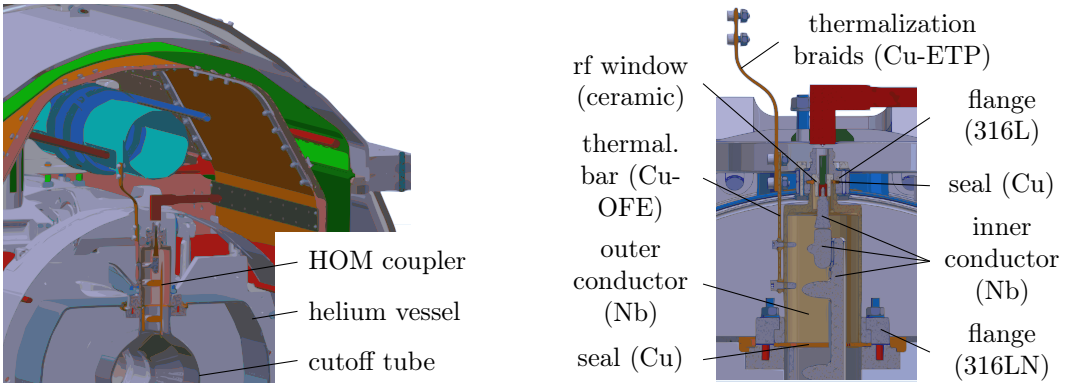

Fig. 5.14. (a) Schematic sectional view of the SPL cryomodule, with the HOM coupler opposite to the fundamental mode coupler (not shown). As the cavity, the cutoff tube on this extremity is immersed in liquid helium at 2 K. (b) Details of the HOM coupler based on the P 06 02 design. The red elbow corresponds to the rf connector and cable at the coaxial output. The copper bar on left is supposed to thermalize the coupler.

5.3.1 Dynamic Heat Load by Surface Currents

In contrast to normal conducting applications, the focus lies on peak temperatures rather than average heat losses. Once the coupler quenches, i. e. it becomes normal conducting, the dissipated rf power on the surface rises by orders of magnitude due to the abrupt increase of the surface resistance as outlined in Sec. 2.2.3. As such, the coupler may potentially burn and melt in parts [1, 129]. Depending on the operating conditions, the power dissipation may vary widely. Quantitative predictions of the dissipated power are ambiguous since it strongly depends on beam excited modes discussed in Sec. 3.4. Furthermore, the surface resistance typically underlies uncertainties, some of which will be introduced by the surface preparation. Both aspects require measurements and statistics to make a reasonable estimate of the dissipated power. Instead of calculating the temperature distribution based on distinct assumptions for the surface resistance, it is proposed to evaluate temperature ranges in correlation with the surface resistance. From those results, conditions are deduced at which the coupler can operate stably.

To begin with, the surface currents on the particular HOM coupler associated with the fundamental mode and concerned higher-order modes are computed from eigenmode simulations using ANSYS® HFSS™ software [94]. As in Sec. 5.2.3, the model involves the high-β SPL cavity, with the particular coupler being considered on both extremities. The antenna is inserted by 20 mm into the cutoff tube on either side. Figure 5.15 represents a selection of magnetic field patterns for different coupler designs and modes. The surface current associated with the n-th mode may be well described by

$$I_{s,n}^2 = \oiint_{\partial\mathbf{\Omega}_{\mathrm{hom}}} \mathbf{H}_n(\mathbf{r}) \cdot \mathbf{H}_n^*(\mathbf{r})\, dA, \tag{5.2}$$

where $\partial\mathbf{\Omega}_{\mathrm{hom}}$ corresponds to the surface of the HOM coupler involving the inner and outer conductor. Let $n=0$ be referred to the fundamental mode while an index larger one ought to be associated with individual HOMs.

Referring to Fig. 5.15(a), the magnetic field associated with the fundamental mode is mainly concentrated at the loop or probe antenna penetrating into the cutoff tube. Corresponding peak values of the electric and magnetic field strengths are summarized in Table 5.2 assuming the nominal accelerating gradient of 25 MV/m provided by the cavity. Between the designs, the surface current $I_{s,0}$ varies by 30 %. Note, field maxima and surface currents are significantly higher throughout for the HOM coupler on the tuner side due to the fact that this coupler is located closer to the cavity than the coupler on the opposite cutoff tube.[1]

Other than the fundamental mode, the selected HOMs shown in Fig. 5.15(b) are scaled such that the extracted power at the coaxial output equals 1 W. Given this normalization, corresponding surface currents summarized in Fig. 5.16 appear

[1] Details of the cavity design including cutoff tubes are given in Sec. A.2.

significantly lower than those obtained for the fundamental mode, which are listed in Table 5.2. The situation may become different if a maximum extracted power of 100 W is assumed. Note, this limit was found to be reasonable in the view of longitudinal beam dynamic studies presented in Sec. 3.4.5. It is important to remark that an extracted power in this order requires the frequency of individual HOMs to be close to harmonics of bunch pattern frequencies. In addition, the surface resistance quadratically increases with the frequency as discussed in Sec. 2.2.3. Thus, for the TM_{022} mode at 2.086 GHz, the resistance is higher by almost one order of magnitude than for the fundamental mode. Note, the quadratic increase with the frequency is well observed for frequencies below 10 GHz [130]. Thus, depending on the detailed conditions, HOMs may have a notable impact on the overall rf surface loss.

Given the modal surface currents according to (5.2), and the frequency dependence of the surface resistance, let the dissipated power density be defined as

$$\frac{\partial}{\partial A} P_{d,n}(\mathbf{r}, R_0) \leq \frac{R_0}{2} \sum_{n=0}^{N} \left(\frac{\omega_n}{\omega_0} \right)^2 \mathbf{H}_n(\mathbf{r}) \cdot \mathbf{H}_n^*(\mathbf{r}), \qquad \mathbf{r} \in \partial\boldsymbol{\Omega}_{\mathrm{hom}}, \tag{5.3}$$

with R_0 being the homogeneous surface resistance at 704.4 MHz. Due to uncertain-

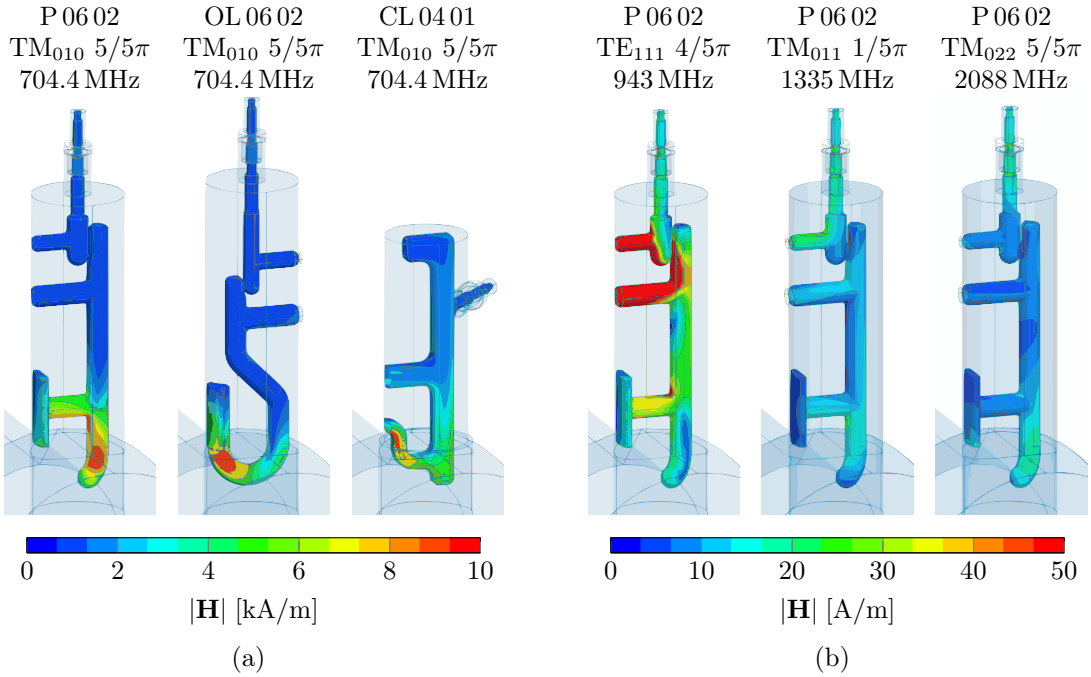

Fig. 5.15. (a) Magnetic field of the fundamental mode on the surface of different HOM couplers. Fields are scaled such that the considered high-β SPL cavity provides the nominal accelerating gradient of 25 MV/m. (b) Magnetic field of different higher-order modes on the surface of the P 06 02 coupler. Fields are scaled to an extracted power of 1 W at the coaxial output.

Table 5.2. Fundamental mode properties related to the HOM coupler surface.

design (Fig. 5.1)	left cavity side† $\lvert\mathbf{E}\rvert_{\mathrm{pk}}$ [MV/m]	$\lvert\mathbf{B}\rvert_{\mathrm{pk}}$ [mT]	I_0§ [A]	P_{ext}§ [mW]	right cavity side‡ $\lvert\mathbf{E}\rvert_{\mathrm{pk}}$ [MV/m]	$\lvert\mathbf{B}\rvert_{\mathrm{pk}}$ [mT]	I_0§ [A]	P_{ext}§ [mW]
P 04 01	13.29	10.19	69.25	14.907	3.36	3.56	24.82	0.962
P 05 02	18.64	14.04	87.88	0.494	4.56	4.59	31.56	0.043
P 06 02	18.15	14.42	94.24	0.045	4.58	5.23	33.80	0.011
CL 04 01	16.37	12.68	64.32	3.427	8.21	6.28	31.00	0.766
OL 04 01	9.64	11.91	70.49	4.412	4.51	6.03	35.29	0.455
OL 06 02	9.54	12.32	71.81	0.210	4.53	6.30	35.99	0.108

† HOM coupler is attached on the side of the tuner.
‡ HOM coupler is attached on the side of the fundamental mode coupler.
§ Values are related to a duty cycle of 10 %.

ties, it is considered as a free parameter rather than being quantitatively predicted. Note, the assumption of a homogeneous distribution is very simplified. As outlined in Sec. 2.2.3, the surface resistance strongly depends on the temperature which generally varies over the coupler surface. Consequently, the upper limit of (5.3) may be considered as conservative if R_0 is associated with the peak temperature $T_{\max}$ on the coupler surface. Apart from the fundamental mode, let the sum in (5.3) involve those modes addressed in Fig. 5.16(a). To provide worst case conditions, let the as-

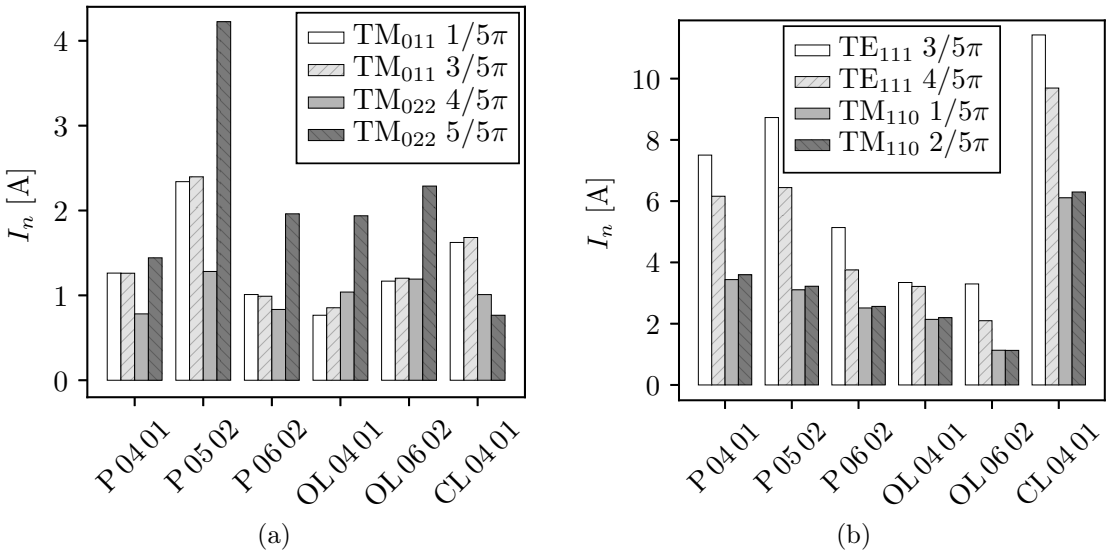

Fig. 5.16. Modal surface currents for HOM couplers on the tuner side as calculated from simulated eigenmodes using (5.2). (a) Monopole and (b) dipole modes of concern for the high-β SPL cavity, each normalized to 1 W extracted power at the coaxial output of the individually considered design.

sociated fields be scaled such that the extracted power at the coaxial output of the coupler equals 100 W in total, with the particular HOMs being weighted according to their geometric shunt resistances as listed in Table 3.6.

Due to relatively low peak magnetic fluxes in Table 5.2, R_0 may sufficiently be described by the resistance associated with the BCS theory in (2.99), that is R_{BCS}. Note, the residual resistance R_{res} for bulk niobium can be estimated to few nanoohms which is much lower than R_{BCS} [131]. In accordance to (2.95)–(2.98), let R_0 be considered as a function of the frequency ω_0, peak temperature on the coupler surface, $T_{\max}$, and the residual resistance ratio RRR, according to

$$R_0 \simeq R_{\mathrm{BCS}}(\omega_0, T_{\max}, \mathrm{RRR}). \tag{5.4}$$

Finally, $T_{\max}$ is obtained from static thermal analyses, provided the heat flux given by (5.3) and the fixed cavity temperature of 2 K. Optionally, thermalizations at the outer conductor of the coupler are considered, similar to the configuration shown in Fig. 5.14(b). The thermal conductivity of niobium varies significantly with the residual resistance ratio. For this reason, the subsequent analyses consider bulk niobium of two different purities, that are RRR = 60 associated with a thermal conductivity taken from [132], and RRR = 300 with the corresponding thermal conductivity found in [133]. Further details on the model including boundary conditions and materials, can be found in [117]. The peak temperature resulting from simulations using ANSYS® software [134], may be considered as a function of the reference surface resistance R_0 and material purity according to

$$T_{\max} = \max_{\mathbf{r}}\{\mathrm{T}(\mathbf{r}, R_0, \mathrm{RRR})\}, \qquad \mathbf{r} \in \partial\boldsymbol{\Omega}_{\mathrm{hom}}. \tag{5.5}$$

Instead of solving the implicit problem given by (5.4) and (5.5) directly, a graphical approach is applied. This allows the deduction of conditions for a stable operation.

Figure 5.17 shows the results of thermal studies for the P 06 02 design assuming both the low and high RRR values. It depicts the simulated maximum temperature on the coupler surface as a function of the reference surface resistance R_0 according to (5.5). Because of notably larger surface currents, the HOM coupler is considered on the tuner side (Table 5.2). Furthermore, three conditions are compared. In the first scenario, the thermalization bare of Fig. 5.14(b) ought to be disregarded while in the second and third scenarios, the outer conductor of the HOM coupler is thermalized via the additional copper bar at 4 K or 2 K, respectively. In order to find the solutions which fulfill (5.4) and (5.5), the inverse function of the BCS surface resistance[2] is depicted for three different frequencies to allow for uncertainties. The

[2]The BCS surface resistances are related to the properties of bulk niobium. They were calculated as in [135] for a critical temperature of $T_c = 9.2\,\mathrm{K}$, a superconducting energy gap of $\Delta = 1.85 k_B T_c$ referring to strong coupling, a London penetration depth of $\lambda_L = 32\,\mathrm{nm}$ and the mean free path being correlated to the material purity according to $\xi = 2.7\,\mathrm{RRR}$.

latter are highlighted in gray. Referring to the simulated temperatures highlighted in blue in Fig. 5.17, their interceptions with the gray zones yield most likely a thermal equilibrium. If due to any transitional effect such as pressure fluctuations, a non-equilibrium state left from the gray zone is taken, then the temperature would rise until entering in an equilibrium state, if any. On the other hand, the temperature would decrease if a state right from the gray zone is taken. For example in Fig. 5.17(a), the coupler will never have a stable temperature below 4.2 K, provided it is thermalized at 4 K. In contrast, without the thermalization bar, the temperature could always return to close to 2 K as long as $R_0 < 5\,\mu\Omega$. Note, in general, a thermalization at 4 K seems inefficient. Using a thermalization bar at 2 K, the cooling mechanism acts only for $T_{\max} > 6\,\mathrm{K}$. Referring to RRR = 60 in Fig. 5.17(a), the results indicate a stable operation up to a temperature of $8 \pm 0.5\,\mathrm{K}$ and $R_0 \leq 10\,\mu\Omega$. The thermalization at 2 K may allow half a degree more and twice the surface resistance. Since surface resistances in this order are very high and unlikely, the coupler would generally operate at temperatures close to 2 K. For RRR = 300 shown in Fig. 5.17(b), the peak temperature may not even exceed 2.1 K up to surface resistances of $R_0 > 0.1\,\mathrm{m}\Omega$ in a non-equilibrium state. By applying a safety margin, a temperature range of $T \leq 7\,\mathrm{K}$ on the coupler surface may be deduced from Fig. 5.17 in order to ensure a stable operation. It is important to remark that this threshold remains valid in the presence of additional loads, for instance, the static thermal conduction through the rf cable as considered next.

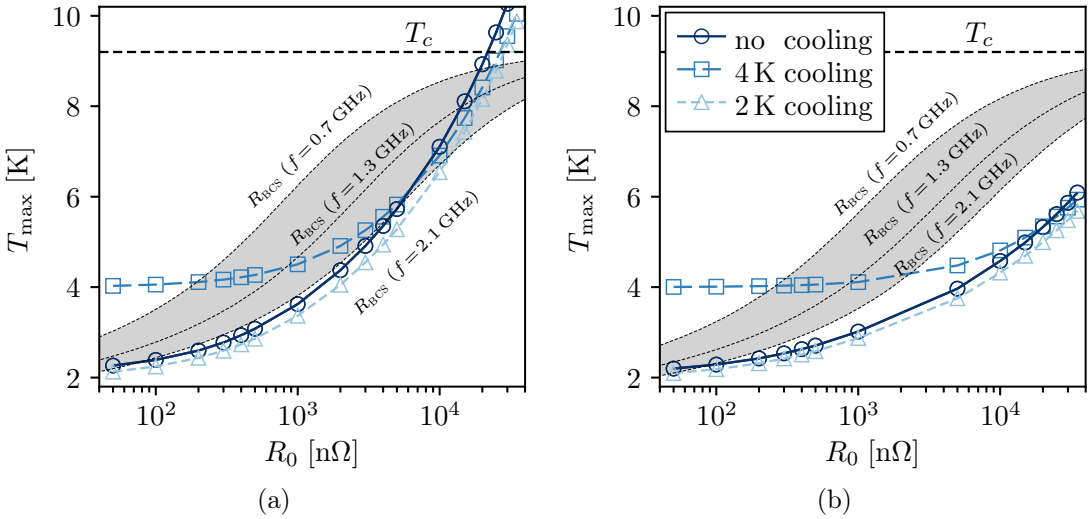

Fig. 5.17. Maximum temperature on the P 06 02 coupler surface versus the surface resistance for different thermalization conditions. The HOM coupler is considered on the tuner side of the cavity. The critical temperature of 9.2 K is highlighted in dashed. For comparison, the BCS resistance as calculated in [135] is depicted for different frequencies. A thermal equilibrium is likely to only exist within the gray highlighted zones. (a) RRR = 60. (b) RRR = 300.

5.3.2 Static Heat Load by Thermal Conduction

The rf cable highlighted in Fig. 5.18 is intended to transmit power associated with parasitic HOMs to a load outside the cryomodule. However, the thermal conduction and additional rf losses along the coaxial line add another heat load to the HOM coupler, which is investigated in the following.[3] This section presents some of the results reported in [136]. They refer to the P 06 02 design considered on the fundamental mode coupler side. Unlike the power deposition on the coupler surface caused by electromagnetic field as discussed in Sec. 5.3.1, static conduction through the rf cable significantly impacts the thermal load of the coupler. This may be easily seen from the simplified one-dimensional problem of heat transfer due to steady-state thermal conduction. Disregarding rf losses, the rate of heat flow Φ_{con} is given by the temperature gradient and thermal conductivity k along the cable according to

$$\Phi_{\mathrm{con}} = \frac{A}{L}\int_{z_1}^{z_2} k(T)\frac{dT}{dz}dz = \frac{A}{L}\int_{T_1}^{T_2} k(T)dT, \tag{5.6}$$

where A and L refer to the cross-sectional area or length of the cable, respectively. Given the data in [136, 137], for a coaxial cable of $L = 1.2\,\mathrm{m}$ length whose outer conductor is made of corrugated copper while the inner conductor corresponds to a copper-clad aluminum wire with cross-sectional areas of $6.4\,\mathrm{mm}^2$ or $18.1\,\mathrm{mm}^2$, respectively, the rate of heat flow becomes approximately 2.5 W between the HOM coupler at $T_1 = 2\,\mathrm{K}$ and the environment outside the cryomodule at $T_2 = 293\,\mathrm{K}$.

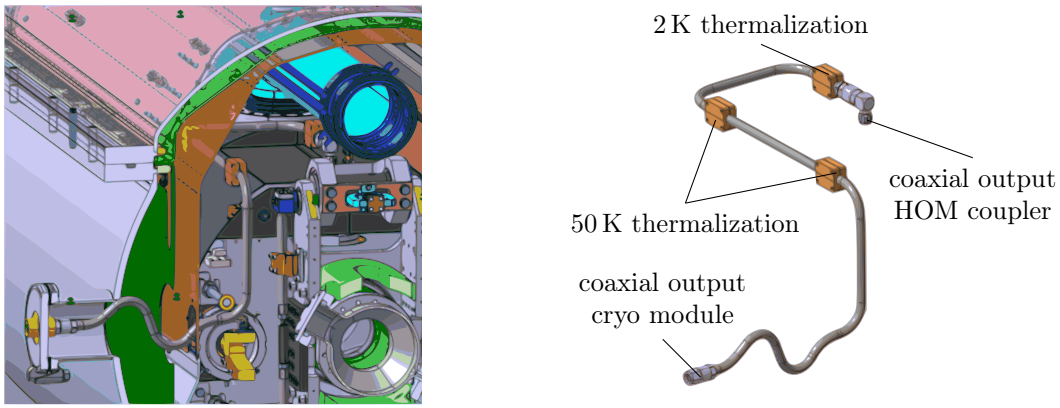

(a) (b)

Fig. 5.18. (a) Schematic sectional view of the SPL cryomodule showing the rf cable connected to the HOM coupler on the tuner side. (b) Detailed view of the rf cable with several intercepts to thermalize the outer conductor so that the thermal load on the coupler is reduced.

[3] The studies are mainly carried out by J. Apeland and may be considered as a continuation and refinement of initial investigations presented in [117].

To reduce the thermal load on the coupler, several heat intercepts are added along the cable as illustrated in Fig. 5.18(b). They are supposed to thermalize the outer conductor at temperatures of 2 K or 50 K.

Temperature profiles for the inner and outer conductor of the final configuration are shown in Fig. 5.19. They are obtained from static thermal analyses using ANSYS® software [134]. Note, all the loads of Sec. 5.3.1 are involved in the simulations. A copper bar attached to the outer conductor of the HOM coupler on one side and a 2 K helium supply line on the other side as illustrated in Fig. 5.14, allow thermalizing the coupler at the corresponding temperature. Unlike Sec. 5.3.1, only the scenario of a 2 K thermalization is discussed. In addition, rf losses within the cable are accounted by a constant attenuation per unit length. The values $\alpha = 0.25\,\mathrm{dB/m}$ and $\alpha = 0.53\,\mathrm{dB/m}$ are chosen such that the corresponding losses are respectively at least twice or four times as high as for common low-loss coaxial cables with foam-dielectric if operating at the frequency of 1 GHz and room temperature [137, 138]. Referring to Fig. 5.19, the maximum temperature gradient between inner and outer conductor occurs at the second 50 K thermalization seen from the coupler. Depending on the predefined cable attenuation, it is in the order of 60 K or 94 K, which is considered as acceptable. Note, thermalizing the inner conductor, for instance, by using sapphire as dielectric material [10], is relatively complex and should only be considered if it is absolutely necessary.

The profiles depicted in Fig. 5.19 approximately apply to both residual resistance ratios addressed in the previous section. However, the temperature on the coupler surface as shown in Fig. 5.20 considerably differs between niobium of RRR = 60

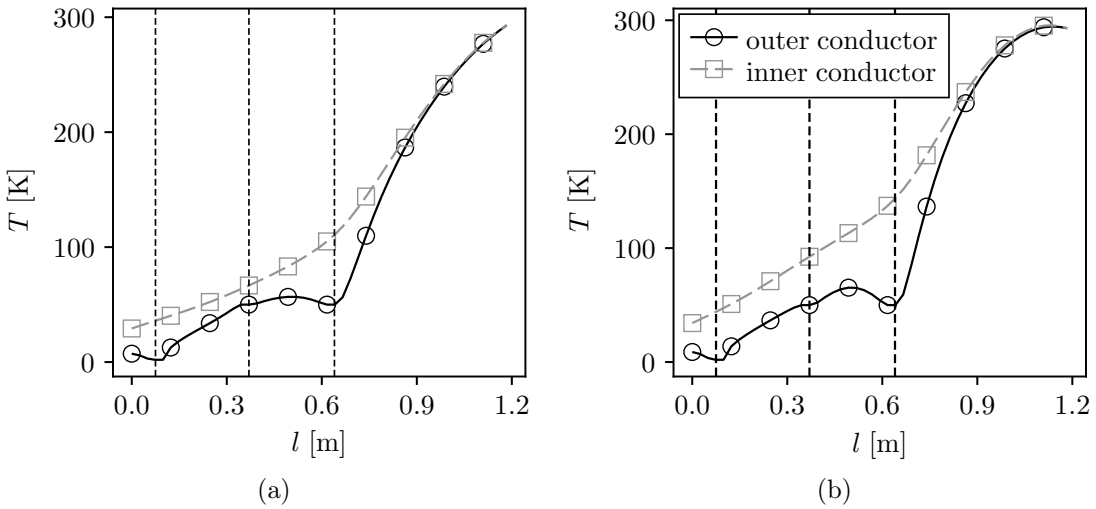

Fig. 5.19. Temperature of inner and outer conductor along the coaxial cable according to the configuration of Fig. 5.18(b), with the intercepts being highlighted by dashed lines. Cable losses of (a) $\alpha = 0.25\,\mathrm{dB/m}$ and (b) $\alpha = 0.53\,\mathrm{dB/m}$ are considered as well as loads of Sec. 5.3.1.

and RRR = 300 due to the higher thermal conductivity of the latter one. It is important to note that the simulations assume perfect thermal contacts everywhere. Consequently, the heat transfer through the rf cable is conservatively estimated. Referring to Fig. 5.20(a), even in the presence of lower rf losses along the coaxial cable, the peak temperature at the antenna tip clearly exceeds the previously defined limit of 7 K for RRR = 60. Indeed a value of RRR = 300 is required to ensure that the coupler remains superconductive during operation even for a larger cable attenuation as depicted in Fig. 5.20(b). The only exception is the inner conductor part attached to the feedthrough shown at the top of Fig. 5.14(b). Temperatures of more than 20 K in this region favor the fabrication of this component out of copper. Table 5.3 summarizes the thermal loads and the rates of heat flow at each thermalization for the different scenarios related to rf losses in the cable. Note, the values only marginally vary between the considered residual resistance ratios as found in [136].

The results underline the need of thermalizing the HOM coupler. A relatively simple integration of a thermalization bar as previously described appears sufficient. It is not necessary to foresee internal cooling pipes within the antenna to be actively cooled by liquid helium at 2 K [16, 101].

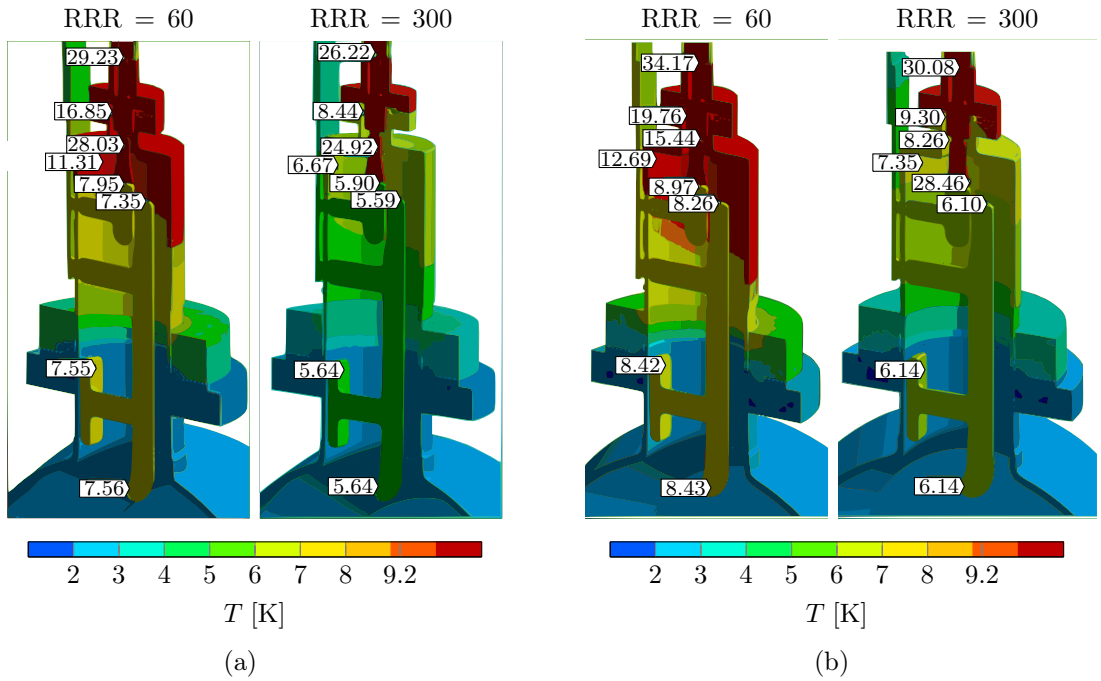

Fig. 5.20. Temperature distribution on the coupler surface as a result of the power deposition by electromagnetic fields, the static thermal conduction through the rf cable and thermalization bar as well as the constant temperature of the cutoff tube being immersed in liquid helium at 2 K. In addition, cable losses of (a) $\alpha = 0.25\,\mathrm{dB/m}$ and (b) $\alpha = 0.53\,\mathrm{dB/m}$ are considered. For each case, two different thermal conductivities of niobium according to the RRR value are compared.

Table 5.3. Power considerations.

probe	case study 1 $\alpha = 0\,\mathrm{dB/m}$	case study 2 $\alpha = 0.25\,\mathrm{dB/m}$	case study 3 $\alpha = 0.53\,\mathrm{dB/m}$
dissipated rf power on coupler†	0.062 W	0.062 W	0.062 W
dissipated rf power in cable	-	6.800 W	13.600 W
cutoff tube at 2 K	−0.559 W	−1.029 W	−1.407 W
thermalization braids at 2 K	−0.492 W	−0.846 W	−1.105 W
cable thermalization at 2 K	−1.788 W	−2.442 W	−3.141 W
total at 2 K	−2.839 W	−4.317 W	−5.653 W
first cable thermal. at 50 K	1.592 W	0.441 W	−0.950 W
second cable thermal. at 50 K	−1.949 W	−4.197 W	−6.474 W
total at 50 K	−0.357 W	−3.756 W	−7.424 W
ambient at 293 K	3.133 W	1.210 W	−0.585 W

† Estimate from the previous studies assuming the HOM coupler operates stable in the superconducting state and extracts about 100 W in total at the coaxial output.

5.3.3 Impact of Thermal Contraction

The impact of thermal contraction on the frequency response, in particular, with respect to stopband characteristics in the vicinity of the fundamental mode, is another important design aspect of HOM couplers. This section presents computational and experimental studies on this subject using the test facility shown in Fig. 5.21.

Similar to Sec. 3.5.3 the frequency response of the filter part slightly alters when

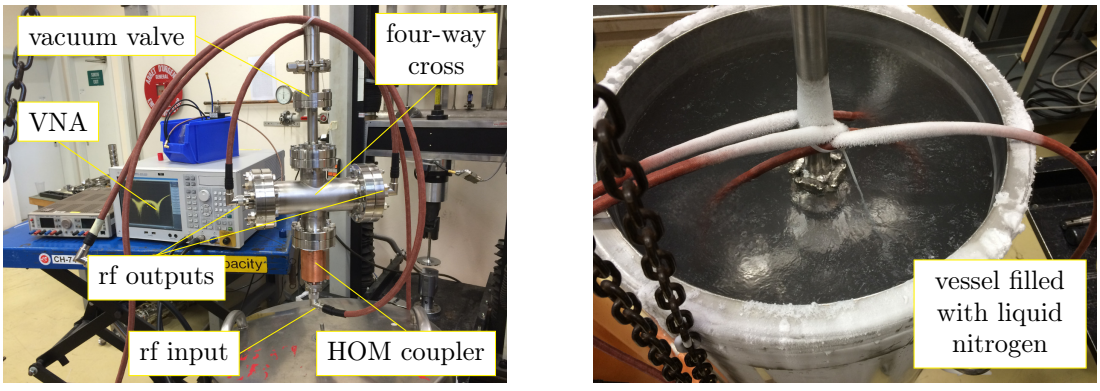

(a) (b)

Fig. 5.21. (a) Test stand to characterize the frequency response of the HOM coupler during cooldown. The coupler is located on the bottom side of the four-way cross while both rf output ports are connected to form a coaxial waveguide on which the HOM coupler is mounted. One of the rf output ports is reflection-free terminated. The remaining port on the top side of the four-way cross is preserved for the vacuum valve. (b) The assembly plunged into the nitrogen bath at 77 K.

cooling the coupler from room temperature, i. e. 293 K down to the operating temperature of 2 K. In addition, the ambient environment changes from normal air with 50 % humidity and atmospheric pressure to vacuum, which alters the relative permittivity ε_r and, thus, the frequency as well [109]. The multi-physics problem is examined by numerical simulations using ANSYS® APDL™ macros [139], with the details being reported in [140]. Quantitative predictions are in part verified by experimental studies using the solid prototype shown in Fig. 5.6(b). In order to measure the frequency response under vacuum and cryogenic temperatures, the coupler is mounted on a custom-built four-way cross as shown in Fig. 5.21(a). The cross is further equipped with an inner conductor connecting the rf outputs to mimic a coaxial waveguide on which the coupler is mounted. The remaining port on the top of the four-way cross in Fig. 5.21(a) is preserved for the vacuum valve. Further details of the assembly can be found in Sec. A.5. The facility is cooled down to 77 K by liquid nitrogen as depicted in Fig. 5.21(b). Since the coupler is fabricated out of copper it is not reasonable to apply liquid helium at 2 K. Moreover, approximately 90 % of the expected structural contractions occur from 293 K to 77 K [141, pp. 26].

Figure 5.22 shows the simulated and measured transmission power gain between the coaxial port of the HOM coupler and one of the coaxial ports provided by the four-way cross while the other one is reflection-free terminated. Measurements and simulations agree reasonably well and reveal positive frequency shifts of 2 MHz to 3 MHz for the finite transmission zeros associated with the equivalent mid-series and mid-shunt ladders. The corresponding simulated structural displacements are depicted in Fig. 5.23(a). The displacement field appears relatively homogeneous since the stainless steel flange provides nearly the same thermal contraction as the

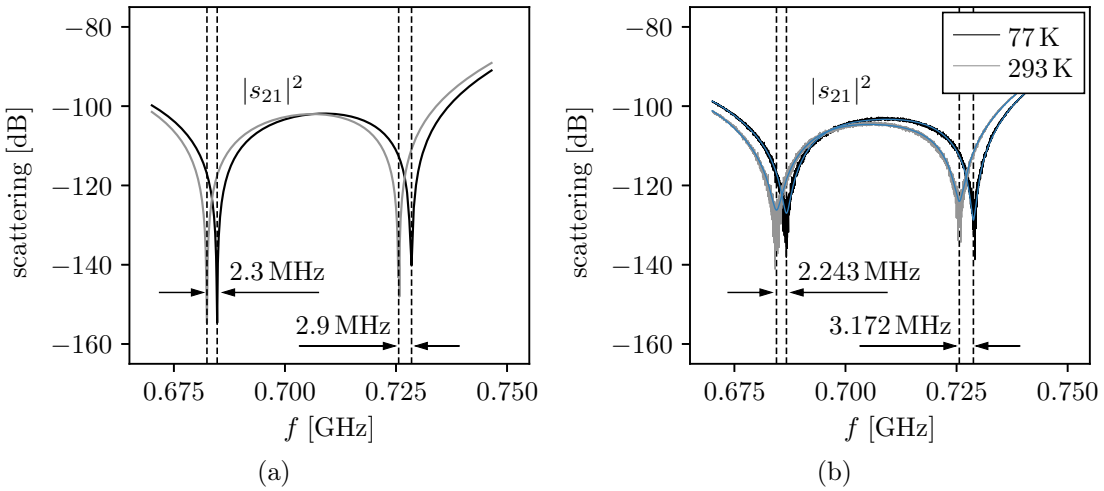

Fig. 5.22. (a) Simulated and (b) measured transmission power gain $|s_{21}|^2$ between the coaxial port of the P 06 02 coupler prototype and one of the coaxial ports provided by the four-way cross according to Fig. 5.21(a). In blue, vector fits applied on measured data.

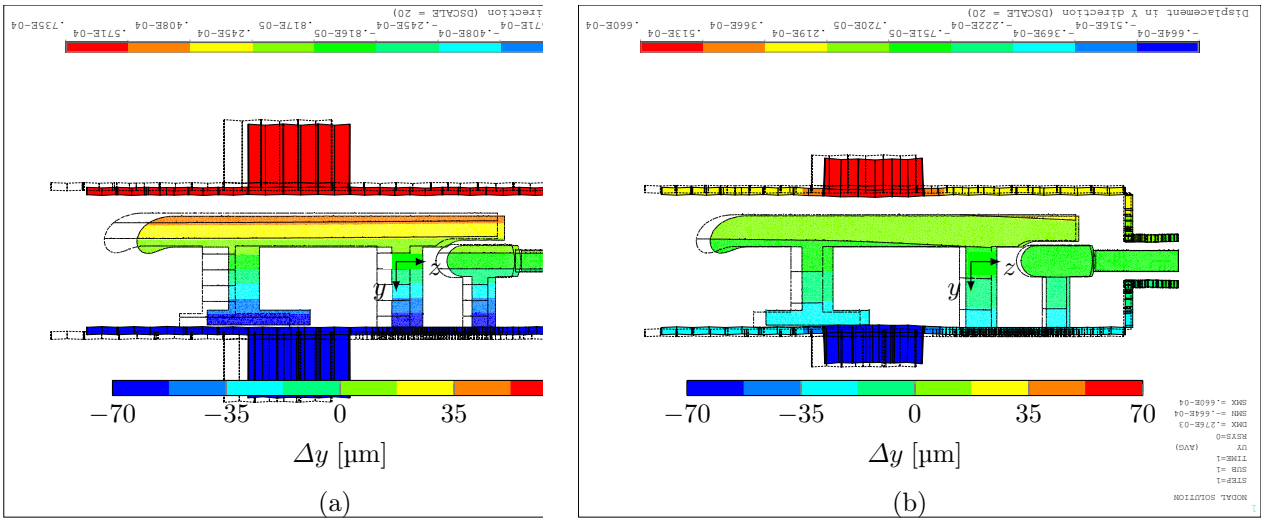

Fig. 5.23. Simulated contraction of the P 06 02 coupler including the stainless steel flange. The displacements in y-direction are scaled by a factor of 10 to illustrate the contraction with respect to room temperature, i. e. 293 K. (a) Solid copper prototype as shown in Fig. 5.6(b) cooled down to 77 K. (b) Equivalent coupler made of niobium and cooled down to 2 K.

outer and inner conductor parts of the HOM coupler made of copper. The situation becomes very different if niobium is considered instead of copper for the latter one. Note, niobium is characterized by a thermal expansion coefficient being approximately half the corresponding value provided by copper or stainless steel [142, p. 111]. As a consequence, the capacitive gap of the mid-series ladder becomes distorted in the region of the flange when cooling the structure from 293 K down to 2 K. This is illustrated in Fig. 5.23(b) by means of numerical simulations for the P 06 02 coupler made of niobium and equipped with a stainless steel flange. The corresponding frequencies of finite transmission zeros decrease by approximately 3 MHz during the cool-down, which is in contrast to the qualitative temperature dependence observed in Fig. 5.22. A similar behavior is observed for the OL 06 02 design with negative frequency shifts in the order of 8 MHz to 9 MHz.

5.4 Multipacting

The phenomenon of an avalanche-like growth of free electrons, first observed by Henneberg [143], occurs frequently during rf conditioning of cavities and couplers. It requires free electrons to be resonantly driven by an rf field such that the cavity wall or coupler surface is repetitively impacted at nearly the same locations. Under this condition, secondary-emission processes may lead to a resonant growth of free electrons. The temperature rapidly rises at the affected locations which ultimately causes excessive rf losses, in particular, for superconducting applications. Since multipacting may considerably extend the processing time of an rf device (soft barriers) or even limit its performance (hard barrier), it should be assessed in the design phase.

In order to evaluate conditions under which multipacting may occur, the equation of motion for electrons exposed to an electromagnetic field is usually solved numerically. Analytical solutions exist only for relatively simple problems such as the harmonic field between parallel plates of infinite size [17, pp. 189] or the TEM mode propagating through a coaxial waveguide of infinite length [144]. The problem of interest is given by the fundamental mode being excited in the high-β SPL cavity while investigating particle trajectories within the HOM coupler attached on the tuner side. During the rf conditioning phase, there is no beam present which may excite any HOMs. Thus, it is reasonable to focus on the fundamental mode, only. Furthermore, it can be assumed that eventual multipacting barriers will likewise apply if the same coupler is considered at the opposite cutoff tube, however, at slightly higher field levels due to the larger distance from the cavity.

Numerical simulations are carried out using ACE3P [145, 146]. At first the electromagnetic field is calculated from an eigenmode simulation. Subsequent statistical analyses by means of 10^4 to 10^5 macro-particles being tracked over 50 to 100 rf cycles, allow exploring resonant particles which repetitively impact the coupler surface at approximately the same locations. Due to limited computational resources, the second part is split over several independent simulations. For this purpose, let the particular coupler be partitioned into subdomains such as sketched in Fig. 5.24(a) for the P 06 02 design. Then, the initial particle emission succeeds from a fraction of the coupler surface, only, which is given by the individually considered region. Furthermore, each simulation incorporates three separate field scans to cover a total range for the accelerating gradient from 5 kV/m to 30 MV/m.

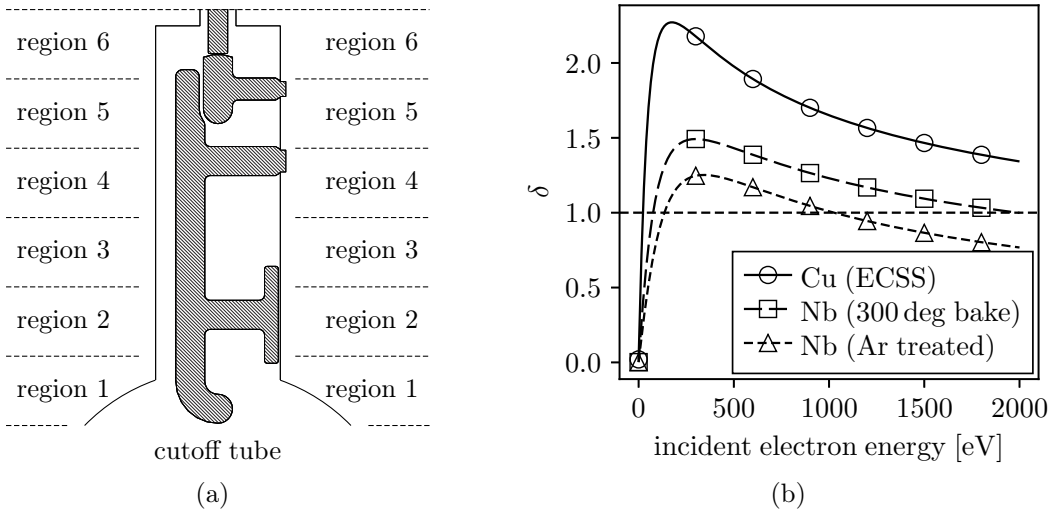

Fig. 5.24. (a) Partition of the coupler surface to provide local initial field emissions. (b) Secondary-emission yield (SEY) for different materials and treatments as a function of the incident electron energy as found in [91].

Secondary-emission processes are described by probabilistic models with characteristic parameters, such as, the secondary-emission yield (SEY) δ and emitted-energy spectrum of secondary electrons [147]. Only the first parameter is used for the numerical studies, which is defined as the ratio of the secondary electron current I_s emitted from the surface, and the corresponding incident electron beam current I_0 according to

$$\delta = \frac{I_s}{I_0}. \tag{5.7}$$

The yield varies with the kinetic energy of incident electrons as shown in Fig. 5.24(b) for different materials and treatments. The data are extracted from the material library provided in [91]. They apply for an incident angle of 0 deg which is a reasonable assumption in the view of electric field lines being quasi perpendicular to the superconductive surface. Referring to Fig. 5.24(b), the SEY of niobium after 300 degC baking is larger than unity for an incident electron energy between 80 eV and 2000 eV. In this regime, the emission of secondary electrons is possible and may favor an exponential growth of charged particles.

The subsequent analyses refer to the P 06 02 and OL 06 02 couplers as well as modifications of them. The electron growth within couplers is studied for copper and niobium after 300 degC baking to compare different yields. Resonant particles as indicator for multipacting are identified in three distinct locations on the coupler surface for both designs. They are separately assessed in the following. Similar analyses can be found, for example, in [85, 104, 148–150].

5.4.1 Mid-Series Ladder

Resonant particles may occur between the capacitive plate of the equivalent mid-series ladder and the outer conductor of the HOM coupler. This is shown in Fig. 5.25 for various designs, with macro-particles being initially emitted from surfaces of 'region 2' according to Fig. 5.24(a). The corresponding incident energy of these resonant particles as well as the average electron enhancement after 70 rf cycles are shown in Fig. 5.26.

The capacitive plate of the original P 06 02 design depicted in Fig. 5.25(a) is characterized by relatively small curvature radii at the boundary. Resonant particles are observed at accelerating gradients from 0.1 MV/m to 0.35 MV/m. However, the corresponding incident energy is well below 80 eV which means that, on average, no secondary electrons are emitted from the surface if referring to niobium after 300 degC baking. Instead, incident particles will be absorbed as indicated by the average electron enhancement being less that unity in Fig. 5.26(b). Unlike niobium, an incident electron energy in the order of 25 eV to 50 eV can be sufficient to emit secondary electrons from a copper surface. A maximum average electron enhancement of approximately 1.25 is found in this case. The capacitive plate of the modified P 06 02 design depicted in Fig. 5.25(b) provides larger curvature radii

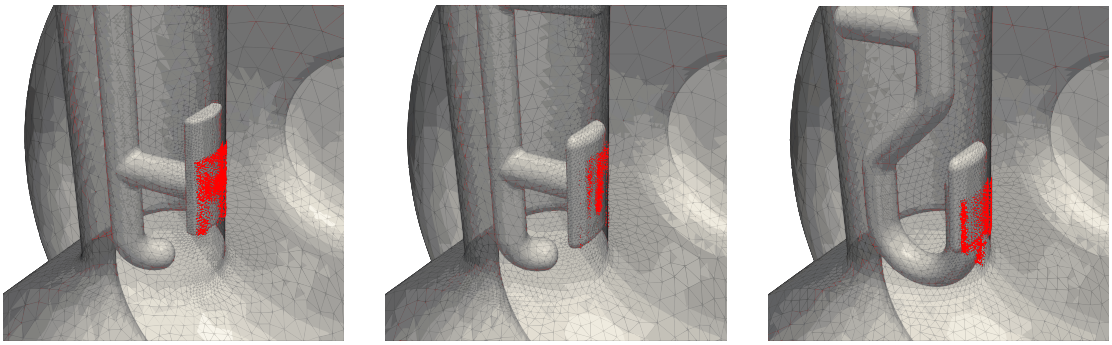

(a) plate 1 (b) plate 2 (c) plate 3

Fig. 5.25. Resonant particles highlighted in red between the outer conductor and the capacitive plate of the equivalent mid-series ladder. Three different geometries with respect to the capacitive plate are compared. (a) Original P 06 02 design. (b) Modified P 06 02 design with increased radius of curvature. (c) Modified OL 06 02 design with increased radius of curvature.

at the boundary than in the previously considered model. It permits a further reduction of the incident electron energy of resonant particles to values below 30 eV. As a result, the average electron enhancement becomes close to unity for copper and below 0.5 for niobium. Likewise before, the capacitive plate of the modified OL 06 02 design depicted in Fig. 5.25(c) is characterized by large curvature radii at the boundary. Compared to the previous designs, the observed resonant particles

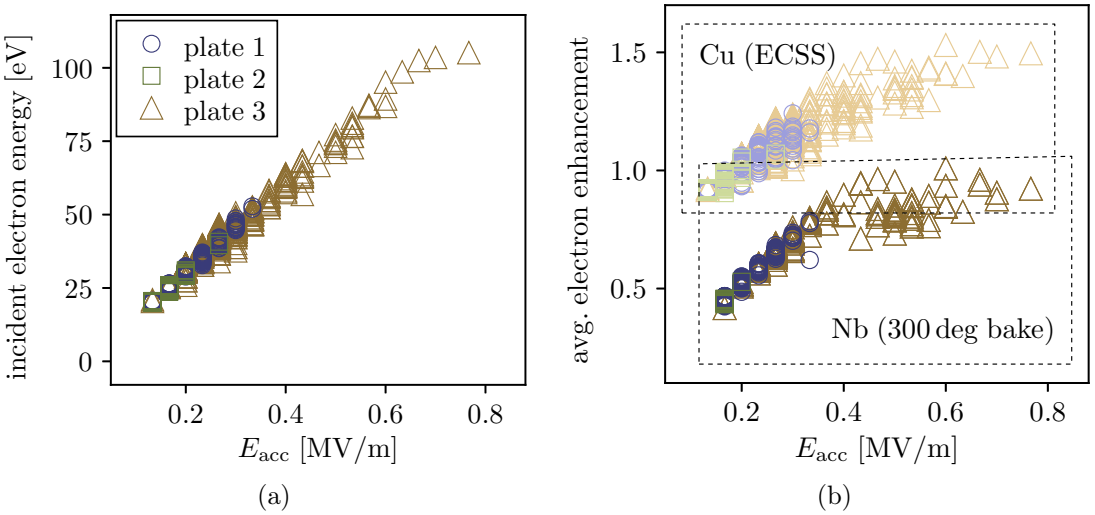

(a) (b)

Fig. 5.26. (a) Incident electron energy and (b) average electron enhancement after 70 rf cycles for resonant particles shown in Fig. 5.25. Darker markers refer to average growth rates obtained for niobium after 300 degC baking while the lighter colors are related to copper according to the characteristic SEYs shown in Fig. 5.24(b).

occur over a larger field range from 0.1 MV/m to 0.8 MV/m, which is owed by the loop antenna. Nevertheless, the average electron enhancement remains below unity for niobium. Consequently, multipacting seems to be well suppressed in the vicinity of equivalent mid-series ladders.

5.4.2 Mid-Shunt Ladder

Similar to the previous case of the equivalent mid-series ladder, resonant particles may occur between the capacitive plates of the equivalent mid-shunt ladder as illustrated in Fig. 5.27 for various designs, with the macro-particles being initially emitted from surfaces of 'region 5' according to Fig. 5.24(a). All designs are related to the P 06 02 coupler. The incident energy of resonant particles and corresponding average electron enhancement after 70 rf cycles are shown in Fig. 5.28.

The capacitive plate on the right-hand side of the original P 06 02 design depicted in Fig. 5.27(a) is characterized by a concave profile. Resonant particles occur in this region for accelerating gradient between 10 MV/m to 17 MV/m, with an incident electron energy being partially above 80 eV. A multipacting barrier emerges for niobium at field levels approximately from 14 MV/m and 17 MV/m, which is indicated in Fig. 5.28(b) by the average electron enhancement being larger than unity. The geometry is successively adapted in order to ultimately suppress multipacting in this region while maintaining filter characteristics of the coupler. As shown in Fig. 5.27, the capacitive plate on the right-hand side was changed from the original concave profile to a flat profile and then to a convex one. In the latter case, the field level at which resonant particles may occur is significantly reduced to approximately 3 MV/m to 5 MV/m, while there incident electron energy falls below 80 eV.

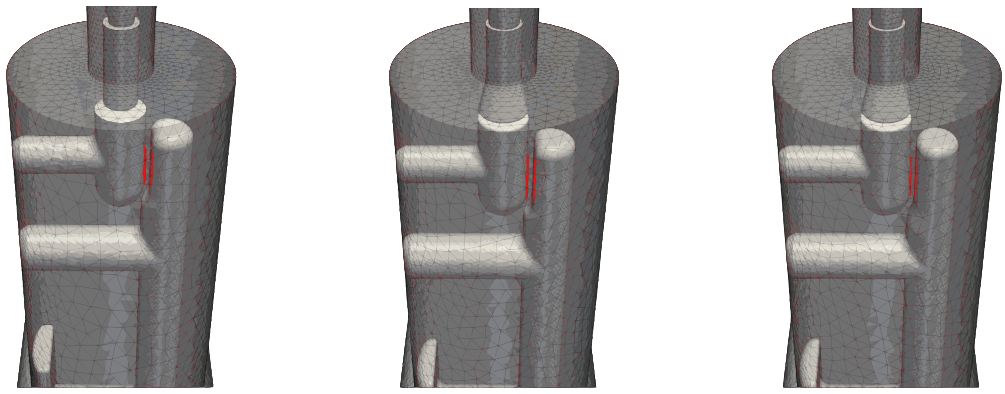

(a) concave (b) flat (c) convex

Fig. 5.27. Resonant particles highlighted in red between the capacitive plates of the equivalent mid-shunt ladder. Different geometries with respect to the capacitive plate on the right-hand side are compared, each related to the P 06 02 coupler. (a) Original design with a concave plate, (b) modified design with a flat plate, and (c) modified design with a convex plate.

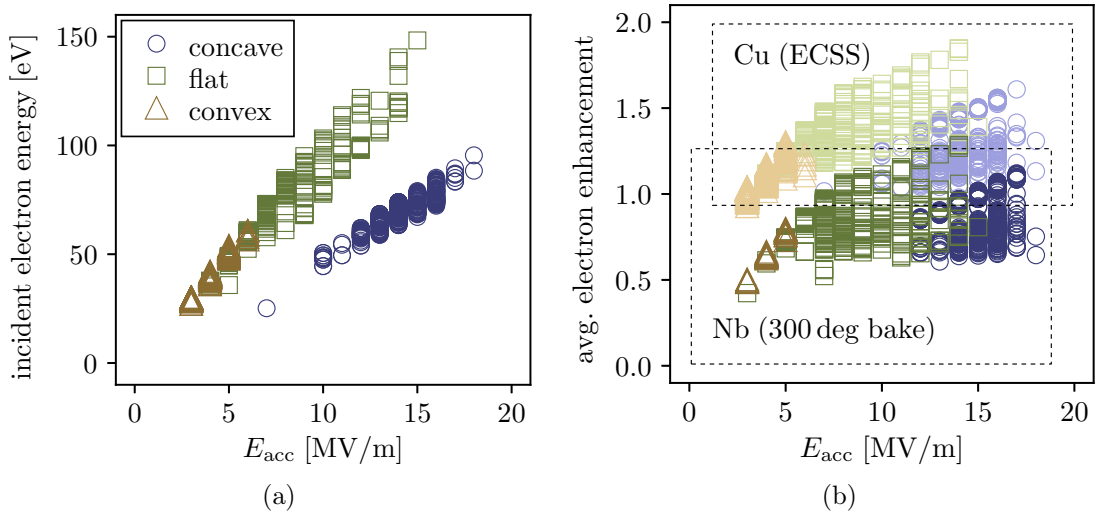

Fig. 5.28. (a) Incident electron energy and (b) average electron enhancement after 70 rf cycles for resonant particles shown in Fig. 5.27. Darker markers refer to average growth rates obtained for niobium after 300 degC baking while the lighter colors are related to copper according to the characteristic SEYs shown in Fig. 5.24(b).

Consequently, the average electron enhancement is throughout lower than unity for niobium. Note, the same modification with slightly different dimensions is applied to the OL 06 02 coupler with equal success.

Trivia: The vertically oriented capacitor at the top of the designs shown in Fig. 5.27 is not affected by multipacting. It was modified barely because of mechanical reasons, such as, a larger gap size.

5.4.3 Antenna

Finally, resonant particles may occur between the inner and outer conductor of the HOM coupler close to the probe or loop antenna. This is shown in Fig. 5.29 for various designs, with macro-particles being initially emitted from surfaces of 'region 1' according to Fig. 5.24(a). The incident energy of these resonant particles which appear at the rear side of the antennas, and corresponding average electron enhancement after 70 rf cycles are shown in Fig. 5.30.

The probe antenna of the original P 06 02 design depicted in Fig. 5.29(a) permits resonant particles at field levels from 13 MV/m to 18 MV/m, with the incident electron energy being widely spread from 50 eV to 1800 eV. Despite the large average electron enhancement of around 1.3, most of the particles reveal a very short life time of less than 15 rf cycles, hence no electron growth in the long term is possible. A slight modification of the probe antenna which is shown in Fig. 5.29(b) provides qualitatively the same behavior as before but at lower accelerating gradients, that is approximately from 7 MV/m to 13 MV/m. As for the original probe antenna, the

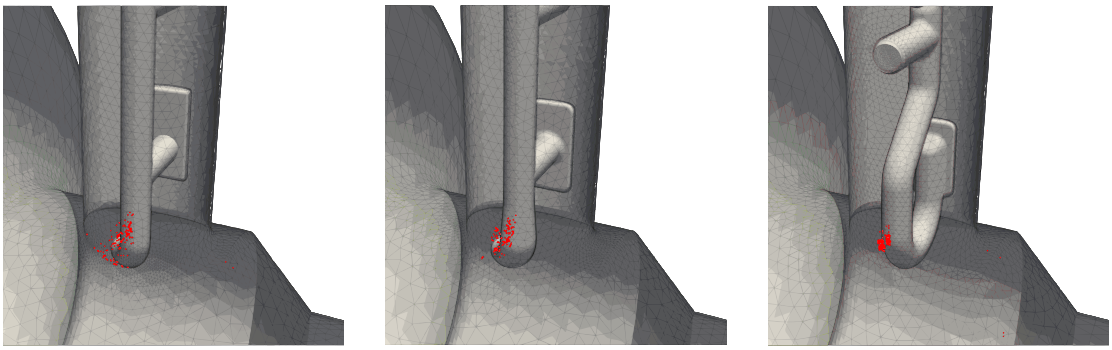

(a) antenna 1 (b) antenna 2 (c) antenna 3

Fig. 5.29. Resonant particles highlighted in red between the inner and outer conductor at the rear side of the antenna. Three different geometries are compared with respect to the antenna shape. (a) Original P 06 02 design using a probe antenna. (b) Modified P 06 02 design with increased thickness of the antenna tip. (c) Original OL 06 02 design using an open-loop antenna.

interpretation as multipacting is vague due to the fact that most of the particles ultimately slip out of resonance after a certain amount of rf cycles [150]. The situation becomes very different for the open-loop antenna of the OL 06 02 design depicted in Fig. 5.29(c). Resonant particles are observed at accelerating gradients from around 17 MV/m to 22 MV/m and above 27 MV/m. The second regime is characterized by incident energies which clearly favor secondary-emission processes for niobium.

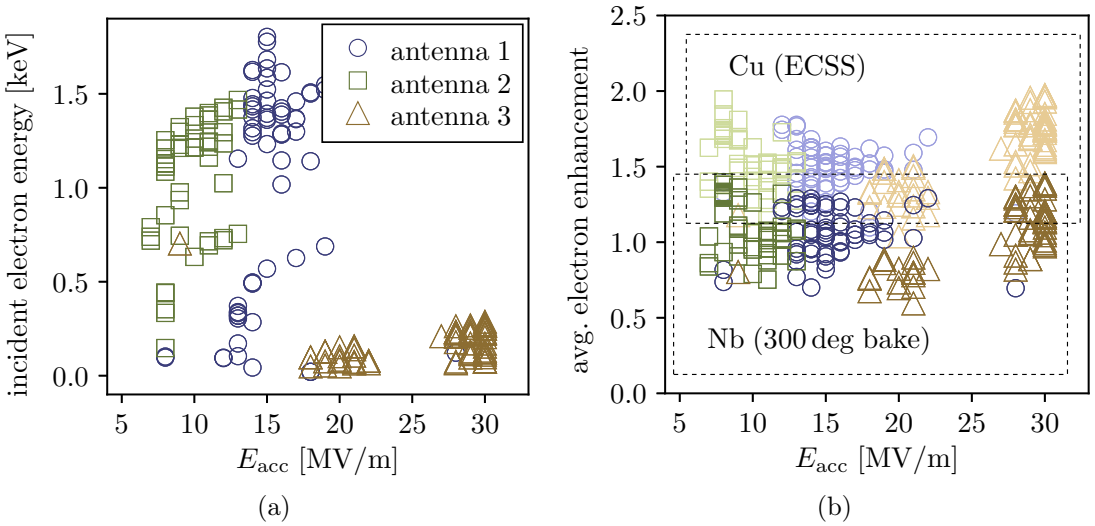

(a) (b)

Fig. 5.30. (a) Incident electron energy and (b) average electron enhancement after 70 rf cycles for resonant particles shown in Fig. 5.29. Darker markers refer to average growth rates obtained for niobium after 300 degC baking while the lighter colors are related to copper according to the characteristic SEYs shown in Fig. 5.24(b).

However, since the cavity is operated at 25 MV/m, any multipacting barrier beyond this field level is regardless. Hence, the design is acceptable with respect to the specifications.

5.5 Summary of the Results

The various design aspects of HOM couplers foreseen for the high-β SPL cavity have been presented. The topological approach for a coupler design is quite heuristic in the view of this multi-physical problem, which is why different designs have been extensively compared to each other after individual optimizations.

HOM couplers providing solely one transmission zero at finite, nonvanishing frequency being tuned to the fundamental mode are highly sensitive to manufacturing tolerances and structural deformations. The high sensitivity which manifests in the rejection of the fundamental mode, applies to the P 04 01, OL 04 01, and CL 04 01 couplers shown in Fig. 5.1. It is worthwhile to note that most of the superconducting HOM couplers found in practice belong to this class and require a precise tuning of the particular band-stop filter during the installation to avoid excessive rf losses when it comes to operation [1]. In contrast, the somewhat more complex P 05 02, P 06 02, and OL 06 02 couplers form the stopband by two transmission zeros at finite, nonvanishing frequency. They achieve the required reflection for the fundamental mode over notably large frequency ranges of more than 100 MHz. Such couplers are found to be very robust against manufacturing errors and structural deformations, for instance, due to thermal contraction.

External coupling factors of concerned HOMs are, in part, difficult to push below $Q_{\text{ext}} = 10^5$ independent of the coupler design. This is primarily due to the cutoff tubes providing too large distances between the cavity and aperture foreseen for the HOM coupler. The particular probe or loop antenna must be inserted into the cutoff by 15 mm to 20 mm to guarantee the desired mode damping.

The thermal behavior of all considered couplers is similar and dominated by the static thermal conduction through the rf cable rather than by the electromagnetic field inside the cavity. A thermalization at 2 K on the coupler tube and further heat intercepts on the rf cable are required to sufficiently reduce the thermal load for the coupler. No active cooling of the antenna by internal pipe flows is needed.

Finally, slight modifications of the favored P 06 02 and OL 06 02 couplers allowed the initially observed multipacting barriers to be suppressed reasonably well for the relevant field levels while keeping the filter characteristics. For comparison, adopted designs of the TESLA coupler are typically characterized by relatively large multipacting barriers [150, 151].

Several prototypes have been fabricated and tested by means of low-power rf measurements. Though, they fulfill the expectations from simulations to a large extent, the fabrication of a solid prototype made of niobium and associated experiments remain open as important development steps towards a final design.

6 Conclusion

This work was motivated by the question of how to design coaxial HOM couplers. Of interest were both the general case and the particular context of the CERN SPL study. Potentially dangerous HOMs have been identified, damping requirements derived, and power levels estimated for the particular case. A first and major contribution to systematically design coaxial microwave filters on the basis of abstract filter or transfer functions has been worked out. It enables both the design of the filter part of HOM couplers and fundamental predictions about the topology. Various couplers adapted to the needs for high-β SPL cavities have been assessed in terms of filter characteristics, HOM damping, mechanical tolerances and robustness as well as thermal loads and multipacting. Some of the computational analyses are validated by prototype measurements.

The specifications of couplers are defined on the basis of potentially dangerous HOMs. For SPL, these are characterized by a frequency close to harmonics of the bunch or pattern frequencies. Their impact on the beam, which is primarily manifested by the emittance growth in the longitudinal phase space along the linac, has been investigated in detail with the result of applying a minimum damping of $Q_{\text{ext}} \leq 10^5$ for all concerned modes. Each coupler must sustain at most 100 W of extracted power if the TM_{011} $3/5\pi$ mode at ~ 1759 MHz in the medium-β SPL cavity and the TM_{031} $5/5\pi$ mode at ~ 2464 MHz in the high-β SPL cavity remain sufficiently far away from the fifth or, respectively, seventh harmonic of the bunch frequency. A recommendation is made to carefully revise and monitor the frequencies of both HOMs during the cryomodule assembly and operation.

The frequency and geometric shunt resistance of potentially dangerous HOMs are typically obtained from eigenmode simulations of the given cavity. The analyses of longitudinal and transverse beam coupling impedances permit another approach to derive these quantities for many modes from the corresponding wake potential. A particular difficulty occurs if the wake potentials are only available in truncated form as this introduces artificial harmonics in the impedance spectra. For resonant structures, the latter may be approximated under certain conditions by an expression of the form

$$f(s) = \sum_{n=1}^{\infty} \left(\frac{c_n}{s - a_n} w_n(s) + \frac{c_n}{s - a_n^*} w_n^*(-s) \right), \tag{6.1}$$

with the complex frequency variable s while the pole and residue a_n, c_n, are associated with the frequency, geometric shunt resistance, and quality factor of the

particular mode n. Artificial harmonics due to the truncation in time domain are taken into account by the weighting functions,

$$w_n(s) = 1 - \exp\left[-(s - a_n)t'\right], \tag{6.2}$$

where t' refers to the time after which the wake potential is truncated. An extended formulation of vector fitting has been worked out which notably simplified the approximation problem (6.1) to a linear least square and eigenvalue problem, being iteratively solved. It enables the evaluation of multiple resonances in the frequency spectrum of truncated time signals, such as scattering matrices derived from time-domain simulations, or longitudinal and transverse wake potentials simulated by particle bunches which pass a cavity at the speed of light. The problems may be quite diverse. For the particular case, resulting mode parameters agree reasonably well for conventional eigenmode simulations and the novel approach on the basis of wake field simulations.

The design process of coaxial HOM couplers has been redefined in various aspects concerning the filter characteristics of coaxial microwave structures and mode coupling, which is not only restricted to the antenna shape. Typically, the design of HOM couplers is derived from a predefined topology adapted to a few potentially dangerous HOMs using numerical simulations, but the presented work aims at the synthesis of filter or transfer functions by means of coaxial microwave structures comprising certain discontinuities.

The synthesis is based on equivalent circuits generally given by a finite cascade of lumped, lossless two-ports and unit elements as sketched in Fig. 6.1. Each discontinuity excites evanescent modes, some of which may be able to extend their influence to the neighboring obstacles depending on the distance. It was empirically found that the structure of Fig. 6.1 remains valid over a wide frequency range even in the presence of evanescent mode coupling between adjacent discontinuities. Given the particular equivalent circuit model of a coaxial waveguide segment, it is possible to adjust individual equivalent lumped and distributed elements by directed geometrical changes such that a desired frequency response is approximated. The procedure has been demonstrated by means of two examples, a third-order and fifth-order elliptic high-pass filter, both adapted to the requirements of the high-β SPL cavity.

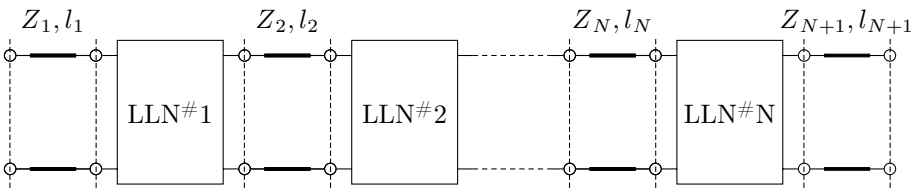

Fig. 6.1. Cascade of lossless lumped networks (LLN) and unit elements in alternating order to equivalently represent coaxial waveguides with multiple discontinuities.

The results are already very promising and well within the specifications. There are various procedural aspects with the potential of improvements, in particular, the synthesis of generalized networks consisting of lumped and unit elements. These methodical enhancements form the basis of future work.

Particularly interesting for the design of coaxial high-pass filters is the microwave structure shown in Fig. 6.2. It is characterized by two inductive posts connecting the inner and outer conductor as well as a capacitive gap by which the inner conductor is interrupted at the center. It was found that the capacitance creates a resonant circuit together with an inductance connected in shunt. The latter is most likely attributed to the coupling between evanescent modes, and may be adjusted over several orders of magnitude by changing the rotation angle or distance between both fixings. This allows the introduction of a transmission zero at any reasonable frequency, for instance, at the operating frequency of a cavity. To the author's best knowledge, these phenomenological findings open up completely new research topics in microwave theory and await field theoretical analyses and explanations.

In addition to the filter characteristics of coaxial HOM couplers, the phenomenon of transmission zeros inherent to cutoff tubes has been assessed. The formation of standing waves in cutoff tubes may cause at distinct frequencies no or very moderate power to be transmitted between the cavity and HOM coupler. This is particularly problematic if the cavity reveals potentially dangerous HOMs at such frequencies as they may not be sufficiently damped, no matter how the coupler is designed. The developed theory aids the designing of cutoff tubes and possibly enables the suppression of transmission zeros in the frequency range of interest. Referring to cutoff tubes of the high-β SPL cavity, the frequencies of concerned HOMs and particular transmission zeros are sufficiently far apart.

Finally, HOM couplers have been analyzed and optimized in a more general context for the high-β SPL cavities. In addition to the characteristic rf behavior, the designs of several HOM couplers have been investigated and compared in terms of

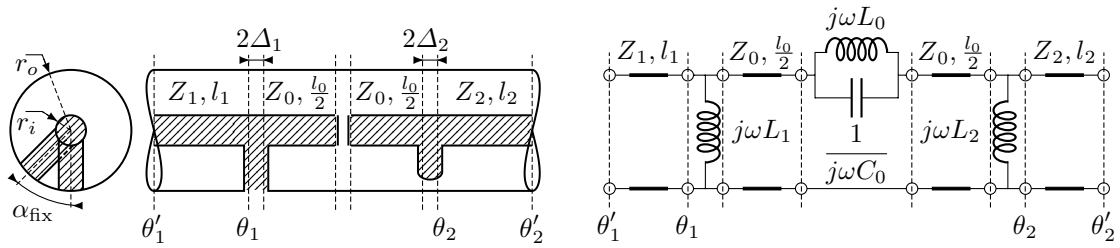

(a) (b)

Fig. 6.2. (a) Cross-sectional and side view of a coaxial structure with two fixings between the inner and outer conductor. The fixings are modeled as cylinders with the radii $r_{\text{fix}1}$ and $r_{\text{fix}2}$. They are rotated against each other in the transverse plane by the angle α_{fix}. The inner conductor of the central waveguide section is interrupted by a distance d_{gap}. (b) Equivalent circuit model.

rf sensitivity to mechanical tolerances and structural deformations, the thermal behavior due to rf surface losses and static thermal conduction through the rf cable, as well as multipacting barriers. The different designs may be grouped in conventional couplers as used for LHC or TESLA cavities and new proposals which partially appear more complex. The latter are characterized by a very low sensitivity for the fundamental mode rejection and much steeper transition between stop and passband. The thermal behavior of all considered couplers is similar and dominated by the static conduction through the rf cable intended to transmit rf power outside the cryomodule. Additional thermalizations are required to ensure a stable operation. Furthermore, slight modifications of selected designs allow ultimately the multipacting barriers to be suppressed reasonably well for the relevant field levels while keeping the filter characteristics.

Bibliography

[1] S. Kim, in *Proc. LINAC08*, Linear Accelerator Conference, Vol. 24 (JACoW, Victoria, British Columbia, Canada, 2008) pp. 11–15.

[2] R. Abela, A. Aghababyan, M. Altarelli, C. Altucci, *et al.*, *XFEL: The European X-Ray Free-Electron Laser - Technical Design Report* (DESY, Hamburg, 2006).

[3] O. S. Brüning, P. Collier, P. Lebrun, S. Myers, *et al.*, *LHC Design Report*, CERN Yellow Reports: Monographs (CERN, Geneva, 2004).

[4] L. D. Landau, J. Phys.(USSR) **10**, 25 (1946), [Zh. Eksp. Teor. Fiz.16,574(1946)].

[5] A. Chao, *Physics of Collective Beam Instabilities in High Energy Accelerators*, Wiley Series in Beam Physics and Accelerator Technology (Wiley, 1993).

[6] J. Gareyte, J.-P. Koutchouk, and F. Ruggiero, *Landau damping dynamic aperture and octupole in LHC*, Tech. Rep. CERN-LHC-Project-Report-91 (CERN, Geneva, 1997).

[7] J. M. Cesaratto *et al.*, *SPS Wideband Transverse Feedback Kicker: Design Report*, Tech. Rep. SLAC-R-1037 (SLAC, 2013).

[8] K. Papke and A. Grudiev, Phys. Rev. Accel. Beams **20**, 082001 (2017).

[9] M. Schenk, A. Grudiev, K. Li, and K. Papke, Phys. Rev. Accel. Beams **20**, 104402 (2017).

[10] Q. Wu and I. Ben-Zvi, in *Proc. of 1st International Particle Accelerator Conference (IPAC'10), Upton, N.Y., USA, May 23-28, 2010*, International Particle Accelerator Conference, Vol. 1 (JACoW, Upton, N.Y., USA, 2010) pp. 3078–3080.

[11] E. Haebel, V. Rödel, F. Gerigk, and Z. T. Zhao, in *Proc. of 8th International Conference on RF Superconductivity (SRF'97), Abano Terme, Padova, Italy, October 6-10, 1997*, International Conference on RF Superconductivity, Vol. 8 (JACoW, Abano Terme, Padova, Italy, 1997) pp. 701–708.

[12] P. Zhang, *Beam position diagnostics with higher order modes in third harmonic superconducting accelerating cavities*, Ph.D. thesis, University of Manchester (2012).

[13] G. Apollinari, I. Béjar Alonso, O. Brüning, M. Lamont, and L. Rossi, *High-Luminosity Large Hadron Collider (HL-LHC): Preliminary Design Report*, CERN Yellow Reports: Monographs (CERN, Geneva, 2015).

[14] S. D. Silva, J. Delayen, and H. Park, in *Proc. of 6th International Particle Accelerator Conference (IPAC'15), Richmond, VA, USA, May 3-8, 2015*, International Particle Accelerator Conference, Vol. 6 (JACoW, Richmond, VA, USA, 2015) pp. 3568–3571.

[15] B. Hall, G. Burt, R. Apsimon, C. J. Lingwood, *et al.*, Phys. Rev. Accel. Beams **20**, 012001 (2017).

[16] J. Mitchell, *Higher Order Modes and Dampersfor the LHC Double Quarter WaveCrab Cavity*, Ph.D. thesis, Lancaster University (2019).

[17] H. Padamsee, T. Hays, and J. Knobloch, *RF superconductivity for accelerators*, Wiley series in beam physics and accelerator technology (Wiley, New York, NY, 1998).

[18] P. Zucchelli, Physics Letters B **532**, 166 (2002).

[19] F. Gerigk, S. Atieh, I. Aviles Santillana, W. Bartmann, *et al.*, *Conceptual Design of the Low-Power and High-Power SPL: A Superconducting H^- Linac at CERN* (CERN, Geneva, 2014).

[20] R. Garoby, in *1st SPL Collaboration Meeting, Geneva, Switzerland, Dec, 2008* (2008) p. 25.

[21] H. Damerau, A. Funken, R. Garoby, S. Gilardoni, *et al.*, *LHC Injectors Upgrade, Technical Design Report, Vol. I: Protons*, Tech. Rep. CERN-ACC-2014-0337 (2014).

[22] F. Gerigk, M. Eshraqi, and M. Schuh, *Choice of the optimum beta for the SPL cavities*, Tech. Rep. sLHC-Project-Note-0001. CERN-sLHC-Project-Note-0001 (CERN, Geneva, 2009).

[23] F. Peauger *et al.*, *Results of SC proton cavity tests (Beta=1 and Beta=0.65)*, Tech. Rep. EuCARD-REP-2013-026 (CEA, 2013).

[24] E. Haebel, Part. Accel. **40**, 141 (1992).

[25] J. Allen, *H-infinity Engineering and Amplifier Optimization*, Systems & Control: Foundations & Applications (Springer Science & Business Media, New York, 2004).

[26] O. Wing, *Classical Circuit Theory* (Springer Science+Business Media, LLC, New York, 2008).

[27] C. Montgomery, R. Dicke, and E. Purcell, *Principles of Microwave Circuits*, Massachusetts Institute of Technology. Radiation Laboratory series. (McGraw-Hill Book Company, Inc., New York, 1948).

[28] W. Cauer, *Theorie der linearen Wechselstromschaltungen*, Theorie der linearen Wechselstromschaltungen No. Bd. 1 (Leipzig Akad.-Verl. Becker & Erler, Leipzig, 1941).

[29] R. Collin, *Foundations for Microwave Engineering*, IEEE Press Series on Electromagnetic Wave Theory (John Wiley & Sons, Inc., New York, 2001).

[30] O. Perron, *Die Lehre von den Kettenbrüchen, Band II: Analytisch-funktionentheoretische Kettenbrüche*, 3rd ed., Die Lehre von den Kettenbrüchen (Vieweg+Teubner Verlag, Stuttgart, 1977).

[31] R. Saal and E. Ulbrich, IRE Transactions on Circuit Theory **5**, 284 (1958).

[32] E. A. Guillemin, *Synthesis of Passive Networks: Theory and Methods Appropriate to the Realization and Approximation Problems* (John Wiley & Sons, Inc. and Champan & Hall, New York and London, 1957).

[33] H. Baher, *Synthesis of electrical networks*, A Wiley-Interscience Publication (John Wiley & Sons Ltd., Chichester, 1984).

[34] A. I. Zverev, *Handbook of Filter Synthesis* (John Wiley & Sons, Inc., New York, 1967).

[35] M. R. Wohlers, *Lumped and Distributed Passive Networks: A Generalized and Advanced Viewpoint*, Electrical Science (Academic Press, Inc., New York, 1969).

[36] S. Darlington, Journal of Mathematics and Physics **18**, 257 (1939).

[37] V. Belevitch, IRE Transactions on Circuit Theory **2**, 337 (1955).

[38] D. C. Youla, J. D. Rhodes, and P. C. Marston, International Journal of Circuit Theory and Applications **1**, 59 (1973).

[39] T. Fujisawa, IRE Transactions on Circuit Theory **2**, 320 (1955).

[40] N. Marcuwitz, *Waveguide Handbook*, Massachusetts Institute of Technology. Radiation Laboratory series. (McGraw-Hill Book Company, Inc., New York, 1951).

[41] D. M. Pozar, *Microwave Engineering*, 4th ed. (John Wiley & Sons, Inc., New York, NY, 2012).

[42] J. G. Van Bladel, *Electromagnetic Fields*, 2nd ed., IEEE Press Series on Electromagnetic Wave Theory (John Wiley & Sons, Inc., Hoboken, New Jersey, 2007).

[43] I. Zagorodnov, K. L. F. Bane, and G. Stupakov, Phys. Rev. ST Accel. Beams **18**, 104401 (2015).

[44] A. Wolski, *Beam dynamics in high energy particle accelerators* (Imperial College Press, London, 2014).

[45] J. Barranco García, R. De Maria, A. Grudiev, R. Tomás García, *et al.*, Phys. Rev. Accel. Beams **19**, 101003 (2016).

[46] J. G. Van Bladel, *Electromagnetic Fields* (Hemisphere Publishing Corporation, Washington, 1985).

[47] K. Brackebusch, T. Galek, and U. van Rienen, in *Proc. of 5th International Particle Accelerator Conference (IPAC'14), Dresden, Germany, June 15-20, 2014*, International Particle Accelerator Conference, Vol. 5 (Dresden, Germany, 2014) pp. 409–411.

[48] J. D. Jackson, *Classical electrodynamics*, 3rd ed. (John Wiley & Sons, Inc., New York, NY, 1999).

[49] R. Calaga, in *Proc. of Chamonix 2012 Workshop on LHC Performance, Chamonix, France, Feb, 2012*, CERN-2012-006, CERN-ATS-2012-069 (Chamonix, France, 2012) pp. 363–372.

[50] A. Farricker, *Higher Order Modes and Beam Dynamics at The European Spallation Source*, Ph.D. thesis, University of Manchester (2017).

[51] R. L. Gluckstern and K. L. F. Bane, Science **42**, 123 (1993).

[52] D. Kajfez, "Encyclopedia of RF and Microwave Engineering," (John Wiley & Sons, Inc., 2005) Chap. *Q* Factor, pp. 3937–3947.

[53] C. J. Gorter and H. B. G. Casimir, Z. techn. Physik **15**, 539 (1934).

[54] F. London and H. London, Proceedings of the Royal Society of London. Series A - Mathematical and Physical Sciences **149**, 71 (1935).

[55] G. Ciovati, "AC/RF Superconductivity," in *CAS - CERN Accelerator School: Course on Superconductivity for Accelerators* (CERN, Geneva, 2014) pp. 57–75.

[56] A. B. Pippard and W. L. Bragg, Proc. of the Royal Society of London. Series A. Mathematical and Physical Sciences **216**, 547 (1953).

[57] D. C. Mattis and J. Bardeen, Phys. Rev. **111**, 412 (1958).

[58] B. Aune, R. Bandelmann, D. Bloess, B. Bonin, *et al.*, Phys. Rev. ST Accel. Beams **3**, 092001 (2000).

[59] T. Junginger, *Investigations of the Surface Resistance of Superconducting Materials*, Ph.D. thesis, University of Heidelberg (2012).

[60] T. Weiland and B. W. Zotter, Part. Accel. **11**, 143 (1981).

[61] B. W. Zotter and S. A. Kheifets, *Impedances and wakes in high-energy particle accelerators* (World Scientific Publishing Co. Pte. Ltd., Singapore, 1998).

[62] W. K. H. Panofsky and W. A. Wenzel, American Institute of Physics , 967 (1956).

[63] Y. H. Chin, in *Proc. of 15th National Particle Accelerator Conference (PAC'93), Washington, DC, USA, May, 1993*, National Conference on Particle Accelerator, Vol. 15 (IEEE, Washington, DC, USA, 1993) pp. 3414–3416.

[64] R. Wanzenberg, *Monopole, dipole and quadrupole passbands of the TESLA 9-cell cavity*, Tech. Rep. DESY-TESLA-2001-33 (DESY, Hamburg, 2001).

[65] J. Tückmantel, *Cavity-Beam-Transmitter Interaction Formula Collection with Derivation*, Tech. Rep. CERN-ATS-Note-2011-002 TECH (CERN, Geneva, 2010).

[66] A. Arnold, *Simulation und Messung der Hochfrequenzeigenschaften einer supraleitenden Photo-Elektronenquelle*, Ph.D. thesis, University of Rostock (2012).

[67] T. Weiland and R. Wanzenberg, "Wake fields and impedances," in *Frontiers of Particle Beams: Intensity Limitations* (Springer Berlin Heidelberg, Berlin, Heidelberg, 1992) pp. 39–79.

[68] A. Bondeson, T. Rylander, and P. Ingelström, *Computational Electromagnetics*, Texts in Applied Mathematics (Springer New York, 2005).

[69] A. Logg, K.-A. Mardal, and G. N. Wells, eds., *Automated Solution of Differential Equations by the Finite Element Method*, Lecture Notes in Computational Science and Engineering, Vol. 84 (Springer, 2012).

[70] U. van Rienen, *Numerical Methods in Computational Electrodynamics: Linear Systems in Practical Applications*, Lecture Notes in Computational Science and Engineering (Springer Berlin Heidelberg, Berlin, 2001).

[71] J. S. Hesthaven and T. Warburton, *Nodal Discontinuous Galerkin Methods: Algorithms, Analysis, and Applications*, Texts in Applied Mathematics (Springer Science+Business Media, LLC, New York, 2008).

[72] A. Ern and G. Jean-Luc, *Theory and Practice of Finite Elements*, Applied Mathematical Sciences, Vol. 159 (Springer Science+Business Media, LLC, New York, 2004).

[73] C. A. Kennedy, M. H. Carpenter, and R. Lewis, Applied Numerical Mathematics **35**, 177 (2000).

[74] N. Gödel, S. Schomann, T. Warburton, and M. Clemens, IEEE Transactions on Magnetics **46**, 2735 (2010).

[75] K. Papke, C. Bahls, and U. van Rienen, in *Proc. of 11th International Computational Accelerator Conference (ICAP'12), Warnemünde, Germany, August 19-24, 2012*, Vol. 11 (JACoW, Warnemünde, Germany, 2012) pp. 275–277.

[76] C. Potratz, H.-W. Glock, and U. van Rienen, in *Proc. of 2nd International Particle Accelerator Conference (IPAC'11), San Sebastián, Spain, September 4-9, 2011*, International Particle Accelerator Conference, Vol. 2 (JACoW, San Sebastián, Spain, 2011) pp. 2241–2243.

[77] B. Gustavsen and A. Semlyen, IEEE Transactions on Power Delivery **14**, 1052 (1999).

[78] B. Gustavsen, IEEE Transactions on Power Delivery **21**, 1587 (2006).

[79] B. Gustavsen and A. Semlyen, IEEE Transactions on Power Delivery **13**, 605 (1998).

[80] A. Boucheffa and M. Francois, in *Proc. of 7th International Conference on RF Superconductivity (SRF'95), Gif-sur-Yvette, France, October 17-20, 1995*, International Conference on RF Superconductivity, Vol. 7 (JACoW, Gif-sur-Yvette, France, 1995) pp. 659–663.

[81] Y. A. Cengel, *Heat Transfer: A Practical Approach*, 2nd ed. (McGraw-Hill Professional, New York, NY, 2002).

[82] F. P. Incropera and D. P. DeWitt, *Fundamentals of Heat and Mass Transfer*, 6th ed. (John Wiley & Sons, Inc., New York City, New York, 2007).

[83] A. C. Eringen and E. S. Şuhubi, *Elastodynamics: Linear theory*, Elastodynamics, Vol. II (Academic Press, 1974).

[84] V. Paramonov, B. Militsyn, and A. Skassyrskaya, Nuclear Instruments and Methods in Physics Research Section A: Accelerators, Spectrometers, Detectors and Associated Equipment **940**, 337 (2019).

[85] K. Papke, A. A. Carvalho, C. Zanoni, and A. Grudiev, Phys. Rev. Accel. Beams **22**, 072001 (2019).

[86] D. A. Field, Communications in Applied Numerical Methods **4**, 709 (1988).

[87] M. Schuh, *Study of Higher Order Modes in Superconducting Accelerating Structures for Linac Applications*, Ph.D. thesis, Inst. Appl. Math., Heidelberg, Heidelberg, Germany (2011).

[88] C. Liu, W. F. O. Müller, W. Ackermann, and T. Weiland, *Various approaches to electromagnetic field simulations for RF cavities*, Tech. Rep. sLHC-Project-Note-0040 (CERN, 2012).

[89] O. Capatina, S. Atieh, I. A. Santillana, G. A. Izquierdo, *et al.*, in *Proc. of 16th International Conference on RF Superconductivity (SRF'13), Paris, France, September 23-27, 2013*, International Conference on RF Superconductivity, Vol. 16 (JACoW, Paris, France, 2013) p. 35.

[90] *COMSOL Multiphysics Ver. 5.3*, COMSOL Multiphysics GmbH, Stockholm, Sweden. (2017).

[91] *CST - Computer Simulation Technology Ver. 2016*, CST AG, Darmstadt, Germany (2016).

[92] F. Peauger, C. Arcambal, S. Berry, N. Berton, *et al.*, in *Proc. of International Conference on RF Superconductivity (SRF'15), Whistler, BC, Canada, Sep, 2015*, International Conference on RF Superconductivity, Vol. 17 (JACoW, Whistler, BC, Canada, 2015) pp. 544–548.

[93] M. Schuh, F. Gerigk, J. Tückmantel, and C. P. Welsch, Phys. Rev. ST Accel. Beams **14**, 051001 (2011).

[94] *ANSYS HFSS - High Frequency Structural Simulator Ver. 2016*, ANSYS Inc., Canonsburg, Pennsylvania, USA (2016).

[95] A. Semlyen and B. Gustavsen, IEEE Transactions on Power Delivery **24**, 345 (2009).

[96] B. Gustavsen, IEEE Transactions on Power Delivery **23**, 2278 (2008).

[97] B. Gustavsen, IEEE Transactions on Advanced Packaging **33**, 257 (2010).

[98] T. Galek, T. Flisgen, U. van Rienen, A. Neumann, *et al.*, in *Proc. of International Computational Accelerator Physics Conference (ICAP'12), Rostock-Warnemünde, Germany, August 19-24, 2012*, International Computational Accelerator Physics Conference (JACoW, Rostock-Warnemünde, Germany, 2012) pp. 152–154.

[99] N. Shipman, G. Burt, R. Calaga, and J. Mitchell, in *Proc. of 8th International Particle Accelerator Conference (IPAC'17), Copenhagen, Denmark, May 14-19, 2017*, International Particle Accelerator Conference, Vol. 8 (JACoW, Geneva, Switzerland, 2017) pp. 3844–3846, https://doi.org/10.18429/JACoW-IPAC2017-THPAB057.

[100] J. Tückmantel, Phys. Rev. ST Accel. Beams **13**, 011001 (2010).

[101] F. Gerigk, *Design of Higher-Order Mode Dampers for the 400 MHz LHC Superconducting Cavities*, Studienarbeit, Technische Universität Berlin, Berlin (1997).

[102] *ROOT - A Data Analysis Framework Ver. 6*, CERN, Geneva, Switzerland (2017).

[103] M. Reiser, *Theory and Design of Charged Particle Beams*, 2nd ed. (Wiley, Weinheim, 2008) p. 647.

[104] S. Molloy, R. Ainsworth, and R. Ruber, in *Proc. of 2nd International Particle Accelerator Conference (IPAC'11), San Sebastián, Spain, September 4-9, 2011*, International Particle Accelerator Conference, Vol. 2 (JACoW, San Sebastián, Spain, 2011) pp. 190–192.

[105] W. W. Hansen and R. F. Post, J. Appl. Phys. **19**, 1059 (1948).

[106] T. G. Jurgens, *Equations for bead pull cavity measurements*, Tech. Rep. FERMILAB-LU-159 (Fermilab, 1990).

[107] H. Padamsee, T. Hays, and J. Knobloch, *RF Superconductivity: Science, Technology, and Applications*, 1st ed., Wiley series in beam physics and accelerator technology (Wiley-VCH, Weinheim, 2009).

[108] M. R. Khalvati, *Stabilization Strategies for Drift Tube Linacs*, Ph.D. thesis, School of Particles and Accelerators, Teheran, Iran (2016).

[109] M. E. V. Valkenburg and W. M. Middleton, *Reference Data for Engineers: Radio, Electronics, Computers and Communications*, 9th ed. (Newnes, Woburn, 2002).

[110] E. Maxwell, P. M. Marcus, and J. C. Slater, Phys. Rev. **76**, 1332 (1949).

[111] P. Zhang, A. D'Elia, W. V. Delsolaro, and K. Artoos, Nuclear Instruments and Methods in Physics Research Section A: Accelerators, Spectrometers, Detectors and Associated Equipment **797**, 101 (2015).

[112] A. Savitzky and M. J. E. Golay, Analytical chemistry **36**, 1627 (1964).

[113] G. Matthaei, L. Young, and E. Jones, *Microwave Filters, Impedance-matching Networks, and Coupling Structures*, Artech House Microwave Library (Artech House, Inc., 1980).

[114] J. Sekutowicz, in *Proc. of 6th International Conference on RF Superconductivity (SRF'93), Newport News, Virginia, USA, October 4-8, 1993*, International Conference on RF Superconductivity, Vol. 6 (Newport News, Virginia, USA, 1993) pp. 426–439.

[115] W. Xu, I. Ben-Zvi, S. Belomestnykh, H. Hahn, *et al.*, in *Proc. of Particle Accelerator Conference (PAC'11), New York, N.Y., USA, March 28 - April 1, 2011*, Particle Accelerator Conference (JACoW, New York, N.Y., USA, 2011) pp. 325–327.

[116] R. Ainsworth, *Parasitic Resonances in High Power Proton Linacs: Major Issues and Mitigation Techniques*, Ph.D. thesis, Royal Holloway, University of London (2014).

[117] K. Papke, F. Gerigk, and U. van Rienen, Phys. Rev. Accel. Beams **20**, 060401 (2017).

[118] J. Sekutowicz, in *Proc. of 3rd International Conference on RF Superconductivity (SRF'00), Argonne National Laboratory, Illinois, USA, September 14-18, 1987*, International Conference on RF Superconductivity, Vol. 3 (Illinois, USA, 1987) pp. 597–604.

[119] B. P. Xiao, S. Belomestnykh, I. Ben-Zvi, J. Skaritka, *et al.*, in *Proc. of 16th International Conference on RF Superconductivity (SRF'13), Paris, France, September 23-27, 2013*, International Conference on RF Superconductivity, Vol. 16 (JACoW, Paris, France, 2013) pp. 1006–1009.

[120] A. Kummert, Circuits, Systems and Signal Processing **8**, 97 (1989).

[121] A. Sertbaş, A. Aksen, and B. S. Yarman, in *IEEE. APCCAS 1998. 1998 IEEE Asia-Pacific Conference on Circuits and Systems. Microelectronics and Integrating Systems. Proceedings (Cat. No.98EX242)* (1998) pp. 295–298.

[122] P. Bernard, E. Chiaveri, E. Haebel, and W. Weingarten, in *Proc. of 5th International Conference on RF Superconductivity (SRF'91), Hamburg, Germany, August 19-23, 1991*, International Conference on RF Superconductivity, Vol. 5 (JACoW, Hamburg, Germany, 1991) pp. 956–962.

[123] R. Fano, Journal of the Franklin Institute **249**, 57 (1950).

[124] S. An, T. Ya-Zhe, Z. Li-Ping, L. Ying-Min, *et al.*, Chinese Physics C **35**, 301 (2011).

[125] C. E. Reece, E. F. Daly, G. K. Davis, W. R. Hicks, *et al.*, in *Proc. of 13th International Conference on RF Superconductivity (SRF'07), Beijing, China, October 14-19, 2007*, International Conference on RF Superconductivity, Vol. 13 (JACoW, Beijing, China, 2007) pp. 540–543.

[126] K. Watanabe, S. Noguchi, E. Kako, T. Shishido, and H. Hayano, Nuclear Instruments and Methods in Physics Research Section A: Accelerators, Spectrometers, Detectors and Associated Equipment **595**, 299 (2008).

[127] J. Eberhardt, *Investigation of Quality Factor of Resonators*, Tech. Rep. CERN-ACC-NOTE-2014-0009 (CERN, 2014).

[128] A. D'Elia, *Design and Characterisation of the Power Coupler Line for the HIE-ISOLDE High-Beta Cavity*, Tech. Rep. HIE-ISOLDE-PROJECT-Note-0011 (CERN, Geneva, 2011).

[129] G. Wu, E. Harms, and T. Khabiboulline, *Evaluation of HOM Coupler Probe Heating for 3.9 GHz cavities*, Tech. Rep. FNAL-TD-08-019 (FermiLab, 2008).

[130] J. P. Turneaure, J. Halbritter, and H. A. Schwettman, Journal of Superconductivity **4**, 341 (1991).

[131] G. Ciovati, R. Geng, J. Mammosser, and J. Saunders, Applied Superconductivity, IEEE Transactions on **21**, 1914 (2011).

[132] *CryoComp Rapid Cryogenic Design*, Eckels Engineering Inc. (2011).

[133] H. Padamsee, Superconductor Science and Technology **14**, R28 (2001).

[134] *ANSYS - ANalysis SYStem Ver. 17.2*, ANSYS Inc., Canonsburg, Pennsylvania, USA (2016).

[135] J. Halbritter, *FORTRAN Program for the Computation of the Surface Impedance of Superconductors*, Tech. Rep. 3/70-6 (Kernforschungszentrum, Karlsruhe (West Germany). Institut fuer Experimentelle Kernphysik, 1970).

[136] J. Apeland, *Thermal Analysis of HOM Coupler for HG-Cavity*, Tech. Rep. 1772707 (CERN, Geneva, 2017).

[137] *1/2" CELLFLEX Low-Loss Foam-Dielectric Coaxial Cable*, Radio Frequency Systems (2018), rev. E.

[138] *RF cables*, HUBER+SUHNER (2018), ed. 2018.

[139] *ANSYS APDL - Parametric Design Language Ver. 17.2*, ANSYS Inc., Canonsburg, Pennsylvania, USA (2016).

[140] K. Papke, *ANSYS modeling of thermal contraction of SPL HOM couplers during cool-down*, Tech. Rep. sLHC-Project-Note-0044 (CERN, Geneva, 2016).

[141] S. W. Van Sciver, *Helium Cryogenics*, International Cryogenics Monograph Series (Springer, New York, NY, 2012).

[142] R. P. Reed and A. F. Clark, *Materials at low temperatures* (American Society for Metals, Metals Park, Ohio, 1983).

[143] W. Henneberg, R. Orthuber, and E. Steudel, Z. Techn. Physik **17**, 115 (1936).

[144] R. Udiljak, D. Anderson, M. Lisak, V. E. Semenov, and J. Puech, Physics of Plasmas **14**, 033508 (2007).

[145] *ACE3P Simulation Suite*, SLAC National Accelerator, 2575 Sand Hill Rd, Menlo Park, CA 94025, USA. (2016).

[146] K. Ko and A. Candel, in *Proc. of 25th Linear Accelerator Conference (LINAC'10), Tsukuba, Japan, September 12-17, 2010*, Linear Accelerator Conference, Vol. 25 (JACoW, Tsukuba, Japan, 2010) pp. 1028–1032.

[147] M. A. Furman and M. T. F. Pivi, Phys. Rev. ST Accel. Beams **5**, 124404 (2002).

[148] C.-K. Ng, L. Ge, C. Ko, Z. Li, and L. Xiao, in *Proc. of Particle Accelerator Conference (PAC'13), Pasadena, California, USA, Sep, 2013*, Particle Accelerator Conference (JACoW, Pasadena, California, USA, 2013) pp. 216–218.

[149] S. U. De Silva and J. R. Delayen, Phys. Rev. ST Accel. Beams **16**, 082001 (2013).

[150] Y. M. Li, K. X. Liu, and R. L. Geng, Phys. Rev. ST Accel. Beams **17**, 022002 (2014).

[151] R. Ainsworth, R. Calaga, and S. Molloy, in *Proc. of 3rd International Particle Accelerator Conference (IPAC'12), New Orleans, USA, May 20-25, 2012*, International Particle Accelerator Conference, Vol. 3 (JACoW, New Orleans, USA, 2012) pp. 2182 –2184.

Appendix

A.1 Eigenmodes in a Circular-Cylindrical Cavity

A circular-cylindrical cavity with beam pipe apertures left open similar to Fig. 2.11 is considered. It serve as a benchmark for impedance analyses in Sec. 3.3.3 based on vector fitting. As in [99], the diameter and length of the cavity are chosen to be 153 mm and 100 mm, respectively. The equivalent parameters of the circular-cylindrical beam pipe are 10 mm and 15 mm, respectively, on either side of the cavity. Table A.1 lists the first 16 resonant monopole modes with transverse magnetic characteristics.

Table A.1. Monopole modes in the pillbox cavity with left-opened beam pipe ports.

mode n	f_n [GHz]	$(R/Q)_n$ [Ω]	Q_n
TM_{010}	1.49988	192.53	3335
TM_{011}	2.12042	100.18	2758
TM_{012}	3.35188	22.60	3319
TM_{020}	3.44360	7.15	4804
TM_{021}	3.75644	30.99	3423
TM_{022}	4.56613	51.81	3490
TM_{013}	4.73988	7.77	3481
TM_{030}	5.39928	4.22	4888
TM_{031}	5.60545	17.98	3352
TM_{023}	5.66403	39.52	3315
TM_{014}	6.17988	4.10	3123
TM_{024}	6.91378	23.24	2737
TM_{033}	7.02755	4.15	2665
TM_{040}	7.35760	5.44	3550
TM_{015}	7.64179	1.83	2212
TM_{042}	7.94758	7.46	1961

A.2 Geometrical Parameters of SPL Cavities

The rotational symmetric SPL cavities are characterized by conjugated elliptic arcs in the longitudinal cross-sectional plane. Accordingly, they are denoted as elliptic

cavities. Figure A.1 shows the longitudinal cross section of a half-cell defined by the half axes of two ellipses, the length of the half-cell, l_{hc}, as well as the iris and equator radii r_1, r_2. Both types of SPL cavities consists of five cells. The half-cells at both extremities slightly differ in their geometrical parameters from those in between. The parameters are listed in Table A.2 for each SPL cavity and half-cell type. Figure A.2 shows the assembly of the high-β SPL cavity involving details of cutoff tubes and ports. Further information are accessible in [19, 23, 88].

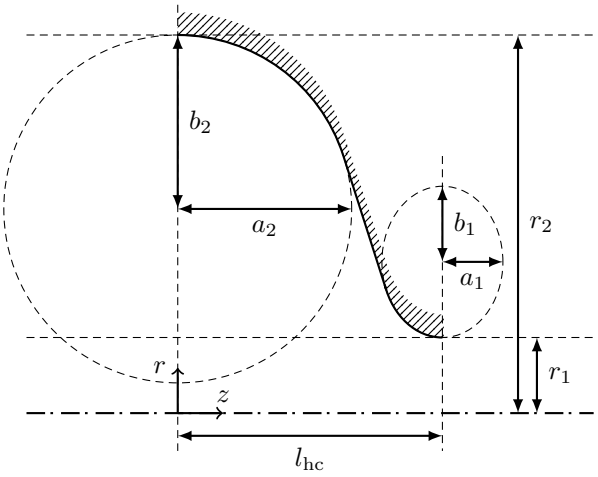

Fig. A.1. Longitudinal cross-sectional view of an elliptic cavity half-cell. The highlighted dashed profile is defined by the half axes of two ellipses as well as the iris and equator radii r_1 and r_2, respectively. The dotted dashed line represents the rotational axis or beam line.

Table A.2. Geometrical parameters of five-cell SPL cavities [19, 23].

parameter	medium-β SPL cavity			high-β SPL cavity		
(Fig. A.1)	left†	mid	right‡	left†	mid	right‡
a_1	15.15	14.26	13.17	18.50	22.10	18.50
b_1	25.00	23.53	21.73	24.90	35.10	24.90
a_2	41.62	47.10	53.02	74.45	77.50	74.45
b_2	39.53	44.75	55.67	83.27	77.50	76.89
l_{hc}	69.00	69.00	69.00	103.07	106.47	103.07
r_1	40.00	48.00	60.00	65.00	64.60	70.00
r_2	184.67	184.67	184.67	190.786	190.786	190.786

† Half end-cell on the side of the tuner.
‡ Half end-cell on the side of the fundamental mode coupler.

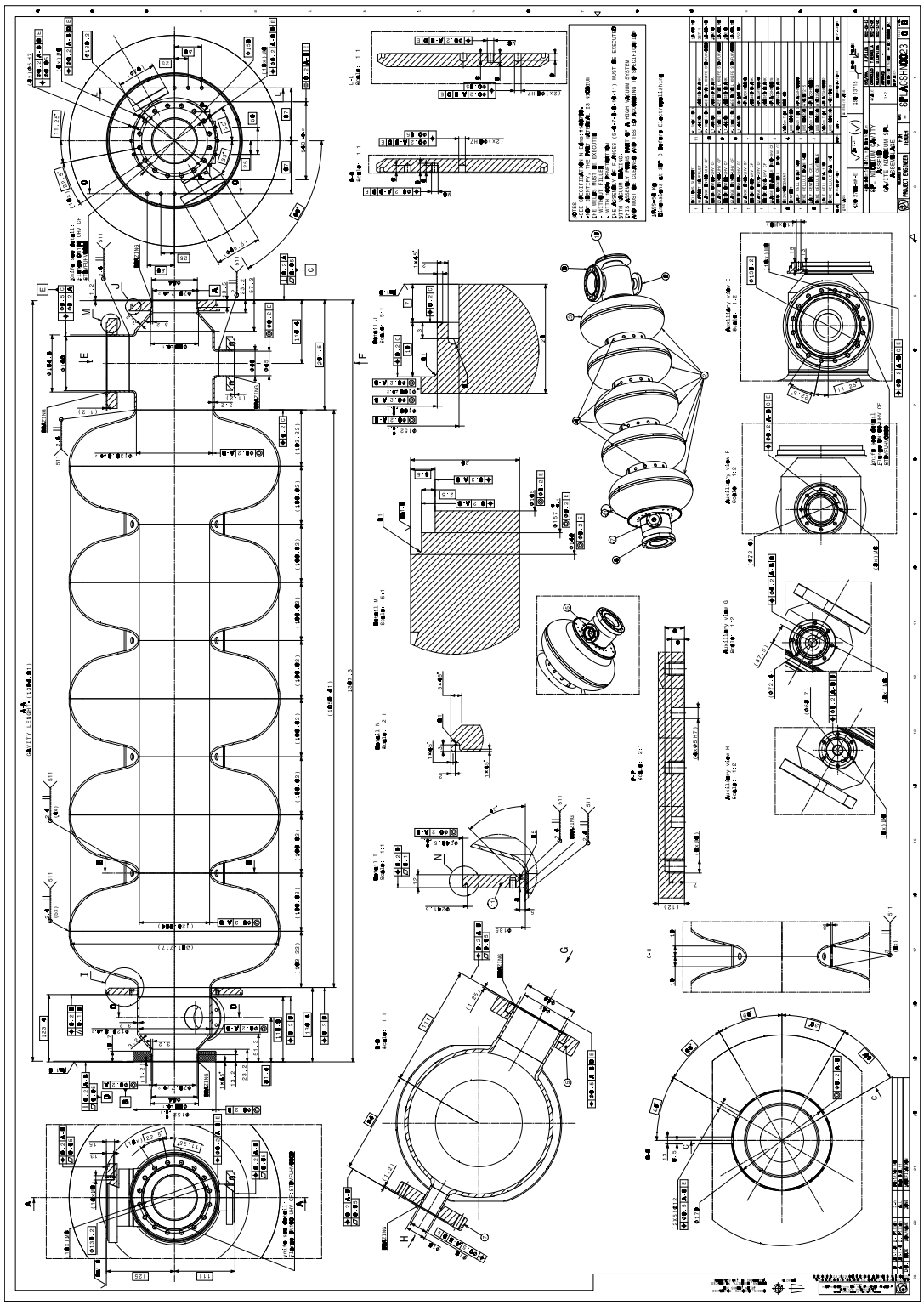

Fig. A.2. Assembly of the high-β SPL cavity [19].

A.3 Design Formulas for Elliptic Filters

Let the squared magnitude of a strictly proper transfer function associated with a normalized low-pass filter, be of the form

$$|H(j\Omega)|^2 = \frac{c_0}{1+|D(j\Omega)|^2} = \frac{c_0}{1+\varepsilon^2|\widetilde{D}(j\Omega)|^2}, \tag{A.1}$$

with real constants c_0, ε, and the normalized frequency Ω. The latter one is defined by the condition $\Omega_p\Omega_s = 1$ with $\Omega_s > \Omega_p$, that is the passband edge frequency Ω_p equals the reciprocal of the stopband edge frequency Ω_s. Furthermore, let the magnitude of the normalized filter function $|\widetilde{D}(j\Omega)|$ be ≤ 1 for $0 \leq \Omega \leq \Omega_p$. By introducing the insertion loss given in units dB according to [34, p. 63],

$$\alpha(\Omega) = -10\log|s_{21}(j\Omega)|^2 = -10\log 4\frac{R_1}{R_2}|H(j\Omega)|^2, \tag{A.2}$$

to characterize the power transmission between a source and load of resistances R_1 and R_2, respectively, the requirements on the anticipated low-pass are formulated as

$$\alpha(\Omega) \leq \alpha_{\max}, \text{ if } \quad 0 \leq \Omega \leq \Omega_p, \tag{A.3}$$

$$\alpha(\Omega) \geq \alpha_{\min}, \text{ if } \Omega_s \leq \Omega \leq \infty. \tag{A.4}$$

The following considerations are focused on elliptic filters of odd order n. Note, the transfer function of even-order filter functions requires additional frequency mapping, so that an asymptotic damping towards infinite frequency is ensured as this is a necessary condition for a transfer function to be strictly proper, and thus to be realizable by reactive lumped elements. Some frequency maps are discussed, for instance, in [31]. The filter function of a normalized elliptic low-pass of odd order n admits the form

$$\widetilde{D}(p) = \widetilde{c}_1 p \prod_{\nu=1}^{(n-1)/2} \frac{p^2 + a_{2\nu}^2}{a_{2\nu}^2 p^2 + 1}, \tag{A.5}$$

where $n = 3, 5, 7, \ldots$. It represents the analytic continuation of $D(j\Omega)$ in the entire complex p-plane [35, pp. 60]. Since $\widetilde{D}(0) = 0$ and $s_{21}(0) = 1$, it follows from (A.1) and (A.2) that $c_0 = 0.25R_2/R_1$. Apart from the zero at vanishing frequency in (A.5), finite zeros $\Omega_{\infty\nu}$ and poles $\Omega_{0\nu}$ are related according to $\Omega_{\infty\nu} = \Omega_{0\nu}^{-1} = a_{2\nu}$. The solutions a_ν given by Jacobian elliptic sine functions as

$$a_\nu = k\,\mathrm{sn}\left(\nu K/n, k\right), \tag{A.6}$$

correspond alternately to the roots and extreme values of the filter function in the passband. Consequently, every second solution is used in (A.5). Referring to (A.6),

K is to the complete elliptic integral of the first kind with the modulus $k = \Omega_s^{-2}$, and may be written as

$$K = K(k) = \int_0^{\frac{\pi}{2}} \frac{d\vartheta}{\sqrt{1 - k^2 \sin^2 \vartheta}}. \tag{A.7}$$

The filter function as given in (A.5) is characterized by equiripple, that is the magnitude of all extreme values in the passband are equal and normalized to one. Likewise, the magnitude of all extreme values in the stopband are equal. Consequently, the scaling factor $\widetilde{c_1}$ may be derived from any of the conditions $|\widetilde{D}(ja_\nu)| = 1$ with $\nu = 1, 3, \ldots, n$. It can be shown that [31]

$$\widetilde{c_1}^{-1} = \frac{1}{a_n} \prod_{\nu=1}^{(n+1)/2} a_{2\nu-1}^2. \tag{A.8}$$

The maximum acceptable insertion loss in the passband, $a_{\max}$, further specifies the constant ε according to

$$\varepsilon^2 = 10^{0.1\alpha_{\max}} - 1. \tag{A.9}$$

To simultaneously ensure the minimum required attenuation in the stopband, $a_{\min}$, the order of the rational function $\widetilde{D}(p)$ must be chosen as

$$n \geq \left\lceil \frac{K(\sqrt{1-k_1^2})}{K(\sqrt{1-k^2})} \frac{K(k)}{K(k_1)} \right\rceil, \tag{A.10}$$

with the attenuation thresholds being accounted by the discrimination factor k_1 according to

$$k_1^2 = \frac{10^{0.1\alpha_{\max}} - 1}{10^{0.1\alpha_{\min}} - 1}, \tag{A.11}$$

while $k = \Omega_s^{-2}$ is sometimes referred as selectivity factor.

A.4 Examples for Filter Synthesis

The realization of elliptic filters is sketched in the following by means of two examples. For convenience, the source and load resistances R_1 and R_2 are considered to be equal and normalized to $1\,\Omega$. Note, the resultant lumped circuit elements may be scaled afterwards according to any desired reference resistance. The value of $90.24\,\Omega$ used in Sec. 4.3.4, results from the characteristic impedance of a coaxial line according to (2.67), provided the diameters of inner and outer conductor are 10 mm and 45 mm, respectively. The stop- and passband edge frequencies for both examples are chosen such that the resulting transfer function provides a transmission zero at 0.704 GHz and a transmission poles at 1.331 GHz. These values, respectively, corre-

spond to the frequencies of the fundamental and dominant high-order mode of the high-β SPL cavity.

A.4.1 Third-Order Elliptic High-Pass Filter

Let the elliptic high-pass filter be specified by the stopband edge of $f_s = 0.787\,\mathrm{GHz}$ and passband edge of $f_p = 1.191\,\mathrm{GHz}$. Furthermore, the insertion loss must not be less than $\alpha_{\min} = 30\,\mathrm{dB}$ within the stopband while being at most $\alpha_{\max} = 3\,\mathrm{dB}$ for frequencies above the passband edge.

Following (4.107), the edge frequencies with respect to the normalized low-pass filter are $\Omega_p = 0.812\,89$ and $\Omega_s = 1.230\,18$. The selectivity factor becomes $k = \Omega_s^{-2} = 0.660\,79$ while (A.11) yields a discrimination factor of $k_1 = 3.156\,36 \times 10^{-2}$. The minimum order required to satisfy the attenuation thresholds follows from (A.10), and is given by $n = 3$. With the zeros and poles as the solutions of elliptic sine functions according to (A.6), the rational filter function with equiripple behavior in pass- and stopband becomes

$$D(p) \propto p\frac{p^2 + 0.727\,39^2}{0.727\,39^2 p^2 + 1}. \tag{A.12}$$

After determining the scaling factors according to (A.8) and (A.9), the transmission power gain satisfies

$$|s_{21}(p)|^2 = \frac{1 + 1.058\,19p^2 + 0.279\,94p^4}{1 - 9.225\,01p^2 - 38.591\,09p^4 - 36.733\,64p^6}. \tag{A.13}$$

It is seen that its zeros coincide with the purely imaginary poles in (A.12) being located at $\pm j\Omega_{01}$ with $\Omega_{01} = 1.374\,78$. The conjugated complex pair occurs twice due to the squared property of the transmission power gain. Following the procedure described in Sec. 2.1.4, the reflected power gain is calculated as

$$s_{11}(p)s_{11}(-p) = \frac{-10.283\,20p^2 - 38.871\,03p^4 - 36.733\,64p^6}{1 - 9.225\,01p^2 - 38.591\,09p^4 - 36.733\,64p^6}. \tag{A.14}$$

By assigning all zeros and poles of the left half plane to $s_{11}(p)$, the reflection coefficient becomes

$$s_{11}(p) = \pm\frac{3.206\,74p + 6.060\,83p^3}{1 + 3.874\,76p + 2.894\,38p^2 + 6.060\,83p^3}. \tag{A.15}$$

Referring to Fig. 2.6, each choice of $s_{11}(p)$ yields a different input impedance $Z_{\mathrm{in},1}(p)$ seen from the source towards the load resistance R_2. Note, this has consequences on the topology of the resulting lumped network. Choosing the negative sign in (A.15)

and inserting in (2.58), the input impedance normalized to $R_1 = 1\,\Omega$ satisfies

$$Z_{\mathrm{in},1}(p) = \frac{1 + 0.668\,02p + 2.894\,38p^2}{1 + 7.081\,50p + 2.894\,38p^2 + 12.121\,66p^3}. \tag{A.16}$$

Since the denominator of (A.12) is an even function of p, the elements of the open-circuit impedance matrix are identified according to (2.60). The impedance functions normalized to $R_1 = R_2 = 1\,\Omega$ are given as

$$z_{11}(p) = \frac{1 + 2.894\,38p^2}{7.081\,50p + 12.121\,65p^3}, \tag{A.17}$$

$$z_{22}(p) = \frac{1 + 2.894\,38p^2}{7.081\,50p + 12.121\,65p^3}, \tag{A.18}$$

$$z_{21}(p) = \frac{1 + 0.529\,09p^2}{7.081\,50p + 12.121\,65p^3}. \tag{A.19}$$

To derive a ladder network realization of the two-port, the driving point impedances z_{11} and z_{22} are expanded into continued fractions. The procedure rests on Properties 2.1.1–2.1.4 of positive real functions and the alteration between impedance and admittance functions as outlined in Sec. 2.1.1. Since $z_{11} = z_{22}$, the resulting network must be symmetric and no private poles are available in either of the driving point impedances. The expansion may be sketched by means of z_{11} as follows. Since the degree of the denominator is larger than the degree of the numerator polynomial, the reciprocal of the impedance function is considered as the starting point. A partial admittance is removed so that the remainder provides zeros at $p = \pm j\Omega_{01}$. After taking the reciprocal of the remainder, the corresponding conjugated complex pole pair is removed according to Property 2.1.3. Again taking the reciprocal of the new remainder, the obtained admittance function reveals a single pole at $p = \infty$, which can be associated with a shunt capacitance. The resulting network is shown in Fig. A.3(a). By mapping the complex p-plane associated with the normalized

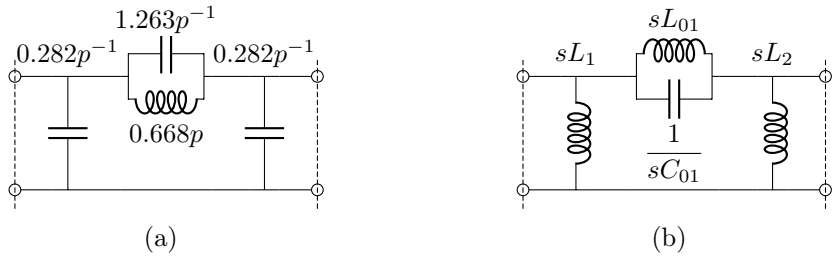

Fig. A.3. (a) Canonical lumped network realization of the normalized low-pass filter function $D(p)$ as given in (A.12) with one transmission zero at finite, nonzero frequency and another one at $p = \infty$. (b) Transformed network after mapping the complex p-plane onto the s-plane according to (4.106) taking into account the specified stop and passband edge frequencies f_s, f_p.

low-pass according to (4.106) onto the s-plane in which the high-pass filter is defined with the desired stop and passband edge frequencies f_s, f_p, the transformed network of Fig. A.3(b) is obtained. Note, capacitances become inductances and vice versa. The final element values are listed in Table A.3 for two different reference resistances.

A.4.2 Fifth-Order Elliptic High-Pass Filter

Let the elliptic high-pass filter be specified by the stopband edge of $f_s = 0.734\,\mathrm{GHz}$ and passband edge of $f_p = 1.276\,\mathrm{GHz}$. Furthermore, the insertion loss must not be less than $\alpha_{\min} = 60\,\mathrm{dB}$ within the stopband while being at most $\alpha_{\max} = 3\,\mathrm{dB}$ for frequencies above the passband edge.

Following (4.107), the edge frequencies with respect to the normalized low-pass filter are $\Omega_p = 0.758\,33$ and $\Omega_s = 1.318\,68$. The selectivity factor becomes $k = \Omega_s^{-2} = 0.575\,07$ while (A.11) yields a discrimination factor of $k_1 = 9.976\,29 \times 10^{-4}$. The minimum order required to satisfy the attenuation thresholds follows from (A.10), and is given by $n = 5$. With the zeros and poles as the solutions of elliptic sine functions according to (A.6), the rational filter function with equiripple behavior in pass- and stopband becomes

$$D(p) \propto p\frac{(p^2 + 0.727\,68^2)(p^2 + 0.474\,68^2)}{(0.727\,68^2p^2 + 1)(0.474\,68^2p^2 + 1)}. \tag{A.20}$$

After determining the scaling factors according to (A.8) and (A.9), the transmission power gain satisfies

$$|s_{21}(p)|^2 = \frac{1 + 1.5097p^2 + 0.808\,41p^4 + 0.180\,12p^6 + 0.014\,235p^8}{1 - 34.066p^2 - 449.34p^4 - 2020.1p^6 - 3772.9p^8 - 2499.1p^{10}}. \tag{A.21}$$

It is seen that its zeros coincide with the purely imaginary poles in (A.20) being located at $\pm j\Omega_{01}$ and $\pm j\Omega_{02}$ with $\Omega_{01} = 1.374\,23$ and $\Omega_{02} = 2.106\,68$. Each conjugated complex pair occurs twice due to the squared property of the transmission power gain. Following the procedure described in Sec. 2.1.4, the reflected power gain is calculated as

$$s_{11}(p)s_{11}(-p) = \frac{-35.575p^2 - 450.15p^4 - 2020.3p^6 - 3772.9p^8 - 2499.1p^{10}}{1 - 34.066p^2 - 449.34p^4 - 2020.1p^6 - 3772.9p^8 - 2499.1p^{10}}. \tag{A.22}$$

By assigning all zeros and poles of the left half plane to $s_{11}(p)$, the reflection coefficient becomes

$$s_{11}(p) = \pm\frac{5.9645p + 37.735p^3 + 49.991p^5}{1 + 7.7160p + 12.736p^2 + 42.438p^3 + 21.683p^4 + 49.991p^5}. \tag{A.23}$$

Table A.3. Lumped circuit parameters of elliptic high-pass realizations.

parameter	unit	third-order elliptic filter†		fifth-order elliptic filter‡	
$R_{1,2}$	[Ω]	1	90.24	1	90.24
L_1	[H]	4.643×10^{-11}	4.190×10^{-9}	4.078×10^{-11}	3.680×10^{-9}
L_{01}	[H]	2.076×10^{-10}	1.873×10^{-8}	2.540×10^{-10}	2.292×10^{-8}
C_{01}	[F]	2.461×10^{-10}	2.727×10^{-12}	2.010×10^{-10}	2.228×10^{-12}
L_2	[H]	4.643×10^{-11}	4.190×10^{-9}	3.121×10^{-11}	2.816×10^{-9}
L_{02}	[H]			6.812×10^{-10}	6.147×10^{-8}
C_{02}	[F]			1.761×10^{-10}	1.952×10^{-12}
L_3	[H]			3.755×10^{-11}	3.388×10^{-9}

† Specifications are $f_s = 0.787\,\text{GHz}$, $\alpha_{\min} = 30\,\text{dB}$, $f_p = 1.191\,\text{GHz}$, $\alpha_{\max} = 3\,\text{dB}$.
‡ Specifications are $f_s = 0.734\,\text{GHz}$, $\alpha_{\min} = 60\,\text{dB}$, $f_p = 1.276\,\text{GHz}$, $\alpha_{\max} = 3\,\text{dB}$.

Referring to Fig. 2.6, each choice of $s_{11}(p)$ yields a different input impedance $Z_{\text{in},1}(p)$ seen from the source towards the load resistance R_2. Note, this has consequences on the topology of the resulting lumped network. Choosing the negative sign in (A.23) and inserting in (2.58), the input impedance normalized to $R_1 = 1\,\Omega$ satisfies

$$Z_{\text{in},1}(p) = \frac{1 + 1.7515p + 12.736p^2 + 4.7022p^3 + 21.683p^4}{1 + 13.681p + 12.736p^2 + 80.173p^3 + 21.683p^4 + 99.982p^5}. \tag{A.24}$$

Since the denominator of (A.20) is an even function of p, the elements of the open-circuit impedance matrix are identified according to (2.60). The impedance functions normalized to $R_1 = R_2 = 1\,\Omega$ are given as

$$z_{11}(p) = \frac{1 + 12.736p^2 + 21.683p^4}{13.681p + 80.173p^3 + 99.982p^5}, \tag{A.25}$$

$$z_{22}(p) = \frac{1 + 12.736p^2 + 21.683p^4}{13.681p + 80.173p^3 + 99.982p^5}, \tag{A.26}$$

$$z_{21}(p) = \frac{1 + 0.754\,84p^2 + 0.119\,31p^4}{13.681p + 80.173p^3 + 99.982p^5}. \tag{A.27}$$

To derive a ladder network realization of the two-port, the driving point impedances z_{11} and z_{22} are expanded into continued fractions. The procedure rests on Properties 2.1.1–2.1.4 of positive real functions and the alteration between impedance and admittance functions as outlined in Sec. 2.1.1. Since $z_{11} = z_{22}$, the resulting network must be symmetric and no private poles are available in either of the driving point impedances. The expansion succeeds in the analogue way as described in Sec. A.4.1. The resulting network is shown in Fig. A.3(a). By mapping the complex p-plane associated with the normalized low-pass according to (4.106) onto the s-plane in which the high-pass filter is defined with the desired stop and passband

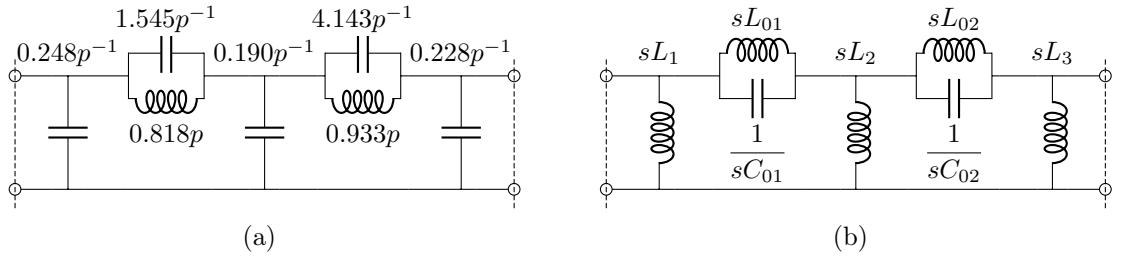

Fig. A.4. (a) Canonical lumped network realization of the normalized low-pass filter function $D(p)$ as given in (A.20) with two transmission zeros at finite, nonzero frequency and another one at $p = \infty$. (b) Transformed network after mapping the complex p-plane onto the s-plane according to (4.106) taking into account the specified stop and passband edge frequencies f_s, f_p.

edge frequencies f_s, f_p, the transformed network of Fig. A.3(b) is obtained. Note, capacitances become inductances and vice versa. The final element values are listed in Table A.3 for two different reference resistances.

A.5 HOM Couplers and Facilities

In the frame of this thesis, a solid coaxial coupler was fabricated out of copper. Likewise, a stainless steel four-way cross was fabricated to characterize the frequency response of HOM couplers foreseen for SPL cavities. The corresponding mechanical drawings were created by F. Pillon on the basis of rf models. Figures A.5 and A.6 show some details of the different assemblies. They present a reference for visualization and discussions in Chapter 5.

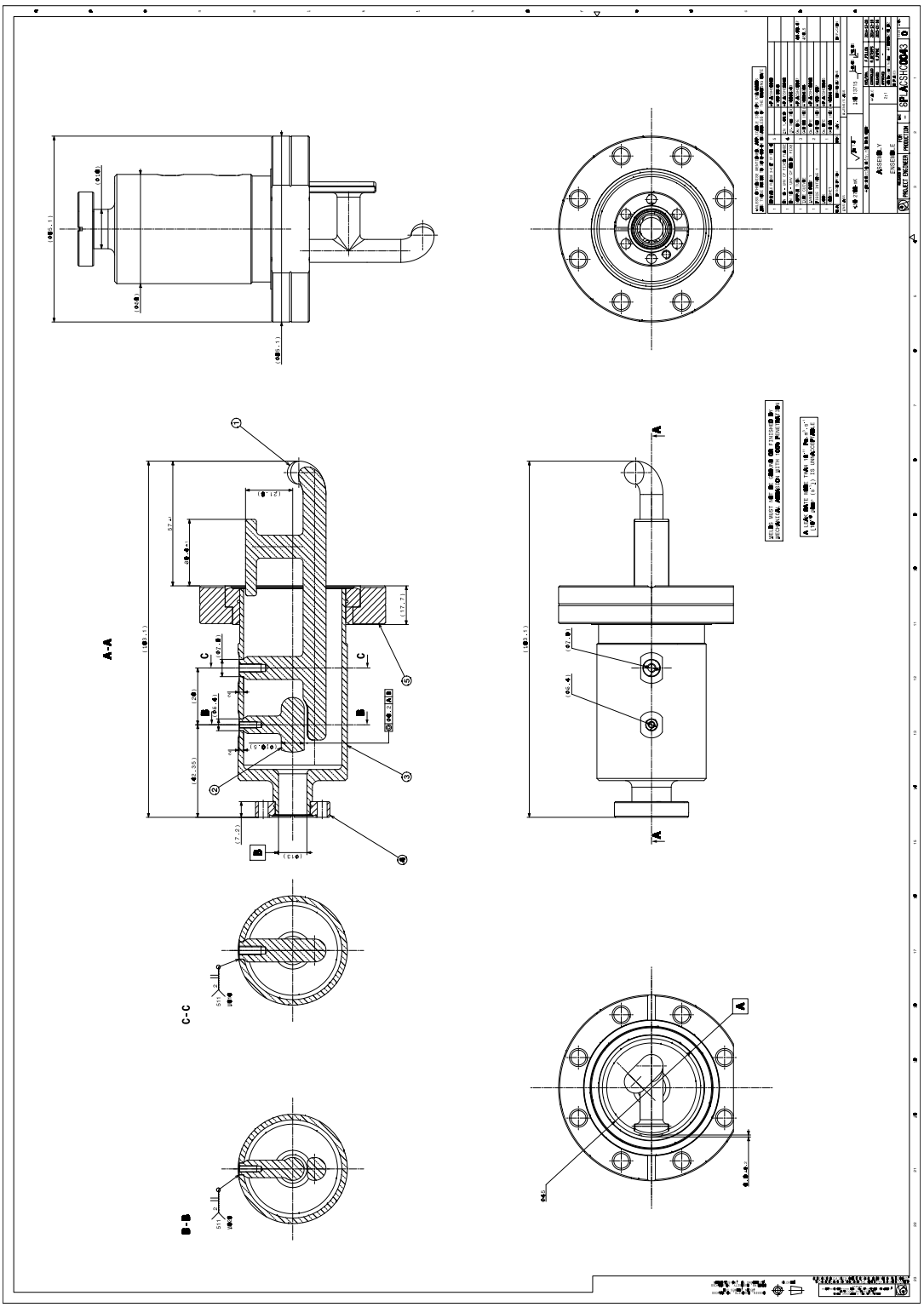

Fig. A.5. Prototype of the P 06 02 coupler fabricated out of copper.

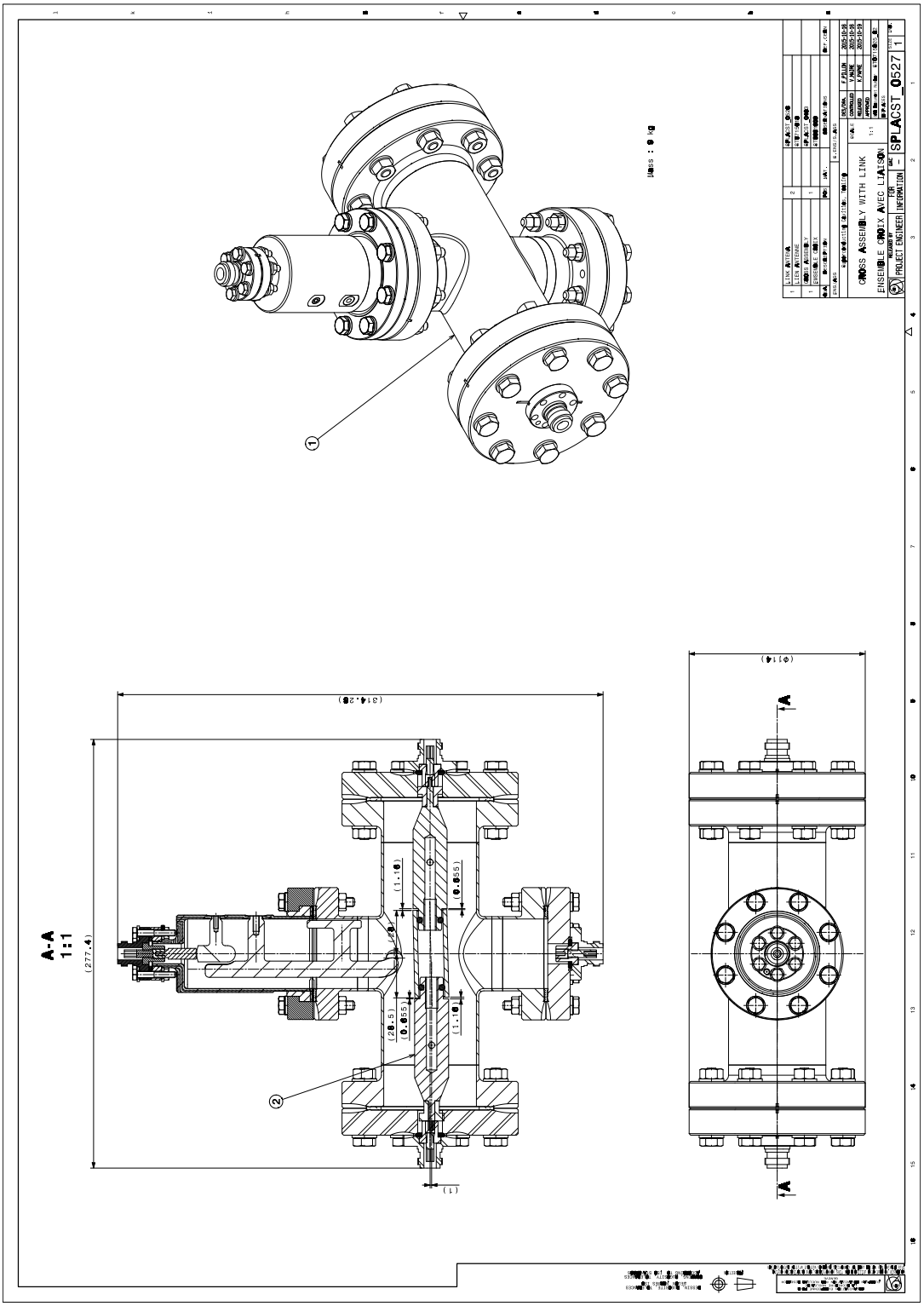

Fig. A.6. Assembly of the four-way cross to measure the frequency response of SPL HOM couplers.

Symbols

a_n, $\bar{a}_n$ poles of the transfer or helper function (introduced on p. 48)
$\mathbf{b}$ magnetic induction
c_0 velocity of light in vacuum
c_n, $\tilde{c}_n$ residues of the transfer or helper function (introduced on p. 48)
$\mathbf{d}$ electric displacement
$\mathbf{e}$ electric field intensity
$\mathbf{e}_i$ unit vector along the coordinate axis i
f frequency
h_{amb} convection heat transfer coefficient to the ambient (introduced on p. 50)
$\mathbf{h}$ magnetic field intensity
$\mathbf{j}$ electric current density
j imaginary unit (square root of -1)
j_{mn}, j'_{mn} n-th root of the Bessel function of first order and m-th mode or its first derivative
$k(T)$ thermal conductivity, generally temperature dependent
k, k_z wave number, general or in longitudinal direction (introduced on pp. 24, 29)
$k_\parallel$, $k_{\parallel,n}$ total or modal loss factor (introduced on p. 40)
$k_\perp$, $k_{\perp,n}$ total or modal kick factor (introduced on p. 40)
k_B Boltzmann constant
$\mathbf{n}$ unit normal vector to the surface $\partial\mathbf{\Omega}$
p normalized complex frequency variable ($p = \Sigma + j\Omega$)
q electric charge of a particle or bunch of particles
$\mathbf{r}$ position vector from the origin ($\mathbf{r} = x\mathbf{e}_x + y\mathbf{e}_y + z\mathbf{e}_z$)
s complex frequency variable ($s = \sigma + j\omega$)
$\mathbf{u}$ displacement vector field
$w_\parallel$, $w_\perp$ longitudinal or transverse wake potentials (introduced on p. 35)
w_n weighting function (defined on p. 67)
$\mathbf{B}$ phasor of a time-harmonic magnetic induction
$D(s)$ filter function (defined on p. 19)
$\mathbf{D}$ phasor of a time-harmonic electric displacement
$\mathbf{E}$ phasor of a time-harmonic electric field intensity
$F(s)$ immittance function (introduced on p. 11)
$H(s)$ transfer function (defined on p. 19)
$\mathbf{H}$ phasor of a time-harmonic magnetic field intensity
$\mathbf{J}$ phasor of a time-harmonic electric current density
$P, P_{\mathrm{loss}}, P_{\mathrm{ext}}$ power, power loss, or extracted power due to coupling mechanisms
Q, Q_0, Q_L, Q_{ext} quality factor, in general, intrinsic, loaded, or external (p. 31)
$(R/Q)_n$, $(R/Q)_{\parallel,n}$, $(R/Q)_{\perp,n}$ geometric shunt resistance, in general, longitudinal, or transverse, each for the mode n (defined on pp. 38, 39)
RRR residual-resistance ratio (introduced on p. 32)

R_s surface resistance (real part of Z_s)
R_{BCS} Surface resistance according to the BCS theory (introduced on p. 33)
R_n shunt resistance for the mode n (defined on p. 38)
SWR voltage standing wave ratio (introduced on p. 32)
T_c critical temperature, for niobium $T_c = 9.2\,\mathrm{K}$
$V_{\parallel}^{(n)}, V_{\perp}^{(n)}$ longitudinal or transverse voltage for a particle passing a cavity which is excited by the n-th mode (defined on p. 38)
$Y(s)$ admittance function (introduced on p. 10)
Y_c characteristic admittance of a transmission line (introduced on p. 24)
$Z(s)$ impedance function (introduced on p. 10)
Z_0 impedance of free space ($Z_0 \approx 377\,\Omega$)
$Z_{\parallel}$, $Z_{\perp}$ longitudinal or transverse beam coupling impedance (defined on p. 35)
Z_c characteristic impedance of a transmission line (introduced on p. 24)
Z_s surface impedance (defined on pp. 28, 32, and 46)
κ coupling coeffiecient (defined on pp. 32, 194)
$\mathbf{S}$ scattering matrix (defined on p. 18)
$\mathbf{T}$ transmission or $ABCD$ matrix (defined on p. 16)
$\mathbf{Y}$ short-circuit admittance matrix (defined on p. 15)
$\mathbf{Z}$ open-circuit impedance matrix (defined on p. 15)
α_T temperature dependent linear thermal expansion coefficient (introduced on p. 51)
$\beta(\omega)$ imaginary part of the wave propagation constant (introduced on p. 24)
β ratio of velocity to the speed of light c_0
ε_0, ε permittivity constant ($\varepsilon_0 \approx 8.854\,\mathrm{pF/m}$), material specific permittivity
ϵ, ϵ_0 longitudinal effective emittance, in general or at the linac input
λ wave length
λ_L London penetration depth (introduced on p. 32)
μ_0, μ vacuum permeability ($\mu_0 \approx 1.256\,\mu\mathrm{H/m}$), or material specific permeability
ω angular frequency
ρ electric charge density in a volume
$\sigma(s)$ helper function to fit a transfer function (introduced on p. 48)
σ electrical conductivity
$\theta(x)$ Heaviside step function
θ terminal pair, terminal plane, or port
ξ mean free path of a single electron (introduced on p. 33)
ζ relative longitudinal coordinate to the bunch center (introduced on p. 33)
$\mathcal{N}$ collection of complex terminal voltages and currents to define network (p. 9)
$\mathcal{U}, \mathcal{U}_e, \mathcal{U}_m$ stored energy, in general, in electric, or in magnetic field
$\Delta\mathcal{E}^{(m)}$ total energy error of a bunch in the m-th cavity (defined on p. 41)
$\Delta\phi_s$ synchronous phase error (introduced on p. 41)
∇ nabla operator
$\mathbf{\Omega}$, $\partial\mathbf{\Omega}$ domain or boundary of the domain
$\mathbf{a}^{\mathsf{H}}, \mathbf{A}^{\mathsf{H}}$ conjugate transpose of the vector $\mathbf{a}$ or matrix $\mathbf{A}$
$\mathbf{a}^{\mathsf{T}}, \mathbf{A}^{\mathsf{T}}$ transpose of the vector $\mathbf{a}$ or matrix $\mathbf{A}$
$\mathbf{I}$ identity matrix
$\Im$ imaginary part of
$\Re$ real part of